



A vegetation study using new remote sensing radar sensors

E. Ndikumana

► To cite this version:

E. Ndikumana. A vegetation study using new remote sensing radar sensors. Environmental Sciences. Doctorat Géomatique, AgroParisTech, Université de Montpellier, 2018. English. NNT: . tel-02611643v1

HAL Id: tel-02611643

<https://hal.inrae.fr/tel-02611643v1>

Submitted on 16 May 2020 (v1), last revised 18 May 2020 (v2)

HAL is a multi-disciplinary open access archive for the deposit and dissemination of scientific research documents, whether they are published or not. The documents may come from teaching and research institutions in France or abroad, or from public or private research centers.

L'archive ouverte pluridisciplinaire **HAL**, est destinée au dépôt et à la diffusion de documents scientifiques de niveau recherche, publiés ou non, émanant des établissements d'enseignement et de recherche français ou étrangers, des laboratoires publics ou privés.

**THESE POUR OBTENIR LE GRADE DE DOCTEUR
DE L'INSTITUT DES SCIENCES ET INDUSTRIES DU VIVANT ET DE
L'ENVIRONNEMENT - AGROPARITECH**

N°: 2018 AGPT 0010

En
GEOMATIQUE

Ecole Doctorale GAIA

(Biodiversité, Agriculture, Alimentation, Environnement, Terres, Eau), n°584

Unité Mixte de Recherche TETIS

**ETUDE DE LA VEGETATION A PARTIR DE NOUVEAUX CAPTEURS
SATELLITAIRES RADAR**

Présentée par
Emile Ndikumana

26 novembre 2018

Sous la direction de:

M. Nicolas BAGHDADI: Directeur de Thèse

M. Dinh Ho Tong Minh: Co-encadrant de Thèse

Devant le jury composé de:

M. Mehrez Zribi	Directeur de Recherche	CNRS	Président et rapporteur
M. Lionel Jarlan	Directeur de Recherche	IRD	Rapporteur
Mme Thuy Le Toan	Ingénieur de Recherche, HDR	CNRS	Examinatrice
M. Valéry Gond	Chercheur, HDR	CIRAD	Examineur
M. Nicolas Baghdadi	Directeur de Recherche	IRSTEA	Directeur de Thèse
M. Dinh Ho Tong Minh	Chargé de Recherche	IRSTEA	Co-encadrant de Thèse



To my family, I missed you, Thank you so much for your patience

ABSTRACT

A Vegetation Study using new Remote Sensing Radar Sensors

In this thesis, we focus on how SAR images can be used to study vegetation. Vegetation lies at the core of human lives by providing both food and economic resources as well as participating in regulating climate. Traditionally, vegetation is classified into three categories: fields, grasslands and forests. We follow this classification in our study. To tackle the first two, we chose to explore rice (in Camargue, France) since rice fields are initially flooded pastures and turn to fields when more mature. We illustrate the last category with forests in Madagascar. The aim of the first part is to provide a better understanding of the capabilities of Sentinel-1 radar images for agricultural land cover mapping through the use of deep learning techniques. We revealed that even with classical machine learning approaches (K nearest neighbors, random forest, and support vector machines), good performance classification could be achieved with F-measure/Accuracy greater than 86% and Kappa coefficient better than 0.82. We found that the results of the two deep recurrent neural network (RNN)-based classifiers clearly outperformed the classical approaches (KNN, SVM and RF). In the second part, the objective is to study the capabilities of multitemporal radar images for rice height and dry biomass retrievals using Sentinel-1 data. To do this, we train Sentinel-1 data against ground measurements with classical machine learning techniques (Multiple Linear Regression (MLR), Support Vector Regression (SVR) and Random Forest (RF)) to estimate rice height and dry biomass. The study is carried out on the same multitemporal Sentinel-1 dataset in the first part. The error of rice height estimation was 16% (7.9 cm), whereas the biomass was 18% (162 g·m⁻²) (both with Random Forest method). Such results indicate that the highly qualified Sentinel-1 radar data could be well exploited for rice biomass and height retrieval and they could be used for operational tasks. Finally, reducing carbon emissions from deforestation and degradation (REDD) requires detailed insight into how the forest biomass is measured and distributed. Studies so far have estimated forest biomass stocks using rough assumptions and unreliable data. We aim to improve on previous approaches by using radar satellite ALOS/PALSAR (25-m resolution) and optical Landsat-derived tree cover (30-m resolution) observations to estimate forest biomass stocks in Madagascar, for the years 2007-2010. The radar signal and in situ biomass were highly correlated ($R^2 = 0.71$) and the root mean square error was 30% (for biomass ranging from 0 to 500 t/ha). Combining radar signal with optical tree cover data appears to be a promising approach for using by L-band SAR to map forest biomass (and hence carbon) over broad geographical scales.

Keywords: SAR images, Sentinel-1, ALOS/PALSAR, Deep learning, Land cover, Rice, Forest.

RÉSUMÉ

Etude de la végétation à partir de nouveaux capteurs satellitaires Radar

Dans cette thèse, nous nous intéressons à la manière dont les images SAR peuvent être utilisées pour étudier la végétation. La végétation est au cœur de la vie humaine en fournissant à la fois des ressources alimentaires, financières et en participant à la régulation du climat. Traditionnellement, la végétation est classée en trois catégories: les champs, les prairies et les forêts. Les travaux de cette thèse s'articulent autour de trois axes : (1) la cartographie de l'occupation du sol, (2) l'estimation des paramètres biophysiques du riz en Camargue à partir des images satellitaires Sentinel-1 (bande C) et enfin (3), la cartographie de la biomasse forestière à Madagascar à partir des données radar ALOS/PALSAR (bande L) combinées avec des données tree cover calculées à partir des données optiques Landsat. L'objectif de la première partie est de fournir une meilleure compréhension du potentiel des images radar Sentinel-1 (bande C) pour cartographier l'occupation du sol à l'aide des techniques d'apprentissage en profondeur. Nous avons obtenu de bons résultats avec la "F-Measure/Accuracy" supérieure à 86% et le meilleur coefficient Kappa de plus de 0,82. Nous avons constaté que les résultats des deux classificateurs basés sur les réseaux neuronaux récurrents profonds (RNN) dépassaient clairement les approches classiques de Machine Learning (KNN, SVM et RF). Dans la seconde partie, l'objectif est d'étudier la capacité des images radar multitemporelles pour l'estimation de la hauteur du riz et de la biomasse sèche à l'aide des données Sentinel-1. Pour ce faire, nous avons utilisé les données de Sentinel-1 en appliquant des techniques classiques d'apprentissage de "Machine Learning" (MLR, SVR et RF) pour estimer la hauteur du riz et la biomasse sèche. L'erreur de l'estimation de la hauteur du riz est de 16% (7.9 cm), et celle la biomasse est de 18% (162 g.m⁻²) (les deux avec la méthode Random Forest). Ces résultats indiquent que les données radar Sentinel-1 pourraient être exploitées pour l'estimation de la biomasse. Enfin, la réduction des émissions de carbone dues à la déforestation nécessite un aperçu de la façon dont la forêt de biomasse est mesurée et distribuée. Nous utilisons des observations du radar satellitaire ALOS/PALSAR (résolution de 25 m) et des données optiques du capteur Landsat (résolution de 30 m) pour estimer les stocks de biomasse forestière à Madagascar, pour les années 2007-2010. Le signal radar et la biomasse in situ étaient fortement corrélés ($R^2 = 0,71$) et l'erreur quadratique moyenne était de 30% (pour la biomasse allant de 0 à 500 t/ha). Le signal radar (données SAR en bande L) combiné avec les données optiques semblent être une approche prometteuse pour cartographier la biomasse forestière.

Mots-clés: SAR, Sentinel-1, ALOS/PALSAR, Deep learning, Occupation du sol, Riz, Forêt.

TABLE OF CONTENTS

Abstract	iii
Résumé	v
	Page
List of Tables	xi
List of Figures	xiii
1 Introduction	1
1.1 Context	1
1.2 Research problem and Objectives	2
1.3 Contributions	3
1.4 Thesis outline	4
2 Synthetic Aperture Radar application on vegetation	7
2.1 Introduction	7
2.2 SAR imagery	7
2.2.1 General information on SAR images	7
2.2.2 SAR resolution	9
2.2.3 Speckle in SAR images	10
2.2.4 Polarimetric signature of a target	10
2.2.5 Sentinel-1 and ALOS/PALSAR characteristics	12
2.3 Sensitivity of Radar Signals to Vegetation	14
2.3.1 SAR scattering mechanisms for vegetation	14
2.3.2 Penetration depth and radar frequency	15
2.3.3 Radar backscatter and biomass	16
2.4 SAR Applications on vegetation	17
2.4.1 Land cover classification	17
2.4.2 Rice parameters estimation	19
2.4.3 Forest biomass retrieval	21
3 Deep Recurrent Neural Network for Agricultural Classification	23
3.1 Introduction	23
3.2 Study Area	24

3.2.1	Camargue Site	24
3.2.2	Ground Data	25
3.3	SAR Data and Processing	26
3.3.1	SAR Data	26
3.3.2	Pre-Processing Data	27
3.3.3	Temporal Filtering	28
3.3.4	Geocoding	28
3.4	Classical Machine Learning Approaches	28
3.4.1	K Nearest Neighbors	28
3.4.2	Random Forest	29
3.4.3	Support Vector Machine	29
3.5	Recurrent Neural Network	29
3.5.1	Long-Short Term Memory (LSTM)	30
3.5.2	Gated Recurrent Unit (GRU)	31
3.5.3	RNN-Based Time Series Classification	31
3.6	Experimental Results	32
3.6.1	Experimental Settings	32
3.6.2	Results	33
3.6.3	Discussion	36
3.7	Conclusions	38
4	Estimation of Rice Height and Biomass	39
4.1	Introduction	39
4.2	Study Area	41
4.2.1	Camargue Study Site	41
4.2.2	Rice Phenomena	41
4.2.3	Ground Data Measurement	43
4.2.4	SAR Data	45
4.3	Method	46
4.3.1	Multiple Linear Regressions	46
4.3.2	Support Vector Regressions	46
4.3.3	Random Forest	46
4.3.4	Model Assessment	47
4.4	Results	47
4.4.1	Experimental Settings	47
4.4.2	Ground Measured Results	48
4.4.3	Backscattering Coefficients According to Rice Parameters	49
4.4.4	Rice Height Estimation	50
4.4.5	Rice Biomass Estimation	52
4.5	Discussion	53
4.6	Conclusions	55

5 Combining ALOS/PALSAR and Landsat-derived tree cover data for forest biomass retrieval	57
5.1 Introduction	57
5.2 Data and Methods	59
5.2.1 Study area	59
5.2.2 Field data	59
5.2.3 Tree cover data	61
5.2.4 SAR data	61
5.2.5 Proposed methodology for biomass retrieval	62
5.2.6 Calibration for Madagascar	64
5.2.7 Carbon estimation and uncertainty	65
5.3 Results	65
5.4 Discussions	68
5.5 Conclusions	71
6 Conclusion and outlook	73
Publications	77
Acknowledgements	79
Bibliography	81
Appendix A	99
Appendix B	117
Appendix C	137
Appendix D: Synthèse en Français	147

LIST OF TABLES

TABLE	Page
2.1 Imaging radar bands	8
2.2 Main characteristics of the Sentinel-1 nominal measurement modes	13
2.3 Typical applications mapped to modes	13
2.4 ALOS-1/PALSAR and Sentinel-1 SAR sensor parameters	14
3.1 The distribution of the number of pixel and plots per class.	26
3.2 The average and standard deviation from cross-validation 5 times on the time series SAR Sentinel-1 data.	33
3.3 The distribution of the agricultural land cover class in 2017.	36
4.1 Agricultural calendar and rice cycle in Camargue [7]	42
4.2 Description of reference plots in Camargue.	44
4.3 Rice height estimation using MLR, SVR and RF methods with 5 folds cross-validation. Best results are in bold.	50
4.4 AIC and BIC for rice height estimation. The smallest values are in bold.	50
4.5 Rice biomass estimation from five folds of cross-validation. The best results are in bold.	52
4.6 AIC and BIC for rice biomass estimation. The smallest values are in bold.	52
5.1 Surface area (ha) and carbon assessment (PgC) in Madagascar with respect to the dry, spiny and moist forest ecoregions.	68

LIST OF FIGURES

FIGURE	Page
2.1 SAR operation	8
2.2 Polarization H and V for Radar	11
2.3 Backscattering contributions from vegetation canopy	15
2.4 Illustration of penetration properties in a tropical forest for X, C and L bands. Three targets are taken into account: Forest, Dry deposits and Soil	16
3.1 Camargue study area. Colored polygons represent 921 reference plots location. The study area is limited by the cyan polygon.	26
3.2 The temporal profiles of the eleven different classes which respect to the VH (a) and VV (b) polarizations.	27
3.3 The average and standard deviation of the eleven different classes for VV and VH polarizations.	27
3.4 RNN Unit (on the left) and unfolded structure (on the right).	30
3.5 The schematic view of the RNN <i>LSTM</i> -based architecture. By replacing <i>LSTM</i> to <i>GRU</i> unit, we get the RNN <i>GRU</i> -based architecture.	32
3.6 Per Class F-Measure of the different approaches.	34
3.7 Confusion matrices on the SAR Sentinel-1 time series data of the different approaches: (a) <i>KNN</i> , (b) <i>RF</i> , (c) <i>SVM</i> , (d) <i>LSTM</i> and (e) <i>GRU</i> . The name of the labels: (1) <i>rice</i> ; (2) <i>sunflower</i> ; (3) <i>lawn</i> ; (4) <i>irrigated grassland</i> ; (5) <i>durum wheat (winter)</i> ; (6) <i>alfalfa</i> ; (7) <i>tomato</i> ; (8) <i>melon</i> ; (9) <i>clover</i> ; (10) <i>swamps</i> ; and (11) <i>vineyard</i>	34
3.8 The agricultural land cover map in Camargue using the RNN-based <i>GRU</i> multitemporal SAR Sentinel-1.	35
3.9 A zoom version of the white-border box in the Figure 3.8 is provided to facilitate visualization of classification results. (a) reference plots; (b) the classical <i>SVM</i> result and (c) the RNN-based <i>GRU</i> result.	35
4.1 Rice crop growth calendar in Camargue.	42
4.2 Camargue study area. (a) The agricultural land cover map in 2017 [125]. The green color indicates the rice extent of the Camargue region. (b) The zoom version of the white polygons represents the location of reference plots where measurements were made at every 12 days from May to September 2017.	44
4.3 The reference plot 1G3 is marked in the figure (coordinates of central point 43°34'30"N, 4°30'32"E) together with its photos at different dates.	45

4.4	Temporal variation of the rice height and biomass versus to acquisition dates of Sentinel-1 data.	48
4.5	Sentinel-1 backscattering coefficients according to (a) Days after sowing; (b) VV and VH distribution; (c) Rice height; (d) Rice biomass.	49
4.6	Rice height estimation using MLR, SVR and RF methods. In this figure, the configurations that provide the best results are considered (with dual-polarization VV and VH model).	51
4.7	Rice height retrieval and in-situ measurements at two reference plots 2M2 and 4M2.	51
4.8	Rice biomass estimation using MLR, SVR and RF methods. In this figure, only the configurations that provide the best results are considered (with dual-polarization VV and VH model for MLR, and with VH model for SVR and RF).	52
4.9	Rice biomass retrieval and in-situ measurements at two reference plots 1G3 and 3M1.	53
5.1	The study site is the entire island of Madagascar. The background is the Landsat-derived tree cover. Red, yellow and black circles represent field sites in dry forest, moist forest and spiny forest, respectively.	60
5.2	Biomass measured in situ in spiny (a), dry (b) and moist (c) forest ecoregions. Number of plots sampled were 60, 84 and 428, respectively.	61
5.3	The joint distribution between Landsat-derived tree cover and biomass measured in situ. More than 98% of plots with AGB > 150 t/ha had tree cover of 95% or greater. .	62
5.4	(a) Biomass measured in situ versus γ_{HV}^0 . (b) Biomass measured in situ versus γ_{HVtree}^0 .	63
5.5	(a) Biomass measured in situ versus γ_{HV}^0 . (b) Biomass measured in situ versus tree cover. (c) Biomass measured in situ versus γ_{HVtree}^0 . The blue line is the best fit of the data.	63
5.6	(a) The biomass inversion performance of this study. (b) Performance in the study of [172]. Top panels are the cross-plot 1:1. Bottom panels are the bias. The biomass retrieval appears to be reliable for biomass ranging from 0 to 300 t/ha.	66
5.7	Biomass maps for Madagascan forests for the year 2010 are shown. The color scale varying from yellow to green to blue illustrates the full biomass range from 0 to 500 t/ha. The spatial distribution of biomass for the entire island of Madagascar shows a west-east gradient. (a) Map from the study of [172] and (b) Map from this work. The bottom panels show a zoom version of red-bordered boxes to facilitate visualization of the biomass results.	67
5.8	Map of change in Madagascar forest carbon stocks in the period 2007-2010. A zoom version of the red-bordered box is provided to facilitate visualization of the carbon loss in Kirindy. The top right panel is the histogram showing distribution of values, excluding values of zero.	69

INTRODUCTION

1.1 Context

The increase of the world population and consequently of its needs exert an increasing pressure on the vegetation. Usually, vegetation is classified into forests, agricultural plants and grasslands. Vegetation has always been an extremely important natural resource for man; first as food (agriculture), then to meet the needs of daily life (forest products, heating), environmental protection (forest biomass), need for farming and finally because of its economic potential. Forests are the first supplement of wood for both construction and fire woods in urban and villages centers.

In the world, exploitations for wood supplement are so anarchic that the extent of the forests has decreased. On the other hand, during these last years, the expanses of agricultural lands have decreased leaving space for the sprawl of the towns and villages. Problems related to the reduction of agricultural lands and forests have been the main concern for political decision-makers. For example, most developed and even developing countries have had to define farms and forests for management in order to avoid forest depletion. Monitoring the dynamics of agricultural land, grassland areas and the inventory of forest resources are the first elements to control to meet the needs of the population.

Regarding the protection of the environment, an awareness of global environmental issues has prompted the international community to adopt solutions to respect ecological constraints in a coordinated manner. For example, various agreements have been signed, such as the Kyoto Protocol (1997) and the United Nations Framework Convention on Climate Change (1992) [169]. In the context of sustainable management of plant resources, decision making, implementation of information tools that include the design of measurement systems, and the acquisition of data by these systems, the processing, and analysis of acquired data are necessary. The monitoring of these plant resources often becomes difficult due to the lack of accessibil-

ity of agricultural areas and especially forest areas. By using remote sensing data available at large areas with different spatial and temporal resolutions, it is possible to monitor forest, agricultural areas, and grasslands at the appropriate time. Currently, observation from space is presented as one of the effective solutions to the permanent acquisition of information on the sustainable management of plant resources and territories. In the same way, new generations of earth observation satellites are constantly being increased. These remote sensing satellites present an opportunity to evaluate the characteristics of the vegetation.

The remote sensing data provide a great opportunity to monitor and provide information on crop fields or forests at a given scale and time. Radar remote sensing techniques are particularly interesting because unlike optical remote sensing techniques, the acquisition of images is independent of weather conditions and light conditions (day, night). Optical sensors are limited by the atmospheric cloud layer in tropical and subtropical areas where rice cultivation is grown on a large scale [11]. Synthetic Aperture Radar (SAR) systems have the ability to penetrate the atmospheric layer to the ground. SAR data are also well suited to distinguish rice from other types of vegetation cover because of the radar's specific response to flooded vegetation [163].

In order to estimate the physical parameters of the vegetation, remote sensing is preferred since it makes it possible to use the properties of the satellites, repetitiveness and sweeping of large areas. Among the space solutions, radar sensors present high sensitivity to the constituent elements of biomass, and therefore seem the most suitable to estimate it with sufficient precision. In addition, centimeter wavelength radar sensors are insensitive to cloud cover, which is beneficial for tropical forest observation include a large biomass where the presence of clouds is recurrent [51]. More advanced radar remote sensing systems are deployed, for example, Sentinel-1 (C-band) and ALOS-1/PALSAR (L-band). Thus, the SAR Radar Remote Sensing domain continues to provide advances in technology, a growing range of data sources, and new research opportunities for vegetation monitoring.

1.2 Research problem and Objectives

As mentioned above, natural resources are under pressure and facing several problems such as exhaustion, misuse or pollution. Actors have studied variety of ways to cope with these pressures over centuries. In this thesis, we decided to focus on the study of vegetation using radar remote sensing focusing on Sentinel-1 and ALOS-1/PALSAR sensors. The application of remote sensing data for forest management has shown that it requires the use of large wavelength sensors (L and P-bands) due to the ability to penetrate in vegetation and soil [50]. For the forest, issues are closely related to the knowledge of the quantity of forest mass. So how to evaluate the amount of vegetation biomass in the long term? What is its dynamics? What is its spatial distribution? Our study leads us to answer all these questions by choosing the type of remote sensing data suitable for vegetation monitoring. Thus, this leads us to the choice of the frequency band in which the selected sensors operate.

The second type of vegetation selected for our study is rice. Rice is a crop, before maturity is similar to irrigated grasslands. While at maturity, the rice looks like wheat. Both crops (rice and wheat) are of paramount importance for feeding the world's population. Rice accounts for about 20% of the world's total grain production, second only to wheat [2]. Questions arise about rice cultivation: how to estimate its biophysical parameters? such as biomass, and height.

This research is based on experimental work with a correlation between the in situ observation results and results provided by the new radar satellites (Sentinel-1 and ALOS/PALSAR). The general objective of this research is to provide a better understanding of the capabilities of radar images for estimations parameters (rice and forest) and mapping the different crops. To apply Sentinel-1 data for rice parameters estimation or land cover mapping, we used the Machine Learning methods. For forest biomass estimation, we combine ALOS/PALSAR with optical Landsat tree cover data in Madagascar.

1.3 Contributions

There are three main axes of this study:

- First, we developed a new method that demonstrates the ability of SAR Sentinel-1 data for land cover classification. Our work has highlighted the relevance of two deep Recurrent Neural Networks approaches that explicitly consider the temporal correlation of Sentinel-1 data in order to discriminate between agricultural classes of land cover, usually characterized by similar but complex temporal behaviors. We can summarize these as following:
 1. we propose a method for mapping agricultural land cover at larger scales using Sentinel-1;
 2. we demonstrate the value-added of time series for crop land, crop group or crop type mapping;
 3. we show the appropriateness of deep learning models (RNNs) which explicitly consider the temporal correlation of the data in order to discriminate among agricultural classes of land cover.
- Second, we evaluated the capabilities of Sentinel-1 SAR data to estimate the biophysical parameters of rice in the Camargue region where three classical machine learning approaches were applied on Sentinel-1 data. We can summarize our contributions as following:
 1. we propose to combine remote sensing data and machine learning methods for the estimation of rice parameters;
 2. we identify ways of growing rice or other practices related to rice cultivation;
 3. we find that radar backscattering coefficients are sensitive to rice biophysical parameters and have a strong correlation with rice height and biomass.

- Third, we combine SAR (ALOS/PALSAR) with optical (Landsat tree cover) data to study their usefulness for forest biomass retrieval. We adapted a method that improves biomass retrieval by combining radar intensity and tree cover data, which has increased the correlation between the radar signal and biomass. We can summarize these as below:

1. we propose a method for forest biomass estimation and carbon for the entire island of Madagascar;
2. we have shown that combination SAR (ALOS/PALSAR) with optical (Landsat tree cover) data appears as a suitable tool for estimating forest biomass with excellent spatial resolution;
3. we produce forest biomass and carbon maps at 25-m in Madagascar for 2007–2010.

1.4 Thesis outline

The content of this thesis is presented in six consecutive chapters. Chapter 1 presents the context, problem statement, research objectives, contributions, and organisation of the thesis.

Chapter 2 provides an overview of literature on Synthetic Aperture Radar applications on vegetation. The purpose of this chapter is to provide the basic information on SAR data. The following chapters are written as independent works that have been submitted to scientific journals and published. Therefore each chapter can be read without the necessity of reading the previous chapter.

In chapter 3, the problem of agricultural classification using multitemporal SAR Sentinel-1 by deep learning application is discussed. This chapter will report the results related to land cover classification in Camargue, southern France, carried out on the basis of deep learning method and Sentinel-1 data acquired in 2017 campaign. The paper of this chapter was published to the Remote Sensing in August 2018 (see Appendix A) [125]).

Chapter 4 presents the estimation of rice Height and Biomass using multi-temporal SAR Sentinel-1 for Camargue. This chapter proposes a better understanding of rice parameters estimation via multi-temporal SAR Sentinel-1 data by applying machine learning methods. The paper of this chapter was submitted to the Remote Sensing in September 2018 (see Appendix B) [126].

Chapter 5 shows the potential value of combining ALOS/PALSAR and Landsat-derived tree cover data for forest biomass retrieval in Madagascar. Combining radar signal with optical tree cover data appears to be a promising approach for using L-band SAR to map forest biomass over broad geographical scales. The paper of this chapter was published to the Remote Sensing of Environment in May 2018 (see Appendix C) [116].

Finally, chapter 6 summarizes this thesis by highlighting the conclusions from previous chapters, contribution to science and the suggestions for further research are also presented.

SYNTHETIC APERTURE RADAR APPLICATION ON VEGETATION**2.1 Introduction**

The remote sensing domain covers all the knowledge and technologies used to determine the biophysical characteristics of objects by remote measurements, without physical contact with them. It is an attractive approach for applications related to vegetation mapping and monitoring. SAR is among the instruments used in remote sensing. SAR is defined as a microwave imaging method used to monitor the diffusion properties of the Earth's surface. The main difference between SAR and the conventional Real Aperture Radar is the higher resolution of SAR, obtained by exploiting the Doppler shifts of the received electromagnetic echoes [40]. The SAR system works by active illumination of the target and coherent recording of the scattered field. In remote sensing, the radar sensors have the advantage of operating independently of natural illumination (active sensor) and weather conditions.

This chapter is devoted to the presentation of SAR data application on vegetation. We discuss the different characteristics of SAR imagery in section 2.2, thereafter, we analyze the sensitivity of SAR data to vegetation (section 2.3). In the end, we talk about the applications of SAR data on vegetation (section 2.4).

2.2 SAR imagery**2.2.1 General information on SAR images**

The acquisition of information about an object or phenomenon by remote sensing requires special instruments. The acquisition principle normally uses the measure of electromagnetic radiation emitted or reflected from objects in a certain frequency range (infrared, visible, microwave). These objects emit or reflect radiation at different wavelengths and intensities depending on their state.

Depending on the range of wavelength in which the sensors operate, we distinguish between passive remote sensing (Optics) and active remote sensing (Radar). The microwave domain includes the wavelength of about 1 mm to 1.3 m. Unlike optical sensors, which are passive systems, active sensors do not depend on solar conditions and can operate day or night. SAR systems can acquire images regardless of weather conditions. These active systems send an electromagnetic signal to illuminate the area to be imaged and measure the signal backscattered by the targets. In figure 2.1, the earth surface is illuminated with an electromagnetic beam emitted by an antenna and the backscattered energy is caught, generally by the same antenna which is connected in reception position.

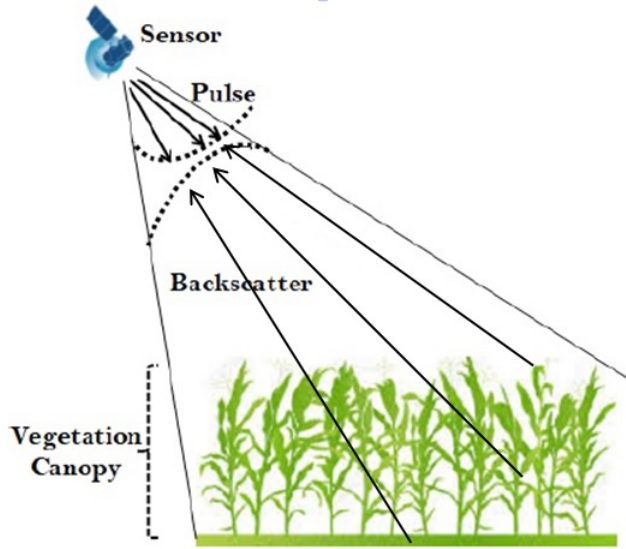


Figure 2.1: SAR operation

The waves used by the radar are generally classified in bands according to their wavelength (λ). The fundamental law often used for electromagnetic waves is the conversion of wavelengths into their frequency (ν) and vice versa: $C = \lambda \cdot \nu$ where C is the speed of light $= 3 \times 10^8 \text{ ms}^{-1}$, λ is the radar wavelength (m), ν is the radar frequency (Hz).

Table 2.1 shows different radar bands and X, C and L are the most commonly used bands.

Band Designation	Wavelength (cm)	Frequency (GHz)
Ka	0.75 – 1.10	27 – 40
K	1.10 – 1.67	18 – 27
Ku	1.67 – 2.40	12 – 18
X	2.40 – 3.75	8 – 12
C	3.75 – 7.50	4 – 8
S	7.50 – 15.0	2 – 4
L	15.0 – 30.0	1 – 2
P	30.0 – 130	0.3 – 1

Table 2.1: Imaging radar bands

The letters shown in Table 2.1, indicate the frequency band at which a radar operates. The letters P, L, S, X and K were introduced during the Second World War for secrecy purposes and

continued to be used even after the war to describe the frequency band without using the exact frequencies at which the radar operates [156].

According to the wavelength, the radar signal is independent of the atmosphere's interaction. Radar signals have longer wavelengths and can pass through clouds and the atmosphere of a planet with little dispersion [102]. The centimetric domain is interesting because the atmosphere does not dissipate the energy of centimetric waves and the images rendering is therefore independent of the meteorological conditions [51]. The waves have a sufficient phase stability to be qualified coherent and allow to know the distance of a target by correlation between the pulses emitted and the echoes received [108, 19].

2.2.2 SAR resolution

The development of new technologies for satellite imagery and the increase in the number of earth observation satellites makes it possible to obtain geographic information that is increasingly accessible and more useful. Satellites are used in more and more fields and differ according to their characteristics and their operating mode. For instance, in a given domain, the satellite choice depends largely on its spatial resolution and spectral band [81, 133]. When we are talking about SAR data, we are usually referring to pixels size. These pixels are typically described by resolution: spatial and temporal resolution. Some data have a very fine spatial resolution, others have many polarimetric bands (mono, multi or full polarimetric). Some have a very short revisit time and others have the possibility of mapping large areas. It is advisable to analyze these different characteristics which controls the choice of a sensor (satellite) for a mission.

2.2.2.1 Spatial resolution

In remote sensing, the distance between the sensor and the target plays a vital role in distinguishing the different characteristics of the objects. Sensors embedded at great distances relative to their target are able to image large areas but are not able to discern the details on the targets [150, 99]. The higher the spatial resolution, is the more we have details on targets. The spatial resolution of the sensor refers to the size of the smallest possible feature that can be detected. High resolution images allow the identification of smaller elements. The current development of satellites allowed us to have images with a spatial resolution equal to or greater than 1 m [182].

To identify the spatial resolution at a point in a radar image, it is important to take the resolution in two aspects: the range and azimuth resolution. The range resolution is proportional to the length of the microwave pulse. Shorter pulse duration gives higher range resolution. The ability of a radar system to distinguish targets at the same range but along different radial lines from the antenna is the azimuthal resolution [32]. As the images consist of pixels (square

matrices of elements), it becomes imperative to determine the relationship between spatial resolution and pixels size.

2.2.2.2 Temporal resolution

Another important resolution in remote sensing is temporal resolution. This resolution refers to the time it takes for a satellite to complete an orbital cycle. This cycle corresponds to the revisit time of a satellite to picture exactly the same scene. The revisit time (temporal resolution) depends on the capacity of the satellite and its sensors, the area of mowing overlap and the latitude at which the satellite is moving. During the different imaging, the image spectral characteristics may vary and the images may differ from each other. This is called multitemporal images. The concept of multitemporal images plays very important role, especially in vegetation monitoring. Indeed, the vegetation being in constant evolution, its monitoring by remote sensing requires a permanent collection of the images.

2.2.3 Speckle in SAR images

Radar images are characterized by the presence of speckle which interferes with sharpness on the images. This corrupts both the amplitude of the images and the phase, which degrades the images quality and, consequently, reduces the efficiency of their analysis and interpretation. In the case of SAR images, the processing is pixel per pixel, and therefore, with the speckle presence in images, their processing becomes more impeded. To reduce the speckle, the designer of the SAR processing system must specifically take into account the need for averaging of several independent samples [168]. Speckle reduction which can be made by filtering is usually done before image interpretation and analysis. Filtering makes it possible to eliminate as much as possible the speckle phenomenon, while minimizing the alterations that the image can undergo by applying a filter: preservation of radiometric information, contours, textures.

2.2.4 Polarimetric signature of a target

The ability of antennas to emit "polarized" waves, for which we can analyze the behavior of the electric field vector during propagation, leads us to the study of polarimetric images. In figure 2.2, the antennas are capable of transmitting and receiving two particular polarizations: one called H (direction of the field \vec{E} perpendicular to the incidence plane), the other called V (direction of the field \vec{E} parallel to the incidence plane).

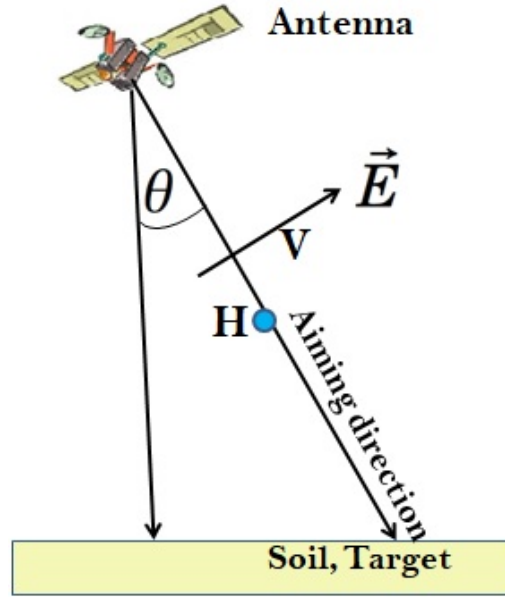


Figure 2.2: Polarization H and V for Radar

We can have a total of 4 possibilities: HH , HV , VH , VV from which one has to be subtracted because for monostatic radars, $HV = VH$. When the two polarizations are the same on emission and reception (HH or VV), the acquisition is said to be in parallel polarization; for two perpendicular directions (HV or VH), it is called cross-polarization [63].

Radar systems can have one, two or all four of these transmit/receive polarization combinations; i.e single polarized [HH or VV (or possibly HV or VH)], dual polarized (HH/HV , VV/VH , or HH/VV), fully polarimetric (HH , VV , HV , and VH). SARs that measure all four modes (HH , HV , VV , VH) are called polarimetric SARs that operate in a quad-pol mode. These concepts of full and dual polarimetry have become popular in SAR remote sensing.

Each polarization has specific sensitivity. The polarization HH has high penetration power into vegetation whereas VV polarization is very sensitive to the vertical elements [142]. HV polarization has a strong sensitivity to the volume of the canopy. The penetration capacity of the waves increases with the wavelength thus the plant structures can be seen at different depths according to the wavelength (P band, L band, C band). For rice canopy monitoring, a diffusion process model may be applicable in C and L bands, but not suitable in Ka and Ku bands (wavelength of 0.75 to 1.10 cm and 1.67 to 2.40 cm respectively). For instance, in the Water Cloud model [72], LAI was a better canopy descriptor for the C band, while the total fresh biomass was a better canopy descriptor for the L band.

The reflection properties of the waves by the objects are expressed in a surface unit (m^2) of interception of the incident electromagnetic radiation by a standard object (sphere). The section of this sphere represents the reflection capacity of the object. This effective section is symbolized by σ . For the remote sensing of terrestrial resources, the effective section by an area

is called the radar backscattering coefficient, σ^0 . The backscattering coefficient σ^0 depends on the following parameters:

- angle of incidence and azimuth (θ, φ);
- polarization (HH, VV, HV, VH);
- dielectric characteristics of the medium: dielectric constant ϵ ;
- geometry of the surface.

We have:

$$(2.1) \quad \sigma^0(\theta, \varphi) = \left\{ \frac{(4\pi)^3}{\lambda^2} \frac{R^4}{SG^2(\theta, \varphi)} \right\} \frac{P_r(\theta, \varphi)}{P_t(\theta, \varphi)}$$

Where λ = emission wavelength (in m);

R = target distance-antenna (in m);

S = target area (in m^2);

G (θ, φ) = gain of the antenna;

$P_r(\theta, \varphi)$ = received power (in W);

$P_t(\theta, \varphi)$ = transmitted power (in W).

2.2.5 Sentinel-1 and ALOS/PALSAR characteristics

The satellite radar synthetic aperture (SAR) is now increasingly used [25], through the platforms such as: ERS SAR; ENVISAT ASAR; RADARSAT-1 SAR; JERS-1 SAR; ALOS/PALSAR; RADARSAT-2; Sentinel-1. In the following, we will focus on the characteristics of the two satellites Sentinel-1 and ALOS/PALSAR because:

- i) Sentinel-1 sensor have a high spatial and temporal resolution and its data are free;
- ii) ALOS/PALSAR have an ability for monitoring and penetration in forest.

a) Sentinel-1

Sentinel-1 is the Copernicus Programme satellite constellation conducted by the European Space Agency. This space mission is composed of two satellites, Sentinel-1A and Sentinel-1B, respectively launched in 2014 and 2016 [3]. As SAR [Sensors](#), Sentinel-1 is an imaging radar which provides data at any weather conditions, day and night imagery, that [operates](#) at C-band (3.75-7.50cm). The Sentinel-1 mission is designed to provide enhanced revisit frequency, coverage, timeliness, and reliability for operational services and applications requiring long time series. The main applications are maritime and land monitoring, emergency management, and mapping applications. The Sentinel-1 SAR operates in one of four nominal acquisition modes (see table 2.2) [163].

Parameter	Interferometric Wide-swath mode (IW)	Wave mode (WV)	Strip Map mode (SM)	Extra Wide-swath mode (EW)
Polarisation	Dual (HH+HV, VV+VH)	Single (HH, VV)	Dual (HH+HV, VV+VH)	Dual (HH+HV, VV+VH)
Incidence angles	31°– 46°	23°– 37°	20°– 47°	20°– 47°
Azimuth resolution	< 20 m	< 5 m	< 5 m	< 40 m
Ground range resolution	< 5 m	< 5 m	< 5 m	< 20 m
Azimuth and range looks	Single	Single	Single	Single
Swath	> 250 km	vignette 20x20 km	> 80 km	> 410 km
Radiometric accuracy	1 dB (3 σ)	1 dB (3 σ)	1 dB (3 σ)	1 dB (3 σ)

Table 2.2: Main characteristics of the Sentinel-1 nominal measurement modes

The application can best be served by specific Sentinel-1 acquisition modes and product types as shown in the table 2.3 [128]. The Interferometric Wide swath mode is the primary operation mode for most applications over land.

Application	Mode			
	SM	IW	EW	WV
Arctic and sea-ice		X	X	
Open ocean ship surveillance		X	X	
Oil pollution monitoring		X	X	
Marine winds		X	X	X
Forestry		X		
Agriculture		X		
Urban deformation mapping		X		
Flood monitoring	X	X		
Earthquake analysis	X	X		
Landslide and volcano monitoring	X	X		

Table 2.3: Typical applications mapped to modes

Knowledge of acquisition modes is an important factor because spatial resolution depends on it. For the temporal resolution, each Sentinel-1 satellite is in a near-polar orbit with a 12-days repeat cycle, i.e in a single pass (ascending or descending). Both Sentinel-1A/B are on the same orbit plane with an orbital phase difference of 180°, thus the temporal resolution is 6 days for the two Sentinel-1 satellites.

b) ALOS-1/PALSAR

ALOS-1/PALSAR is a satellite that was launched (24 January 2006) by the Japan Aerospace Exploration Agency (JAXA) [124]. This satellite provided data between 2006 and 2011 while ALOS-2, which was launched in 2014, still provides data. ALOS-1/PALSAR data are often used for mapping and the earth observation, for monitoring natural resources and disasters. ALOS-1 satellite has 3 instruments (sensors) for remote sensing:

- PRISM (Panchromatic Remote Sensing Instrument for Stereo Mapping): a panchromatic

sensor for mapping in stereo mode. Its main application is the realization of digital elevation models;

- AVNIR2 (Advanced Visible and Near Infrared Radiometer Type 2): a multispectral sensor for the observation of the occupation of the ground;
- PALSAR (Phased Array type L-band SAR): a sensor active in the microwave field for observing the Earth's surface during the day and at night on clear or cloudy days.

PALSAR is an active microwave sensor that uses the L-band frequency. It allows imagery acquisition with dual polarizations: HH+HV or VV+VH, simple polarization HH or VV and acquisitions with full polarimetric mode (HH+HV+VH+VV) in L-band. Table 2.4 shows the main characteristics of two satellites.

Characteristics	ALOS-1/PALSAR	Sentinel-1
Country or Operator	Japan	ESA
Launch date	24/01/2006	03/04/2014
Altitude	691.65 km	693 km
Sensor type	SAR	SAR
Spectral Band	L-Band	C-Band
Wavelength	$\lambda = 23 \text{ cm}$	$\lambda = 5.5 \text{ cm}$
Frequency	1.2 GHz	5.405 GHz
Polarization	HH/HV + VV/VH	VV, VH
Spatial resolution	10 m	10m
Temporal resolution	46 days	12 days
Incidence angle	8 – 30°	20 – 47°

Table 2.4: ALOS-1/PALSAR and Sentinel-1 SAR sensor parameters

2.3 Sensitivity of Radar Signals to Vegetation

2.3.1 SAR scattering mechanisms for vegetation

For vegetation, there are three radar backscattering contributions to be taken account: a) the leaves); b) the stalks; c) a layer that covers the ground, which may or may not be covered by water (wetlands). The backscattering of a target zone for a particular wavelength will vary according to the physical conditions of the layer, such as the size of the diffusers in the target area, electrical properties of the target and the moisture content. The wavelength and polarization of the SAR pulses and the observation angles will also affect the backscatter. For example, we can schematize this phenomenon on rice as follows (figure 2.3):

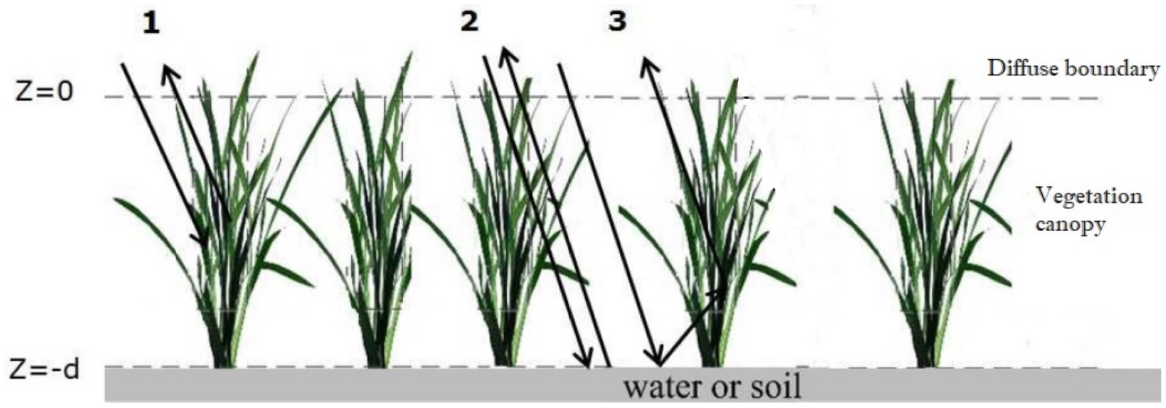


Figure 2.3: Backscattering contributions from vegetation canopy

In the microwave zone, a vegetation can be modeled as a volume delimited by air above and ground surface scattered below (canopy). The backscatter coefficient represents the sum of the contributions of the canopy itself, the direct backscatter by the ground and the multiple scattering between the canopy scattering elements and the soil surface [166]. On the figure 2.3, there are three mechanisms:

- 1) canopy backscatter (volume scatter);
- 2) direct soil backscatter;
- 3) soil-canopy interactive scatter.

The backscatter coefficient of the canopy (including soil contribution) is given by:

$$(2.2) \quad \sigma^0(\theta) = \sigma_{canopy}^0(\theta) + \sigma_{soil}^0(\theta) + \sigma_{soil-canopy}^0(\theta)$$

where $\sigma_{vegetation}^0(\theta)$ is contribution of the vegetation volume; $\sigma_{soil}^0(\theta)$ is contribution of soil surface, $\sigma_{soil-canopy}^0(\theta)$ is the ground and canopy contribution and θ is the incidence angle relative to nadir. The soil backscatter coefficient depends on the soil roughness, the dielectric properties and the moisture content of the soil surface layer. When radar is used to monitor vegetation, we use incidence angle greater than 40° [166].

Wang et al., 2013 [174] have analyzed the behavior of 3 scattering mechanisms (single bounce, double bounce and volume scattering) under multi-incidence angle configuration. In their study, they proposed to use the difference of polarimetric parameters between two incidence angle acquisitions. The behavior of scattering mechanisms has shown that single bounce and volume scattering over their test sites become saturated if incidence angle is bigger than 40° . Part of each of these mechanisms in the total backscatter of the vegetation cover varies according to the configuration of the sensors and the characteristics of the vegetation studied.

2.3.2 Penetration depth and radar frequency

The electromagnetic scattering properties depend on the nature of the target and the wavelength used. In a dense forest, the backscattering behavior depends on the sensor used. Thus, in L-band, the forest reacts according to the three types of diffusion mentioned above (figure

2.3). The signal passes through the vegetation and sometimes reaches the ground. It interacts with the soil and vegetation following interactions called double rebounds. In C-band, the signal acts on the vegetation. In some cases, for instance if it is a crop, the signal can reach the ground, but in forest case, the signal enters the forest but does not reach the ground, it is reflected. In X-band, the signal does not penetrate the vegetation, it is directly reflected in contact with the canopy. These scattering effects, which take into account the sensor configuration, are shown in Figure 2.4.

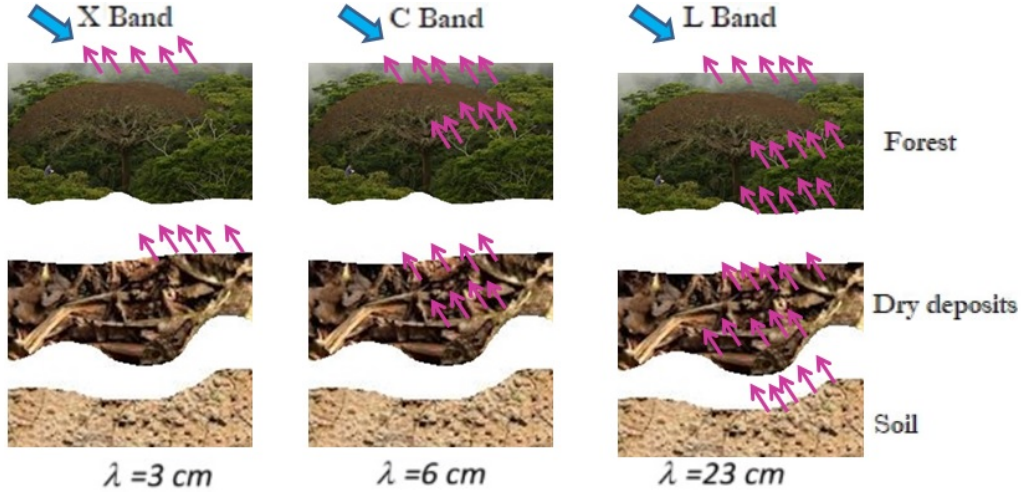


Figure 2.4: Illustration of penetration properties in a tropical forest for X, C and L bands. Three targets are taken into account: Forest, Dry deposits and Soil

Ulaby et al., 1979 [167] and Brown et al., 2003 [13] showed that the penetration capacity of the Radar signal depends on the radar frequency. As the sensor wavelength increases, the penetration power of the radar wave increases. The signal emitted in L or C-bands is consequently more able to reach the ground than those emitted in X-band.

2.3.3 Radar backscatter and biomass

Information about biomass conditions is essential for vegetation management planning. Vegetation management activities require reliable forecasts of the development of all constituent stands in the area being studied. Many studies have been conducted on vegetation biomass estimation. In the central Amazon basin (Tapajos region), SAR technology has been applied in establishing the relationship between the backscattering coefficient and the areal density of above-ground biomass in generating tropical forest. Luckman et al. (1997) [106] utilized SAR instruments as ERS-1 (C-band) and JERS-1 (L-band) determine the dependence of backscattering coefficient on biomass density at different radar wavelengths and polarization. The results have shown that longer wavelength (L-band) SAR satellite could be used to select different levels of forest biomass. Results also showed that the cross polarization is more sensitive to changes in biomass density. The shorter wavelength (C-band) SAR imagery is limited for distinguishing vegetation and bare soil when vegetation is dry.

On the other hand, Dobson et al. 1992 [30] tested polarimetric airborne SAR data at P, L and C-bands in plantations of maritime pines near Landes, France. SAR backscatter is found to increase linearly with biomass but at a certain time, it saturates. The biomass saturation levels are about 200 tons/ha at P-band and 100 tons/ha at L-band, and at C-band the backscattering coefficient is practically insensitive to total aboveground biomass. Thus, the values of the backscatter coefficients increase with increasing biomass, whether in L or P band and reach a saturation value occurring earlier in the L-band.

2.4 SAR Applications on vegetation

Currently, remote sensing data are widely used in various fields and the sensors are sometimes complementary depending on the case study [54, 85, 45, 131, 132]. Remote sensing data are analyzed to extract useful information about earth. Generally, the retrieving information methods from remote sensing images regroup into three categories:

- i) Information extraction based on the visual images interpretation;
 - ii) Classification based on semi-automatic processing by the computer (for instance, digital images classification and surface parameters calculation);
 - iii) Quantitative information retrieval for empirical and physically based inversion approaches.
- In this section, we review the studies on land cover classification, rice parameters estimation, and forest biomass retrieval.

2.4.1 Land cover classification

This process consists of regrouping pixels according to their spectral resemblance or thematic classes (i.e classification principle); the algorithms used are classifiers [184, 65, 75]. The choice of classification methods depends on the objective to be achieved. The classes are entities (objects) with common characters and may have the same spectral or thematic aspect. The image classification methods require, first of all, an analysis of the statistical properties characterizing the luminance of the image. The similarity levels of the pixels in the image are determined to affect each pixel in its class. There are two classification types: supervised classification and unsupervised classification.

a) Supervised classification

In a supervised classification, the identity and location of certain objects on an image are known a priori through the combination of field observations and maps. The operator assumes to have a good knowledge of the classes themes of the image. On the image he tries to use specific homogeneous zones that represent a region known and thus serving as a sample of training areas. These areas, called areas of interest, should be well chosen to distinguish useful information classes. This information is the spectral signature of the sample. In principle, the spectral signature can be used to uniquely characterize, identify, and dis-

criminate by class/type any given object in an image over a sufficiently broad wavelength band. The spectral signature characterizes an object as a function of the wavelength. The specular or textural characteristics of these training zones are applied to the rest of the image to have a classification over the entire image [161]. Part of training areas is used to check if the classification is consistent with reality i.e if the known areas are correctly identified. The supervised classification requires prior knowledge of the classes (its spectral signature) and the study area.

b) Unsupervised classification

For this type of classification, the classes are calculated automatically on the basis of several frequency bands of the image. The grouping of pixels is done according to the spectral distance computing and the user identifies the good number and the type of classes retained. In the unsupervised classification the analyst plays no role in class attribution until the computations are completed [121]. In the unsupervised classification, several algorithms are used and fall into two categories: hierarchical ascending classification and sequential classification.

- Hierarchical ascending classification:

The principle is that we use as many classes as there are pixels. We start with pixels that have a great resemblance i.e which are separated by a small spectral distance. These first two pixels form the first core, then we choose other pixels closer (spectral distance) of this first core and the operation continues until the number of classes desired.

- Sequential classification: For this category of classification, we first determine the number of classes and we choose random pixels to define the center of classes and thus we have the first core whose center of gravity is calculated. Then we calculate the spectral distance between the pixels with respect to this center of gravity.

c) Deep learning method

To understand what deep learning is, it is better to start defining machine learning. In general terms, machine learning is devoted to developing and using algorithms that learn from raw data in order to make predictions [177]. Machine learning systems are used to identify features of objects in images. These applications use a class of techniques named deep learning [93].

Deep learning is part of machine learning, where a multilayer architecture is used to show the relationships between the input data and the results (output). Deep Learning techniques operate with the multi-level learning of details. Thus, deep learning can represent

and organize several levels of information to express complex relationships between data. Through the different layers, we move from low-level parameters to higher level parameters, where the different levels correspond to different abstraction levels of data. Deep Learning techniques use different layers of a non-linear processing unit for feature extraction and transformation; each layer takes as input, the output of the preceding one. Therefore the deep learning system have three main components: the input data, the core deep networks, and the output data.

In practice, input data and output results depend on the application type. For instance, in classification task, the inputs are the features extracted from the pixels of images and the outputs are the spectral-spatial features or information label. When the input-output data pairs have been clearly defined, the relationship between these data is then constructed by a deep architecture with multiple levels of operations. Thus, if the basic deep network has been well formed, it can be used to predict the output results [186].

In this study, deep learning architecture is composed of multilayer neural networks formed using the back-propagation algorithm. In the architecture of Neural Network, we distinguish Convolutional Neural Networks (CNN) and the Recurrent Neural Network (RNN). A CNN will learn to recognize patterns in space. Thus, a CNN network will learn to recognize the components of an image (for example, lines, curves, etc.) and then combine these components to recognize larger structures (eg faces, objects, and so on.). While an RNN will learn similarly to recognize patterns across time series information.

The mechanism by which the two types of Neural Networks represent these models, however, is different. In the case of a CNN, we look for the same patterns in all the different subfields of the image. For temporal succession tasks, systems are needed that combine the flexibility of neural networks with an evolutionary memory of the past. This is the RNNs' role. In the case of RNN we are feeding the hidden layers from the previous step as an additional input into the next step. While the RNN builds up memory in this process, it is not looking for the same patterns over different slices of time in the same way as CNN is looking for the same patterns over different regions of space. Techniques have been developed to preserve the long-term memory of RNNs: Long Short Term Memory (LSTM). A LSTM consists of a sequence of memory registers on which it can act to determine the part of the information that it wishes to keep or to add to it.

2.4.2 Rice parameters estimation

The rest of this section deals with different methods of rice parameters estimation from remote sensing data. The parameter estimation method is based on the correspondence between a set of features values extracted from the signals acquired using the remote sensing data and the continuous variables related to the characteristics of the target parameters. We discuss the

methodologies for statistical and machine learning parameter retrieval.

In statistical methods, most of the studies carried out on the biophysical parameters estimation of rice are based on the empirical relationships between in situ measurements and remote sensing data. There are others statistical methods which are based on the inversion of physical models [48, 164, 82, 17]. The first approach involves the availability of a reference samples set (in situ), i.e., measurements of the desired target variable associated with the corresponding of the remote sensor data [103]. The estimation results depend on the reference samples that are collected in situ. The collection of in situ measurements is usually a long and expensive task. During these measurements, errors can occur and are due to several reasons:

- manual measurements made by human (lack of precision);
- atmospheric conditions when taking measurements;
- the vegetation type on the measurement site;
- the ground topography.

In fact, these errors influence the relationships between in situ measurements and the sensor. These relationships are therefore widely dependent on the in-situ measurement conditions and the types of sensors used [34]. Now the issue is to estimate the rice parameters using SAR data. The method that is often used is a relationship inversion between backscatter coefficient of sensor and rice parameters. The statistical regression techniques, such as multiple linear regression (MLR) are usually used to estimate rice parameters. The multiple linear regression is a common parametric regression approach which can be solved by least squares. The regression techniques use empirical functions for parameters estimating.

In addition to the parametric methods used, there are other non-parametric approaches such as Support Vector Regression (SVR) and Random Forest (RF). Random forests are a combination of tree predictors such that each tree depends on the values of a random vector sampled independently and with the same distribution for all trees in the forest [12]. These non-parametric approaches are named machine learning models where we have the input data and the output data. In statistical terms, the input data are the predictor variables and the output data are the target variables. To understand this, we consider schematically that the observed value y of the target variable results from the $F(x)$ function of the predictors and the random noise $\epsilon(x)$. The objective of a machine learning model is to obtain a "good approximation" f of the signal F from an observations set. The function f is the prediction function which allows to obtain $F(x)$ estimations.

Statistical machine learning tools (MLR, SVR, and RF) can be minutely selected. Their choice will often be the result of an iterative process in which different models are successively trained and evaluated. The machine learning is a method based on the training of data. It helps us build decision support systems that adapt to data and for which no processing algorithm is listed in advance.

2.4.3 Forest biomass retrieval

Nowadays, global warming remains a subject of debate for scientists, environmentalists, socialists, politicians and economists [153]. The role of the forest in climate change has generated interest in understanding the carbon storage capacity of the forest. Protecting and estimating forest areas becomes a challenge for the planet. The basic work could be to determine the amount of forest biomass. However, due to the inaccessibility of forest areas, remote sensing in general and the SAR approach, in particular, seemed to be a practical way of estimating forest biomass. Because of its sensitivity to woody components, the L-band is the most commonly used SAR data type for estimating forest biomass [16]. However, the L-band is only efficient at a certain threshold of forest biomass, beyond which the radar signal becomes saturated [145].

Different approaches to forest biomass estimation from high-resolution images have been evaluated. For instance, In southern Finland, Kurvonen, L. et al., 1999 [87] estimated forest biomass using a semi-empirical model with JERS-1 and ERS-1 SAR images. Using an inversion method, they found a relative retrieval RMSE varying from 30 to 5% (the size of the forest area varied from 5 to 30 000 ha). These results showed promising accuracies in using L-band SAR data for forest biomass estimation.

Many studies have tested the potential of SAR sensors to estimate forest biomass from canopy characteristics [147, 137]. Sandberg et al., 2011 [147] made a survey on the relation between polarimetric SAR backscatter at L- and P-bands and forest biomass. Results obtained using L-band indicated a RMSE between 31% and 46% of the mean biomass using HV-polarized backscatter. For P-band data, the results were better than for L-band (the RMSEs were between 18 and 27%) [147]. On the other hand, Proisy et al., 2010 [137] have evaluated the effects of canopy structure on the polarimetric radar response of mangrove forests. They used C, L and P-bands data with a polarimetric scattering model based on a radiative transfer approach. In their study, Le Toan et al., 2011 [90] clearly showed that the BIOMASS P-band radar appears to be the only sensor capable of providing the necessary global knowledge about the world's forest biomass and its changes.

In the seventh ESA Earth Observation Mission, a "BIOMASS" satellite will be launched in 2020, the main mission of which will be determined by the distribution and evolution of vegetation biomass on a global scale. This satellite will carry a P-band Synthetic Aperture Radar (SAR), which will provide interferometric and polarimetric observations of forest areas. With this mission, scientists want to determine the amount of biomass and carbon stored in the world's forests, to better decipher the carbon cycle. Biomass data will also be used to map land elevations under areas of high vegetation density to obtain information on the geology of the basements [4].

DEEP RECURRENT NEURAL NETWORK FOR AGRICULTURAL CLASSIFICATION

3.1 Introduction

Spatial information about agricultural practices plays an important role for the sustainable development of agronomics, environment, and economics [14, 38]. In fact, the importance of agricultural practices has long been recognized by the international community (e.g., Food and Agriculture Organization) [134]. Remote sensing satellite imagery is a valuable aid in providing and understanding this spatial distribution of agricultural practices. Particularly, recent years have seen the arrival of many satellites to acquire high spatial resolution data on various spectral domains. The Sentinel-1 radar and Sentinel-2 optical sensors from the European Space Agency (ESA) are suited for monitoring agricultural areas. However, like all optical sensors, the use of Sentinel-2 data is limited if the cloud layer is large [31]. In contrast, Sentinel-1 is a Synthetic Aperture Radar (SAR) system that can acquire images in any type of weather with the advantage of providing images regardless of weather conditions. SAR data are well suited to distinguish rice from other types of vegetation cover [91]. The ESA Sentinel-1 SAR sensor (launched in 2014) (short revisit time: 12 days, and then 6 days after the launch of the second satellite in 2016, 20 m spatial resolution and two polarizations) allows a precise temporal follow-up of agricultural crop growth [163]. The ESA provides free data which makes it possible to envisage fine agricultural monitoring for various applications, in particular for providing detailed spatial agricultural land cover distribution.

In the Camargue region, farming is a major activity contributing to the productivity of the region. Among agricultural practices, rice cultivation is the most important one. It plays a crucial role in the development of cropping systems because the irrigation of rice allows the leaching of salt and, consequently, the introduction of other species into the rotation of crops [77]. In this region, to preserve the essential services for regulating agricultural systems for the environment, it is important to understand the operation of the farms [27]. In response to this demand, the spatial extent of agricultural land cover is essential. In the literature of

remote sensing for classification, the natural choice is based on supervised machine learning methods [41, 95], which use training sets to classify pixels of unknown identity. Various supervised learning algorithms are available, each with its strengths and weaknesses [41, 175, 104]. The most recent methodological developments are focused on active learning and semisupervised learning approaches, which make use of unlabeled data for training [96, 46, 122, 165]. Although the improvement in learning accuracy is considerable when unlabeled data are used in conjunction with a small amount of labeled data, the use of this approaches is still not common in agricultural land cover classifications. In practice, for agricultural applications, most of works in remote sensing are based on the standard algorithms, such as K nearest neighbor (KNN), random forest (RF), and support vector machine (SVM) [70, 37]. These approaches, however, are not designed to work with time series data and, therefore, they ignore their temporal dependency.

Unlike the literature cited above, in this chapter we assess the use of deep neural networks to consider the temporal correlation of the data. In fact, through recent advances in machine learning, there has been an increased interest in time series classification using deep convolutional neural networks (CNNs) and recurrent neuron networks (RNNs) that can take advantage of neural networks for end-to-end classification of a time series [55]. Moreover, RNN approaches can be used to work on pixel-based time series [55]. Accordingly, we focus our attention on RNN approaches for the classification. Thanks to their property, RNNs offer models to explicitly manage temporal dependencies among data (e.g., long short term memory ($LSTM$) [62] and Gated Recurrent Unit (GRU) [23]), which makes them suitable for the mining of multitemporal SAR Sentinel-1 data.

The objective of this work is to evaluate the potential of high spatial and temporal resolution Sentinel-1 remote sensing data to : (i) Map different agricultural land covers; and (ii) assess the new deep learning technique by comparing it with the standard machine learning approaches. For this, we propose to use two deep RNN approaches to explicitly consider the temporal correlation of Sentinel-1 data, which will be applied on the region of Camargue.

This chapter is organized as follows: In Section 3.2, the Camargue study area is introduced; in Section 3.3, the processing SAR Sentinel-1 is reported; in Section 3.4, the classical machine learning approaches are briefly introduced; in section 3.5, the two deep RNNs models are presented; in Section 5.3, results are shown and a discussion is provided; and finally conclusions are drawn in Section 3.7.

3.2 Study Area

3.2.1 Camargue Site

The Camargue region, located in south-eastern France, is a coastal area of the Mediterranean Sea. It has a Mediterranean climate with mild winters, a long summer period (hot

and dry), irregular rainfall and sunshine. Its climate has peculiarities related to its geographical location south of the Rhone corridor, between the Cevennes and the Southern Alps. The autumns are watered by brief but important precipitations and winters sometimes are rigorous due to mistral (<https://fr.wikipedia.org/wiki/Camargue#Climat>, last accessed March 2018). This zone covers the current perimeter of the Camargue Regional Natural Park, with an area of around 110,000 ha [107]. The study site is composed of five landscapes: Agriculture area, urban zone, water area, forests and natural environment. The agriculture zone can be defined by using the official Graphical Parcel Register (RPG) data, provided freely by the French government (<https://www.data.gouv.fr>). We used the recent version of RPG 2015 for our study in order to delimit the agricultural areas. In our study area, this corresponds to 54,082 ha (see the cyan polygon in Figure 4.2), in which the permanent moors, orchards, and olive trees areas are 17,859 ha, and the remaining 36,223 ha is used for common agricultural activities. In this 36,223 ha agricultural zone, rice is the most dominant crop (with 44% and 16,000 ha in 2011 [27]) and has an important function in the economic, ecological and social equilibrium of the region.

3.2.2 Ground Data

A field survey was carried out on 921 reference plots in July 2017 to collect the land cover information. The boundary of reference plots was drawn manually, based on the high resolution 60 cm World Imagery layer of ArcGIS data online (accessed in July 2017). We chose 11 observed surface classes: (1) *Rice*; (2) *sunflower*; (3) *lawn*; (4) *irrigated grassland*; (5) *durum wheat (winter)*; (6) *alfalfa*; (7) *tomato*; (8) *melon*; (9) *clover*; (10) *swamps*; and (11) *vineyard*. Figure 4.2 shows the position of ground samples and the distribution of the pixel number per class and number of plots is shown on Table 3.1.

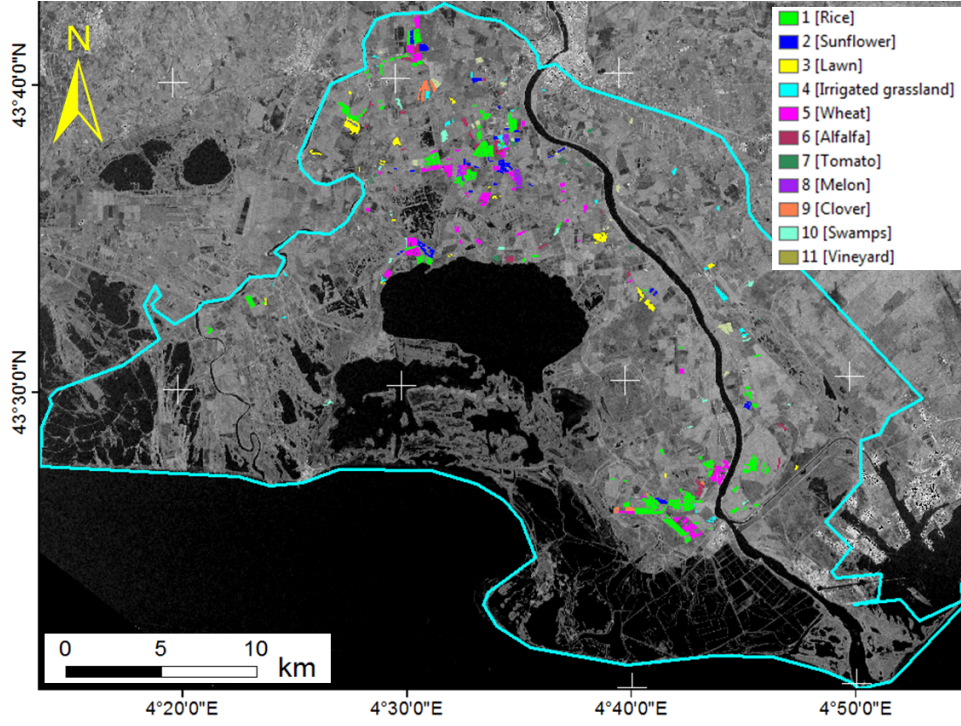


Figure 3.1: Camargue study area. Colored polygons represent 921 reference plots location. The study area is limited by the cyan polygon.

ID	Vegetation Class	Number of Plots	Number of Pixels	Surface Area (ha)	Area (%)
(1)	Rice	284	23,275	931	35.2
(2)	Sunflower	77	5541	222	8.4
(3)	Lawn	27	5018	201	7.6
(4)	Irrigated grassland	53	3528	141	5.3
(5)	Wheat	304	13,057	522	19.7
(6)	Alfalfa	59	4580	183	6.9
(7)	Tomato	15	1362	55	2.1
(8)	Melon	24	1978	79	2.9
(9)	Clover	26	1918	77	2.9
(10)	Swamps	19	2535	101	3.8
(11)	Vineyard	33	3409	136	5.2
Total		921	66,201	2648	100

Table 3.1: The distribution of the number of pixel and plots per class.

3.3 SAR Data and Processing

3.3.1 SAR Data

Since wheat cultivation is the only winter crop presence after May and the major agricultural practices in Camargue are in summer (e.g., from May to September), we focus our data analysis on this period. The Sentinel-1A/1B SAR dataset includes 25 acquisitions in terrain observation with progressive scan (TOPS) mode from May to September 2017 (5 months), with a revisit period of 6 days. This is dual-polarization (VV + VH) data, resulting in 50 images. Figure 3.2 summarizes the temporal profiles of the 11 agricultural classes per polarization. Each time series is made up of 25 points (one for each acquisition). Figure 3.3 provides information on the temporal dynamic of these classes by giving their average and standard deviation.

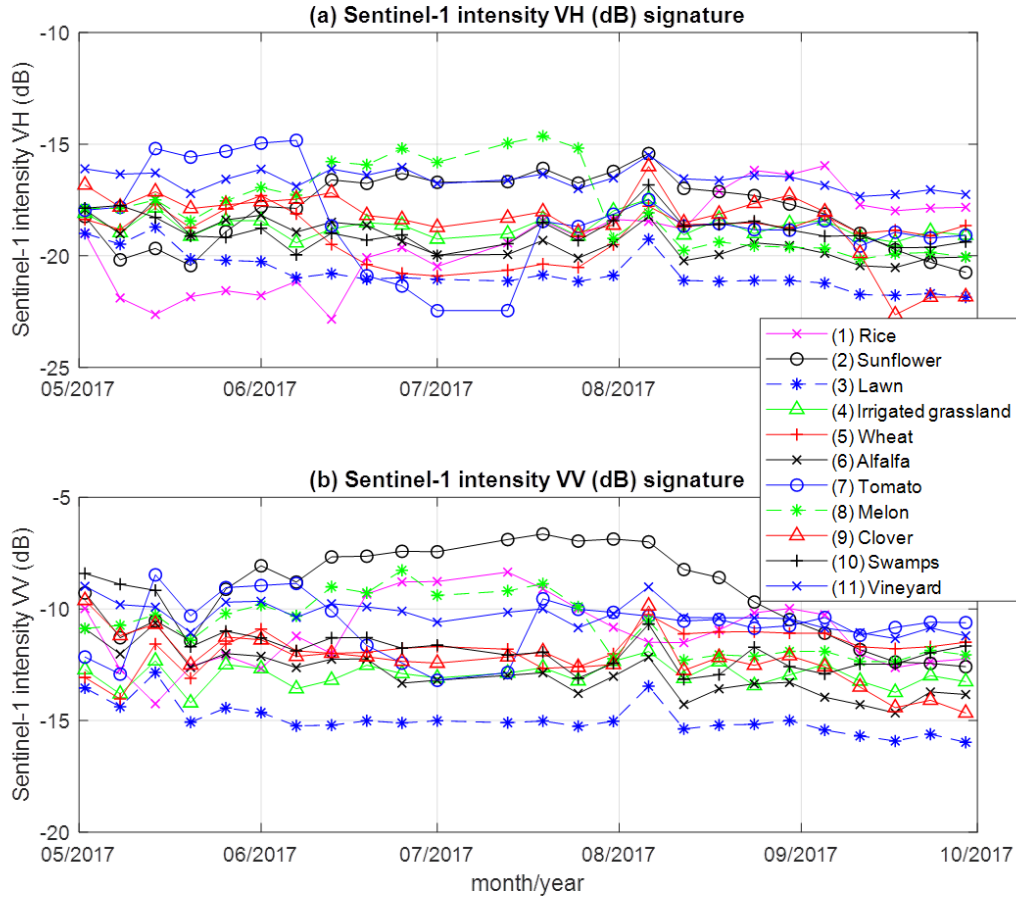


Figure 3.2: The temporal profiles of the eleven different classes which respect to the VH (a) and VV (b) polarizations.

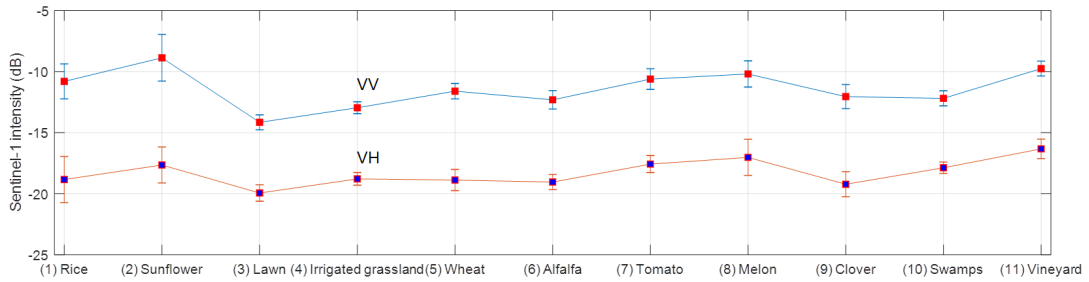


Figure 3.3: The average and standard deviation of the eleven different classes for VV and VH polarizations.

3.3.2 Pre-Processing Data

First, a master image was chosen and all images are coregistered, taking into account TOPS mode, to the master image [136]. Five-look (5 range looks) intensity images are generated and radiometrically calibrated for range spreading loss, antenna gain, normalized reference area and the calibration constant that depends on the parameters in the Sentinel-1 SAR header.

3.3.3 Temporal Filtering

Reliable estimates of the intensity from a distributed target require that the estimated number of looks (ENL) is sufficiently large. Speckle filtering is often used to increase the ENL with loss of spatial resolution [139]. In properly coregistered multitemporal datasets, it is possible to employ the technique of temporal filtering, which, in principle, increases radiometric resolution without degrading spatial resolution. The temporally filtered images usually show markedly diminished speckle, with little or no reduction in spatial resolution. In this chapter, we improve the time series SAR Sentinel-1 dataset by exploiting a temporal filtering method developed by Quegan, S. et al., 2001 [139] to reduce noise, while retaining, as much as possible, the fine structures present in the images.

3.3.4 Geocoding

After pre-processing and filtering, all the processed images are in the imaging geometries of the master image. In order to create a unified dataset, all image data have to be orthorectified into map coordinates. This is done by creating a simulated SAR image from a SRTM DEM 30 m, and using the simulated SAR image to coregister the two image sets (polarizations). The pixel size of the orthorectified image data is 20 m. After geocoding, all intensity images are transformed to the logarithmic dB scale, normalized to values between 0–255 (8 bits) and input into classifiers. The SAR Sentinel-1 data are processed by the TomoSAR platform, which offers SAR, interferometry and tomography processing [61, 60]. Finally, for each pixel, a 25×2 matrix (25 acquisitions and two polarizations: VV + VH) is generated as input for classifiers.

3.4 Classical Machine Learning Approaches

Among supervised machine learning approaches, we use K nearest neighbor (KNN), random forest (RF), and support vector machine (SVM) approaches as a baseline for comparing the performance of Sentinel-1 image data for land cover classification with deep recurrent neural network approaches in Section 5.3. The rationale for this choice is mainly because they are the most popular in remote sensing [70, 37, 83] and remain competitive w.r.t. other approaches in many scenarios. In this section, we provide a brief introduction of these methods for the sake of complete.

3.4.1 K Nearest Neighbors

KNN is classified as a non-parametric machine learning method, because it simply remembers all of its training data. Despite its simplicity, KNN has been successful in a large number of classification problems, including remote sensing satellite images. The principle of KNN is that in the set of training data, it finds a group of K samples that are closest to unknown samples (based on a certain distance function, e.g., Euclidean) [176]. In KNN approach, the class of an unknown sample is determined by applying a majority vote on the classes of its K nearest neighbors [138, 176].

3.4.2 Random Forest

The Random Forest algorithm has demonstrated its ability to yield high quality mappings for a different varieties of crop type systems with a much faster computation when compared to other state of the art classifiers [143, 69, 8]. The classifier relies on aggregating the results of an ensemble of simpler decision tree classifiers. In other words, it is a meta-estimator that fits a number of decision tree classifiers on various subsamples of the dataset, and uses averaging to improve the predictive accuracy and control over-fitting [12]. To reduce the computational complexity of the algorithm and the correlation between subsamples, tree construction can be stopped when a maximum depth is reached or when the number of samples on the node is less than a minimum sample threshold.

3.4.3 Support Vector Machine

The Support Vector Machine algorithm has been proved to be superior to most other image classification algorithms in terms of classification accuracy [1]. *SVM* is basically a binary classifier that delineates two classes by fitting an optimal separating hyperplane to the training data in the multidimensional feature space to maximize the margin between them [84]. *SVM* uses a kernel function to project the data from input space into feature space. Several kernels can be used: Linear, radial basis function (RBF), and polynomial or sinusoidal kernels. Linear and RBF kernels are the most commonly used. While linear kernels are computationally more efficient, nonlinear kernels, such as RBF kernels, tend to outperform linear kernels. For RBF kernels, two parameters should be specified: (i) The complexity parameter C which controls the trade-off between the maximization of the margin between the training data vectors and the training error decision limit; and (ii) the gamma parameter that is the width of the kernel function. Increasing C values usually require increasing computational time and high C values also increase risks of over-fitting.

3.5 Recurrent Neural Network

Recurrent neural networks are well-designed machine learning techniques that stand out for their quality in different fields of activity, such as signal processing, natural language processing and speech recognition [158, 100]. Contrary to convolutional neural networks, RNNs clearly manage the temporal data dependencies, since the output of the neuron in time $t-1$ is used with the next input, to feed the neuron itself at time t . A diagram of a typical neural RNN is detailed in Figure 3.4. Among different RNN models, we have Long-Short Term Memory (*LSTM*) [62] and Gated Recurrent Unit (*GRU*) [23], which are the two most well known RNN units. The main difference between them is related to the number of parameters to learn. Considering the same size of the hidden state, the *LSTM* model has more parameters than the *GRU* unit.

In the following, we will briefly analyze the two RNN units (*LSTM* and *GRU*). For each of them, we aim to provide and discuss the equations that describe its internal behavior. The \odot

symbol represents an element-wise multiplication, while σ and \tanh are Sigmoid and Hyperbolic Tangent function, respectively. The input of a RNN unit is a sequence of variables (x_1, \dots, x_t) , where each element x_t is a vector and t refers to the corresponding timestamp.

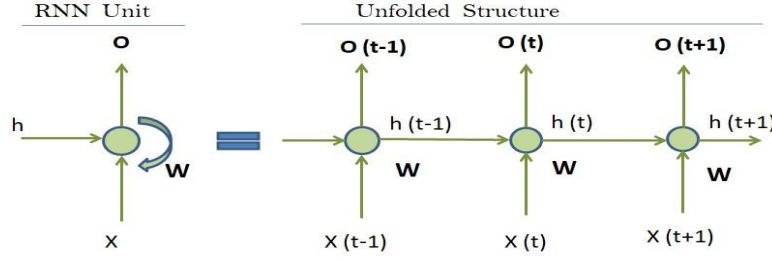


Figure 3.4: RNN Unit (on the left) and unfolded structure (on the right).

3.5.1 Long-Short Term Memory (LSTM)

The existing RNN models fail to learn long-term dependencies because of the problem of vanishing and exploding gradients. To overcome this challenge, the *LSTM* model is used [62]. The Equations (1)–(6) formally describes the LSTM neuron. The *LSTM* set consists of two cell states: The C_t memory and the h_t hidden state. Three different gates intervene in the control of the flow of information: The input (i_t), the forget (f_t) and the output (o_t). All three gates mix the current entry, x_t , with the hidden state, h_{t-1} , from the previous timestamp. Also, the gates have two major functions: (i) They regulate the quantity of information to forget/remember during the process; (ii) they deal with the problem of gradient disappearance/bursting. We can see that the gates are implemented by a sigmoid. This function gives values between 0 and 1. The *LSTM* unit also uses a temporary cell state, y_t , that resizes the current input. This current cell is applied by a hyperbolic tangent function that gives values between -1 and 1 . The sigmoid and the hyperbolic tangent work per element. i_t sets the amount of information to keep ($i_t \odot y_t$), while f_t indicates how much memory should be kept in the current step ($f_t \odot c_{t-1}$). The input of an RNN is a sequence of variables (x_1, \dots, x_n) , where x_t is a generic element that represents a feature vector and t refers to the corresponding timestamp.

Finally, o_t has an impact on the new hidden state, h_t , which determines how much information from the current memory will be on the output step. The different matrices, W_{**} , and bias coefficients, b_* , are the parameters used during model formation. The memory, C_t , and the hidden state, h_t , are both transmitted at the next step.

$$(3.1) \quad i_t = \sigma(W_{ix}x_t + W_{ih}h_{t-1} + b_i)$$

$$(3.2) \quad f_t = \sigma(W_{fx}x_t + W_{fh}h_{t-1} + b_f)$$

$$(3.3) \quad y_t = \tanh(W_{yx}x_t + W_{yh}h_{t-1} + b_y)$$

$$(3.4) \quad c_t = i_t \odot y_t + f_t \odot c_{t-1}$$

$$(3.5) \quad o_t = \sigma(W_{ox}x_t + W_{oh}h_{t-1} + b_o)$$

$$(3.6) \quad h_t = o_t \odot \tanh(c_t)$$

3.5.2 Gated Recurrent Unit (GRU)

To facilitate the computation and implementation of the *LSTM* model, the authors [23] develop a new RNN unit. The neuron *GRU* is illustrated in Equations (7)–(9). This new unit operates as the *LSTM* model by performing the gates and cell states but, conversely to the *LSTM* pattern, the *GRU* unit has two gates: Update (z_t) and reset (r_t), and also we have a cell state, the hidden state, (h_t). In addition, the two gates merge the current input (x_t) with information from previous timestamps (h_{t-1}). The update gate efficiently regulates the compromise between the amount of information from the previously hidden state (which will be included in the current hidden state) and the amount of information of the current timestamp that is to be kept. This acts in the same way as the unit memory cell *LSTM* that supports the RNN to remember information in the future.

Furthermore, the reset gate analyzes the amount of information from previous timestamps that could be embedded in the current information. Since each hidden unit has reset and updates gates, they register dependencies at different levels. Units that are more likely to capture short-term dependencies may have a frequently-enabled reset gate [23].

$$(3.7) \quad z_t = \sigma(W_{zx}x_t + W_{zh}h_{t-1} + b_z)$$

$$(3.8) \quad r_t = \sigma(W_{rx}x_t + W_{rh}h_{t-1} + b_r)$$

$$(3.9) \quad h_t = z_t \odot h_{t-1} + (1 - z_t) \odot \tanh(W_{hx}x_t + W_{hr}(r_t \odot h_{t-1}) + b_h)$$

3.5.3 RNN-Based Time Series Classification

To complete the classification task, at each RNN unit we make a deep architecture, putting together five units. The use of several units, similar to what is frequently done for CNN models in several convolutional layers [9], will extract high-level non-linear time dependencies that are in the remote sensing time series. This is done for both *LSTM* and *GRU*. The RNN model follows a new sequence at the input, but it makes no prediction by itself. For this purpose, A SoftMax [49] layer is stacked on the last recurrent unit to predict the final multi-class. The SoftMax layer has the same number of neurons as classes to predict. For layer normalization reasons, the SoftMax priority is given instead of the Sigmoid function, because the value of the SoftMax layer can be considered as a probability distribution on classes that total up to 1, whereas in the case of the sigmoid, the neurons give values between 0 and 1. Each sample belongs absolutely to a single class, which leads us to the choice of SoftMax. This schema is instantiated for both *LSTM* and *GRU* units, thus coming up with two different classifiers: An

LSTM-based and a *GRU*-based classification scheme. Figure 3.5 shows a schematic view of the *LSTM*-based architecture for each pixel in our chapter (e.g., 25 points input VV/VH, 5 *LSTM* units, 512 hidden dimensions and 11 classes output).

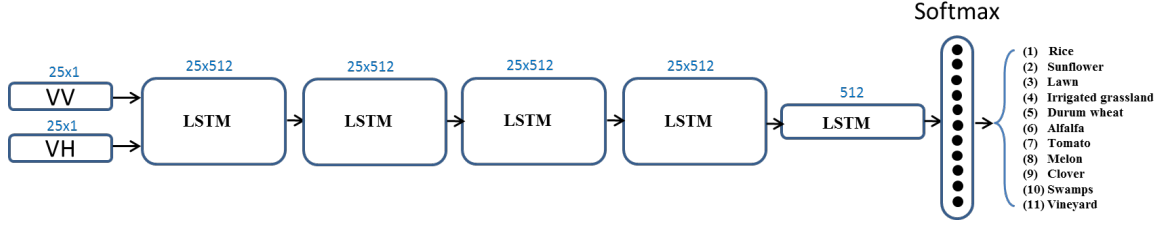


Figure 3.5: The schematic view of the RNN *LSTM*-based architecture. By replacing *LSTM* to *GRU* unit, we get the RNN *GRU*-based architecture.

3.6 Experimental Results

3.6.1 Experimental Settings

We compared RNN-based classification approaches (*LSTM* and *GRU*) with standard machine learning approaches. For the *RF* model, we set the number of trees at 400 and a maximum tree depth of 25. For the *KNN* model, we set the number of nearest neighbors at 10. For the *RF* model, the number of randomly selected features at each node is kept at its default value for a classification problem (i.e., the square root of the total number of variables [130]). For the *SVM* model, we use the RBF kernel with a default gamma (i.e., $1/\text{number of samples}$ [20]) and a parameter of complexity equal to 10^5 . For *RF* and *KNN*, we use the python implementation provided by the Scikit-learn library [130], while for *SVM* we use the LibSVM implementation.

For RNN-based classifiers, we define the number of hidden dimensions equal to 512 (General speaking, the choice of the number of hidden dimensions depends on the volume of the training dataset available. If the dataset is small, we have to use a simple model in order to estimate fewer weight parameters and vice versa. For example, in the work [68], the number of units is set to 64 and 512 for *Thau* and *Reunion* test sites, respectively. We experimentally found that our best performance was achieved by setting 512, after trying with 64, 128, 254, 512 and 1024. An initial learning rate of 5×10^{-4} , ρ of 0.9 and a decline of 5×10^{-5} was employed. We implement the model via the *Keras* python library with *Theano* as the back end [24]. To train the model, we used the *Rmsprop* strategy, which is a variant of stochastic gradient descent [26]. The loss function being optimized is categorical cross entropy, which is the standard loss function used in all multiclass classification jobs [185]. The model is trained for 250 epochs, with a batch size set at 64.

For the different methods, we apply cross-validation 5 times on the dataset, with a split procedure in two steps: (1) At the polygon-level to separate train and test instances and (2) at the pixel-level to extract each instance [71, 88]. In other words, we impose that pixels of

the same object belong exclusively to the training or to the test set. In this way, the initial set of data (66,201 pixels) is reduced to 57,585 pixels, since our polygons are not the same size. In detail, the set of data (57,585 pixels) is randomly divided into 5 partitions (folds) of equal size. Then, four folds are used to train the models (about 46,068 pixels), and the fifth fold (about 11,517 pixels) is used for the test phase. The operation is repeated five times, so that each fold is like a possible test set. Finally, the score measurements are calculated by concatenating the predicted labels per fold with respect to the real classes. Experiments were performed on a workstation Intel(R) Xeon(R) CPU E5-2667 v4@3.20Ghz with 256 GB of RAM and GPU TITAN X. The training step takes, on average, 166 min to learn each RNN model on the training set and less than 3 min to classify the pixel time series in the test set. In order to assess classification performances, we use not only the global accuracy and kappa measures, but also average and per-class F-measures.

3.6.2 Results

The multitemporal Sentinel-1 data, processed as in Section 3.3, are used as an input for classification using classical approaches (*KNN*, *RF*, and *SVM*) in Section 3.4 and two RNN-based models (*LSTM* and *GRU*) in Section 3.5. The summary of the results of different classification approaches is reported in Table 3.2. This is the performance from cross-validation 5 times on Sentinel SAR-1 time series data, showing the average and standard deviation values of the F-measure, Accuracy, and Kappa assessment metrics from 5 repetitions. For this multi-temporal SAR Sentinel-1, all classifier performance metrics are very high, showing the quality of the dataset for agricultural classification tasks.

Classifier	F-Measure	Accuracy	Kappa
<i>KNN</i>	86.1 \pm 0.6%	85.6 \pm 0.6%	0.823 \pm 0.009
<i>RF</i>	87.1 \pm 0.9%	86.9 \pm 1.2%	0.833 \pm 0.015
<i>SVM</i>	87.3 \pm 1.5%	87.1 \pm 1.6%	0.837 \pm 0.019
<i>LSTM</i>	89.2 \pm 1.7%	89.1 \pm 1.6%	0.862 \pm 0.020
<i>GRU</i>	89.8 \pm 1.6%	89.6 \pm 1.6%	0.869 \pm 0.019

Table 3.2: The average and standard deviation from cross-validation 5 times on the time series SAR Sentinel-1 data.

Second, to illustrate more precise comprehension of the behavior of the different classifiers, we report a per-class F-measure comparison in Figure 3.6. In this figure, the eleven classes are evaluated according to the different methods (*KNN*, *RF*, *SVM*, *LSTM* and *GRU*) used in the classification. In addition, confusion matrices are also reported in Figure 3.7. In both figures, results show a better performance using RNN-based classification approaches over classical machine learning methods (*KNN*, *RF* and *SVM*). Between the two RNN models, the *GRU*-based method obtains slightly better results than the *LSTM*. This is as expected, due to the fact that the *GRU* unit is considered as an improvement of the *LSTM* unit [23].

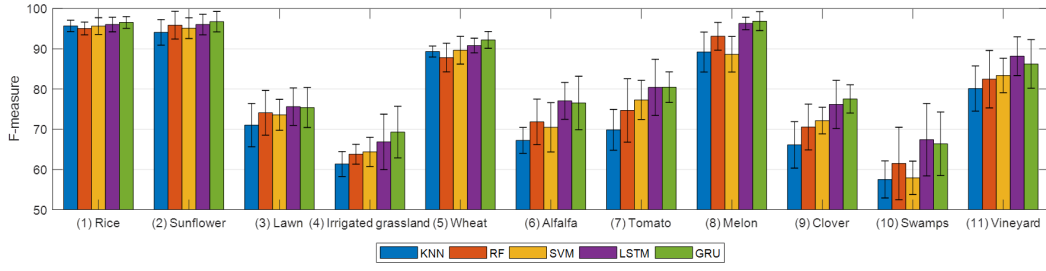
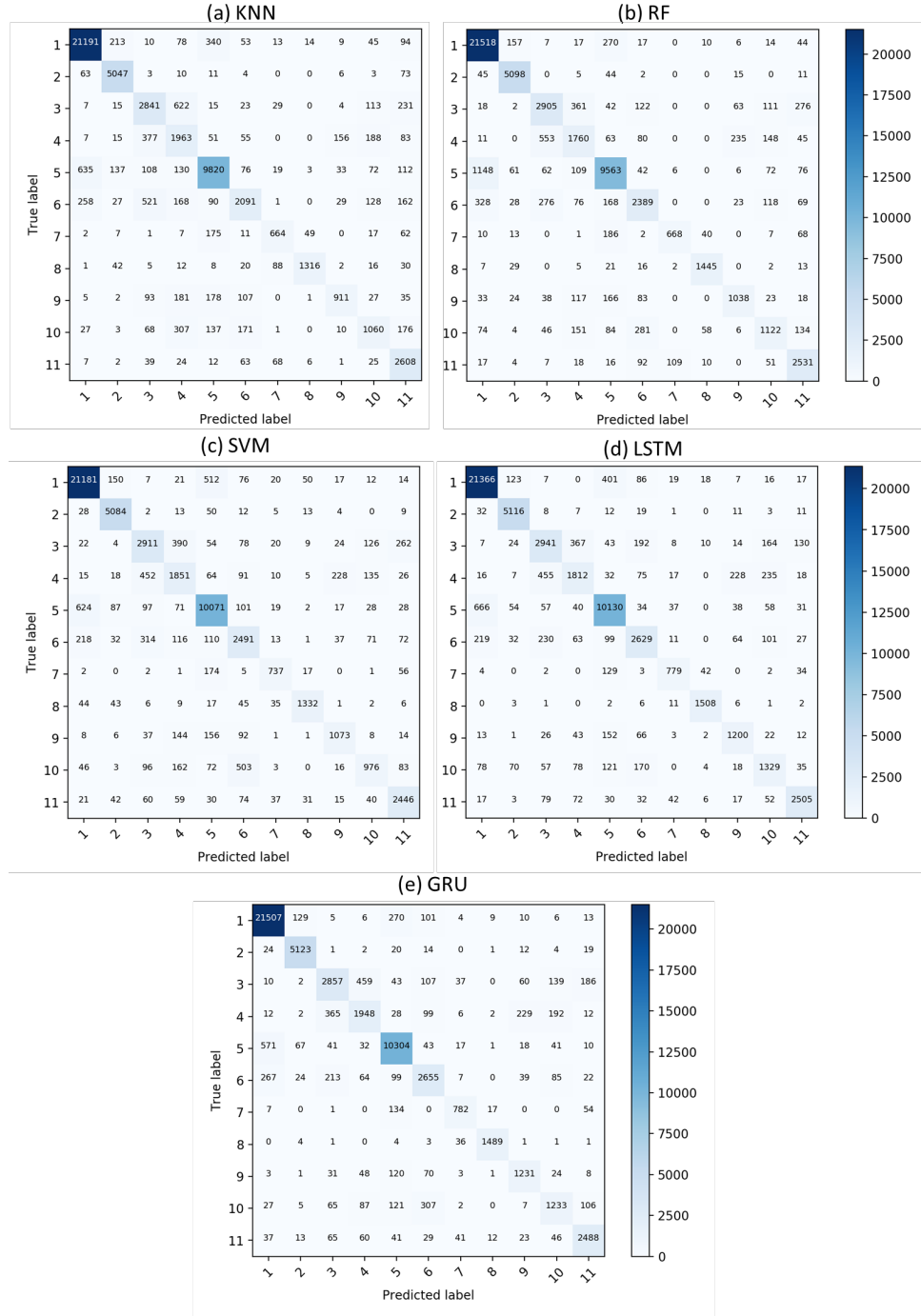


Figure 3.6: Per Class F-Measure of the different approaches.


 Figure 3.7: Confusion matrices on the SAR Sentinel-1 time series data of the different approaches: **(a)** KNN, **(b)** RF, **(c)** SVM, **(d)** LSTM and **(e)** GRU. The name of the labels: (1) rice; (2) sunflower; (3) lawn; (4) irrigated grassland; (5) durum wheat (winter); (6) alfalfa; (7) tomato; (8) melon; (9) clover; (10) swamps; and (11) vineyard.

Finally, by applying the best RNN-based *GRU* classifier for the whole area study, we established the agricultural land cover map for Camargue in 2017 (see Figure 3.8). Figure 3.9 is a zoomed version of the white-border box in the Figure 3.8, to facilitate visualization of classification results for the RNN-based *GRU* and the *SVM* approach w.r.t the reference plots. The classification results for both approaches were matched with the reference plots, and were slightly smoother in the RNN-based *GRU* result. Among different agricultural classes, rice is the dominant practice (with 29.3% and 10,627 ha, see Table 3.3) by its extent and presence in almost all areas of the region.

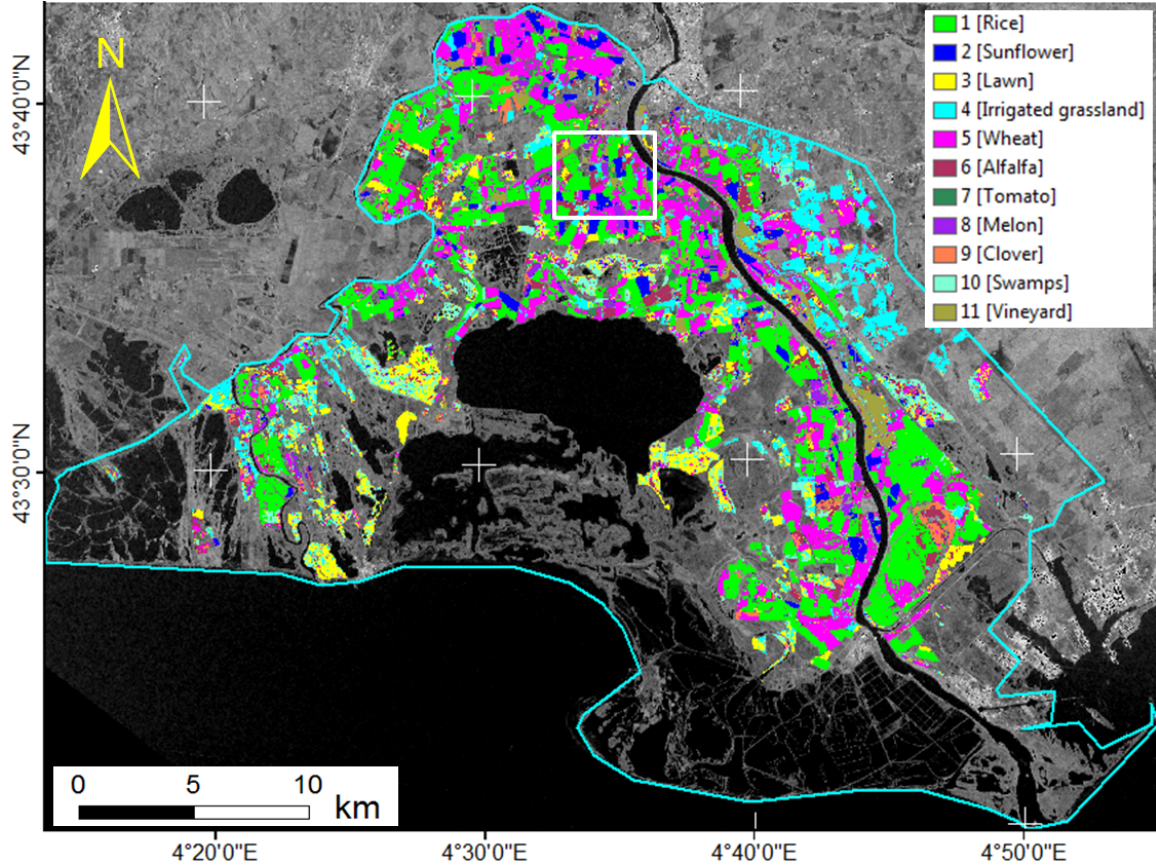


Figure 3.8: The agricultural land cover map in Camargue using the RNN-based *GRU* multitemporal SAR Sentinel-1.

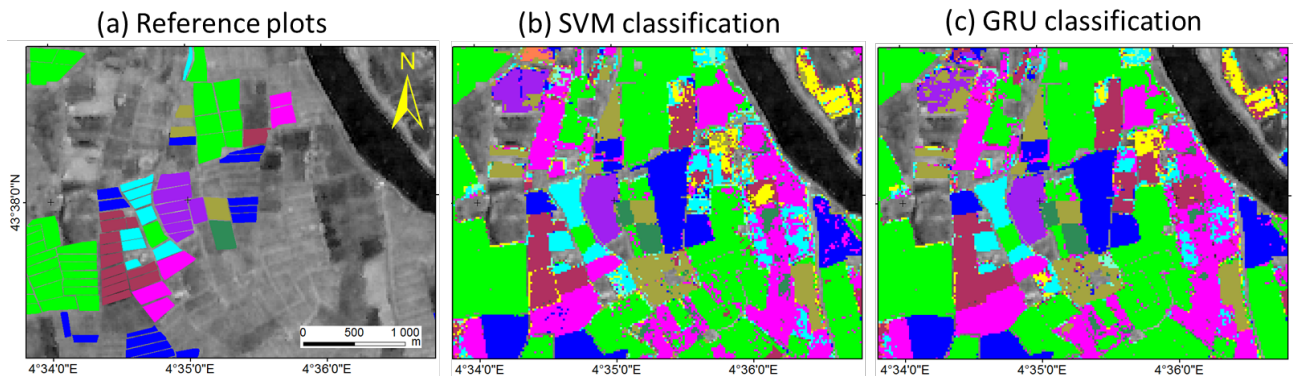


Figure 3.9: A zoom version of the white-border box in the Figure 3.8 is provided to facilitate visualization of classification results. (a) reference plots; (b) the classical *SVM* result and (c) the RNN-based *GRU* result.

ID	Class	Area (ha)	Percent
(1)	Rice	10,627	29.3
(2)	Sunflower	1676	4.6
(3)	Lawn	3357	9.4
(4)	Irrigated grassland	4148	11.5
(5)	Wheat	7439	20.5
(6)	Alfalfa	2593	7.2
(7)	Tomato	592	1.6
(8)	Melon	622	1.7
(9)	Clover	884	2.4
(10)	Swamps	2591	7.2
(11)	Vineyard	1694	4.6
Total		36,223	100

Table 3.3: The distribution of the agricultural land cover class in 2017.

3.6.3 Discussion

In this work we show that the multitemporal Sentinel-1 data can be used to classify different agriculture classes in Camargue, France. We obtained good results, using both classical approaches and the advance deep RNN techniques. The metric of validation indicates good performance, in which F-measure/Accuracy was greater than 86% and Kappa coefficient was better than 0.82. Together, these results confirm the suitability of Sentinel-1 time series data for agriculture land cover applications.

First, we show that even with the classical approaches, good classification performance could be achieved with radar time series data. This was expected to be challenging, because radar images are characterized by considerable speckle noise, which does not exist in optical images. We note that the same performance can not be straightforwardly transferred to the case of having few radar data. Good performance can be achieved by the fact that Sentinel-1 SAR with 6 days revisit time allows not only a precise temporal follow-up of the agriculture crop growth, but also mostly noise-free data, thanks to the multitemporal speckle filtering. It is worth pointing out that, nowadays, the Sentinel-1 constellation is the only satellite system providing dense time series with global coverage. It is therefore a good candidate for operational agriculture land cover mapping.

We can observe that RNN-based classification approaches have better performance over classical machine learning methods (*KNN*, *RF* and *SVM*). Between the two deep RNN models, the *GRU*-based method has slightly better results than the *LSTM* one. To give a more precise comprehension of the behavior of the different methods, from Figure 3.6, we can see that the performance gain offered by the RNN-based methods involve all the eleven classes, resulting in equally good result on all the them. Conversely, *KNN*, *RF* and *SVM* show different behaviors for different classes. Both classifiers obtain the best performances on the *Rice* class (1) and the lowest performances on the *Irrigated grassland* class (4). This behavior can be explained by considering the temporal profiles of both VV and VH presented in Figure 3.2. The *Rice* class

(depicted with pink lines in Figure 3.2) has a clear and distinct profile, with a strong dynamic (with large standard deviation value, see Figure 3.3), facilitating its detection. The *Irrigated grassland* class (depicted with green diamond lines in Figure 3.2) has a weak temporal behavior, with a small standard deviation value (see Figure 3.3), and intersects the temporal profiles of all the other classes multiple times. This is probably the reason why the standard approaches are not able to correctly detect this class, since they ignore the temporal correlation of the data. On the other hand, the RNN-based approaches discriminate well among all the classes, since they can extract and summarize the important signal portions that help the discriminative task among the different agriculture classes.

Based on Figure 3.7, which shows the confusion matrices for each method, we can see that a high misclassification rate is recorded between the *Irrigated grassland* (4) and *Swamps* (10) classes. This is true for all the different classifiers. However, for the RNN-based approaches, this misclassification error is not as high. Conversely, in the case of *KNN*, *RF* and *SVM*, this misclassification behavior is significant. In fact, the standard machine learning approaches are under strain, and they are responsible for a considerable misclassification rate. In addition, the standard machine learning approaches are not always good at dealing with imbalanced classification problems [159, 189]. Thanks to the joint optimization of nonlinear input transformations along with classification, deep learning approaches provide here a valuable strategy to discriminate among the different agriculture classes. In addition, as expected, the ability of RNNs to deal with the temporal correlations characterizing the SAR Sentinel-1 data result in a gain in performance on all classes, with particular emphasis on those classes that exhibit similar temporal behaviors for longer periods. Together, these results confirm that the RNN models (both *LSTM*-based and *GRU*-based) are well suited to detect and exploit temporal dependencies, as opposed to common classification approaches that do not explicitly leverage temporal correlations. Our finding is consistent with previous reports, in which Deep Learning outperformed the classical machine learning approaches [55, 68].

In this chapter, we selected *KNN*, *RF* and *SVM* due to their most popular supervised classification algorithms in the remote sensing community. Although they were introduced way back in the early 2000s, they still remain competitive w.r.t. other approaches in many scenarios, and they represent the algorithms to which any new method needs to be compared to. Considering the setting of remote sensing time series analysis (both optical and SAR), to date, no other classifier reaches the same generality and classification performance of these approaches, and this is why we decided to compare our RNNs proposals to them. Unfortunately, to the best of our knowledge, we are not aware of any other (more recent) classification methods that are commonly employed to perform supervised classification on time series SAR data. To summarize our position, this comparison allows us to appreciate more keenly how important it is to have techniques that can be employed to intelligently exploit temporal dependency among data w.r.t. standard machine learning approaches employed in the remote sensing field. Due

to the promising results we have obtained with RNNs, we think that, in the near future, these techniques will play an important role in the analysis of remote sensing time series.

For agricultural land cover in Camargue 2017, we can observe that the region areas are occupied mostly by rice (29.3% and 10,627 ha) and wheat (20.5% and 7439 ha) distributions. We note that the performance of both RNN-based *LSTM* and *GRU* classifiers is best on the *Rice* class, with the same F-measure metric of 96%. As a consequence, an RNN-based classifier is a valuable tool to discriminate the rice from other agriculture classes. In Camargue, there is a great variability in the types of rice farms [27], and the rice areas vary according to the year. The rice areas cultivated have significantly decreased from 16,000 ha in 2011 (e.g., in [27]) to 10,627 ha (our estimation) in 2017. The decreased phenomena of the rice extent could lead to a negative effect to the sustainable development of Camargue. Future works on this region could be focused on considering the assimilation of new source remote sensing data, such as Sentinel-1 radar, in crop models to estimate rice production, to follow farming practices, and to be able to propose strategies for sustainable agricultural development.

3.7 Conclusions

In this chapter, we studied the potential of high spatial and temporal resolution Sentinel-1 remote sensing data for different agriculture land cover mapping applications and assessed the new deep learning techniques. We proposed to use two deep RNN approaches to explicitly consider the temporal correlation of Sentinel-1 data, which were applied on the Camargue region.

We demonstrated that even with the classical approaches (*KNN*, *RF* and *SVM*), good classification performance could be achieved with Sentinel-1 SAR image time series. We experimentally demonstrated that the use of recurrent neural networks to deal with SAR Sentinel-1 time series data yields a consistent improvement in agricultural classes as compared with classical machine learning approaches. The experiments highlight the appropriateness of a specific class of deep learning models (RNNs) which explicitly consider the temporal correlation of the data in order to discriminate among agricultural classes of land cover, typically characterized by similar but complex temporal behaviors. We observed for the *Rice* class the same high performance of both RNN-based *LSTM* and *GRU* classifiers, with a F-measure of 96%. We found that in the Camargue region, rice land cover is still dominant, but decreasing significantly. Future work could be focused on estimating rice production yields in order to propose strategies for sustainable agriculture development.

Finally, although the number of exploitable optical images are limited due to cloud cover, the use of multi-source data including optical and SAR radar data will be an important subject of future research.

ESTIMATION OF RICE HEIGHT AND BIOMASS

4.1 Introduction

Rice is one of the most important cereal grains and serves as a staple food resource for more than half of the world's population. For this reason, rice consumption increases dramatically together with population raising, and the demand for rice is predicted to be strong [171, 148]. International Food Policy Research Institute analyses show that the demand for rice is increasing by about 1.8% per year. It will be difficult to increase rice production to satisfy this demand because land and water resources become more scarce with increasing competition from fast-growing non-farming sectors [64]. Especially, rice crop is a heat and water-loving crop [149], then, sometimes the rice badly suffers from cold stress during the seedling stage when it is grown in winter environment [155]. Therefore, monitoring the global productivity of rice is one of the adequate solutions to meet the demand for rice.

Rice parameters (height, dry biomass, leaf area index, salinity, etc.) are primarily monitored through two approaches, including field measurements by farmers and model retrievals from remote sensing data. While the field measurement is time-consuming, remote sensing is able to perform rice parameters measurement on a large scale without directly contacting the crop [76]. Spatial remote sensing provides the opportunity to have information on a regional scale with high spatial and temporal resolution. Data acquired from satellites provides a great tool for tracking temporal changes in soil and crop conditions, mapping their characteristics over large areas. There are two kinds of remote sensing techniques: one uses optical sensors and the other uses synthetic aperture radar data (SAR) sensors. In addition, the fusion of optical and SAR data can be exploited as well [15, 35]. Optical sensors (e.g., UAV, multispectral, and hyperspectral data) are suited for monitoring agricultural areas [180, 123, 114]. For example, the joint analysis of time series of vegetation and water indices derived from these sensors, such as Normalized Difference Vegetation Index (NDVI), Enhanced Vegetation Index (EVI), and Normalized Difference Water Index (NDWI), can be used to estimate rice parameters [180, 181].

However, a large cloud coverage can limit the use of optical sensors [31].

Unlike passive optical sensors, SAR systems are capable of producing high-quality images of the earth even in cloud cover conditions. Most rice fields are always found in cloudy cover conditions, and SAR sensors can work in these conditions, so it is more effective for monitoring rice fields than optical sensors [92]. Furthermore, for agriculture, SAR data can provide information on activities such as plowing, field preparation, planting, and the state of growth of the crops from germination to maturity stages. Recent studies have shown the high potentialities of using such data for crop monitoring [98, 154]. Thus, the application of SAR data in agriculture is becoming more popular. In previous studies, many investigations have been carried out on monitoring of rice growing. Various of them are based on rice parameters estimation [144, 183, 73], the others are focused on the used water within the rice fields [109], and some of them are on soil penology and organic matters [44]. Besides several SAR data which were used to map and monitor rice such as RADARSAT-1/2 [97], ENVISAT ASAR [22], ERS-1/2 [86], Sentinel-1 data is one of them. The Sentinel-1 mission is based on a constellation of two satellites (A and B). Sentinel-1 as a C-band SAR imaging satellite constellation ensures the continuity of ERS and ENVISAT missions [157, 163]. Sentinel-1 data are systematically acquired in terrain observation with progressive scan (TOPS) mode with a 6-day revisit period (We note that outside the European zones, it drops to 12 days.). Dense time series of open access Sentinel-1 data at high spatial resolution (20 m) offers new opportunities for monitoring agriculture [162]. In addition, Torres et al., [163] reported that C-band SAR data were particularly well suited for monitoring and mapping rice because of their abilities to acquire information on rice growing areas with frequent cloud cover and a remarkable increase in backscattering coefficients throughout the rice growth cycle. Ferrazzoli et al., [36] also showed that the sensitivity of C-band sensors to plant biomass depends on the type of crop.

In Camargue, the rice crop plays a crucial role for the hydrological balance [28]. This region is one of the main rice producers and suppliers in France [125]. Therefore, understanding and analyzing rice growth of Camargue is significant for agriculture in France. The aim of the chapter is to analyze the capability of SAR Sentinel-1 data to assess the rice parameters in Camargue. Rice crop height is an important agronomic feature linked to plant type and yield potential. The rice plant height estimation, particularly, is considered a simple method for determining rice growth because this parameter greatly influences the yield potential. Rice biomass is regarded as an important indicator of ecological and management processes in the vegetation.

In the literature of remote sensing, various machine learning algorithms are available for regression [10, 141, 12, 66]. In practice, the algorithms are selected based on the trade-off between the performances in terms of estimation of a given biophysical parameter, computation time and interpretability of the results [84]. Most of remote sensing works are based on clas-

sical algorithms, such as Multiple Linear Regression (MLR), Support Vector Regression (SVR) and Random Forest (RF) [127, 170]. Although they have been introduced since the early 2000s, they still compete with other approaches in many applications. In this chapter, classical machine learning methods (Multiple Linear Regression, Support Vector Regression and Random Forest) are applied in order to estimate rice height and dry biomass in the Camargue region.

This chapter includes six sections. In Section 4.2, characteristics of the study site, weather, cultivation of Camargue area and the information of ground truth measurement are described. Section 4.3 presents the principle of three methods used to estimate rice parameters (Multiple Linear Regression, Support Vector Regression and Random Forest). The results are shown in Section 5.3. The discussions are presented in Section 4.5 and finally, the Section 4.6 involves the main conclusions of this chapter.

4.2 Study Area

4.2.1 Camargue Study Site

Camargue is located in southern France; centered coordination is approximately at $43^{\circ}32'N$ latitude and $4^{\circ}30'E$ longitude. Among 110,000 ha of total area, 54,000 ha are used for agriculture and the rest is protected for nature conservation [125]. Placed between two branches of the Rhône and the Mediterranean Sea, Camargue region is a low-land containing alluvial deposits of the Rhone and the Mediterranean Sea. That is mainly characterized by the absence of important relief in which we distinguish two areas [6]. Starting from the north to south of Camargue, there are plots behind the Rhône river and from the south along the sea, there are much saltwater regions.

Agriculture is the main economic sector of the Camargue region although the semi-arid Mediterranean climate is disadvantageous for rice cultivation because Mediterranean climate is rainy in winter and dry in summer, then it is not easy for planting paddy rice in summer. Temperature and precipitation are important factors that affect directly crops cultivation, especially rice crops. The annual average temperature of this region is about $7^{\circ}C$ (January) to $26^{\circ}C$ (July). Besides that, precipitation also varies greatly during a year with less than 10 mm in July and 160 mm in September (due to short periods of heavy rain). Based on those features, in Camargue, there is one rice crop activity per year from May to September when the temperature and precipitation are the highest. Flooded rice cultivation allows the water needed for soil desalination and to introduce other crops such as wheat, sunflower, and fodder to be rotated. In the Camargue region, the rice crop has an important impact on the ecological, economic, and social equilibrium [28, 120].

4.2.2 Rice Phenomena

The temporal observation of rice growth is important for understanding the radar responses of rice plots at different stages of growth. Camargue has a single cropping season of rice; the

agricultural calendar is shown in Table 4.1.

Nature of Work and Vegetative Cycle	Executive Date
Stubble	October to November
Land preparation	March to April
Use of fertilizers and herbicides	Middle April
Watering and seeding	25 April to 16 May
Lifting and sodding	May to June
Post-emergence herbicide	June to July
Earing-flowering	July to August
Maturation, harvest	15-20 September to October

Table 4.1: Agricultural calendar and rice cycle in Camargue [7]

The rice crop in Camargue is an intensive type irrigated with direct seeding. Temperature and light are key factors in crop growth:

- For levee, a minimum temperature of 12°C;
- For flowering, a minimum temperature of 20°C.

There are three major periods of rice cultivation: the sowing period (starting according to the weather conditions from the end of April to middle May), the growth period (up to September) and the harvest period (end of September to the beginning of October). In Camargue, the sowing date is from 24 April to 16 May, followed by a germination stage from May to June. At the germination stage, water is not evacuated. If the surface is bumpy, two risks are present: (1) either the water height is too high and the seedling dies; (2) the land is bare and the seedling germinates badly. Constant monitoring of water levels, which have a significant role as thermal regulators, should be carried out. Continuous water movement compensates the variations of air temperature. A high water depth protects the seedling in case of cooling. However, it is necessary to rapidly lower the level as soon as the ambient conditions become again favorable.

The growing period begins from the successful germination to the flowering/maturation stage. Figure 4.1 shows clearly the development of rice plants in Camargue.

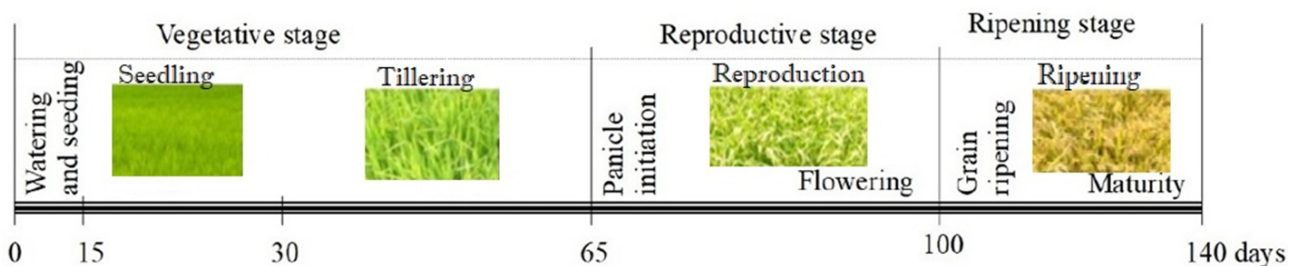


Figure 4.1: Rice crop growth calendar in Camargue.

Three essential factors play a role in the success of seedling emergence: water temperature, with an average above 15°C with the nocturnal minimum around 10°C; the constancy of the insulation; the fight against parasites: larvae or algae. After the emergence, the rice plot is dried up to 10 or 12 times. Drying can last a day or sometimes half a day. Temporary drying

inhibits the development of parasites and activates the rice rooting. Between 25 July and 25 August comes the flowering period. The height of crops does not increase much at this stage. Flowering period requires a warm climate, without wind, without rain. After flowering comes the ripening period where the farmers begin to evaluate their future harvest at the end of August. The harvest stage occurs from the end of September to the beginning of October, all ripening rice crops are reaped. At the end of the harvest, two options are possible. For the first option, rice farmers normally have a long period enough to prepare their rice plots. In irrigated rice farming, as is the case in the Camargue, special attention is paid to leveling, using a laser-guided blade. The use of this equipment aims to obtain perfectly flat plots, in order to manage water precisely. This method is also used after harvest period between seasons for maintenance of irrigation canals (“waterways”). In Spring, once the last surface preparation is carried out to obtain a suitable seedbed, ditches are dug in the plots to facilitate their filling and emptying during cultivation, and then watering is done; we have a continuous cultural cycle. For the second option, farmers work very quickly to sow as early as autumn, usually with wheat which is the second crop in rice farms in Camargue.

4.2.3 Ground Data Measurement

Ground truth measurements of rice parameters (rice height and rice biomass) were collected in eleven reference plots (Figure 4.2) which were about 2 to 6 hectares. A plot survey was carried out from May 2017 to September 2017 on the 11 rice reference plots selected to cover the variability encountered in both soils and agricultural practices. The reference plots were chosen in such a way that they could be represented the paddy rice fields in Camargue and they should not be adjacent parcels. The ground surveys were conducted based on the Sentinel-1 data acquisitions to measure rice height and biomass through the full growth rice cycle. In that respect, the following measurements were made every 12 days: 2 locations per plot for biomass assessment (1 m² for each location), 30 points per plot for crop height measurements. Figure 4.2 shows the position of ground surveys. The rice height has been taken on all the 11 plots. In contrast, rice biomass had been only taken on 1G1, 1G3, 2M1, 2M2, 3M1. The number of plots used to cut the biomass is reduced to five; we could not cut the biomass on all the plots otherwise it would be a waste and it would have had an impact on the production. The biomass was dried to have the dry biomass that is used in our analyses.

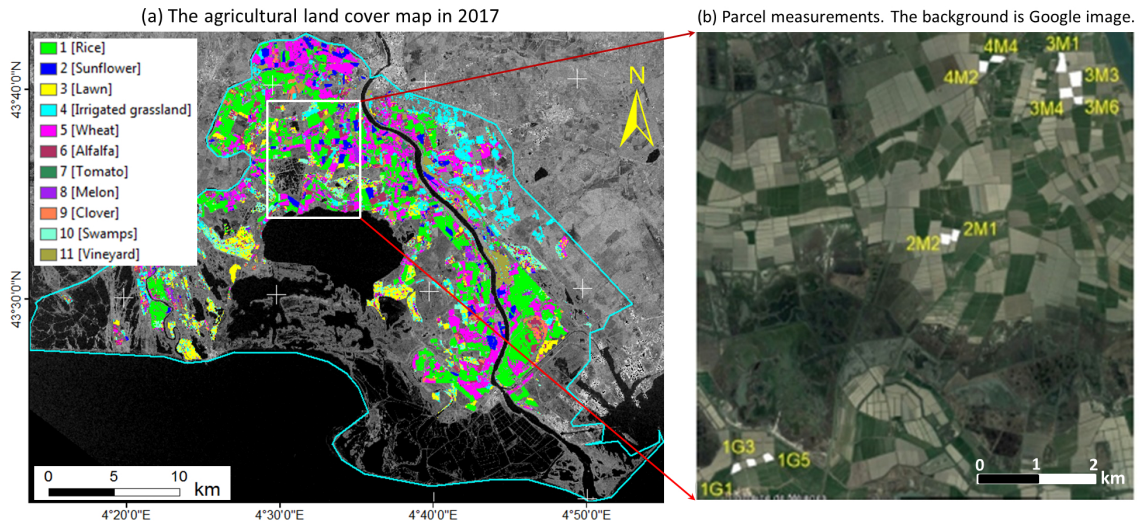


Figure 4.2: Camargue study area. (a) The agricultural land cover map in 2017 [125]. The green color indicates the rice extent of the Camargue region. (b) The zoom version of the white polygons represents the location of reference plots where measurements were made at every 12 days from May to September 2017.

In addition, information such as the label, surface (in hectare), the sowing date, rice variety and harvest date are known for each plot and represented in Table 4.2.

Plot Identity	Area (ha)	Sowing Date	Rice Variety	Harvest Date (DoY)
1G1	2.4	10 May 2017	Ronaldo	09 October 2017 (282)
1G3	2.14	10 May 2017	Ronaldo	09 October 2017 (282)
1G5	2.03	10 May 2017	Ronaldo	09 October 2017 (282)
2M1	3.5	12 May 2017	Eurosis	29 September 2017 (272)
2M2	3	12 May 2017	Eurosis	29 September 2017 (272)
3M1	6	15 May 2017	Ronaldo	11 October 2017 (284)
3M3	5	15 May 2017	Opale	11 October 2017 (284)
3M4	4	15 May 2017	Ronaldo	14 October 2017 (287)
3M6	2.5	15 May 2017	Ronaldo	14 October 2017 (287)
4M2	3.5	15 May 2017	Brio	10 October 2017 (283)
4M4	3.5	15 May 2017	Brio	09 October 2017 (282)

Table 4.2: Description of reference plots in Camargue.

Regarding the parameters displayed in Table 4.2, the sowing date is not the same for all plots and the harvest date also is not at the same time. The variability observed is due to the local conditions at the time of sowing and also is due to the rice variety. The harvest period takes place between 29 September (DoY 272) and 14 October (DoY 287). After harvesting, the rice in Camargue is dried and preserved in the geographical area at a humidity level allowing its (good) conservation in silos whose temperature conditions are controlled. The ground measurements of rice height and rice biomass were collected at the same time with SAR Sentinel-1 images acquisition over reference plots. The Figure 4.3 shows one of eleven plots with its pictures that were taken during the ground survey.

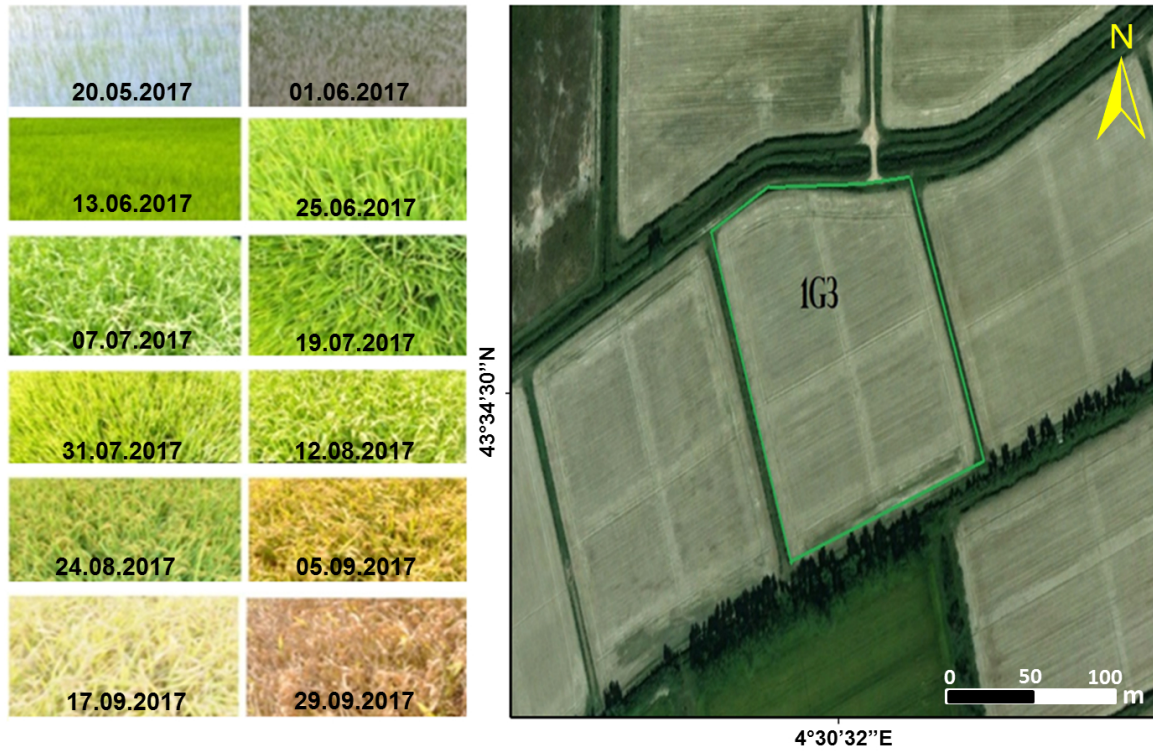


Figure 4.3: The reference plot 1G3 is marked in the figure (coordinates of central point $43^{\circ}34'30''N$, $4^{\circ}30'32''E$) together with its photos at different dates.

In summary, for rice height in-situ data, there are 132 measurements, whereas, for rice biomass, we only have 50 measurements.

4.2.4 SAR Data

The Sentinel-1 SAR data includes 25 TOPS mode acquisitions from May 2017 to September 2017, with 6 revisit days. This is dual-polarization (VV and VH) data, leading to 50 images in total. First of all, a reference image was selected and all images are coregistered to it by taking into account the TOPS acquisition [136]. Five-look (in range) intensity radar data are generated and radiometrically calibrated for antenna gain, range spreading loss, normalized reference area and the calibration constant using information from Sentinel-1 SAR header.

Reliable estimates using backscattering coefficients require that the estimated number of looks (ENL) is large. To increase the ENL, speckle filtering can be used with loss of spatial resolution. In this chapter, we improve the time series SAR Sentinel-1 dataset by exploiting a temporal adaptive filtering to reduce speckle while keeping as much as possible the fine structures present in radar images [139]. Finally, all images are orthorectified into map coordinates. This can be done by simulating SAR image from the SRTM DEM 30 m and using it to do coregistration. The image pixel size of the final data is 20 m. The Sentinel-1 SAR data are processed by using the TomoSAR platform (i.e., a platform supports the entire processing from SAR, Interferometry, Polarimetry, to Tomography (so-called TomoSAR)) developed by Dinh Ho Tong Minh and Yen-Nhi Ngo [58]. In details, the full description of this SAR dataset can be

found in [125].

4.3 Method

4.3.1 Multiple Linear Regressions

Multiple Linear regression (MLR) is one form of Linear Regression which is used to describe the variations of a dependent variable (which varies under the influence of other system parameters) associated with the variations of several independent variables (which varies without being influenced by the other system parameters) [10]. The truth data in use include in-situ measurements of rice height, rice biomass, Day after Sowing (DaS—which is counted from the first day when farmers sow in their plots), backscattering coefficients VV and VH polarizations. The purpose is that using the ground measurements to predict rice height and biomass values based on DaS with single polarization (VV or VH) and dual-polarization (VH and VV). Therefore, the application of MLR equation to estimate rice height and rice biomass in each polarization is different. For example, the equation below was used in case of dual-polarization:

$$(4.1) \quad biomass = x_0 + x_1\sigma_{VH} + x_2\sigma_{VV} + x_3DaS$$

where σ_{VH} and σ_{VV} are the backscattering coefficients in the decibel unit, in VH and VV polarization, respectively; DaS stands for Day after Sowing. To estimate rice height, we substitute rice biomass by rice height in Equation (4.1). In VV polarization model, we just exclude the term σ_{VH} in Equation (4.1). Similarly, in VH polarization model, we just exclude the term σ_{VV} in Equation (4.1). We use the same input parameters for SVR and RF methods.

4.3.2 Support Vector Regressions

The Support Vector Regression (SVR) is a non-parametric technique and non-linear regression method. This method is considered a non-parametric technique because it relies on kernel functions. SVR algorithms use kernel functions which take data as input and transform it into the required form [33]. The basic idea is to transform the input data into a higher dimensional feature space, where the problem can be solved in a linearized manner [84]. In the end, training the SVR involves solving a quadratic optimization problem. There are several kernels: linear, polynomial, sinusoidal and radial basis function (RBF) kernels. Although linear kernels can be computationally efficient, nonlinear kernels (e.g., RBF) have a better performance over linear kernels [66]. For RBF kernels, two parameters need to be tuned: (i) the sigma parameter (i.e., the width of the kernel function), and (ii) the complexity C parameter to control the trade-off between the maximization of the margin between the training error decision limit and the training data vectors. Both parameters are optimized in the estimation process to improve performance.

4.3.3 Random Forest

As SVR, the Random Forest (RF) method is also a non-parametric method used in vegetation parameters estimation. Random forest is an ensemble learning technique developed by

Breiman [12] to improve the classification and regression trees method by combining a large set of decision trees [123]. The classical method of regression is based on the division of the data set according to their homogeneity. A decision tree is from top to bottom on a root node and consists of sharing the data into subsets that contain instances with similar values. In addition, each node of every tree is split based on another random subset of parameters. This randomization provides a certain level of robustness to outliers and overfitting [12]. The result is usually aggregated by taking the average of the predictions from all trees. RF relies on the number of trees and the number of parameters to be used at each node split [170]. To improve performance, both parameters need to be optimized in the estimation process.

4.3.4 Model Assessment

For the performance analysis of three methods (MLR, SVR, RF), we apply a five-cross-validation method ($KFolds = 5$). In order to verify the effectiveness of three methods applied in Sentinel-1 data (VH, VV, VH and VV polarizations), the retrieved rice height and biomass are compared with ground truth measurements. The model assessments are validated through correlation coefficient (R^2) and Root Mean Square Error (RMSE):

$$(4.2) \quad RMSE = \sqrt{\frac{1}{n} \sum_{i=1}^n (Y_i - X_i)^2}$$

$$(4.3) \quad R^2 = \frac{\sum_{i=1}^n [(Y_i - \bar{Y}_i)(X_i - \bar{X}_i)]}{\sqrt{\sum_{i=1}^n (Y_i - \bar{Y}_i)^2} \times \sqrt{\sum_{i=1}^n (X_i - \bar{X}_i)^2}}$$

where Y_i and \bar{Y}_i are the estimated variables and their mean values, X_i and \bar{X}_i are the ground truth measurement variables and their mean, n is the number of data. A good retrieval result contains a low RMSE value and a high correlation coefficient.

To select the best model among different machine learning methods, we also use Akaike's Information Criterion (AIC) and Bayesian Information Criterion (BIC) [18].

4.4 Results

4.4.1 Experimental Settings

We evaluated rice parameters using Sentinel-1 data with standard machine learning approaches. The aim of these approaches is to use the ground measurements to train models (based on DaS with single polarization (VV or VH) and dual-polarization (VH and VV)) to predict rice height and biomass values. We note that using both VV and VH polarizations we are able to estimate DaS with the RMSE less than 3 days. There is any ways to combine VV and VH polarizations (e.g., VV+VH, VV-VH, VV/VH, etc). However, to avoid many model considerations and also to verify the helpfulness of combination VV and VH, we do a Principal Component Analysis (PCA) [80] to construct a new predictor that combines VH and VV. We

keep the first and the second PCA components to run through MLR, SVR, RF methods.

For the *MLR* model, it does not require to chose the optimal parameters since they can be estimated directly. In contrast, for both *RF* and *SVR* models, to improve performance, it is important to tune the parameters which are optimized in the estimation process. In this chapter , the parameters are defined by a grid search to get the best performance [170]. For both *RF* and *SVR* models, we found that the parameters were quite similar in both single and dual polarizations. For the *SVR* model, we use the RBF kernel with the complexity parameter of 50 and the gamma of 0.9 for rice biomass, whereas, for rice height, they equal to 0.7 and 60, respectively. For the *RF* model, we set the number of parameters to be used at each node split at 7 and the number of trees at 80 for both rice biomass and height estimations. For all three methods, we use the *Matlab* implementation provided by the Regression Learner.

4.4.2 Ground Measured Results

From all recorded measurements of rice height and biomass, the mean value of each plot was provided. Figure 4.4a presents the temporal variance of rice height versus the acquisition dates of Sentinel-1 data for all plots.

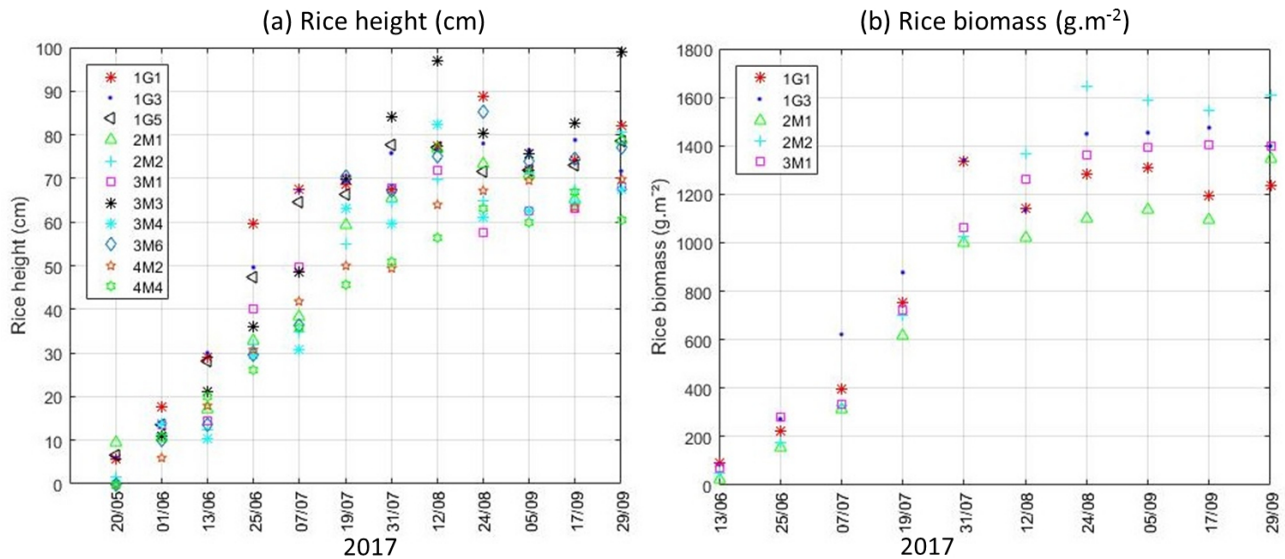


Figure 4.4: Temporal variation of the rice height and biomass versus to acquisition dates of Sentinel-1 data.

During the vegetative period (from May to July), rice height increases rapidly, and then small variation is observed during the reproductive phase (from July to September), while it stays constant in the ripening period. Rice height measurements show a high variability due to a quick growth of rice during the first three months (Figure 4.4a). The same observation is found for rice biomass, before the ripening period, it increases rapidly and during this stage, the biomass is stabilized (Figure 4.4b). The same trend was observed in [179, 92, 86].

4.4.3 Backscattering Coefficients According to Rice Parameters

Figure 4.5a shows the behavior of VV and VH backscattering coefficients during the entire rice growth. As expected, it can be observed that the VV backscatter values are higher than the VH polarization. In the vegetative stage (16 days to 65 days after sowing), the dynamic range of VV and VH backscatters is very high (about 7 dB). In the reproductive stage (65 days to 100 days), the VH backscatter tends to saturate, whereas the VV goes down. In the last ripening stage (after 100 days), both VH and VV backscatters tend to slightly decrease.

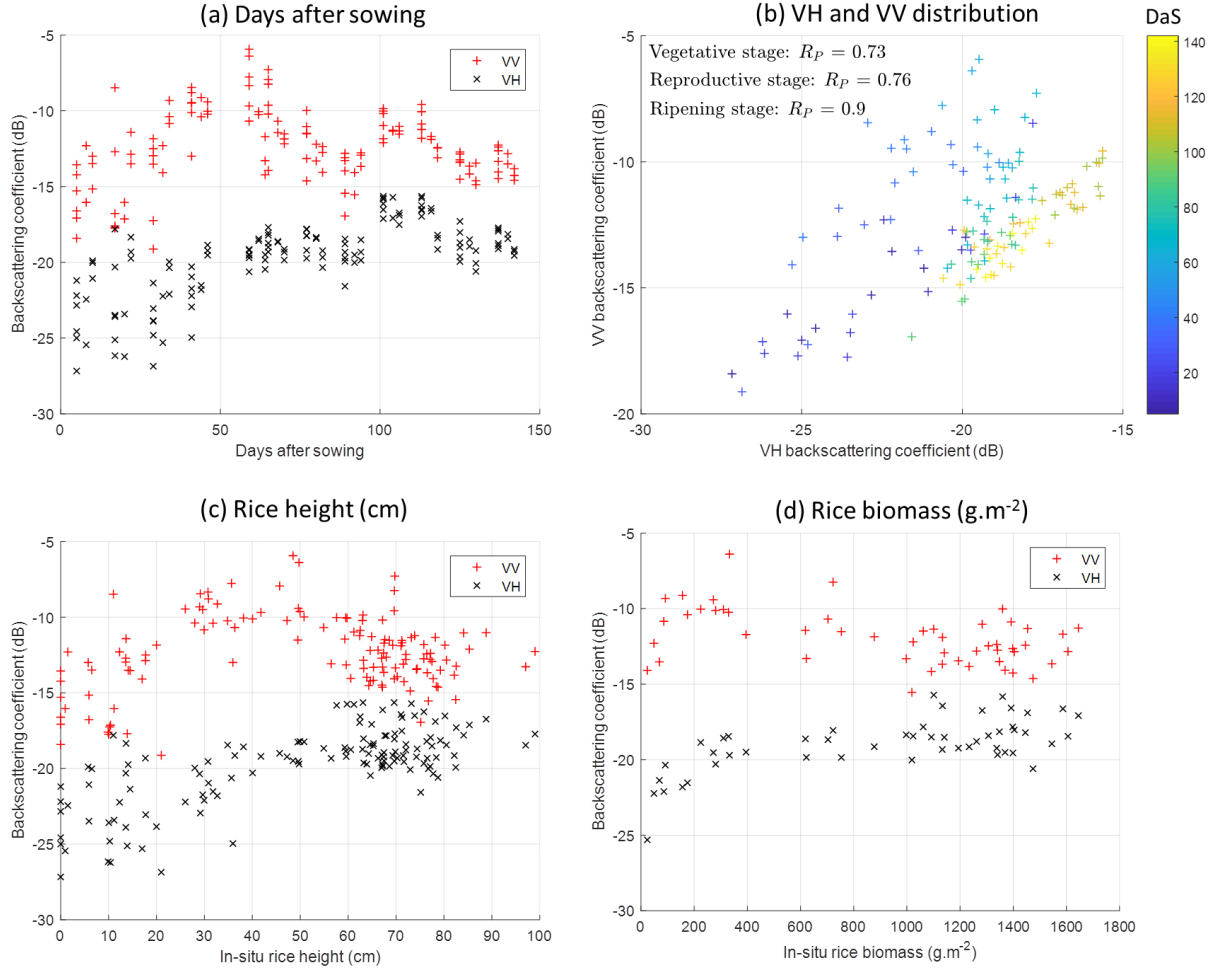


Figure 4.5: Sentinel-1 backscattering coefficients according to (a) Days after sowing; (b) VV and VH distribution; (c) Rice height; (d) Rice biomass.

Figure 4.5b shows a scatter plot on VV and VH backscattering coefficients distribution together with their Pearson correlation coefficient R_P according to vegetative, reproductive and ripening stages. Although they are highly correlated at each stage, if we put all together in a full cycle, the Pearson correlation is decreased to 0.52. In Figure 4.5c,d, the behavior of VV and VH backscattering coefficients is similar with respect to both rice height and biomass. Both VH and VV backscatters increase strongly in the vegetative stage. On the other hand, in reproductive and ripening stages, while VH backscatter still slightly grows, the VV visibly decreases.

4.4.4 Rice Height Estimation

The relevance of three methods MLR, SVR and RF applied in Sentinel-1 data with (VH, VV, both VH and VV polarizations) was analyzed using RMSE and R^2 values. Tables 4.3 and 4.4 report the regression results of rice height estimation with the three methods MLR, SVR, and RF.

	VV		VH		VH and VV		PCA (VH and VV)	
Methods	R^2	RMSE (cm)	R^2	RMSE (cm)	R^2	RMSE (cm)	R^2	RMSE (cm)
MLR	0.79	12.5	0.79	12.3	0.80	12.2	0.79	12.4
SVR	0.87	10.3	0.88	10.2	0.89	9.1	0.89	9.2
RF	0.90	8.4	0.88	8.9	0.92	7.9	0.91	8.2

Table 4.3: Rice height estimation using MLR, SVR and RF methods with 5 folds cross-validation. Best results are in bold.

	AIC				BIC			
Methods	VV	VH	VV and VH	PCA (VH and VV)	VV	VH	VV and VH	PCA (VH and VV)
MLR	295.6	293.7	294.8	296.7	295.9	294.1	295.3	297.1
SVR	273.4	272.3	261.2	262.4	273.8	272.6	261.7	262.9
RF	250.0	256.6	245.0	249.2	250.4	257.0	245.5	249.7

Table 4.4: AIC and BIC for rice height estimation. The smallest values are in bold.

The method used to estimate parameters is supposed to be efficient when its RMSE, AIC and BIC values are as small as possible. The RF method is better than the other methods: $R^2 = 0.92$, RMSE = 16% (7.9 cm) (with the dual-polarization VV and VH model). For PCA (VV and VH) models, as comparison with the dual-polarization VV and VH cases, they are quite similar. In other words, VV and VH give complementary information in the estimations. Figure 4.6 shows the results of estimating the rice height by plotting the best configuration for each method.

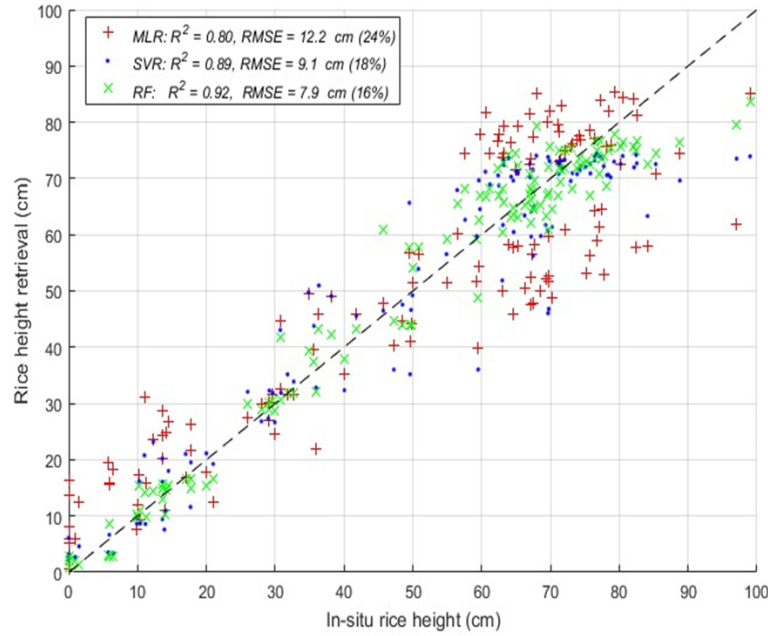


Figure 4.6: Rice height estimation using MLR, SVR and RF methods. In this figure, the configurations that provide the best results are considered (with dual-polarization VV and VH model).

As shown in Figure 4.6, the correlations (R^2) obtained by using MLR, SVR and RF are 0.8, 0.89, 0.92 respectively. MLR gives the biggest value of RMSE (12.2 cm—24%), followed by SVR with RMSE = 9.1 cm (18%) and RF with the minimum RMSE = 7.9 cm (16%).

Next, in Figure 4.7, the rice height retrieval respect to in-situ data during the cultured period is shown for example on two plots: 2M2 and 4M2. The continuous line presents the estimated height of rice, while the following small circles show the in-situ rice height measurements. Visibly, the correlation between the retrieved and in-situ rice height of the two parcels is good. The rice height retrieval and the in-situ rice height are increasing and close together as the result of rice growth.

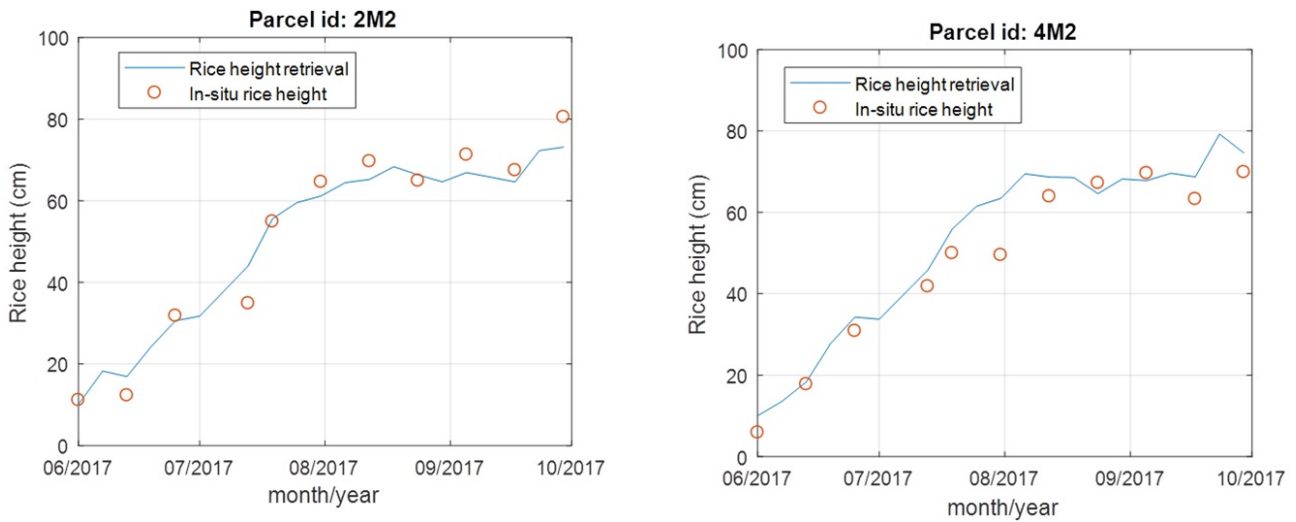


Figure 4.7: Rice height retrieval and in-situ measurements at two reference plots 2M2 and 4M2.

4.4.5 Rice Biomass Estimation

Tables 4.5 and 4.6 show all the results of rice biomass inversion performance of MLR, SVR, and RF. The best performance is obtained by the MLR method using dual-polarization VV and VH model: $R^2 = 0.85$, $RMSE = 206 \text{ g}\cdot\text{m}^{-2}$ (22%). For SVR and RF methods, the best performance is obtained by using the VH polarization model: $R^2 = 0.87$, $RMSE = 175 \text{ g}\cdot\text{m}^{-2}$ (19%) for the SVR method: $R^2 = 0.9$, $RMSE = 162 \text{ g}\cdot\text{m}^{-2}$ (18%) for the RF method, respectively.

	VV		VH		VH and VV		PCA (VH and VV)	
Methods	R^2	RMSE ($\text{g}\cdot\text{m}^{-2}$)	R^2	RMSE ($\text{g}\cdot\text{m}^{-2}$)	R^2	RMSE ($\text{g}\cdot\text{m}^{-2}$)	R^2	RMSE ($\text{g}\cdot\text{m}^{-2}$)
MLR	0.81	230	0.81	216	0.85	206	0.83	213
SVR	0.86	178	0.87	175	0.86	207	0.86	193
RF	0.90	167	0.90	162	0.88	177	0.89	174

Table 4.5: Rice biomass estimation from five folds of cross-validation. The best results are in bold.

	AIC				BIC			
Methods	VV	VH	VV and VH	PCA (VH and VV)	VV	VH	VV and VH	PCA (VH and VV)
MLR	242.2	239.4	239.4	240.8	241.3	238.5	238.2	239.6
SVR	231.0	230.3	241.6	236.6	230.1	229.4	240.4	235.4
RF	228.3	227.0	232.8	232.1	227.4	226.0	231.6	230.9

Table 4.6: AIC and BIC for rice biomass estimation. The smallest values are in bold.

Figure 4.8 presents the effectiveness of three methods to estimate rice biomass. The correlation coefficients R^2 are 0.85, 0.87, 0.90 for MLR, SVR and RF methods, respectively. In addition, the RMSE values are $206 \text{ g}\cdot\text{m}^{-2}$ (22%), $175 \text{ g}\cdot\text{m}^{-2}$ (19%), and $162 \text{ g}\cdot\text{m}^{-2}$ (18%), respectively.

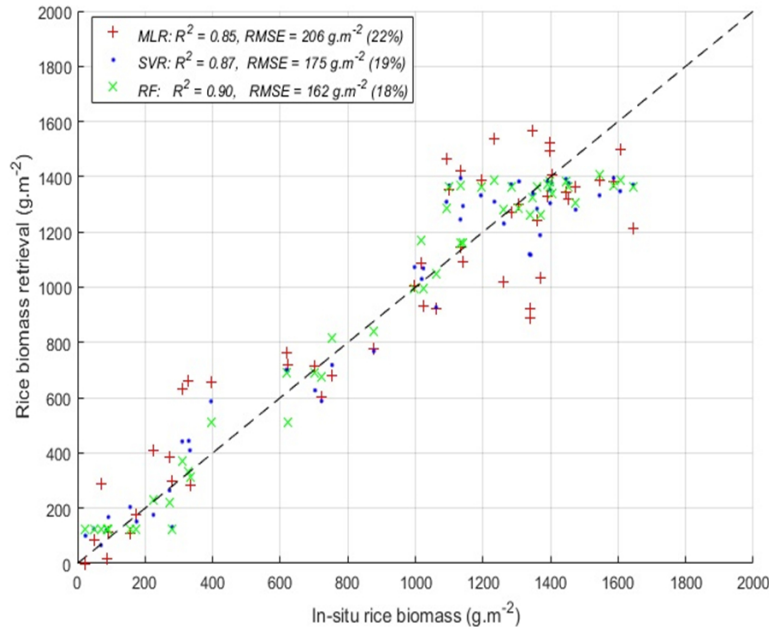


Figure 4.8: Rice biomass estimation using MLR, SVR and RF methods. In this figure, only the configurations that provide the best results are considered (with dual-polarization VV and VH model for MLR, and with VH model for SVR and RF).

As seen in Figure 4.9, for example, at two reference plots 1G3 and 3M1, the scatter plots between retrieved and in-situ rice biomass indicate the same behavior along the growth stage

with continuous line for rice biomass retrieval and circles for in-situ rice biomass.

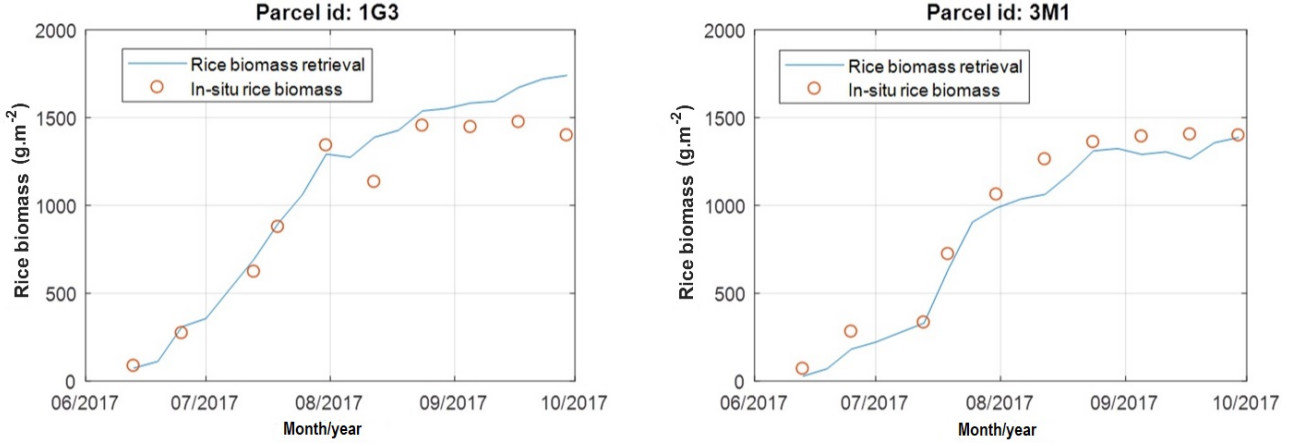


Figure 4.9: Rice biomass retrieval and in-situ measurements at two reference plots 1G3 and 3M1.

4.5 Discussion

In this chapter, we show that the Sentinel-1 can be used to estimate rice height and biomass in Camargue with a high accuracy. The dynamics in rice height and biomass can be observed by the backscatter behaviors in each of the two polarizations (VV and VH). Good results can be obtained by using classical approaches (MLR, SVR, and RF). The validated metric indicates good performance, in which the correlation coefficient R^2 was greater than 0.8. We show that there is a better performance using non-parametric methods (SVR and RF) over the parametric MLR method. Thus, these demonstrated results confirm the great potential of Sentinel-1 data for rice height and biomass retrievals.

First of all, even with the traditional approaches, we show that good retrieved performance could be yielded with Sentinel-1 SAR data. This is not straightforward due to the speckle noise nature in radar images. Good performance can be explained by the fact that 6 days time series Sentinel-1 SAR data allows not only a good follow-up of the rice growth but also mostly noise-free dataset, thanks to the speckle adaptive filtering. In addition, for rice biophysical parameter estimations, the Day after Sowing information, which can be retrieved directly from Sentinel-1 data within the accuracy of 3 days (our estimation), allows us to mitigate the potential problem on the radar signal saturation. This situation is different from forest applications, where the forest age is challenged to retrieval. For example, for forest biomass estimations, many works have to use prior knowledge (e.g., Landsat-derived tree cover [116]) or advanced techniques (e.g., SAR tomography [56, 57]) to mitigate the radar signal saturated problem. Finally, we note that outside the European zones, there is a limitation for Sentinel-1 data since the revisit period will be 12 days. However, it should be emphasized that, nowadays, the Sentinel-1 constellation is the only system which can provide free and global coverage radar data. Therefore, it is a good candidate for operational rice monitoring tasks.

Using in-situ measurements at Camargue, we show that radar backscattering coefficients are sensitive to rice biophysical parameters and have a strong correlation with rice height and biomass. This observation is consistent with reports from the literature [92, 78] due to the sensitivity of radar signals to rice structures. The backscatter of VH and VV polarizations can be separated into two main parts. In the first part, the VV and VH increase with the rice growth until 50 cm height (See Figure 4.5c). At this stage, the main backscattering mechanism is contributed by the interaction between the stem and the underlying water surface (e.g., double bounce). In the second part (where rice grows from 50 cm to 100 cm (maturity)), although the VV goes down, the VH is still slightly increased. Indeed, at this stage, the backscattering mechanisms are contributed not only by the double bounce interaction but also from the volume stem directly. Beyond 50 cm, the double bounce phenomenon can be reduced, and the stem and leaves of the rice are not remained vertical. While they lead to the power decrease of the VV backscatter, the VH signal is increased due to its sensitivity to random volume backscattering. Similar interactions were also reported by Lopez-Sanchez et al. [101]. The same trend of backscattering coefficients versus rice biomass is observed. When rice biomass reaches around $800 \text{ g}\cdot\text{m}^{-2}$ (See Figure 4.5d), this is the period when the rice stem is no longer vertical and the leaves have already deviated from the stem. Interestingly, it is worth pointing out that there is a jump in both VV and VH backscatter at 100 DaS days (See figure 4.5a). This is mainly because there is a rapid transition from always irrigated rice fields at the reproductive stage to no longer irrigated status at the ripening stage.

We can observe that non-parametric methods (SVR and RF) have better performance over the parametric MLR method for estimating rice parameters (See Tables 4.3 and 4.5). Between the SVR and RF models, the RF method obtains slightly better results than the SVR. With the RF method, the correlation coefficient R^2 and RMSE were 0.92 and 16% for rice height, 0.90 and 18% for rice dry biomass. For rice height, all methods (MLR, SVR, and RF) yield the best performances with the dual-polarization VV and VH model. For rice biomass, we observe that the combination of VH and VV polarizations does not bring to the good result as a single VH polarization in SVR and RF methods. This can be explained by the fact that the VH backscattering is mainly from the depolarizing part represents a small proportion of biomass, but it is highly correlated with the total biomass [115]. The RMSE was 16% (7.9 cm) for rice height, which is better than the result (13.3 cm) reported in the recent literature [188]. For rice biomass, the RMSE was 18% ($162 \text{ g}\cdot\text{m}^{-2}$), which is better than the recent results (RMSE = $170.49 \text{ g}\cdot\text{m}^{-2}$) reported by Jing et al. [79], who used an Artificial Neural Network (ANN) inversion method on the C-band RADARSAT data. Last but not least, our rice biomass estimation ($162 \text{ g}\cdot\text{m}^{-2}$) is much better than the performance ($200 \text{ g}\cdot\text{m}^{-2}$) from L-band ALOS/PALSAR data [187].

In parallel with machine learning algorithms, there is also another approach to estimate rice parameters. This is physical model-based inversion (such as Karam Model [82], Water

Cloud Model [48], etc.). However, physical models are complicated and related to certain rice growth models, which require a wide area for the experiment station to measure model parameters. These limitations of physical model-based inversion methods make sense to work on machine learning methods [127, 170]. We demonstrated in this chapter that the non-parametric methods (SVR and RF) had a good performance in estimating the rice biophysical parameters.

Finally, among agricultural practices in the Camargue region, the rice crop plays a crucial role in the cropping systems. This is mainly because the rice irrigation allows the leaching of salt and consequently leads to the introduction of other species (e.g., wheat, sunflower, etc) into the rotation of crops [120]. However, the rice areas tend to decrease from 16,000 ha in 2011 ([28]) to 10,627 ha ([125]) in 2017. The downward trend of the rice extent can lead to a negative impact on the sustainable agricultural development. Future studies should be considered the remote sensing assimilation, such as Sentinel-1 radar for rice height and biomass as our demonstration, in crop models to better follow farming practices, estimate rice production and provide strategies for the sustainable agricultural development.

4.6 Conclusions

In this chapter, we studied the potential of Sentinel-1 remote sensing data for rice height and dry biomass estimations. We proposed to use three classical machine learning approaches to predict rice parameters from Sentinel-1 data, which were applied in the Camargue region.

We demonstrated that good regression performance could be yielded with Sentinel-1 data even with the classical approaches (MLR, SVR, and RF). We found that non-parametric methods (SVR and RF) had better performance over the parametric MLR method for estimating rice parameters. Between the SVR and RF models, the RF method obtains slightly better results than the SVR. Correlation coefficient R^2 and RMSE were 0.90 and 18% ($162 \text{ g} \cdot \text{m}^{-2}$) for rice dry biomass, 0.92 and 16% (7.9 cm) for rice height, which indicated a high accuracy of Sentinel-1 SAR retrieval. In other words, we demonstrated that Sentinel-1 remote sensing data could be an alternative and reliable approach to monitor regional rice height and estimate dry biomass, compared with direct field measurements. Future work on the Camargue region could be focused on exploiting Sentinel-1 data to improve crop models to better estimate rice production yields in order to be able to propose strategies for sustainable agricultural development.

In the context of the Copernicus program, there are two missions: radar Sentinel-1 and optical Sentinel-2. In future research, the data combination from the two satellites will be a necessity as it will be possible to carry out large-scale missions. Radar and optical data can be complementary to each other because they offer different perspectives on the Earth's surface providing different information content according to their specificity [15, 74, 35]. Both types of data can also be merged to provide information from multiple sources and to provide improved results for decision making [52].

COMBINING ALOS/PALSAR AND LANDSAT-DERIVED TREE COVER DATA FOR FOREST BIOMASS RETRIEVAL

5.1 Introduction

Forest biomass plays a key role in the global climate [129]. However, compared to biomass in other ecosystems, forest biomass remains poorly quantified, owing to the practical difficulties in measuring stocks over broad geographic scales. Overcoming this obstacle is important, because quantifying forest biomass is essential for countries planning to participate in the Reducing Emissions from Deforestation and Degradation (REDD) program [67]. REDD offers incentives (e.g., monetary compensation) for countries to preserve their forestland in the interest of reducing carbon emissions and thereby lessening the risk of climate change. Both above-ground and below-ground biomass are present, but above-ground biomass (AGB) is more commonly measured. In recent years, progress has been made in mapping forest biomass by using a range of remote sensing technologies [146, 5, 172]. Nonetheless, these studies are limited by their dependence on optical sensors (relatively insensitive to biomass), low resolution (from 250 m (Vieilledent) to 500 m (Baccini) to 1000 m (Saatchi)) and inadequate sampling intensity. For example, the results of Saatchi (2011) and Baccini (2012) show strong discrepancies at the local scale and there are no evident reasons for preferring one map over the other.

Unlike passive optical sensors, radar systems are capable of producing high quality images of the earth even in cloud cover conditions. Synthetic aperture radar (SAR) allows for continuous global spatial coverage and systematic acquisitions, both of which are essential for constructing relevant temporal series. The potential of SAR for forest biomass estimation has been highlighted since the early 1990s [89]. Radar intensity depends on the overall geometrical and dielectric features of these various scatterers, whose geometrical volume and wood density give the whole forest biomass. As a general rule, increasing intensity values goes with increasing biomass whether at L or P-bands, until a saturation value, which occurs earlier at L-band [29].

The L-band ALOS mission is considered pioneering in the systematic acquisition of data that has allowed the imaging of the planet over time at high resolution. This strategy of systematic acquisition enabled the production by the Japan Aerospace Exploration Agency (JAXA) of mosaic images of up to 25-m resolution [151]. These mosaics are radar images preprocessed by the JAXA, made freely available in tiles of 1 degree squared for the years 2007-2010 [152]. The L-band ALOS PALSAR data have been widely used to estimate the forest biomass. For example, the ALOS PALSAR data were exploited to estimate the biomass of forests threatened by oil palm plantations in Malaysia [119], while in Sumatra, texture features from ALOS PALSAR data were used [160]. However, estimation of forest biomass using ALOS PALSAR data currently has limitations, because the L-band saturates at about 150 t/ha. Savanna vegetation has lower carbon stocks and is thus more easily estimated with these data. For example, [112] produced a country-level map of Cameroon's savanna biomass at 25-m resolution. In most studies, the cross-polarization (HV) is preferred for estimating biomass because it minimizes the contribution of coupling terms with the ground. Indeed, the HV intensity mainly from the depolarizing part (oriented branches) represents a small proportion of biomass, but it is highly correlated with the total biomass. These studies are based on the fact that the HV intensities are positively correlated with biomass. However, the signal sensitivity decreases as the biomass increases, up to a point called the saturation point, where sensitivity is lost. At L-band HV, this saturation point is about 150 t/ha [112]. After the saturation point, many studies [178, 105, 112] have highlighted a weak negative correlation of intensity with biomass. In other words, with high biomass values, the ALOS PALSAR signals decrease. The non-monotonic relationship between intensity and biomass means that corrective models must be established when the range of biomass includes high values. One attempt to retrieve biomass greater than 150 t/ha is the European Space Agency (ESA) P-band BIOMASS mission, to be launched in 2020. Taking advantage of the 300 t/ha saturation point for P-band, this mission aims for more precise measures of global forest biomass [90, 117] and hence better understanding of the terrestrial carbon cycle by measuring global forest biomass.

However, the potential for using L-band radar to estimate high biomass values has not been completely explored. In this study, we propose a new approach to retrieve the full range of biomass using L-band ALOS PALSAR data based on prior knowledge from the global tree cover map at 30-m resolution produced by [53]. To do this, we use a very large number of forest plots (572) dispersed across Madagascar from 2007-2013. Madagascar has a wide variety of forest types (dry forest, spiny forest, and tropical moist forest) known to differ in AGB. It is thus a particularly interesting region for studying spatial variation in the distribution of biomass (and hence of carbon) stocks using radar data.

The chapter is organized as follows: in section 5.2, the study site is introduced and the proposed methodology is shown; in section 5.3, the relationship between radar measurements and AGB is evaluated and the inversion results are presented; in section 5.4, we interpret and

discuss for each result; in section 5.5, we present our conclusions.

5.2 Data and Methods

5.2.1 Study area

A continental island almost 1600 km long lying off the south-eastern coast of Africa in Indian Ocean, Madagascar stretches between 12°S and 25°S latitude, from Cape Amber in the north to Cape St. Mary in the south, and averages about 500 km in width. Within its area of 587 040 km^2 , three types of climates occur. The east coast has a humid tropical climate. West of this coast, the climate is moderate in the north and arid in the south. The broad climatic gradients on the island are associated with elevation and position relative to the dominant southeastern trade winds [47]. Over these climatic gradients occur a large range of tropical forest types, from dry spiny forests in the sub-desert southern regions, to cloud forests at the tops of the northern and eastern mountains. The east coast, exposed to the trade winds, receives the highest rainfall with 3500 mm/year. Forests in the northeast, are particularly wet and lush. Vegetation of western, southern and eastern Madagascar is comprised mainly of dry forest, spiny forest and moist forest, respectively. The moist forests are characterized by dense evergreen vegetation with a canopy exceeding 30 m. Trees of the dry forests shed their leaves in the dry season to limit evapotranspiration, whereas plants of the spiny forests are strongly adapted to drought. Figure 5.1 shows the study area and biomass measured in situ.

5.2.2 Field data

Field data are available from nine forest inventories carried out over the period 1996-2013. Collaboration with different institutions (governmental institutions, conservation NGOs, research institutes) allowed us to obtain data from a large number of forest plots (1771) in the three forest ecoregions of Madagascar (moist, dry and spiny forest ecoregions). However, in this work, we used only the forest inventories from 2007-2013 to match with the ALOS PALSAR data, in which 572 plots were selected based on flat field slope and homogeneity within plots. The radius of the plots was 30 m in moist forest (plot size of 0.28 ha) and 20 m in dry or spiny forest (plot size of 0.13 ha). Figure 5.2 shows the number of plots and its distribution with respect to each ecoregion. We calculated the AGB biomass (in metric tons) of each tree using the pantropical biomass allometric equation developed by [21]:

$$(5.1) \quad AGB = 0.0673 \times (\rho \times DBH^2 \times H)^{0.976}$$

Where ρ is the tree wood density in g/cm^3 , DBH is the diameter at breast height in cm, H is the tree height in m. Details about the computation of AGB at the plot level are published in [172].

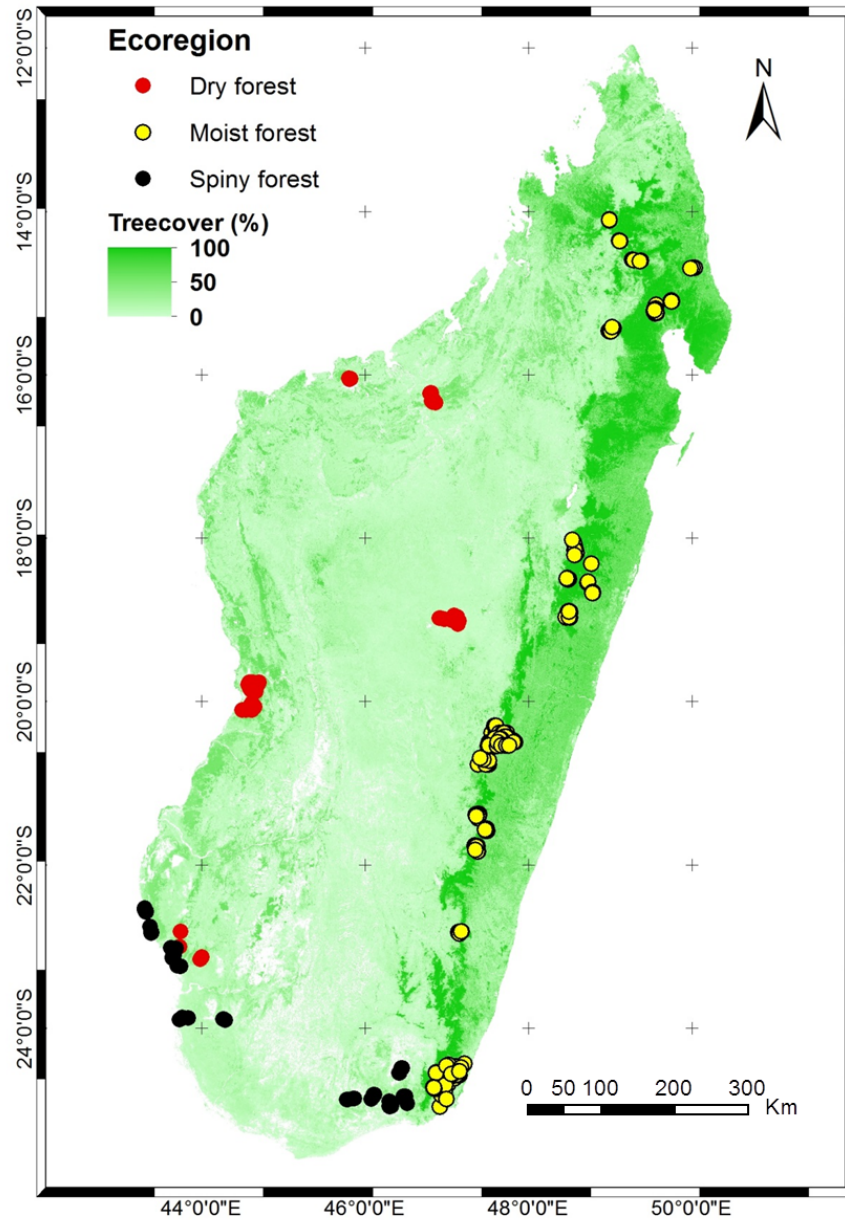


Figure 5.1: The study site is the entire island of Madagascar. The background is the Landsat-derived tree cover. Red, yellow and black circles represent field sites in dry forest, moist forest and spiny forest, respectively.

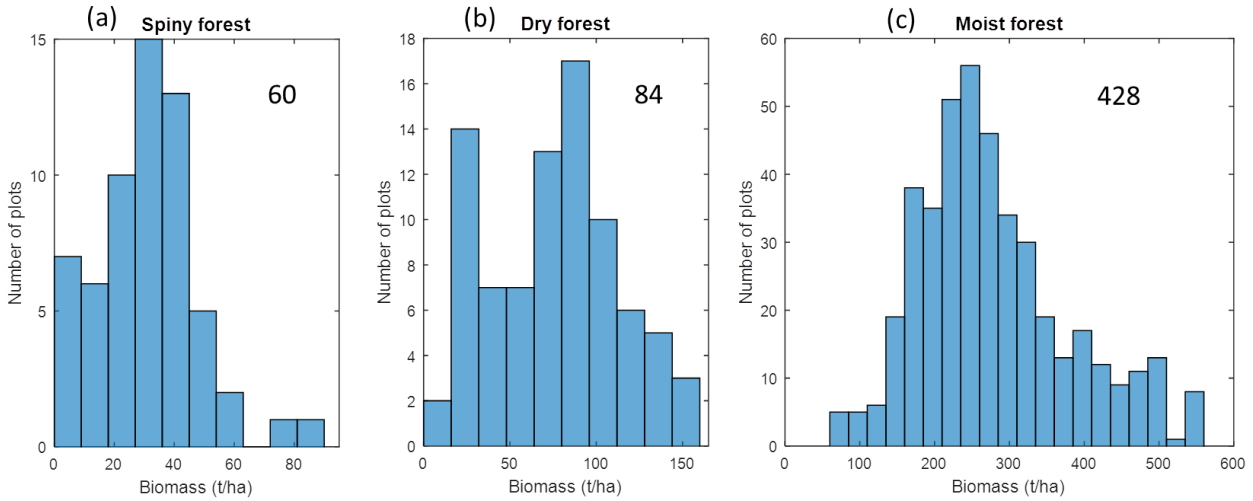


Figure 5.2: Biomass measured in situ in spiny (a), dry (b) and moist (c) forest ecoregions. Number of plots sampled were 60, 84 and 428, respectively.

5.2.3 Tree cover data

Tree cover data are available globally at 30-m resolution from 2000-2012 in [53]. The primary purpose of that study was to quantify global forest change over the study period. This dataset was obtained by analyzing 654 178 Landsat 7 Enhanced Thematic Mapper Plus scenes, from a total of 1.3 million available. The final results were obtained by training three separate classifiers: one to detect forest loss during the study period, one to detect forest gain during the study period, and one to detect forest cover at the start of the study period. For pixels that were classified as forest loss, the year of loss could essentially be determined by isolating the year of max normalize different vegetation index drop. This resulted in a baseline map of tree cover for the year 2000, forest loss and forest gain during 2001 and 2012. To support our analysis, tree cover maps for Madagascar for 2007, 2008, 2009 and 2010 were generated from the baseline tree cover map of 2000 using the yearly loss/gain information. Detailed discussion of the optical Landsat-derived tree cover dataset can be found in [53]. In the present study, the dataset for tree cover at 30-m resolution was resampled to 25-m to combine with the SAR data. Figure 5.3 shows the distribution of tree cover in 2010 and biomass measured in situ.

5.2.4 SAR data

520 ALOS PALSAR mosaic tiles with 25-m resolution covering all of Madagascar from 2007-2010 were provided freely by the JAXA. Mosaic data are spatially square (1° of latitude and 1° of longitude). The radar signal can be converted into γ^0 values using the following equation:

$$(5.2) \quad \gamma^0 = 10 \times \log_{10}(DN^2) + CF$$

where γ^0 is the normalized intensity, DN is the digital number and CF is the calibration factor, which equals -83.0 as described in [151].

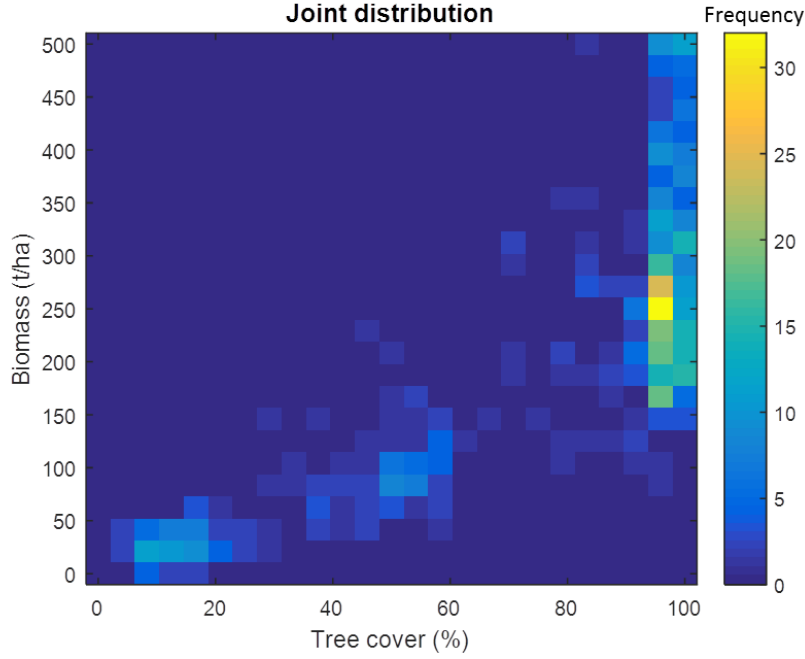


Figure 5.3: The joint distribution between Landsat-derived tree cover and biomass measured in situ. More than 98% of plots with AGB > 150 t/ha had tree cover of 95% or greater.

The 520 ALOS images used in this study were processed by JAXA using the large-scale mosaicking algorithm described in [152]. This algorithm includes ortho-rectification, slope correction and radiometric calibration between neighboring strips. At this stage, the resulting multilook images were perfectly coregistrated, and the equivalent number of looks of ALOS PALSAR data was 16. We further improve this four years SAR dataset by exploiting a multi-image filtering developed by [140] to reduce noise while retaining as much as possible the fine structures present in the images.

5.2.5 Proposed methodology for biomass retrieval

Based on results reported from the literature on sensitivity of the L-band intensity in relation to biomass (see section 5.1), it is possible to use the L-band HV to estimate biomass for up to a maximum of 150 t/ha. For higher values of biomass, L-band intensity is weakly sensitive variation in biomass. In this section, we present a method to address this problem.

First of all, we propose to weight the radar intensity by the tree cover factor from section 5.2.3 using the following formula:

$$(5.3) \quad \gamma_{HVtree}^0 = 10 \times \log_{10}(treecover \times DN_{HV}^2) + CF$$

where γ_{HVtree}^0 is the intensity weighted by tree cover and the value for tree cover varies from 0 to 1.

Figure 5.4 shows the distribution of γ_{HV}^0 , γ_{HVtree}^0 and biomass measured in situ, for the year 2010. A significant growth was observed in intensity with low biomass levels, followed by

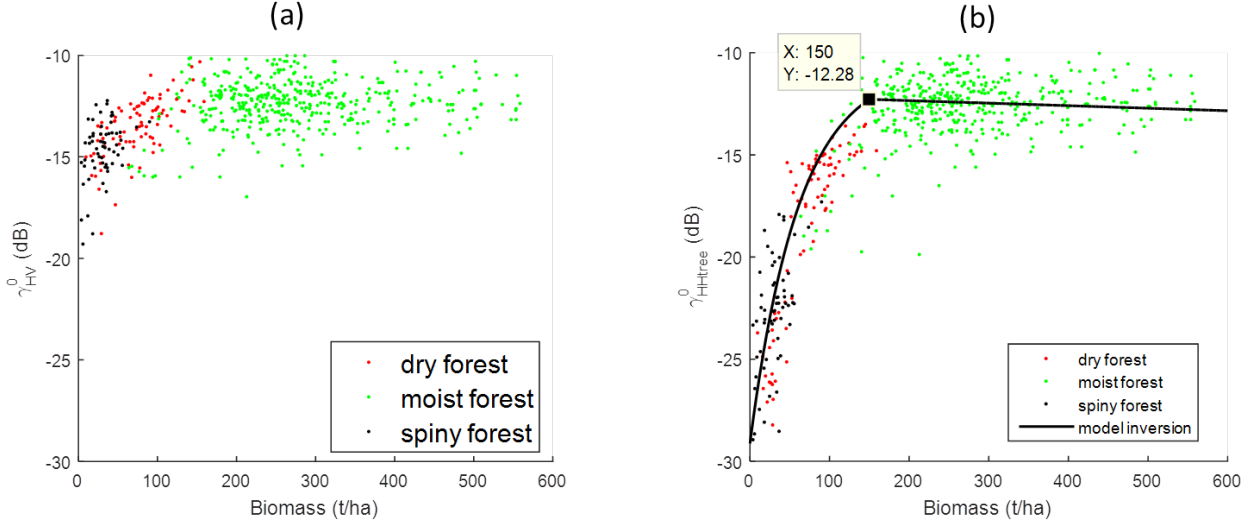


Figure 5.4: (a) Biomass measured in situ versus γ_{HV}^0 . (b) Biomass measured in situ versus γ_{HVtree}^0 .

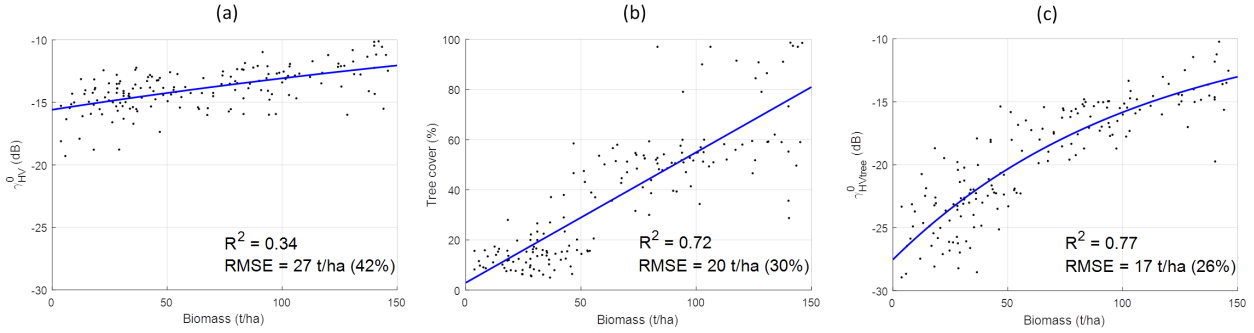


Figure 5.5: (a) Biomass measured in situ versus γ_{HV}^0 . (b) Biomass measured in situ versus tree cover. (c) Biomass measured in situ versus γ_{HVtree}^0 . The blue line is the best fit of the data.

a loss of sensitivity and a slight decrease in signal intensity beginning at 150 t/ha. The range of γ_{HVtree}^0 is much higher than that of γ_{HV}^0 . In the high range of biomass values, there is no difference between the sensitivity of γ_{HV}^0 and γ_{HVtree}^0 . In fact, as seen Fig. 5.3, we found that of plots where biomass was greater than 150 t/ha, 98% had tree cover of 95% or more. Based on this observation, we proposed to use tree cover of 95% as a threshold to recognize the high range of biomass values.

To highlight the usefulness of γ_{HVtree}^0 in our approach, we compare the sensitivity of γ_{HV}^0 (unweighted radar intensity), γ_{HVtree}^0 (radar intensity weighted by tree cover) and tree cover with in situ biomass values in the low range (e.g., < 150 t/ha) in Fig. 5.5. The highest correlation is observed with the weighted radar intensity data. The γ_{HV}^0 data exhibit a much lower sensitivity to biomass ($R^2 = 0.34$) than do the γ_{HVtree}^0 data ($R^2 = 0.77$). One possible explanation of this result is that radar intensity integrates noise signals from the ground and this problem can be partly mitigated by incorporating tree cover data from optical images. Finally, by comparing γ_{HVtree}^0 and tree cover in Fig. 5.5b and 5.5c, the γ_{HVtree}^0 data exhibit a higher sensitivity to biomass ($R^2 = 0.77$ versus 0.72) and a smaller root mean square error (RMSE) (26% versus 30%).

For biomass lower than 150 t/ha, we fit an exponential model to link radar signal to biomass [118], described as:

$$(5.4) \quad \gamma_{HVtree}^0 = a + b \times (1 - e^{-c \times AGB})$$

where AGB is the biomass measured in situ, a , b and c are coefficients to be estimated from the data.

For higher values of biomass, we fitted a linear model [113], described as:

$$(5.5) \quad \gamma_{HVtree}^0 = m + n \times AGB$$

where m and n are coefficients to be estimated from the data.

By using Eq. 5.4 and 5.5, an estimation of biomass \widehat{AGB} can be calculated from γ_{HVtree}^0 . However, in our approach, a bias in the inversion can be introduced. In the statistical literature, this phenomenon is referred to as regression dilution, in that random error in the independent variable leads to systematic underestimation of the regression slope [43, 42]. To correct for such bias, we compensate the biomass by a ratio β , described as:

$$(5.6) \quad Bias[\widehat{AGB}] = \beta \times AGB$$

where $Bias[\widehat{AGB}] = E[\widehat{AGB} - AGB]$ and $E(\cdot)$ denotes expected operator, i.e., averaging over a number of observations.

5.2.6 Calibration for Madagascar

A common method for biomass retrieval is to exploit an inverse model based on the empirical regression derived from the available set of in situ and radar plot data. In this work, using 572 biomass plots for fitting with each year's SAR data, e.g. for the year 2010, we found that :

For biomass lower than 150 t/ha:

$$(5.7) \quad \widehat{AGB} = -\frac{1}{c} \times \ln(1 - \frac{\gamma_{HVtree}^0 - a}{b})$$

With $a = -29.13 \pm 0.09$, $b = 18.47 \pm 0.14$ and $c = 0.01623 \pm 0.00034$. In the low range of biomass values, γ_{HVtree}^0 is very highly correlated with biomass ($R^2 = 0.77$ and $p < 10^{-5}$).

For higher biomass values and tree cover greater than 95% :

$$(5.8) \quad \widehat{AGB} = \frac{\gamma_{HVtree}^0 - m}{n}$$

With $m = -12.14 \pm 0.28$ and $n = -9.28 \cdot 10^{-4} \pm 9.35 \cdot 10^{-5}$. In the high range of biomass values, γ_{HVtree}^0 is less strongly correlated with biomass ($R^2 = 0.18$ and $p = 0.017$).

Figure 5.4b plots these equations 5.7 and 5.8, showing the fit between the weight the radar intensity and the in situ biomass.

Finally, the estimated biomass can be calculated as:

$$(5.9) \quad Biomass = (1 + \beta) \times \widehat{AGB}$$

With $\beta = 0.2392 \pm 0.0515$.

5.2.7 Carbon estimation and uncertainty

The calibration described in section 5.2.6 allows estimation of above-ground biomass in Madagascan forests. To calculate carbon stock, we convert biomass into carbon units using the 0.47 ratio [172]. We apply a filter to this carbon data based on the tree cover map and only include pixels with $> 25\%$ tree cover. In others words, we follow a conservative approach in defining forest: only land with tree cover not less than 25% was considered as forest [53, 151].

The model inversion between biomass and radar is affected by the uncertainties in radar signal, tree cover estimate and in situ biomass data. The radar signal is impacted by a number of factors related to forest structure and environments. The signal can also be affected by variation in the performance of the signal emitter over time. However, the ALOS PALSAR γ_{HV}^0 was found to be very stable at 0.065 dB over its lifetime 2006-2010 [151]. Regarding the tree cover dataset, there is little uncertainty, with classification error less than 1% [53]. Regarding in situ biomass measurements, the data collection procedures in the sources we used varied somewhat across organizations, but all the different protocols allowed estimating biomass in t/ha at the center of each forest plot. Application of an uncertainty analysis at each stage is out of the scope of this study. If all sources of uncertainties can be estimated, an explicit equation can be applied to ALOS PALSAR data [111]. Nonetheless, in this work, uncertainties related to the carbon estimates are estimated by Monte Carlo simulations. Such uncertainties affect the definition of the inverse model (imprecision and bias), as the in situ biomass estimates are used to fit parameters of the model. A new inverse model is derived by estimating the coefficients (a, b, c, m, n, β) and biomass is estimated at each generation (with 1000 realisations). For each pixel, the dispersion of biomass values resulting from the 1000 possible models is used to calculate the standard deviation in the uncertainty associated with the estimation of biomass (and hence of carbon).

5.3 Results

The methods proposed in section 5.2.5 were applied to ALOS PALSAR data in Madagascar. The RMSE and the correlation R^2 were used to evaluate performance of the SAR dataset for

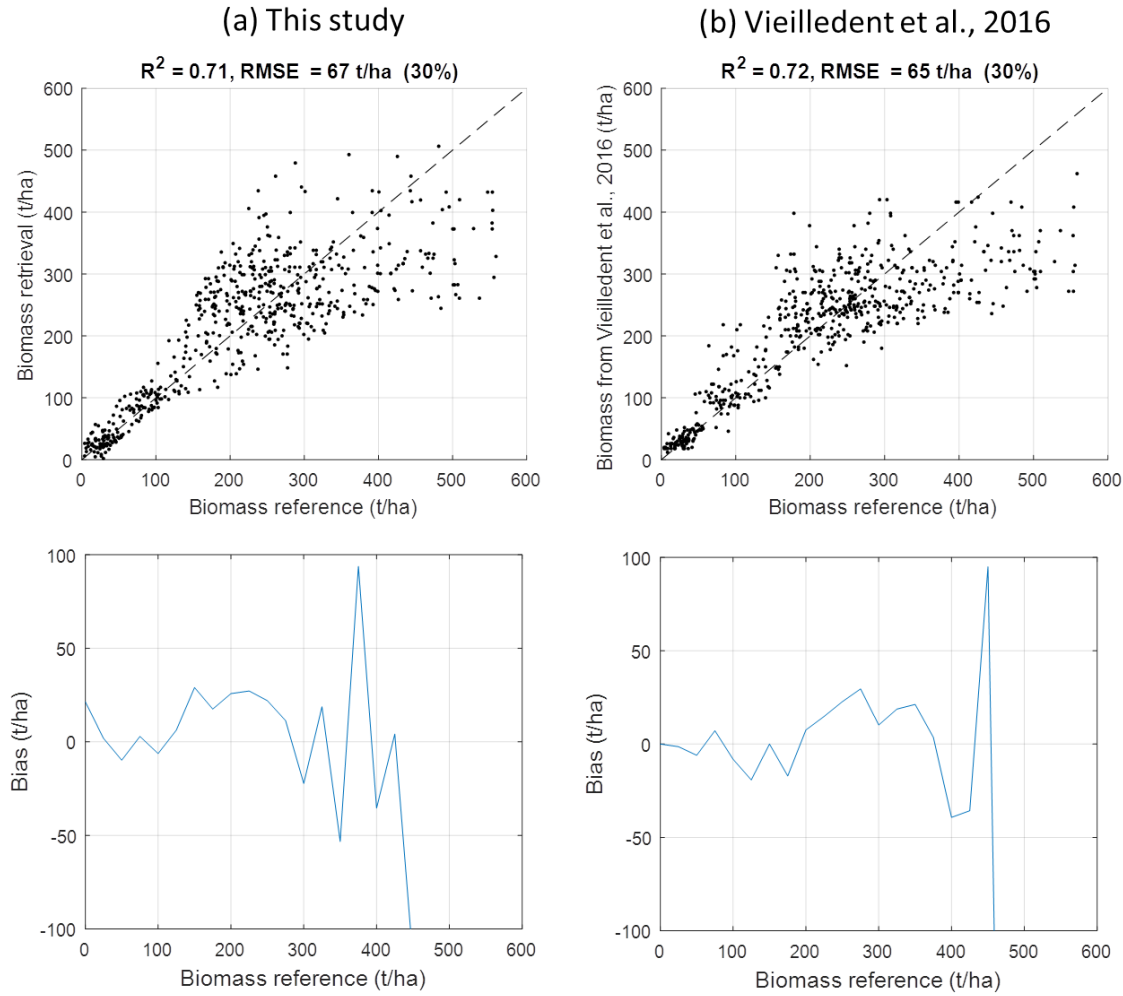


Figure 5.6: (a) The biomass inversion performance of this study. (b) Performance in the study of [172]. Top panels are the cross-plot 1:1. Bottom panels are the bias. The biomass retrieval appears to be reliable for biomass ranging from 0 to 300 t/ha.

each year using all in situ plots available. The same performance for biomass retrieval with respect to in situ data was found for all four years. The results, presented in Fig. 5.6a, showed a RMSE of 30% (for biomass ranging from 0 to 500 t/ha) and $R^2 = 0.71$, for the year 2010. To avoid overfitting, we carried out a 10-fold cross-validation procedure [110]. For biomass values in the range 0-150 t/ha, the average RMSE in 2010 was 26% and $R^2 = 0.77$, whereas for biomass values in the range 0-300 t/ha in the same year, the average RMSE was 28% and $R^2 = 0.72$.

Second, 520 ALOS PALSAR 25-m resolution images were used to retrieve biomass for 2007, 2008, 2009 and 2010. The biomass maps for these four years were found to be similar in their biomass content. An example of the biomass map for 2010 is shown in Figure 5.7b. To appreciate the 25-m pixel size of the biomass map, a zoom version in an $0.5^\circ \times 0.5^\circ$ window was shown in the bottom. The distribution of biomass at 25-m resolution shows details of spatial biomass density, indicating a west-east gradient.

Third, using our map at 25-m resolution, we estimated the forest carbon stocks for dry, spiny

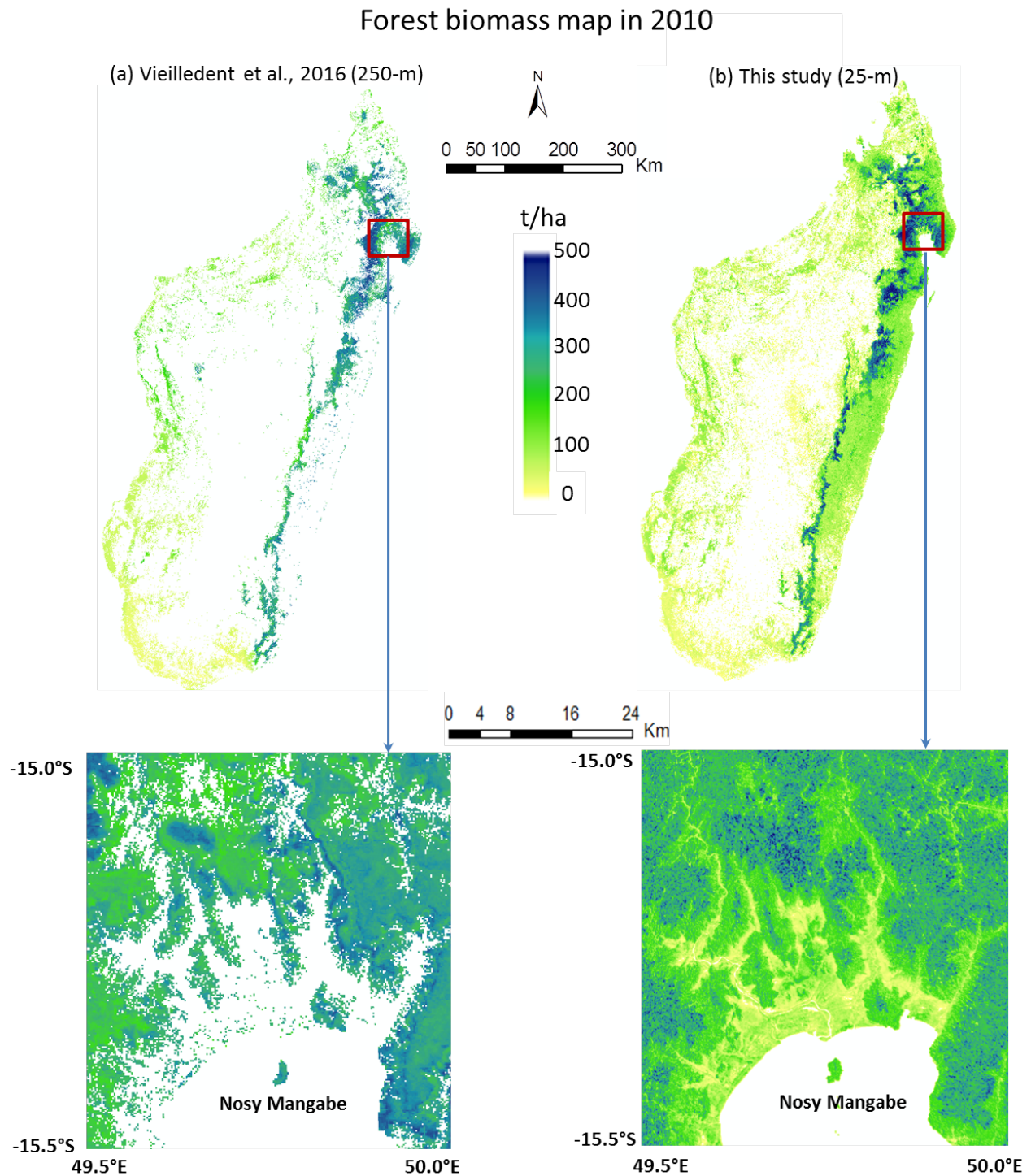


Figure 5.7: Biomass maps for Madagascan forests for the year 2010 are shown. The color scale varying from yellow to green to blue illustrates the full biomass range from 0 to 500 t/ha. The spatial distribution of biomass for the entire island of Madagascar shows a west-east gradient. (a) Map from the study of [172] and (b) Map from this work. The bottom panels show a zoom version of red-bordered boxes to facilitate visualization of the biomass results.

Table 5.1: Surface area (ha) and carbon assessment (PgC) in Madagascar with respect to the dry, spiny and moist forest ecoregions.

	2007		2008		2009		2010	
	Area (ha)	Carbon (PgC)	Area (ha)	Carbon (PgC)	Area (ha)	Carbon (PgC)	Area (ha)	Carbon (PgC)
Dry	4,770	0.1635±0.0078	4,725	0.1623±0.0079	4,695	0.1601±0.0079	4,639	0.1528±0.0076
Spiny	355,857	0.0112±0.0011	352,230	0.0111±0.0011	346,299	0.0108±0.0011	341,805	0.0104±0.0011
Moist	13,263	0.9426±0.0215	13,228	0.9295±0.0213	13,193	0.9207±0.0211	13,147	0.9141±0.0211
Total	18,390	1.1173±0.0304	18,305	1.1029±0.0303	18,235	1.0916±0.0301	18,129	1.0773±0.0298

and moist ecoregions, respectively (see Tab. 5.1). The total forest carbon in the four years 2007, 2008, 2009 and 2010 is 1.1173 ± 0.0304 , 1.1029 ± 0.0303 , 1.0916 ± 0.0301 and 1.0773 ± 0.0298 PgC ($1 \text{ PgC} = 10^{15} \text{ g carbon}$), respectively. Over the four years carbon stocks were found to have decreased by approximately 0.01 PgC/year. Finally, using the carbon map in 2007 and in 2010, we established the forest carbon change over the period 2007-2010 (see Fig. 5.8).

5.4 Discussions

In this work we show that radar signal intensity combined with tree cover data can be used to estimate biomass across the entire range of biomass values in Madagascan forests. As seen in Fig. 5.5, weighting the radar signal by tree cover data increased the correlation between the radar signal and biomass. The weighted radar intensity follows a logarithmic regression and biomass reaches a certain threshold at which the signal becomes saturated and then quickly decreases. The present analysis confirms the possibility of exploiting such behavior in an inversion scheme to retrieve the full range of biomass up to 500 t/ha. Relative error in performance of biomass retrieval was 30% and the correlation between the weighted radar intensity and biomass was high ($R^2 = 0.71$) at 25-m resolution. Finally, we showed that biomass can be mapped efficiently even in tropical dense forests. Together, these results considerably add to our confidence in the ability of current and future missions such as L-band ALOS-2, L-band SAOCOM and P-band BIOMASS to provide accurate wall-to-wall biomass mapping. In particular, the arrival of the P-band sensor BIOMASS, which will exploit a volume layer through tomographic processing [56], will make it possible to estimate forest biomass with relative error of only about 11% at 4-ha resolution [59, 57].

First, we showed that the inversion method described in section 5.2.5 can be applied to retrieve the full range of biomass values. Our analysis was successfully conducted for forests of the entire island of Madagascar. It is worth noting that the inversion for high range of biomass values (e.g. greater than 150 t/ha) is mainly based on the fact that L-band radar signal decreases with increasing height of forest vegetation, a phenomenon that is well-known in the L-band literature [178, 105, 112]. In addition, even at the longer wavelength P-band (wavelength 69 cm), the relationship between the ground layer and biomass exhibits a negative trend [56], similar to that observed for the L-band. The decrease can be explained by signal extinction, which likely to be higher in the presence of tall trees (and hence of high biomass).

Forest carbon stocks change map 2007-2010

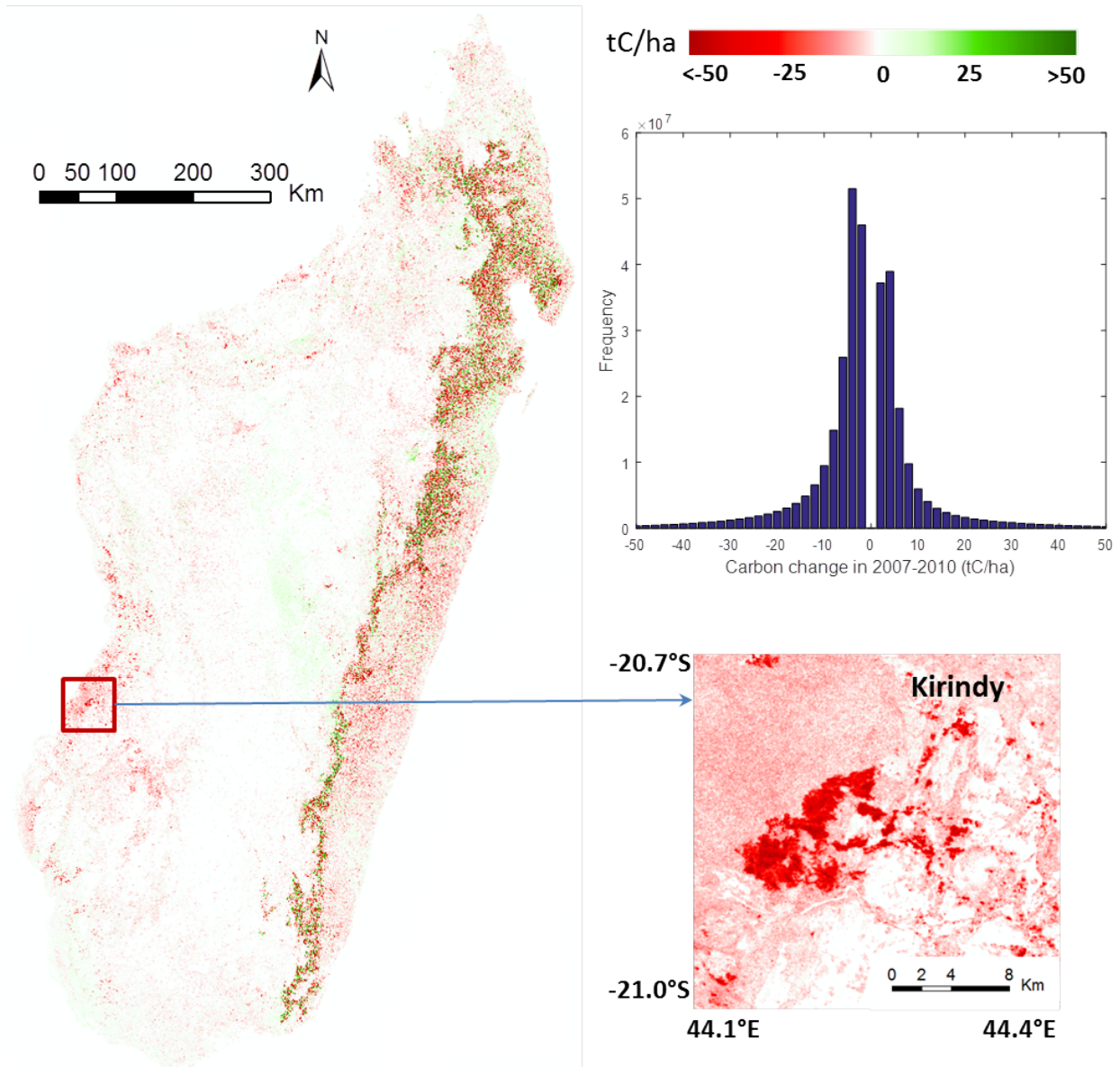


Figure 5.8: Map of change in Madagascar forest carbon stocks in the period 2007-2010. A zoom version of the red-bordered box is provided to facilitate visualization of the carbon loss in Kirindy. The top right panel is the histogram showing distribution of values, excluding values of zero.

To place this result in perspective, we compared our analysis with the work of [172]. Their map was generated by using a correlative approach based on a bioclimatic envelope model and data from all 1771 forest plots inventoried during the period 1996-2013 over a large climatic gradient. The reader is referred to [172] for details. In fact, Vieilledent's map is represented as the most accurate biomass map available at 250-m resolution for the year 2010 in Madagascar. The comparisons are shown in Fig. 5.6 and Fig. 5.7. For the year 2010, from Fig. 5.6, the correlation R^2 and relative error are quite similar between the two maps. However, thanks to the 25-m resolution of the ALOS PALSAR data, our map of biomass distribution is more detailed than Vieilledent's map at 250-m resolution (see Fig. 5.7). For example, in the bottom panels of Fig. 5.7, our map shows details of savanna ecosystems close to the coast such as forest savanna, woody savanna, and gallery forests, whereas in Vieilledent's map, they cannot be shown, owing to the limitation of the data available in the bioclimatic envelope model [172]. Furthermore, it is worth pointing out that if we only consider the low range of biomass values (i.e., < 150 t/ha), our result is slightly better than that of Vieilledent ($R^2 = 0.77$ versus 0.76 and $RMSE = 26\%$ versus 31%). This is important because almost 80% of forest cover of Madagascar has biomass values less than 150 t/ha.

Third, we calculated that the values for total forest carbon in 2010 was 1.0773 ± 0.0298 PgC, whereas by using Vieilledent's map at 250-m resolution, it was 0.8738 PgC. It is worth recalling the results of others studies, for example those of [146] and [5]. These results were predicted for the year 2010 by [172] as 0.7490 PgC and 0.6392 PgC for Saatchi's and Baccini's, respectively. In all cases, we found that their results were underestimated for the total forest carbon stocks, owing to the low resolution of the maps used, with pixel size ranging from 250 m (Vieilledent) to 500 m (Baccini) to 1000 m (Saatchi) and to the limitation of the data in the model inversion, where missing data was treated as zeros. In our estimation, carbon stocks tended to decrease over 2007-2010 by approximately 0.01 PgC/year, caused by anthropogenic deforestation and probably climate change, both of which are known or suspected to lead to decrease carbon stocks in tropical forests elsewhere [172]. As shown by Fig. 5.8, most of the affected areas nationally are in areas of tropical moist forests, i.e., in the east of the island (see also Tab.5.1). Indeed, in Madagascar, around 57 000 ha were deforested each year in the period 2000-2010 (see [173]). Assuming a mean carbon stock of 100 tC/ha, we obtain an annual carbon loss of 0.006 PgC. The difference (0.004 PgC) could be attributed to degradation (caused by direct human actions, climatic events or both).

Finally, to highlight our results on changes in carbon stocks, Fig. 5.8 includes a zoom of an area (outlined in red) near Kirindy. This area of strong carbon stock loss is associated with deforestation, caused by the cyclone Fanele in 2009 followed by uncontrolled fires in the following years [94]. In addition, for each year in Madagascar, the forest carbon gain is usually < 5 tC/year [39, 135], equivalent to < 15 tC for the three-year period 2007-2010. Interestingly, this was confirmed by the histogram in Fig. 5.8, showing very few pixels with values of carbon

change over 15 tC/ha.

5.5 Conclusions

In this study, we have developed a methodology for retrieving the full range of forest biomass values in Madagascar. The methods are based on 572 forest plots and 520 ALOS PALSAR mosaic tiles with 25-m resolution acquired from 2007 to 2010 over the entire island. The method improved the biomass inversion by combining radar intensity and data on tree cover, which resulted in increasing the correlation between the radar signal and biomass. The correlation between the radar signal and biomass measured in situ was high ($R^2 = 0.71$), and the RMSE was 30% (for biomass ranging from 0 to 500 t/ha). For the low range of biomass values (e.g., < 150 t/ha), the correlation was higher ($R^2 = 0.77$, $RMSE = 26\%$). The ALOS/PALSAR mosaic data from all of Madagascar were inverted into biomass values. The spatial distribution of biomass at 25-m resolution for the entire island shows a west-east gradient. The biomass map also shows details of savanna ecosystems close to the coast such as forest savanna, woody savanna, and gallery forests. Over 2007-2010 period, carbon stocks were found to have decreased constantly, owing to anthropogenic deforestation and probably to climate change. We expect these results to serve as a more accurate benchmark than the heretofore state-of-the-arts results of [146, 5, 172]. Our results reinforce the science basis for current and future missions such as ALOS-2, SAOCOM and BIOMASS, increasing our confidence that they can provide accurate wall-to-wall biomass mapping, and thereby enabling progress on REDD initiatives. Combining radar signal with optical tree cover data appears to be a promising approach for using by L-band SAR to map forest biomass (and hence carbon) over broad geographical scales.

CONCLUSION AND OUTLOOK

The general objective of the thesis work was to evaluate the contribution of satellite radar data, acquired by Sentinel-1 and ALOS-1/PALSAR (in C and L bands, respectively), in addition to optical data (Landsat), for monitoring forests and crops, especially rice. This research required the acquisition of satellite and terrain data to determine the spatial distribution of land cover, analyze the sensitivity of the radar data during the vegetative period, and evaluate different biophysical parameters of the vegetation. This thesis work was done in three parts.

The aim of the first part is to provide a better understanding of the capabilities of Sentinel-1 radar images for agricultural land cover mapping through the use of deep learning techniques. The analysis is carried out on multitemporal Sentinel-1 data over an area in Camargue, France. The data set was processed in order to produce an intensity radar data stack from May 2017 to September 2017. We improved this radar time series dataset by exploiting temporal filtering to reduce noise, while retaining as much as possible the fine structures present in the images. We revealed that even with classical machine learning approaches (K nearest neighbors, random forest, and support vector machines), good performance classification could be achieved with F-measure/Accuracy greater than 86% and Kappa coefficient better than 0.82. We found that the results of the two deep recurrent neural network (RNN)-based classifiers clearly outperformed the classical approaches. Finally, our analyses of the Camargue area results show that the same performance was obtained with two different RNN-based classifiers on the *Rice* class, which is the most dominant crop of this region, with a F-measure metric of 96%. These results thus highlight that in the near future these RNN-based techniques will play an important role in the analysis of remote sensing time series. Finally, although the number of exploitable optical images are limited due to cloud cover, the use of multi-source data including optical and SAR radar data will be an important subject of future research.

In the second part, the objective is to study the capabilities of multitemporal radar images for rice height and dry biomass retrievals using Sentinel-1 data. To do this, we train Sentinel-1

data against ground measurements with classical machine learning techniques (Multiple Linear Regression (MLR), Support Vector Regression (SVR) and Random Forest (RF)) to estimate rice height and dry biomass. The study is carried out on the same multitemporal Sentinel-1 dataset in the first part. The ground in-situ measurements were made in the same period to collect rice height and dry biomass over 11 rice fields. The images were processed in order to produce a radar stack in C-band including dual-polarization VV (Vertical receive and Vertical transmit) and VH (Vertical receive and Horizontal transmit) data. We found that non-parametric methods (SVR and RF) had a better performance over the parametric MLR method for rice biophysical parameter retrievals. The accuracy of rice height estimation showed that rice height retrieval was strongly correlated to the in-situ rice height from dual-polarization, in which Random Forest yielded the best performance with correlation coefficient $R^2 = 0.92$ and the root mean square error (RMSE) 16% (7.9 cm). In addition, we demonstrated that the correlation of Sentinel-1 signal to the biomass was also very high in VH polarization with $R^2 = 0.9$ and RMSE = 18% (162 g·m⁻²) (with Random Forest method). Such results indicate that the highly qualified Sentinel-1 radar data could be well exploited for rice biomass and height retrieval and they could be used for operational tasks. Finally, in the context of the Copernicus program, there are two missions: radar Sentinel-1 and optical Sentinel-2. In future research, the data combination from the two satellites will be a necessity as it will be possible to carry out large-scale missions. Radar and optical data can be complementary to each other because they offer different perspectives on the Earth's surface providing different information content according to their specificity. Both types of data can also be merged to provide information from multiple sources and to provide improved results for decision making.

Finally, reducing carbon emissions from deforestation and degradation (REDD) requires detailed insight into how the forest biomass is measured and distributed. Studies so far have estimated forest biomass stocks using rough assumptions and unreliable data. High-resolution data and robust methods are required to capture the spatial variability of forest biomass with sufficient precision. We aim to improve on previous approaches by using radar satellite ALOS PALSAR (25-m resolution) and optical Landsat-derived tree cover (30-m resolution) observations to estimate forest biomass stocks in Madagascar, for the years 2007-2010. The radar signal and in situ biomass were highly correlated ($R^2 = 0.71$) and the root mean square error was 30% (for biomass ranging from 0 to 500 t/ha). Using our map at 25-m resolution for the entire island of Madagascar, we estimated the total above-ground forest carbon for the four years 2007, 2008, 2009 and 2010 to be 1.1173 ± 0.0304 , 1.1029 ± 0.0303 , 1.0916 ± 0.0301 and 1.0773 ± 0.0298 PgC, respectively. Carbon stocks were found to have decreased constantly over this period due to anthropogenic deforestation and likely also to climate change. We expect these results to serve as a more accurate benchmark than the heretofore state-of-the-arts results. Our results reinforce the science basis for current and future missions such as ALOS-2, and BIOMASS, increasing our confidence that they can provide accurate global biomass mapping, and thereby enabling progress on REDD initiatives. Combining radar signal with optical

tree cover data appears to be a promising approach for using by L-band SAR to map forest biomass (and hence carbon) over broad geographical scales.

PUBLICATIONS

The research presented in this thesis has been published in journals and conferences as listed below:

Journals publications

1. E. Ndikumana, D. Ho Tong Minh, N. Baghdadi, D. Courault and L. Hossard, "Deep Recurrent Neural Network for Agricultural Classification using multitemporal SAR Sentinel-1 for Camargue, France", *Remote Sens.* 2018, 10, 1217; doi:10.3390/rs10081217
2. E. Ndikumana, D. Ho Tong Minh, D. Nguyen Hai Thu, N. Baghdadi, D. Courault, L. Hossard, and I. El Moussawi, "Estimation of Rice Height and Biomass using multitemporal SAR Sentinel-1 for Camargue, southern France", *Remote Sens.* 2018, 10, 0; doi:10.3390/rs10000000
3. D. Ho Tong Minh, E. Ndikumana, Ghislain Vieilledent, D. McKey, N. Baghdadi, "Potential value of combining ALOS PALSAR and Landsat-derived tree cover data for forest biomass retrieval in Madagascar", *Remote Sensing of Environment*, 2018, vol. 213, p. 206-214; doi:10.1016/j.rse.2018.04.056
4. D. Ho Tong Minh, D. Ienco, R. Gaetano, N. Lalande, E. Ndikumana, F. Osman, and P. Maurel, "Deep Recurrent Neural Networks for Winter Vegetation Quality Mapping via Multitemporal SAR Sentinel-1", in *IEEE Geoscience and Remote Sensing Letters*, vol. 15, no. 3, pp. 464-468, March 2018. doi: 10.1109/LGRS.2018.2794581

Conferences presentation

1. E. Ndikumana, D. Ho Tong Minh, N. Baghdadi, D. Courault and L. Hossard, "Applying deep learning for agricultural classification using multitemporal SAR Sentinel-1 for Camargue, France", in *SPIE 2018, Berlin*, 10789-39, 10-13 September 2018.
2. E. Ndikumana, D. Ho Tong Minh, D. Nguyen Hai Thu, N. Baghdadi, D. Courault, L. Hossard, and I. El Moussawi, "Rice height and biomass estimations using multitemporal SAR Sentinel-1: Camargue case study", in *SPIE 2018, Berlin*, 10783-31, 10-13 September 2018.

ACKNOWLEDGEMENTS

I wish to express my sincere gratitude to my supervisors. Many thanks to Dr. Nicolas Baghdadi for giving me the opportunity to work with him on remote sensing, specifically on radar and for his profound knowledge in this field which has immensely impacted this project. In the same way, I would like to thank Dr. Dinh Ho Tong Minh for his quality co-supervision. Thank you for your many ideas and good advice. This co-supervision has given rise to rich exchanges, and it is really from the synthesis of these points of view that the methods developed in this thesis were born. Let me take this opportunity to extend my appreciation to Laurent Demagistri for guiding me on the right path in my professional career in remote sensing during my internship for my Master 2.

I cannot ignore the involvement of the Burundi Government for the funding of my PhD research during these three years. I would like to take a few moments to thank Mr. Emmanuel Ntahomvukiye for his quality decision-making at the appropriate time.

I would also like to thank all the people with whom I had the joy of collaborating and without whom my thesis work would not have been the same: Dr. Mohammad El Hajj, Dr. Nicolas Paget. In his incentive to research, Dr. Nicolas Paget reminded me every time that science awaits me to innovate. I am so glad to have met them and worked together. I thank you for your good mood. With you, every question, every exchange was a real pleasure.

I can't finish without expressing my utmost appreciation to Dr. Dominique Courault, Dr. Laure Hossard, Ibrahim El Moussawi and Dang Nguyen Hai Thu for their collaboration during the field work. I equally want to express my gratitude to Xavier Guillot and Pierre Megias for allowing me to use their rice fields as experiment sites.

I would like to thank the jury members

Dr Mehrez Zribi	Research Director	CESBIO	Toulouse	Rapporteur
Dr Lionel Jarlan	Research Director	IRD	Toulouse	Rapporteur
Dr Thuy Le Toan	Research engineer, HDR	CNRS	Toulouse	Examiner
Dr Valery Gond	CIRAD Researcher, HDR	CIRAD	Montpellier	Examiner

to have accepted to participate in the jury of this thesis.

Finally, I would like to thank all those who surrounded me during these years of the thesis within the UMR TETIS, the IRSTEA people with whom I had the opportunity to work together or exchange ideas.

BIBLIOGRAPHY

- [1] N. A. ABADE, O. A. D. C. JÚNIOR, R. F. GUIMARÃES, AND S. N. DE OLIVEIRA, *Comparative analysis of modis time-series classification using support vector machines and methods based upon distance and similarity measures in the brazilian cerrado-caatinga boundary*, Remote Sensing, 7 (2015), pp. 12160–12191.
- [2] G. ACQUAAH, *Principles of plant genetics and breeding*, John Wiley & Sons, 2009.
- [3] E. S. AGENCY, *Sentinel-1 user handbook*, 2013.
- [4] M. ARCIONI, P. BENSI, M. FEHRINGER, F. FOIS, F. HÉLIÈRE, C.-C. LIN, AND K. SCIPAL, *The biomass mission, status of the satellite system*, in Geoscience and Remote Sensing Symposium (IGARSS), 2014 IEEE International, IEEE, 2014, pp. 1413–1416.
- [5] A. BACCINI, S. J. GOETZ, W. S. WALKER, N. T. LAPORTE, M. SUN, D. SULLAMENASHE, J. HACKLER, P. S. A. BECK, R. DUBAYAH, M. A. FRIEDL, S. SAMANTA, AND R. A. HOUGHTON, *Estimated carbon dioxide emissions from tropical deforestation improved by carbon-density maps*, Nature Climate Change, 2 (2012), pp. 182–185.
- [6] J.-B. BASSENE, S. QUIEDEVILLE, D. CHABROL, F. LANÇON, AND P. MOUSTIER, *Organisation en réseau et durabilité systémique de deux filières alimentaires (riz biologique et petit épeautre en france)*, Actes des, 8 (2014).
- [7] J. BEAU, *La culture du riz en camargue, aspects techniques et commerciaux actuels*, Méditerranée, 22 (1975), pp. 53–68.
- [8] M. BELGIU AND L. DRĂGUȚ, *Random forest in remote sensing: A review of applications and future directions*, ISPRS Journal of Photogrammetry and Remote Sensing, 114 (2016), pp. 24–31.
- [9] Y. BENGIO, A. C. COURVILLE, AND P. VINCENT, *Representation learning: A review and new perspectives*, IEEE TPAMI, 35 (2013), pp. 1798–1828.
- [10] D. S. BERNSTEIN, *Matrix mathematics: Theory, facts, and formulas with application to linear systems theory*, vol. 41, Princeton University Press Princeton, 2005.
- [11] A. BOUVET, T. LE TOAN, AND N. LAM-DAO, *Monitoring of the rice cropping system in the mekong delta using envisat/asar dual polarization data*, IEEE Transactions on Geoscience and Remote Sensing, 47 (2009), pp. 517–526.
- [12] L. BREIMAN, *Random forests*, Machine learning, 45 (2001), pp. 5–32.

- [13] S. C. BROWN, S. QUEGAN, K. MORRISON, J. C. BENNETT, AND G. COOKMARTIN, *High-resolution measurements of scattering in wheat canopies-implications for crop parameter retrieval*, IEEE Transactions on Geoscience and Remote Sensing, 41 (2003), pp. 1602–1610.
- [14] C. BUCKLEY AND P. CARNEY, *The potential to reduce the risk of diffuse pollution from agriculture while improving economic performance at farm level*, Environmental science and policy, 25 (2013), pp. 118–126.
- [15] M. CAMPOS-TABERNER, F. J. GARCIA-HARO, G. CAMPS-VALLS, G. GRAU-MUEDRA, F. NUTINI, L. Busetto, D. KATSANTONIS, D. STAVRAKLOUDIS, C. MINAKOU, L. GATTI, ET AL., *Exploitation of sar and optical sentinel data to detect rice crop and estimate seasonal dynamics of leaf area index*, Remote Sensing, 9 (2017), p. 248.
- [16] O. CARTUS, M. SANTORO, AND J. KELLNDORFER, *Mapping forest aboveground biomass in the northeastern united states with alos palsar dual-polarization l-band*, Remote Sensing of Environment, 124 (2012), pp. 466–478.
- [17] L. CHAI, J. SHI, L. ZHANG, AND L. JIANG, *A parameterized microwave model for short vegetation layer*, in Geoscience and Remote Sensing Symposium (IGARSS), 2010 IEEE International, Ieee, 2010, pp. 3023–3026.
- [18] A. CHAKRABARTI AND J. K. GHOSH, *Aic, bic and recent advances in model selection*, in Philosophy of Statistics, P. S. Bandyopadhyay and M. R. Forster, eds., vol. 7 of Handbook of the Philosophy of Science, North-Holland, Amsterdam, 2011, pp. 583 – 605.
- [19] Y. CHAMBENOIT, *Approches interactives pour l'analyse des images RSO multi-temporelles*, PhD thesis, Université de Marne-la-Vallée, 2004.
- [20] C.-C. CHANG AND C.-J. LIN, *LIBSVM: A library for support vector machines*, ACM TIST, 2 (2011), pp. 27:1–27:27.
- [21] J. CHAVE, M. REJOU-MACHAIN, A. BURQUEZ, E. CHIDUMAYO, M. S. COLGAN, W. B. DELITTI, A. DUQUE, T. EID, P. M. FEARNside, R. C. GOODMAN, M. HENRY, A. MARTINEZ-YRIZAR, W. A. MUGASHA, H. C. MULLER-LANDAU, M. MENCUCINI, B. W. NELSON, A. NGOMANDA, E. M. NOGUEIRA, E. ORTIZ-MALAVASSI, R. PELISSIER, P. PLOTON, C. M. RYAN, J. G. SALDARRIAGA, AND G. VIEILLEDENT, *Improved allometric models to estimate the aboveground biomass of tropical trees*, Global Change Biology, 20 (2014), pp. 3177–3190.
- [22] J. CHEN, H. LIN, AND Z. PEI, *Application of envisat asar data in mapping rice crop growth in southern china*, IEEE Geoscience and Remote Sensing Letters, 4 (2007), pp. 431–435.

- [23] K. CHO, B. VAN MERRIENBOER, Ç. GÜLÇEHRE, D. BAHDANAU, F. BOUGARES, H. SCHWENK, AND Y. BENGIO, *Learning phrase representations using RNN encoder-decoder for statistical machine translation*, in EMNLP, 2014, pp. 1724–1734.
- [24] F. CHOLLET, *keras*.
<https://github.com/fchollet/keras>, 2015.
- [25] N. CLASSEAU, *Apports de l'imagerie satellitaire radar à des études environnementales: exemples en Guyane française*, PhD thesis, Université de Marne-la-Vallée, 2001.
- [26] Y. N. DAUPHIN, H. DE VRIES, J. CHUNG, AND Y. BENGIO, *Rmsprop and equilibrated adaptive learning rates for non-convex optimization*, CoRR, abs/1502.04390 (2015).
- [27] S. DELMOTTE, P. TITTONELL, J.-C. MOURET, R. HAMMOND, AND S. LOPEZ-RIDAURA, *On farm assessment of rice yield variability and productivity gaps between organic and conventional cropping systems under mediterranean climate*, European Journal of Agronomy, 35 (2011), pp. 223–236.
- [28] S. DELMOTTE, P. TITTONELL, J.-C. MOURET, R. HAMMOND, AND S. LOPEZ-RIDAURA, *On farm assessment of rice yield variability and productivity gaps between organic and conventional cropping systems under mediterranean climate*, European Journal of Agronomy, 35 (2011), pp. 223 – 236.
- [29] M. DOBSON, F. ULABY, T. LETOAN, A. BEAUDOIN, E. KASISCHKE, AND N. CHRISTENSEN, *Dependence of radar backscatter on coniferous forest biomass*, Geoscience and Remote Sensing, IEEE Transactions on, 30 (1992), pp. 412–415.
- [30] M. C. DOBSON, F. T. ULABY, T. LETOAN, A. BEAUDOIN, E. S. KASISCHKE, AND N. CHRISTENSEN, *Dependence of radar backscatter on coniferous forest biomass*, IEEE Transactions on Geoscience and remote Sensing, 30 (1992), pp. 412–415.
- [31] M. DRUSCH, U. D. BELLO, S. CARLIER, O. COLIN, V. FERNANDEZ, F. GASCON, B. HORSCH, C. ISOLA, P. LABERINTI, P. MARTIMORT, A. MEYGRET, F. SPOTO, O. SY, F. MARCHESE, AND P. BARGELLINI, *Sentinel-2 esa optical high-resolution mission for gmes operational services*, Remote Sensing of Environment, 120 (2012), pp. 25 – 36.
- [32] R. L. EASTON JR, *Fourier methods in imaging*, John Wiley & Sons, 2010.
- [33] R.-E. FAN, P.-H. CHEN, AND C.-J. LIN, *Working set selection using second order information for training support vector machines*, urnal of Machine Learning Research, 6 (2005), p. 1889–1918.
- [34] R. FENSHOLT, I. SANDHOLT, AND M. S. RASMUSSEN, *Evaluation of modis lai, fapar and the relation between fapar and ndvi in a semi-arid environment using in situ measurements*, Remote sensing of Environment, 91 (2004), pp. 490–507.

- [35] S. FERRANT, A. SELLES, M. LE PAGE, P.-A. HERRAULT, C. PELLETIER, A. AL-BITAR, S. MERMOZ, S. GASCOIN, A. BOUVET, M. SAQALLI, ET AL., *Detection of irrigated crops from sentinel-1 and sentinel-2 data to estimate seasonal groundwater use in south india*, Remote Sensing, 9 (2017), p. 1119.
- [36] P. FERRAZZOLI, S. PALOSCIA, P. PAMPALONI, G. SCHIAVON, S. SIGISMONDI, AND D. SOLIMINI, *The potential of multifrequency polarimetric sar in assessing agricultural and arboreous biomass*, IEEE Transactions on Geoscience and Remote Sensing, 35 (1997), pp. 5–17.
- [37] R. FLAMARY, M. FAUVEL, M. D. MURA, AND S. VALERO, *Analysis of multitemporal classification techniques for forecasting image time series*, IEEE Geosci. Remote Sensing Lett., 12 (2015), pp. 953–957.
- [38] J. A. FOLEY, R. DEFRIES, G. P. ASNER, C. BARFORD, G. BONAN, S. R. CARPENTER, F. S. CHAPIN, M. T. COE, G. C. DAILY, H. K. GIBBS, ET AL., *Global consequences of land use*, science, 309 (2005), pp. 570–574.
- [39] J. C. FOX, G. VIEILLEDENT, C. K. YOSI, J. N. POKANA, AND R. J. KEENAN, *Above-ground forest carbon dynamics in papua new guinea: Isolating the influence of selective-harvesting and El Nino*, Ecosystems, 14 (2011), pp. 1276–1288.
- [40] G. FRANCESCHETTI AND R. LANARI, *Synthetic aperture radar processing*, CRC press, 2018.
- [41] M. A. FRIEDL AND C. E. BRODLEY, *Decision tree classification of land cover from remotely sensed data*, Remote sensing of environment, 61 (1997), pp. 399–409.
- [42] C. FROST AND S. G. THOMPSON, *Correcting for regression dilution bias: Comparison of methods for a single predictor variable*, Journal of the Royal Statistical Society, 163 (2000), pp. 173–189.
- [43] W. A. FULLER, ed., *Measurement Error Models*, John Wiley, New York,, 1987.
- [44] T. GE, B. LI, Z. ZHU, Y. HU, H. YUAN, M. DORODNIKOV, D. L. JONES, J. WU, AND Y. KUZYAKOV, *Rice rhizodeposition and its utilization by microbial groups depends on n fertilization*, Biology and Fertility of Soils, 53 (2017), pp. 37–48.
- [45] H. GHASSEMIAN, *A review of remote sensing image fusion methods*, Information Fusion, 32 (2016), pp. 75–89.
- [46] L. GOMEZ-CHOVA, G. CAMPS-VALLS, J. MUNOZ-MARI, AND J. CALPE, *Semisupervised image classification with laplacian support vector machines*, IEEE Geoscience and Remote Sensing Letters, 5 (2008), pp. 336–340.
- [47] S. GOODMAN AND J. BENSTEAD, eds., *The natural history of Madagascar*, University of Chicago Press,, 2003.

- [48] A. GRAHAM AND R. HARRIS, *Extracting biophysical parameters from remotely sensed radar data: a review of the water cloud model*, Progress in Physical Geography, 27 (2003), pp. 217–229.
- [49] A. GRAVES, A. MOHAMED, AND G. E. HINTON, *Speech recognition with deep recurrent neural networks*, in ICASSP, 2013, pp. 6645–6649.
- [50] R. P. GUPTA, *Remote sensing geology*, Springer, 2017.
- [51] I. HAJNSEK, F. KUGLER, S.-K. LEE, AND K. P. PAPATHANASSIOU, *Tropical-forest-parameter estimation by means of pol-insar: The indrex-ii campaign*, IEEE transactions on Geoscience and Remote Sensing, 47 (2009), pp. 481–493.
- [52] D. HALL, *Mathematical techniques in multisensor data fusion: Norwood: Artech house inc*, (1992).
- [53] M. C. HANSEN, P. V. POTAPOV, R. MOORE, M. HANCHER, S. A. TURUBANOVA, A. TYUKAVINA, D. THAU, S. V. STEHMAN, S. J. GOETZ, T. R. LOVELAND, A. KOMMAREDDY, A. EGOROV, L. CHINI, C. O. JUSTICE, AND J. R. G. TOWNSHEND, *High-resolution global maps of 21st-century forest cover change*, Science, 342 (2013), pp. 850–853.
- [54] O. HELLWICH, A. REIGBER, AND H. LEHMANN, *Sensor and data fusion contest: Test imagery to compare and combine airborne sar and optical sensors for mapping*, in Geoscience and Remote Sensing Symposium, 2002. IGARSS'02. 2002 IEEE International, vol. 1, IEEE, 2002, pp. 82–84.
- [55] D. HO TONG MINH, D. IENCO, R. GAETANO, N. LALANDE, E. NDIKUMANA, F. OSMAN, AND P. MAUREL, *Deep recurrent neural networks for winter vegetation quality mapping via multitemporal sar sentinel-1*, IEEE Geoscience and Remote Sensing Letters, 15 (2018), pp. 464–468.
- [56] D. HO TONG MINH, T. LE TOAN, F. ROCCA, S. TEBALDINI, M. MARIOTTI D'ALESSANDRO, AND L. VILLARD, *Relating P-band synthetic aperture radar tomography to tropical forest biomass*, Geoscience and Remote Sensing, IEEE Transactions on, 52 (2014), pp. 967–979.
- [57] D. HO TONG MINH, T. LE TOAN, F. ROCCA, S. TEBALDINI, L. VILLARD, M. RÉJOU-MÉCHAIN, O. L. PHILLIPS, T. R. FELDPAUSCH, P. DUBOIS-FERNANDEZ, K. SCIPAL, AND J. CHAVE, *Sar tomography for the retrieval of forest biomass and height: Cross-validation at two tropical forest sites in french guiana*, Remote Sensing of Environment, 175 (2016), pp. 138 – 147.
- [58] D. HO TONG MINH AND Y.-N. NGO, *Tomosar platform supports for sentinel-1 tops persistent scatterers interferometry*, in Geoscience and Remote Sensing Symposium (IGARSS), 2017 IEEE International, IEEE, 2017, pp. 1680–1683.

- [59] D. HO TONG MINH, S. TEBALDINI, F. ROCCA, T. LE TOAN, L. VILLARD, AND P. DUBOIS-FERNANDEZ, *Capabilities of BIOMASS tomography for investigating tropical forests*, Geoscience and Remote Sensing, IEEE Transactions on, 53 (2015), pp. 965–975.
- [60] D. HO TONG MINH AND YEN-NHI NGO, *Tomosar platform supports for sentinel-1 tops persistent scatterers interferometry*, in 2017 IEEE International Geoscience and Remote Sensing Symposium (IGARSS), July 2017, pp. 1680–1683.
- [61] D. HO TONG MINH, YEN-NHI NGO, N. BAGHDADI, AND P. MAUREL, *TomoSAR platform: a new Irstea service as demand for SAR, Interferometry, Polarimetry and Tomography*, in ESA Living Planet Symposium 2016; Proceedings of, 2016, pp. 1–8.
- [62] S. HOCHREITER AND J. SCHMIDHUBER, *LSTM can solve hard long time lag problems*, in NIPS, 1996, pp. 473–479.
- [63] N. HOLAH, *Potentiel des nouveaux capteurs radar multi-polarisation et polarimétrie pour la caractérisation des états de surface en milieu agricole*, PhD thesis, Université d’Orléans, 2005.
- [64] M. HOSSAIN, *Rice supply and demand in asia: a socioeconomic and biophysical analysis*, in Applications of Systems Approaches at the Farm and Regional Levels Volume 1, Springer, 1997, pp. 263–279.
- [65] F. HU, G.-S. XIA, Z. WANG, X. HUANG, L. ZHANG, AND H. SUN, *Unsupervised feature learning via spectral clustering of multidimensional patches for remotely sensed scene classification*, IEEE Journal of Selected Topics in Applied Earth Observations and Remote Sensing, 8 (2015).
- [66] T. HUANG, V. KECMAN, AND I. KOPRIVA, *Kernel based algorithms for mining huge data sets: Supervised, semi-supervised, and unsupervised learning*, Springer, (2006).
- [67] M. HUFTY AND A. HAAKENSTAD, *Reduced emissions for deforestation and degradation - a critical review*, The Journal of Sustainable Development, 5 (2011), pp. 1–24.
- [68] D. IENCO, R. GAETANO, C. DUPAQUIER, AND P. MAUREL, *Land cover classification via multitemporal spatial data by deep recurrent neural networks*, IEEE Geoscience and Remote Sensing Letters, 14 (2017), pp. 1685–1689.
- [69] J. INGLADA, M. ARIAS, B. TARDY, O. HAGOLLE, S. VALERO, D. MORIN, G. DEDIEU, G. SEPULCRE, S. BONTEMPS, P. DEFOURNY, ET AL., *Assessment of an operational system for crop type map production using high temporal and spatial resolution satellite optical imagery*, Remote Sensing, 7 (2015), pp. 12356–12379.
- [70] J. INGLADA, A. VINCENT, M. ARIAS, AND C. MARAIS-SICRE, *Improved early crop type identification by joint use of high temporal resolution sar and optical image time series*, Remote Sensing, 8 (2016).

- [71] J. INGLADA, A. VINCENT, M. ARIAS, B. TARDY, D. MORIN, AND I. RODES, *Operational high resolution land cover map production at the country scale using satellite image time series*, Remote Sensing, 9 (2017).
- [72] Y. INOUE, T. KUROSU, H. MAENO, S. URATSUKA, T. KOZU, K. DABROWSKA-ZIELINSKA, AND J. QI, *Season-long daily measurements of multifrequency (ka, ku, x, c, and l) and full-polarization backscatter signatures over paddy rice field and their relationship with biological variables*, Remote Sensing of Environment, 81 (2002), pp. 194–204.
- [73] Y. INOUE, E. SAKAIYA, AND C. WANG, *Capability of c-band backscattering coefficients from high-resolution satellite sar sensors to assess biophysical variables in paddy rice*, Remote Sensing of Environment, 140 (2014), pp. 257–266.
- [74] K. IRWIN, D. BEAULNE, A. BRAUN, AND G. FOTOPOULOS, *Fusion of sar, optical imagery and airborne lidar for surface water detection*, Remote Sensing, 9 (2017), p. 890.
- [75] S. D. JAWAK, P. DEVLİYAL, AND A. J. LUIS, *A comprehensive review on pixel oriented and object oriented methods for information extraction from remotely sensed satellite images with a special emphasis on cryospheric applications*, Advances in Remote Sensing, 4 (2015), p. 177.
- [76] W. JAYAWARDHANA AND V. CHATHURANGE, *Extraction of agricultural phenological parameters of sri lanka using modis, ndvi time series data*, Procedia Food Science, 6 (2016), pp. 235–241.
- [77] M. J.C., *Etude de l'agrosystème rizicole en camargue dans ses relations avec le milieu et le système culturel : aspects particuliers de la fertilité*, Université des Sciences et Techniques du Languedoc, 1 (1988).
- [78] M. JIA, L. TONG, Y. ZHANG, AND Y. CHEN, *Rice biomass estimation using radar backscattering data at s-band*, IEEE journal of selected topics in applied earth observations and remote sensing, 7 (2014), pp. 469–479.
- [79] Z. JING, Y. ZHANG, K. WANG, AND R. SHI, *Retrieving rice yield and biomass from radarsat-2 sar data with artificial neural network (ann)*, in Remote Sensing and Modeling of Ecosystems for Sustainability X, vol. 8869, International Society for Optics and Photonics, 2013, p. 88690X.
- [80] I. T. JOLLIFFE, *Principal component analysis*, Springer, 2nd (2002).
- [81] C. O. JUSTICE, E. VERMOTE, J. R. TOWNSHEND, R. DEFRIES, D. P. ROY, D. K. HALL, V. V. SALOMONSON, J. L. PRIVETTE, G. RIGGS, A. STRAHLER, ET AL., *The moderate resolution imaging spectroradiometer (modis): Land remote sensing for global change research*, IEEE transactions on geoscience and remote sensing, 36 (1998), pp. 1228–1249.

- [82] M. A. KARAM, A. K. FUNG, AND Y. M. ANTAR, *Electromagnetic wave scattering from some vegetation samples*, IEEE Transactions on Geoscience and Remote Sensing, 26 (1988), pp. 799–808.
- [83] R. KHATAMI, G. MOUNTRAKIS, AND S. V. STEHMAN, *A meta-analysis of remote sensing research on supervised pixel-based land-cover image classification processes: General guidelines for practitioners and future research*, Remote Sensing of Environment, 177 (2016), pp. 89–100.
- [84] S. B. KOTSIANTIS, I. D. ZAHARAKIS, AND P. E. PINTELAS, *Machine learning: a review of classification and combining techniques*, Artificial Intelligence Review, 26 (2006), pp. 159–190.
- [85] T. KUPLICH, C. D. C. FREITAS, AND J. SOARES, *The study of ers-1 sar and landsat tm synergism for land use classification*, International Journal of Remote Sensing, 21 (2000), pp. 2101–2111.
- [86] T. KUROSU, M. FUJITA, AND K. CHIBA, *Monitoring of rice crop growth from space using the ers-1 c-band sar*, IEEE Transactions on Geoscience and Remote Sensing, 33 (1995), pp. 1092–1096.
- [87] L. KURVONEN, J. PULLIAINEN, AND M. HALLIKAINEN, *Retrieval of biomass in boreal forests from multitemporal ers-1 and jers-1 sar images*, IEEE Transactions on Geoscience and Remote Sensing, 37 (1999), pp. 198–205.
- [88] N. KUSSL, M. LAVRENIUK, S. SKAKUN, AND A. SHELESTOV, *Deep learning classification of land cover and crop types using remote sensing data*, IEEE Geoscience and Remote Sensing Letters, 14 (2017), pp. 778–782.
- [89] T. LE TOAN, A. BEAUDOIN, J. RIOM, AND D. GUYONI, *Relating forest biomass to SAR data*, 30 (1992), pp. 403 – 411.
- [90] T. LE TOAN, S. QUEGAN, M. DAVIDSON, H. BALZTER, P. PAILLOU, K. PAPATHANASSIOU, S. PLUMMER, F. ROCCA, S. SAATCHI, H. SHUGART, ET AL., *The biomass mission: Mapping global forest biomass to better understand the terrestrial carbon cycle*, Remote sensing of environment, 115 (2011), pp. 2850–2860.
- [91] T. LE TOAN, F. RIBBES, L.-F. WANG, N. FLOURY, K.-H. DING, J. A. KONG, M. FUJITA, AND T. KUROSU, *Rice crop mapping and monitoring using ers-1 data based on experiment and modeling results*, IEEE Transactions on Geoscience and Remote Sensing, 35 (1997), pp. 41–56.
- [92] T. LE TOAN, F. RIBBES, L.-F. WANG, N. FLOURY, K.-H. DING, J. A. KONG, M. FUJITA, AND T. KUROSU, *Rice crop mapping and monitoring using ers-1 data based on experiment and modeling results*, IEEE Transactions on Geoscience and Remote Sensing, 35 (1997), pp. 41–56.

- [93] Y. LECUN, Y. BENGIO, AND G. HINTON, *Deep learning*, nature, 521 (2015), p. 436.
- [94] R. J. LEWIS AND K. H. BANNAR-MARTIN, *The impact of cyclone fanele on a tropical dry forest in madagascar*, Biotropica, 44 (2012), pp. 135–140.
- [95] C. LI, J. WANG, L. WANG, L. HU, AND P. GONG, *Comparison of classification algorithms and training sample sizes in urban land classification with landsat thematic mapper imagery*, Remote Sensing, 6 (2014), pp. 964–983.
- [96] J. LI, J. M. BIOUCAS-DIAS, AND A. PLAZA, *Semisupervised hyperspectral image segmentation using multinomial logistic regression with active learning*, IEEE Transactions on Geoscience and Remote Sensing, 48 (2010), pp. 4085–4098.
- [97] K. LI, B. BRISCO, S. YUN, AND R. TOUZI, *Polarimetric decomposition with radarsat-2 for rice mapping and monitoring*, Canadian Journal of Remote Sensing, 38 (2012), pp. 169–179.
- [98] S. LI, P. NI, G. CUI, P. HE, H. LIU, L. LI, AND Z. LIANG, *Estimation of rice biophysical parameters using multitemporal radarsat-2 images*, in IOP Conference Series: Earth and Environmental Science, vol. 34, IOP Publishing, 2016, p. 012019.
- [99] T. LILLESAND, R. W. KIEFER, AND J. CHIPMAN, *Remote sensing and image interpretation*, John Wiley & Sons, 2014.
- [100] T. LINZEN, E. DUPOUX, AND Y. GOLDBERG, *Assessing the ability of lstms to learn syntax-sensitive dependencies*, TACL, 4 (2016), pp. 521–535.
- [101] J. M. LOPEZ-SANCHEZ, J. D. BALLESTER-BERMAN, AND I. HAJNSEK, *First results of rice monitoring practices in spain by means of time series of terrasar-x dual-pol images*, IEEE Journal of selected topics in applied earth observations and remote sensing, 4 (2011), pp. 412–422.
- [102] W. LOWRIE, *Fundamentals of geophysics*, Cambridge university press, 2007.
- [103] D. LU, Q. CHEN, G. WANG, L. LIU, G. LI, AND E. MORAN, *A survey of remote sensing-based aboveground biomass estimation methods in forest ecosystems*, International Journal of Digital Earth, 9 (2016), pp. 63–105.
- [104] D. LU AND Q. WENG, *A survey of image classification methods and techniques for improving classification performance*, International journal of Remote sensing, 28 (2007), pp. 823–870.
- [105] R. M. LUCAS, A. L. MITCHELL, A. ROSENQVIST, C. PROISY, A. MELIUS, AND C. TICEHURST, *The potential of l-band sar for quantifying mangrove characteristics and change: case studies from the tropics*, Aquatic conservation: marine and freshwater ecosystems, 17 (2007), pp. 245–264.

- [106] A. LUCKMAN, J. BAKER, T. M. KUPLICH, C. D. C. F. YANASSE, AND A. C. FRERY, *A study of the relationship between radar backscatter and regenerating tropical forest biomass for spaceborne sar instruments*, Remote Sensing of Environment, 60 (1997), pp. 1–13.
- [107] G. MANFRON, S. DELMOTTE, L. Busetto, L. HOSSARD, L. RANGHETTI, P. A. BRIVIO, AND M. BOSCHETTI, *Estimating inter-annual variability in winter wheat sowing dates from satellite time series in camargue, france*, International journal of applied earth observation and geoinformation, 57 (2017), pp. 190–201.
- [108] S. MARTIN, *An introduction to ocean remote sensing*, Cambridge University Press, 2014.
- [109] G. MAZZA, A. E. AGNELLI, G. ORASEN, M. GENNARO, G. VALÈ, AND A. LAGOMARSINO, *Reduction of global warming potential from rice under alternate wetting and drying practice in a sandy soil of northern italy*, Italian Journal Of Agrometeorology-Rivista Italiana Di Agrometeorologia, 21 (2016), pp. 35–44.
- [110] G. MCLACHLAN, K.-A. DO, AND C. AMBROISE, *Analyzing microarray gene expression data*, vol. 422, John Wiley & Sons, 2005.
- [111] S. MERMOZ, T. LE TOAN, L. VILLARD, M. RÉJOU-MÉCHAIN, AND J. SEIFERT-GRANZIN, *Biomass assessment in the cameroon savanna using alos palsar data*, Remote sensing of environment, 155 (2014), pp. 109–119.
- [112] S. MERMOZ, M. RÉJOU-MÉCHAIN, L. VILLARD, T. LE TOAN, V. ROSSI, AND S. GOURLET-FLEURY, *Decrease of l-band sar backscatter with biomass of dense forests*, Remote Sensing of Environment, 159 (2015), pp. 307–317.
- [113] S. MERMOZ, M. REJOU-MECHAIN, L. VILLARD, T. L. TOAN, V. ROSSI, AND S. GOURLET-FLEURY, *Decrease of l-band {SAR} backscatter with biomass of dense forests*, Remote Sensing of Environment, 159 (2015), pp. 307 – 317.
- [114] F. MIN WANG, J. FENG HUANG, AND X.-Z. WANG, *Identification of optimal hyperspectral bands for estimation of rice biophysical parameters.*, Journal of integrative plant biology, 50 3 (2008), pp. 291–9.
- [115] D. H. T. MINH, T. LE TOAN, F. ROCCA, S. TEBALDINI, M. M. D’ALESSANDRO, AND L. VILLARD, *Relating p-band synthetic aperture radar tomography to tropical forest biomass*, IEEE Transactions on Geoscience and Remote Sensing, 52 (2014), pp. 967–979.
- [116] D. H. T. MINH, E. NDIKUMANA, G. VIEILLEDENT, D. MCKEY, AND N. BAGHDADI, *Potential value of combining alos palsar and landsat-derived tree cover data for forest biomass retrieval in madagascar*, Remote Sensing of Environment, 213 (2018), pp. 206–214.

- [117] D. H. T. MINH, S. TEBALDINI, F. ROCCA, T. LE TOAN, L. VILLARD, AND P. C. DUBOIS-FERNANDEZ, *Capabilities of biomass tomography for investigating tropical forests*, IEEE Transactions on Geoscience and Remote Sensing, 53 (2015), pp. 965–975.
- [118] E. MITCHARD, S. SAATCHI, S. LEWIS, T. FELDPAUSCH, I. WOODHOUSE, B. S. C. ROWLAND, AND P. MEIR, *Measuring biomass changes due to woody encroachment and deforestation / degradation in a forest savanna boundary region of central Africa using multi-temporal L-band radar backscatter*, Remote Sensing of Environment, 115 (2011), pp. 2861 – 2873.
- {DESDynI} VEG-3D Special Issue.
- [119] A. C. MOREL, S. S. SAATCHI, Y. MALHI, N. J. BERRY, L. BANIN, D. BURSLEM, R. NILUS, AND R. C. ONG, *Estimating aboveground biomass in forest and oil palm plantation in sabah, malaysian borneo using {ALOS} {PALSAR} data*, Forest Ecology and Management, 262 (2011), pp. 1786 – 1798.
- [120] J.-C. MOURET, *Etude de l'Agrosystème rizicole en Camargue dans ses relations avec le milieu et le système cultural: aspects particuliers de la fertilité*, PhD thesis, Montpellier 2, 1988.
- [121] A. MOVIA, A. BEINAT, AND F. CROSILLA, *Shadow detection and removal in rgb vhr images for land use unsupervised classification*, ISPRS Journal of Photogrammetry and Remote Sensing, 119 (2016), pp. 485–495.
- [122] J. MUNOZ-MARI, F. BOVOLO, L. GOMEZ-CHOVA, L. BRUZZONE, AND G. CAMP-VALLS, *Semisupervised one-class support vector machines for classification of remote sensing data*, IEEE Transactions on Geoscience and Remote Sensing, 48 (2010), pp. 3188–3197.
- [123] O. MUTANGA, E. ADAM, AND M. A. CHO, *High density biomass estimation for wetland vegetation using worldview-2 imagery and random forest regression algorithm*, International Journal of Applied Earth Observation and Geoinformation, 18 (2012), pp. 399–406.
- [124] K. NAKAMURA, K. DOI, AND K. SHIBUYA, *Fluctuations in the flow velocity of the antarctic shirase glacier over an 11-year period*, Polar Science, 4 (2010), pp. 443–455.
- [125] E. NDIKUMANA, D. HO TONG MINH, N. BAGHDADI, D. COURAULT, AND L. HOSSARD, *Deep recurrent neural network for agricultural classification using multitemporal sar sentinel-1 for camargue, france*, Remote Sensing, 10 (2018), p. 1217.
- [126] E. NDIKUMANA, D. HO TONG MINH, H. DANG NGUYEN, N. BAGHDADI, D. COURAULT, L. HOSSARD, AND I. EL MOUSSAWI, *Estimation of rice height and biomass using multitemporal sar sentinel-1 for camargue, southern france*, Remote Sensing, 10 (2018), p. 1394.

- [127] M. NEUMANN, S. S. SAATCHI, L. M. ULANDER, AND J. E. FRANSSON, *Assessing performance of l-and p-band polarimetric interferometric sar data in estimating boreal forest above-ground biomass*, IEEE Transactions on Geoscience and Remote Sensing, 50 (2012), pp. 714–726.
- [128] S. ONLINE, <https://sentinel.esa.int/web/sentinel/user-guides/sentinel-1-sar/applications/mapping-applications-s1-modes> (accessed 26 july 2018), ESA, (2018).
- [129] Y. PAN, R. A. BIRDSEY, J. FANG, R. HOUGHTON, P. E. KAUPPI, W. A. KURZ, O. L. PHILLIPS, A. SHVIDENKO, S. L. LEWIS, J. G. CANADELL, P. CIAIS, R. B. JACKSON, S. W. PACALA, A. D. MCGUIRE, S. PIAO, A. RAUTIAINEN, S. SITCH, AND D. HAYES, *A large and persistent carbon sink in the world's forests*, Science, 333 (2011), pp. 988–993.
- [130] F. PEDREGOSA, G. VAROQUAUX, A. GRAMFORT, V. MICHEL, B. THIRION, O. GRISEL, M. BLONDEL, P. PRETTENHOFER, R. WEISS, V. DUBOURG, J. VANDERPLAS, A. PASSOS, D. COUNAPEAU, M. BRUCHER, M. PERROT, AND E. DUCHESNAY, *Scikit-learn: Machine learning in Python*, Journal of Machine Learning Research, 12 (2011), pp. 2825–2830.
- [131] C. POHL AND J. VAN GENDEREN, *Remote sensing image fusion: an update in the context of digital earth*, International Journal of Digital Earth, 7 (2014), pp. 158–172.
- [132] —, *Structuring contemporary remote sensing image fusion*, International Journal of Image and Data Fusion, 6 (2015), pp. 3–21.
- [133] C. POHL AND J. L. VAN GENDEREN, *Review article multisensor image fusion in remote sensing: concepts, methods and applications*, International journal of remote sensing, 19 (1998), pp. 823–854.
- [134] A. POLSOT, A. SPEEDY, AND E. KUENEMAN, *Good agricultural practices—a working concept*, FAO Internal Workshop on Good Agricultural Practices, 1 (2004), p. 41.
- [135] L. POORTER, F. BONGERS, T. AIDE, A. A. ZAMBRANO, P. BALVANERA, J. BECKNELL, V. BOUKILI, P. BRANCALION, E. BROADBENT, R. CHAZDON, D. CRAVEN, J. DE ALMEIDA-CORTEZ, G. CABRAL, B. DE JONG, J. DENSLOW, D. DENT, S. DEWALT, J. DUPUY, S. DURAN, N. ESPIRITO-SANTO, M. FANDINO, R. CZSAR, J. HALL, J. HERNANDEZ-STEFANONI, C. JAKOVAC, A. JUNQUEIRA, D. KENNARD, S. LETCHER, J. LICONA, M. LOHBECK, E. MARIN-SPIOTTA, M. MARTINEZ-RAMOS, P. MASSOCA, J. MEAVE, R. MESQUITA, F. MORA, R. MUNOZ, R. MUSCARELLA, Y. NUNES, S. OCHOA-GAONA, A. DE OLIVEIRA, E. ORIHUELA-BELMONTE, M. PENA-CLAROS, E. PEREZ-GARCIA, D. PIOTTO, J. POWERS, J. RODRIGUEZ-VELAZQUEZ, I. ROMERO-PEREZ, J. RUIZ, J. SALDARRIAGA, A. SANCHEZ-AZOFEIFA, N. SCHWARTZ, M. STEININGER, N. SWENSON, M. TOLEDO, M. URIARTE, M. VAN

- BREUGEL, H. VAN DER WAL, M. VELOSO, H. VESTER, A. VICENTINI, I. VIEIRA, T. V. BENTOS, G. WILLIAMSON, AND D. ROZENDAAL, *Biomass resilience of neotropical secondary forests*, *Nature*, 530 (2016), pp. 211–214.
- [136] P. PRATS-IRAOLA, R. SCHEIBER, L. MAROTTI, S. WOLLSTADT, AND A. REIGBER, *TOPS interferometry with TerraSAR-X*, *IEEE Transactions on Geoscience and Remote Sensing*, 50 (2012), pp. 3179–3188.
- [137] C. PROISY, E. MOUGIN, F. FROMARD, V. TRICHON, AND M. KARAM, *On the influence of canopy structure on the radar backscattering of mangrove forests*, *International Journal of Remote Sensing*, 23 (2002), pp. 4197–4210.
- [138] Y. QIAN, W. ZHOU, J. YAN, W. LI, AND L. HAN, *Comparing machine learning classifiers for object-based land cover classification using very high resolution imagery*, *Remote Sensing*, 7 (2014), pp. 153–168.
- [139] S. QUEGAN AND Y. JIONG JIONG, *Filtering of multichannel SAR images*, *IEEE Transactions on Geoscience and Remote Sensing*, 39 (2001), pp. 2373–2379.
- [140] S. QUEGAN, T. LE TOAN, J. J. YU, F. RIBBES, AND N. FLOURY, *Multitemporal ers sar analysis applied to forest mapping*, *Geoscience and Remote Sensing, IEEE Transactions on*, 38 (2000), pp. 741–753.
- [141] C. E. RASMUSSEN AND C. K. I. WILLIAMS, *Gaussian processes for machine learning*, MIT Press, (2006).
- [142] A. REFICE, A. D’ADDABBO, AND D. CAPOLONGO, *Flood Monitoring Through Remote Sensing*, Springer, 2017.
- [143] V. F. RODRIGUEZ-GALIANO, B. GHIMIRE, J. ROGAN, M. CHICA-OLMO, AND J. P. RIGOL-SANCHEZ, *An assessment of the effectiveness of a random forest classifier for land-cover classification*, *ISPRS Journal of Photogrammetry and Remote Sensing*, 67 (2012), pp. 93–104.
- [144] C. ROSSI AND E. ERTEN, *Paddy-rice monitoring using tandem-x*, *IEEE Transactions on Geoscience and Remote Sensing*, 53 (2015), pp. 900–910.
- [145] S. SAATCHI, M. MARLIER, R. L. CHAZDON, D. B. CLARK, AND A. E. RUSSELL, *Impact of spatial variability of tropical forest structure on radar estimation of aboveground biomass*, *Remote Sensing of Environment*, 115 (2011), pp. 2836–2849.
- [146] S. S. SAATCHI, N. L. HARRIS, S. BROWN, M. LEFSKY, E. T. A. MITCHARD, W. SALAS, B. R. ZUTTA, W. BUERMAN, S. L. LEWIS, S. HAGEN, S. PETROVA, L. WHITE, M. SILMAN, AND A. MOREL, *Benchmark map of forest carbon stocks in tropical regions across three continents*, *Proceedings of the National Academy of Sciences of the United States of America*, 108 (2011), pp. 9899–9904.

- [147] G. SANDBERG, L. M. ULANDER, J. E. FRANSSON, J. HOLMGREN, AND T. LE TOAN, *L-and p-band backscatter intensity for biomass retrieval in hemiboreal forest*, Remote Sensing of Environment, 115 (2011), pp. 2874–2886.
- [148] P. A. SECK, A. DIAGNE, S. MOHANTY, AND M. C. WOPEREIS, *Crops that feed the world 7: rice*, Food Security, 4 (2012), pp. 7–24.
- [149] Y. SHAO, X. FAN, H. LIU, J. XIAO, S. ROSS, B. BRISCO, R. BROWN, AND G. STAPLES, *Rice monitoring and production estimation using multitemporal radarsat*, Remote sensing of Environment, 76 (2001), pp. 310–325.
- [150] G. A. SHAW AND H.-H. K. BURKE, *Spectral imaging for remote sensing*, Lincoln laboratory journal, 14 (2003), pp. 3–28.
- [151] M. SHIMADA, T. ITOH, T. MOTOOKA, M. WATANABE, T. SHIRAISHI, R. THAPA, AND R. LUCAS, *New global forest /non-forest maps from ALOS PALSAR data (2007-2010)*, Remote Sensing of Environment, 155 (2014), pp. 13 – 31.
- [152] M. SHIMADA AND T. OHTAKI, *Generating large-scale high-quality sar mosaic datasets: Application to palsar data for global monitoring*, IEEE Journal of Selected Topics in Applied Earth Observations and Remote Sensing, 3 (2010), pp. 637–656.
- [153] S. SHRIVASTAVA, D. EGAMBERDIEVA, AND A. VARMA, *Plant growth-promoting rhizobacteria (pgpr) and medicinal plants: The state of the art*, in Plant-Growth-Promoting Rhizobacteria (PGPR) and Medicinal Plants, Springer, 2015, pp. 1–16.
- [154] P. C. SILVESTRO, S. PIGNATTI, H. YANG, G. YANG, S. PASCUCCI, F. CASTALDI, AND R. CASA, *Sensitivity analysis of the aquacrop and safye crop models for the assessment of water limited winter wheat yield in regional scale applications*, PloS one, 12 (2017), p. e0187485.
- [155] B. K. SINGH, A. K. SINGH, N. MEETEI, A. MUKHERJEE, N. MANDAL, ET AL., *Qtl mapping for cold tolerance at the seedling stage in rice.*, International Journal of Bio-Resource & Stress Management, 7 (2016).
- [156] M. I. SKOLNIK, *Introduction to radar*, Radar Handbook, 2 (1962).
- [157] P. SNOEIJ, E. ATTEMA, M. DAVIDSON, B. DUESMANN, N. FLOURY, G. LEVRINI, B. ROMMEN, AND B. ROSICH, *The sentinel-1 radar mission: status and performance*, in Radar Conference-Surveillance for a Safer World, 2009. RADAR. International, IEEE, 2009, pp. 1–6.
- [158] K. SOMA, R. MORI, R. SATO, N. FURUMAI, AND S. NARA, *Simultaneous multichannel signal transfers via chaos in a recurrent neural network*, Neural Computation, 27 (2015), pp. 1083–1101.

- [159] Y. TANG, Y.-Q. ZHANG, N. V. CHAWLA, AND S. KRASSER, *Sums modeling for highly imbalanced classification*, IEEE Transactions on Systems, Man, and Cybernetics, Part B (Cybernetics), 39 (2009), pp. 281–288.
- [160] R. B. THAPA, M. WATANABE, T. MOTOHKA, AND M. SHIMADA, *Potential of high-resolution ALOS PALSAR mosaic texture for aboveground forest carbon tracking in tropical region*, Remote Sensing of Environment, 160 (2015), pp. 122 – 133.
- [161] E. TONYE, A. AKONO, AND A. N. NYOUNGUI, *Le traitement des images de télédétection par l'exemple*, Gordon and Breach Science Publishers Paris, 2000.
- [162] N. TORBICK, D. CHOWDHURY, W. SALAS, AND J. QI, *Monitoring rice agriculture across myanmar using time series sentinel-1 assisted by landsat-8 and palsar-2*, Remote Sensing, 9 (2017), p. 119.
- [163] R. TORRES, P. SNOEIJ, D. GEUDTNER, D. BIBBY, M. DAVIDSON, E. ATTEMA, P. POTIN, B. ROMMEN, N. FLOURY, M. BROWN, ET AL., *Gmes sentinel-1 mission*, Remote Sensing of Environment, 120 (2012), pp. 9–24.
- [164] A. TOURE, K. P. THOMSON, G. EDWARDS, R. J. BROWN, AND B. G. BRISCO, *Adaptation of the mimics backscattering model to the agricultural context-wheat and canola at l and c bands*, IEEE Transactions on Geoscience and Remote Sensing, 32 (1994), pp. 47–61.
- [165] D. TUIA, M. VOLPI, L. COPA, M. KANEVSKI, AND J. MUNOZ-MARI, *A survey of active learning algorithms for supervised remote sensing image classification*, IEEE Journal of Selected Topics in Signal Processing, 5 (2011), pp. 606–617.
- [166] F. ULABY, C. ALLEN, G. EGER III, AND E. KANEMASU, *Relating the microwave backscattering coefficient to leaf area index*, Remote Sensing of Environment, 14 (1984), pp. 113–133.
- [167] F. T. ULABY, G. A. BRADLEY, AND M. C. DOBSON, *Microwave backscatter dependence on surface roughness, soil moisture, and soil texture: Part ii-vegetation-covered soil*, IEEE Transactions on Geoscience Electronics, 17 (1979), pp. 33–40.
- [168] F. T. ULABY, D. G. LONG, W. J. BLACKWELL, C. ELACHI, A. K. FUNG, C. RUF, K. SARABANDI, H. A. ZEBKER, AND J. VAN ZYL, *Microwave radar and radiometric remote sensing*, vol. 4, University of Michigan Press Ann Arbor, 2014.
- [169] N. UNIES, *Convention-cadre des nations unies sur les changements climatiques*, New York, 9 (1992).
- [170] S. VAFAEI, J. SOOSANI, K. ADELI, H. FADAEI, H. NAGHAVI, T. D. PHAM, AND D. TIEN BUI, *Improving accuracy estimation of forest aboveground biomass based on incorporation of alos-2 palsar-2 and sentinel-2a imagery and machine learning: a case study of the hyrcanian forest area (iran)*, Remote Sensing, 10 (2018), p. 172.

- [171] N. VAN NGUYEN AND A. FERRERO, *Meeting the challenges of global rice production*, 2006.
- [172] G. VIEILLEDENT, O. GARDI, C. GRINAND, C. BURREN, M. ANDRIAMANJATO, C. CAMARA, C. GARDNER, L. GLASS, A. RASOLOHERY, H. RATSIMBA, V. GOND, AND J. RAKOTOARIJAONA, *Bioclimatic envelope models predict a decrease in tropical forest carbon stocks with climate change in Madagascar*, *Journal of Ecology*, 104 (2016), pp. 703–715.
- [173] G. VIEILLEDENT, C. GRINAND, F. A. RAKOTOMALALA, R. RANAIVOSOA, J.-R. RAKOTOARIJAONA, T. F. ALLNUTT, AND F. ACHARD, *Combining global tree cover loss data with historical national forest-cover maps to look at six decades of deforestation and forest fragmentation in madagascar*, *bioRxiv*, (2017).
- [174] H. WANG, S. ALLAIN, S. MERIC, AND E. POTTIER, *Scattering mechanism analysis using multi-angular polarimetric radarsat-2 datasets*, in 6th International Workshop and Science and Applications of SAR Polarimetry and Polarimetric Interferometry, ESA Symposium, 2013, pp. 1–6.
- [175] B. WASKE AND M. BRAUN, *Classifier ensembles for land cover mapping using multitemporal sar imagery*, *ISPRS Journal of Photogrammetry and Remote Sensing*, 64 (2009), pp. 450–457.
- [176] K. Q. WEINBERGER, J. BLITZER, AND L. K. SAUL, *Distance metric learning for large margin nearest neighbor classification*, in *Advances in neural information processing systems*, 2006, pp. 1473–1480.
- [177] J. F. WILEY, *R Deep Learning Essentials*, Packt Publishing Ltd, 2016.
- [178] I. H. WOODHOUSE, *Predicting backscatter-biomass and height-biomass trends using a macroecology model*, *IEEE Transactions on Geoscience and remote sensing*, 44 (2006), pp. 871–877.
- [179] F. WU, C. WANG, H. ZHANG, B. ZHANG, AND Y. TANG, *Rice crop monitoring in south china with radarsat-2 quad-polarization sar data*, *IEEE Geoscience and Remote Sensing Letters*, 8 (2011), pp. 196–200.
- [180] X. XIAO, S. BOLES, S. FROLKING, C. LI, J. Y. BABU, W. SALAS, AND B. MOORE, *Mapping paddy rice agriculture in south and southeast asia using multi-temporal modis images*, *Remote Sensing of Environment*, 100 (2006), pp. 95 – 113.
- [181] X. XIAO, S. BOLES, J. LIU, D. ZHUANG, S. FROLKING, C. LI, W. SALAS, AND B. MOORE, *Mapping paddy rice agriculture in southern china using multi-temporal modis images*, *Remote Sensing of Environment*, 95 (2005), pp. 480 – 492.



- [182] Q. YU, P. GONG, N. CLINTON, G. BIGING, M. KELLY, AND D. SCHIROKAUER, *Object-based detailed vegetation classification with airborne high spatial resolution remote sensing imagery*, Photogrammetric Engineering & Remote Sensing, 72 (2006), pp. 799–811.
- [183] O. YUZUGULLU, E. ERTEN, AND I. HAJNSEK, *Estimation of rice crop height from x-and c-band polsar by metamodel-based optimization*, IEEE Journal of Selected Topics in Applied Earth Observations and Remote Sensing, 10 (2017), pp. 194–204.
- [184] A. ZEHTABIAN AND H. GHASSEMIAN, *An adaptive pixion extraction technique for multispectral/hyperspectral image classification*, IEEE Geoscience and Remote Sensing Letters, 12 (2015), pp. 831–835.
- [185] L. ZHANG AND B. DU, *Deep learning for remote sensing data: A technical tutorial on the state of the art*, IEEE Geoscience and Remote Sensing Magazine, 4 (2016), pp. 22–40.
- [186] L. ZHANG, L. ZHANG, AND B. DU, *Deep learning for remote sensing data: A technical tutorial on the state of the art*, IEEE Geoscience and Remote Sensing Magazine, 4 (2016), pp. 22–40.
- [187] Y. ZHANG, H. HUANG, X. CHEN, J. WU, AND C. WANG, *Mapping paddy rice biomass using alos/palsar imagery*, in Education Technology and Training, 2008. and 2008 International Workshop on Geoscience and Remote Sensing. ETT and GRS 2008. International Workshop on, vol. 2, IEEE, 2008, pp. 207–210.
- [188] Y. ZHANG, X. LIU, S. SU, AND C. WANG, *Retrieving canopy height and density of paddy rice from radarsat-2 images with a canopy scattering model*, International journal of applied earth observation and geoinformation, 28 (2014), pp. 170–180.
- [189] Z.-Q. ZHAO, *A novel modular neural network for imbalanced classification problems*, Pattern Recognition Letters, 30 (2009), pp. 783–788.

APPENDIX A

Deep Recurrent Neural Network for Agricultural Classification using multi- temporal SAR
Sentinel-1 for Camargue, Southern France

Article

Deep Recurrent Neural Network for Agricultural Classification using multitemporal SAR Sentinel-1 for Camargue, France

Emile Ndikumana ¹, Dinh Ho Tong Minh ^{1,*}, Nicolas Baghdadi ¹, Dominique Courault ² and Laure Hossard ³

¹ UMR TETIS, IRSTEA, University of Montpellier, 34093 Montpellier, France; emile.ndikumana@irstea.fr (E.N.); nicolas.baghdadi@irstea.fr (N.B.)

² UMR 1114 EMMAH, INRA, University of Avignon, 84914 Avignon, France; dominique.courault@inra.fr

³ UMR 0951 INNOVATION, INRA, University of Montpellier, 34060 Montpellier, France; laure.hossard@inra.fr

* Correspondence: dinh.ho-tong-minh@irstea.fr

Received: 5 July 2018; Accepted: 1 August 2018; Published: 3 August 2018



Abstract: The development and improvement of methods to map agricultural land cover are currently major challenges, especially for radar images. This is due to the speckle noise nature of radar, leading to a less intensive use of radar rather than optical images. The European Space Agency Sentinel-1 constellation, which recently became operational, is a satellite system providing global coverage of Synthetic Aperture Radar (SAR) with a 6-days revisit period at a high spatial resolution of about 20 m. These data are valuable, as they provide spatial information on agricultural crops. The aim of this paper is to provide a better understanding of the capabilities of Sentinel-1 radar images for agricultural land cover mapping through the use of deep learning techniques. The analysis is carried out on multitemporal Sentinel-1 data over an area in Camargue, France. The data set was processed in order to produce an intensity radar data stack from May 2017 to September 2017. We improved this radar time series dataset by exploiting temporal filtering to reduce noise, while retaining as much as possible the fine structures present in the images. We revealed that even with classical machine learning approaches (K nearest neighbors, random forest, and support vector machines), good performance classification could be achieved with F-measure/Accuracy greater than 86% and Kappa coefficient better than 0.82. We found that the results of the two deep recurrent neural network (RNN)-based classifiers clearly outperformed the classical approaches. Finally, our analyses of the Camargue area results show that the same performance was obtained with two different RNN-based classifiers on the *Rice* class, which is the most dominant crop of this region, with a F-measure metric of 96%. These results thus highlight that in the near future these RNN-based techniques will play an important role in the analysis of remote sensing time series.

Keywords: SAR; Sentinel-1; agricultural land cover map; recurrent neural network; long-short term memory; gated recurrent unit; K nearest neighbors; random forest; vector support machines; Camargue; France

1. Introduction

Spatial information about agricultural practices plays an important role for the sustainable development of agronomics, environment, and economics [1,2]. In fact, the importance of agricultural practices has long been recognized by the international community (e.g., Food and Agriculture Organization) [3]. Remote sensing satellite imagery is a valuable aid in providing and understanding this spatial distribution of agricultural practices. Particularly, recent years have seen the arrival of many

satellites to acquire high spatial resolution data on various spectral domains. The Sentinel-1 radar and Sentinel-2 optical sensors from the European Space Agency (ESA) are suited for monitoring agricultural areas. However, like all optical sensors, the use of Sentinel-2 data is limited if the cloud layer is large [4]. In contrast, Sentinel-1 is a Synthetic Aperture Radar (SAR) system that can acquire images in any type of weather with the advantage of providing images regardless of weather conditions. SAR data are well suited to distinguish rice from other types of vegetation cover [5]. The ESA Sentinel-1 SAR sensor (launched in 2014) (short revisit time: 12 days, and then 6 days after the launch of the second satellite in 2016, 20 m spatial resolution and two polarizations) allows a precise temporal follow-up of agricultural crop growth [6]. The ESA provides free data which makes it possible to envisage fine agricultural monitoring for various applications, in particular for providing detailed spatial agricultural land cover distribution.

In the Camargue region, farming is a major activity contributing to the productivity of the region. Among agricultural practices, rice cultivation is the most important one. It plays a crucial role in the development of cropping systems because the irrigation of rice allows the leaching of salt and, consequently, the introduction of other species into the rotation of crops [7]. In this region, to preserve the essential services for regulating agricultural systems for the environment, it is important to understand the operation of the farms [8]. In response to this demand, the spatial extent of agricultural land cover is essential.

In the literature of remote sensing for classification, the natural choice is based on supervised machine learning methods [9,10], which use training sets to classify pixels of unknown identity. Various supervised learning algorithms are available, each with its strengths and weaknesses [9,11,12]. The most recent methodological developments are focused on active learning and semisupervised learning approaches, which make use of unlabeled data for training [13–16]. Although the improvement in learning accuracy is considerable when unlabeled data are used in conjunction with a small amount of labeled data, the use of this approaches is still not common in agricultural land cover classifications. In practice, for agricultural applications, most of works in remote sensing are based on the standard algorithms, such as K nearest neighbor (KNN), random forest (RF), and support vector machine (SVM) [17,18]. These approaches, however, are not designed to work with time series data and, therefore, they ignore their temporal dependency.

Unlike the literature cited above, in this paper we assess the use of deep neural networks to consider the temporal correlation of the data. In fact, through recent advances in machine learning, there has been an increased interest in time series classification using deep convolutional neural networks ($CNNs$) and recurrent neuron networks ($RNNs$) that can take advantage of neural networks for end-to-end classification of a time series [19–21]. Moreover, RNN approaches can be used to work on pixel-based time series [19]. Accordingly, we focus our attention on RNN approaches for the classification. Thanks to their property, $RNNs$ offer models to explicitly manage temporal dependencies among data (e.g., long short term memory ($LSTM$) [22] and Gated Recurrent Unit (GRU) [23]), which makes them suitable for the mining of multitemporal SAR Sentinel-1 data.

The objective of this work is to evaluate the potential of high spatial and temporal resolution Sentinel-1 remote sensing data to : (i) Map different agricultural land covers; and (ii) assess the new deep learning technique by comparing it with the standard machine learning approaches. For this, we propose to use two deep RNN approaches to explicitly consider the temporal correlation of Sentinel-1 data, which will be applied on the region of Camargue.

This paper is organized as follows: In Section 2, the Camargue study area is introduced; in Section 3, the processing SAR Sentinel-1 is reported; in Section 4, the classical machine learning approaches are briefly introduced; in section 5, the two deep $RNNs$ models are presented; in Section 6, results are shown and a discussion is provided; and finally conclusions are drawn in Section 7.

2. Study Area

2.1. Camargue Site

The Camargue region, located in south-eastern France, is a coastal area of the Mediterranean Sea. It has a Mediterranean climate with mild winters, a long summer period (hot and dry), irregular rainfall and sunshine. Its climate has peculiarities related to its geographical location south of the Rhone corridor, between the Cevennes and the Southern Alps. The autumns are watered by brief but important precipitations and winters sometimes are rigorous due to mistral (<https://fr.wikipedia.org/wiki/Camargue#Climat>, last accessed March 2018). This zone covers the current perimeter of the Camargue Regional Natural Park, with an area of around 110,000 ha [24]. The study site is composed of five landscapes: Agriculture area, urban zone, water area, forests and natural environment. The agriculture zone can be defined by using the official Graphical Parcel Register (RPG) data, provided freely by the French government (<https://www.data.gouv.fr>). We used the recent version of RPG 2015 for our study in order to delimit the agricultural areas. In our study area, this corresponds to 54,082 ha (see the cyan polygon in Figure 1), in which the permanent moors, orchards, and olive trees areas are 17,859 ha, and the remaining 36,223 ha is used for common agricultural activities. In this 36,223 ha agricultural zone, rice is the most dominant crop (with 44% and 16,000 ha in 2011 [8]) and has an important function in the economic, ecological and social equilibrium of the region.

2.2. Ground Data

A field survey was carried out on 921 reference plots in July 2017 to collect the land cover information. The boundary of reference plots was drawn manually, based on the high resolution 60 cm World Imagery layer of ArcGIS data online (accessed in July 2017). We chose 11 observed surface classes: (1) Rice; (2) sunflower; (3) lawn; (4) irrigated grassland; (5) durum wheat (winter); (6) alfalfa; (7) tomato; (8) melon; (9) clover; (10) swamps; and (11) vineyard. Figure 1 shows the position of ground samples and the distribution of the pixel number per class and number of plots is shown on Table 1.

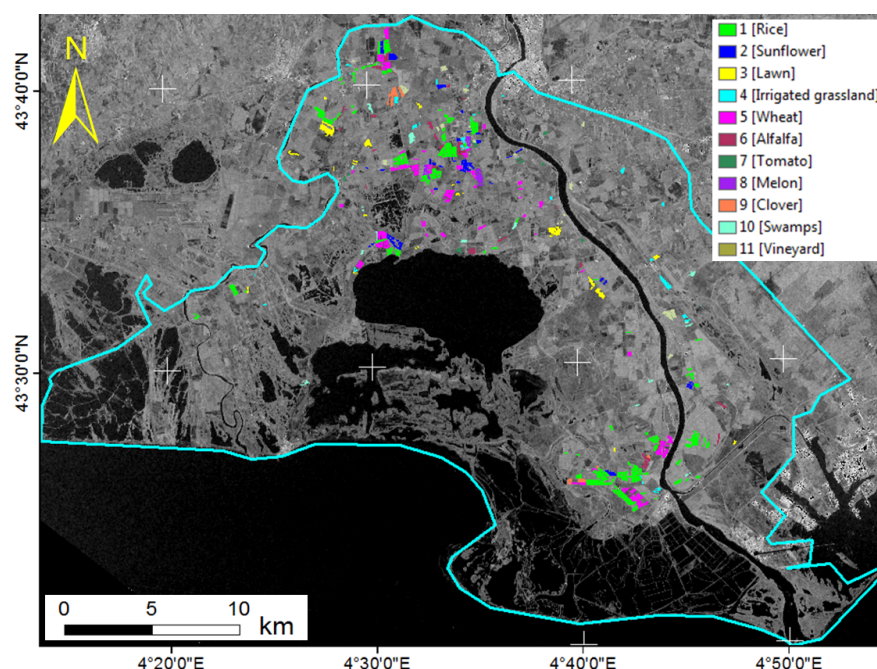


Figure 1. Camargue study area. Colored polygons represent 921 reference plots location. The study area is limited by the cyan polygon.

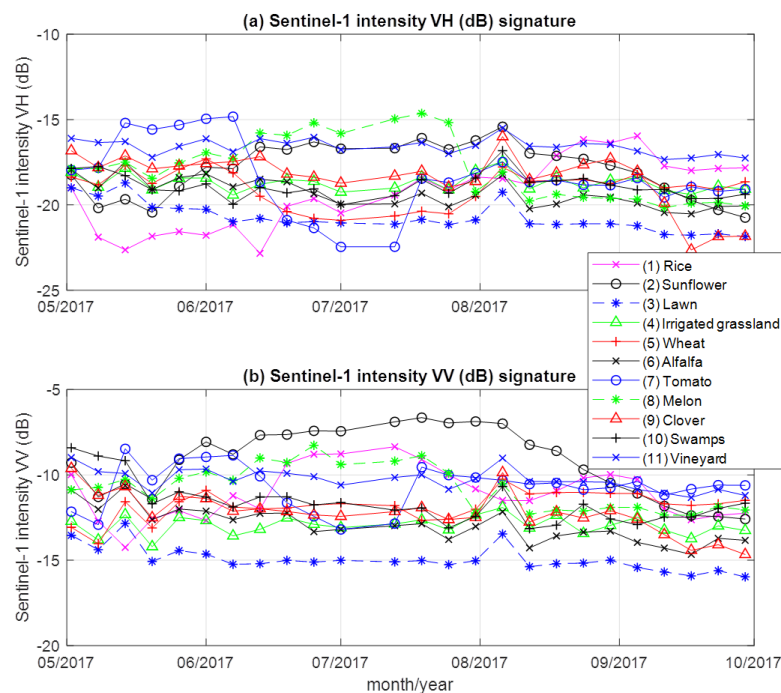
Table 1. The distribution of the number of pixel and plots per class.

ID	Vegetation Class	Number of Plots	Number of Pixels	Surface Area (ha)	Area (%)
(1)	Rice	284	23,275	931	35.2
(2)	Sunflower	77	5541	222	8.4
(3)	Lawn	27	5018	201	7.6
(4)	Irrigated grassland	53	3528	141	5.3
(5)	Wheat	304	13,057	522	19.7
(6)	Alfalfa	59	4580	183	6.9
(7)	Tomato	15	1362	55	2.1
(8)	Melon	24	1978	79	2.9
(9)	Clover	26	1918	77	2.9
(10)	Swamps	19	2535	101	3.8
(11)	Vineyard	33	3409	136	5.2
Total		921	66,201	2648	100

3. SAR Data and Processing

3.1. SAR Data

Since wheat cultivation is the only winter crop presence after May and the major agricultural practices in Camargue are in summer (e.g., from May to September), we focus our data analysis on this period. The Sentinel-1A/1B SAR dataset includes 25 acquisitions in terrain observation with progressive scan (TOPS) mode from May to September 2017 (5 months), with a revisit period of 6 days. This is dual-polarization (VV + VH) data, resulting in 50 images. Figure 2 summarizes the temporal profiles of the 11 agricultural classes per polarization. Each time series is made up of 25 points (one for each acquisition). Figure 3 provides information on the temporal dynamic of these classes by giving their average and standard deviation.

**Figure 2.** The temporal profiles of the eleven different classes which respect to the VH (a) and VV (b) polarizations.

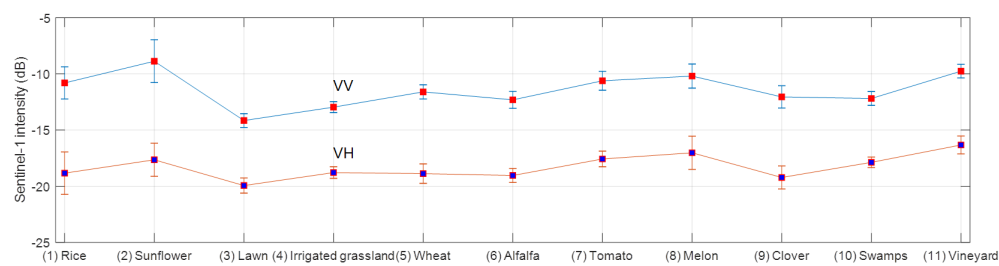


Figure 3. The average and standard deviation of the eleven different classes for VV and VH polarizations.

3.2. Pre-Processing Data

First, a master image was chosen and all images are coregistered, taking into account TOPS mode, to the master image [25]. Five-look (5 range looks) intensity images are generated and radiometrically calibrated for range spreading loss, antenna gain, normalized reference area and the calibration constant that depends on the parameters in the Sentinel-1 SAR header.

3.3. Temporal Filtering

Reliable estimates of the intensity from a distributed target require that the estimated number of looks (ENL) is sufficiently large. Speckle filtering is often used to increase the ENL with loss of spatial resolution [26]. In properly coregistered multitemporal datasets, it is possible to employ the technique of temporal filtering, which, in principle, increases radiometric resolution without degrading spatial resolution. The temporally filtered images usually show markedly diminished speckle, with little or no reduction in spatial resolution. In this paper, we improve the time series SAR Sentinel-1 dataset by exploiting a temporal filtering method developed by [26] to reduce noise, while retaining, as much as possible, the fine structures present in the images.

3.4. Geocoding

After pre-processing and filtering, all the processed images are in the imaging geometries of the master image. In order to create a unified dataset, all image data have to be orthorectified into map coordinates. This is done by creating a simulated SAR image from a SRTM DEM 30 m, and using the simulated SAR image to coregister the two image sets (polarizations). The pixel size of the orthorectified image data is 20 m. After geocoding, all intensity images are transformed to the logarithmic dB scale, normalized to values between 0–255 (8 bits) and input into classifiers. The SAR Sentinel-1 data are processed by the TomoSAR platform, which offers SAR, interferometry and tomography processing [27,28]. Finally, for each pixel, a 25×2 matrix (25 acquisitions and two polarizations: VV + VH) is generated as input for classifiers.

4. Classical Machine Learning Approaches

Among supervised machine learning approaches, we use K nearest neighbor (KNN), random forest (RF), and support vector machine (SVM) approaches as a baseline for comparing the performance of Sentinel-1 image data for land cover classification with deep recurrent neural network approaches in Section 6. The rationale for this choice is mainly because they are the most popular in remote sensing [17,18,29] and remain competitive w.r.t. other approaches in many scenarios. In this section, we provide a brief introduction of these methods for the sake of complete.

4.1. K Nearest Neighbors

KNN is classified as a non-parametric machine learning method, because it simply remembers all of its training data. Despite its simplicity, KNN has been successful in a large number of classification

problems, including remote sensing satellite images. The principle of *KNN* is that in the set of training data, it finds a group of K samples that are closest to unknown samples (based on a certain distance function, e.g., Euclidean) [30]. In *KNN* approach, the class of an unknown sample is determined by applying a majority vote on the classes of its K nearest neighbors [30,31].

4.2. Random Forest

The Random Forest algorithm has demonstrated its ability to yield high quality mappings for a different varieties of crop type systems with a much faster computation when compared to other state of the art classifiers [32–34]. The classifier relies on aggregating the results of an ensemble of simpler decision tree classifiers. In other words, it is a meta-estimator that fits a number of decision tree classifiers on various subsamples of the dataset, and uses averaging to improve the predictive accuracy and control over-fitting [35]. To reduce the computational complexity of the algorithm and the correlation between subsamples, tree construction can be stopped when a maximum depth is reached or when the number of samples on the node is less than a minimum sample threshold.

4.3. Support Vector Machine

The Support Vector Machine algorithm has been proved to be superior to most other image classification algorithms in terms of classification accuracy [36]. *SVM* is basically a binary classifier that delineates two classes by fitting an optimal separating hyperplane to the training data in the multidimensional feature space to maximize the margin between them [37]. *SVM* uses a kernel function to project the data from input space into feature space. Several kernels can be used: Linear, radial basis function (RBF), and polynomial or sinusoidal kernels. Linear and RBF kernels are the most commonly used. While linear kernels are computationally more efficient, nonlinear kernels, such as RBF kernels, tend to outperform linear kernels. For RBF kernels, two parameters should be specified: (i) The complexity parameter C which controls the trade-off between the maximization of the margin between the training data vectors and the training error decision limit; and (ii) the gamma parameter that is the width of the kernel function. Increasing C values usually require increasing computational time and high C values also increase risks of over-fitting.

5. Recurrent Neural Network

Recurrent neural networks are well-designed machine learning techniques that stand out for their quality in different fields of activity, such as signal processing, natural language processing and speech recognition [38,39]. Contrary to convolutional neural networks, RNNs clearly manage the temporal data dependencies, since the output of the neuron in time $t - 1$ is used with the next input, to feed the neuron itself at time t . A diagram of a typical neural RNN is detailed in Figure 4. Among different RNN models, we have Long-Short Term Memory (*LSTM*) [22] and Gated Recurrent Unit (*GRU*) [23], which are the two most well known RNN units. The main difference between them is related to the number of parameters to learn. Considering the same size of the hidden state, the *LSTM* model has more parameters than the *GRU* unit.

In the following, we will briefly analyze the two RNN units (*LSTM* and *GRU*). For each of them, we aim to provide and discuss the equations that describe its internal behavior. The \odot symbol represents an element-wise multiplication, while σ and \tanh are Sigmoid and Hyperbolic Tangent function, respectively. The input of a RNN unit is a sequence of variables (x_1, \dots, x_t) , where each element x_t is a vector and t refers to the corresponding timestamp.

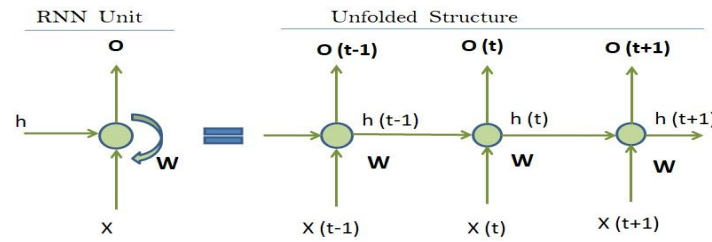


Figure 4. RNN Unit (on the left) and unfolded structure (on the right).

5.1. Long-Short Term Memory (LSTM)

The existing RNN models fail to learn long-term dependencies because of the problem of vanishing and exploding gradients. To overcome this challenge, the *LSTM* model is used [22]. The Equations (1)–(6) formally describes the LSTM neuron. The *LSTM* set consists of two cell states: The C_t memory and the h_t hidden state. Three different gates intervene in the control of the flow of information: The input (i_t), the forget (f_t) and the output (o_t). All three gates mix the current entry, x_t , with the hidden state, h_{t-1} , from the previous timestamp. Also, the gates have two major functions: (i) They regulate the quantity of information to forget/remember during the process; (ii) they deal with the problem of gradient disappearance/bursting. We can see that the gates are implemented by a sigmoid. This function gives values between 0 and 1. The *LSTM* unit also uses a temporary cell state, y_t , that resizes the current input. This current cell is applied by a hyperbolic tangent function that gives values between -1 and 1 . The sigmoid and the hyperbolic tangent work per element. i_t sets the amount of information to keep ($i_t \odot y_t$), while f_t indicates how much memory should be kept in the current step ($f_t \odot c_{t-1}$). The input of an RNN is a sequence of variables (x_1, \dots, x_n) , where x_t is a generic element that represents a feature vector and t refers to the corresponding timestamp.

Finally, o_t has an impact on the new hidden state, h_t , which determines how much information from the current memory will be on the output step. The different matrices, W_{**} , and bias coefficients, b_* , are the parameters used during model formation. The memory, C_t , and the hidden state, h_t , are both transmitted at the next step.

$$i_t = \sigma(W_{ix}x_t + W_{ih}h_{t-1} + b_i) \quad (1)$$

$$f_t = \sigma(W_{fx}x_t + W_{fh}h_{t-1} + b_f) \quad (2)$$

$$y_t = \tanh(W_{yx}x_t + W_{yh}h_{t-1} + b_y) \quad (3)$$

$$c_t = i_t \odot y_t + f_t \odot c_{t-1} \quad (4)$$

$$o_t = \sigma(W_{ox}x_t + W_{oh}h_{t-1} + b_o) \quad (5)$$

$$h_t = o_t \odot \tanh(c_t) \quad (6)$$

5.2. Gated Recurrent Unit (GRU)

To facilitate the computation and implementation of the *LSTM* model, the authors [23] develop a new RNN unit. The neuron *GRU* is illustrated in Equations (7)–(9). This new unit operates as the *LSTM* model by performing the gates and cell states but, conversely to the *LSTM* pattern, the *GRU* unit has two gates: Update (z_t) and reset (r_t), and also we have a cell state, the hidden state, (h_t). In addition, the two gates merge the current input (x_t) with information from previous timestamps (h_{t-1}). The update gate efficiently regulates the compromise between the amount of information from the previously hidden state (which will be included in the current hidden state) and the amount of information of the current timestamp that is to be kept. This acts in the same way as the unit memory cell *LSTM* that supports the RNN to remember information in the future.

Furthermore, the reset gate analyzes the amount of information from previous timestamps that could be embedded in the current information. Since each hidden unit has reset and updates gates, they register dependencies at different levels. Units that are more likely to capture short-term dependencies may have a frequently-enabled reset gate [23].

$$z_t = \sigma(W_{zx}x_t + W_{zh}h_{t-1} + b_z) \quad (7)$$

$$r_t = \sigma(W_{rx}x_t + W_{rh}h_{t-1} + b_r) \quad (8)$$

$$h_t = z_t \odot h_{t-1} + (1 - z_t) \odot \tanh(W_{hx}x_t + W_{hr}(r_t \odot h_{t-1}) + b_h) \quad (9)$$

5.3. RNN-Based Time Series Classification

To complete the classification task, at each RNN unit we make a deep architecture, putting together five units. The use of several units, similar to what is frequently done for CNN models in several convolutional layers [40], will extract high-level non-linear time dependencies that are in the remote sensing time series. This is done for both *LSTM* and *GRU*.

The RNN model follows a new sequence at the input, but it makes no prediction by itself. For this purpose, A SoftMax [41] layer is stacked on the last recurrent unit to predict the final multi-class. The SoftMax layer has the same number of neurons as classes to predict. For layer normalization reasons, the SoftMax priority is given instead of the Sigmoid function, because the value of the SoftMax layer can be considered as a probability distribution on classes that total up to 1, whereas in the case of the sigmoid, the neurons give values between 0 and 1. Each sample belongs absolutely to a single class, which leads us to the choice of SoftMax. This schema is instantiated for both *LSTM* and *GRU* units, thus coming up with two different classifiers: An *LSTM*-based and a *GRU*-based classification scheme. Figure 5 shows a schematic view of the *LSTM*-based architecture for each pixel in our paper (e.g., 25 points input VV/VH, 5 *LSTM* units, 512 hidden dimensions and 11 classes output).

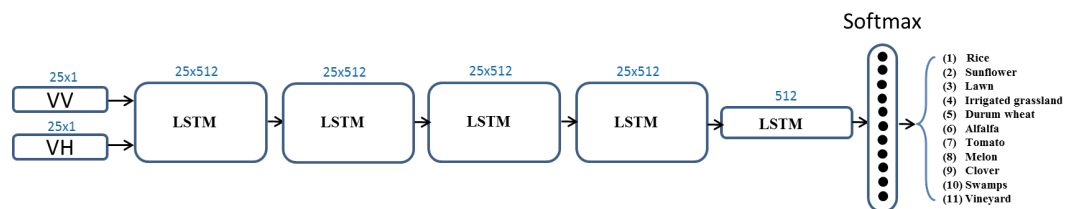


Figure 5. The schematic view of the RNN *LSTM*-based architecture. By replacing *LSTM* to *GRU* unit, we get the RNN *GRU*-based architecture.

6. Experimental Results

6.1. Experimental Settings

We compared RNN-based classification approaches (*LSTM* and *GRU*) with standard machine learning approaches.

For the *RF* model, we set the number of trees at 400 and a maximum tree depth of 25. For the *KNN* model, we set the number of nearest neighbors at 10. For the *RF* model, the number of randomly selected features at each node is kept at its default value for a classification problem (i.e., the square root of the total number of variables [42]). For the *SVM* model, we use the RBF kernel with a default gamma (i.e., $1/\text{number of samples}$ [43]) and a parameter of complexity equal to 10^5 . For *RF* and *KNN*, we use the python implementation provided by the Scikit-learn library [42], while for *SVM* we use the LibSVM implementation [43].

For RNN-based classifiers, we define the number of hidden dimensions equal to 512 (General speaking, the choice of the number of hidden dimensions depends on the volume of the training dataset available. If the dataset is small, we have to use a simple model in order to estimate fewer weight

parameters and vice versa. For example, in the work [20], the number of units is set to 64 and 512 for *Thau* and *Reunion* test sites, respectively. We experimentally found that our best performance was achieved by setting 512, after trying with 64, 128, 254, 512 and 1024). An initial learning rate of 5×10^{-4} , ρ of 0.9 and a decline of 5×10^{-5} was employed. We implement the model via the *Keras* python library with *Theano* as the back end [44]. To train the model, we used the *Rmsprop* strategy, which is a variant of stochastic gradient descent [45]. The loss function being optimized is categorical cross entropy, which is the standard loss function used in all multiclass classification jobs [46]. The model is trained for 250 epochs, with a batch size set at 64. For the different methods, we apply cross-validation 5 times on the dataset, with a split procedure in two steps: (1) At the polygon-level to separate train and test instances and (2) at the pixel-level to extract each instance [47,48]. In other words, we impose that pixels of the same object belong exclusively to the training or to the test set. In this way, the initial set of data (66,201 pixels) is reduced to 57,585 pixels, since our polygons are not the same size. In detail, the set of data (57,585 pixels) is randomly divided into 5 partitions (folds) of equal size. Then, four folds are used to train the models (about 46,068 pixels), and the fifth fold (about 11,517 pixels) is used for the test phase. The operation is repeated five times, so that each fold is like a possible test set. Finally, the score measurements are calculated by concatenating the predicted labels per fold with respect to the real classes. Experiments were performed on a workstation Intel(R) Xeon(R) CPU E5-2667 v4@3.20Ghz with 256 GB of RAM and GPU TITAN X. The training step takes, on average, 166 min to learn each RNN model on the training set and less than 3 min to classify the pixel time series in the test set.

In order to assess classification performances, we use not only the global accuracy and kappa measures, but also average and per-class F-measures.

6.2. Results

The multitemporal Sentinel-1 data, processed as in Section 3, are used as an input for classification using classical approaches (*KNN*, *RF*, and *SVM*) in Section 4 and two RNN-based models (*LSTM* and *GRU*) in Section 5. The summary of the results of different classification approaches is reported in Table 2. This is the performance from cross-validation 5 times on Sentinel SAR-1 time series data, showing the average and standard deviation values of the F-measure, Accuracy, and Kappa assessment metrics from 5 repetitions. For this multi-temporal SAR Sentinel-1, all classifier performance metrics are very high, showing the quality of the dataset for agricultural classification tasks.

Table 2. The average and standard deviation from cross-validation 5 times on the time series SAR Sentinel-1 data.

Classifier	F-Measure	Accuracy	Kappa
<i>KNN</i>	86.1 \pm 0.6%	85.6 \pm 0.6%	0.823 \pm 0.009
<i>RF</i>	87.1 \pm 0.9%	86.9 \pm 1.2%	0.833 \pm 0.015
<i>SVM</i>	87.3 \pm 1.5%	87.1 \pm 1.6%	0.837 \pm 0.019
<i>LSTM</i>	89.2 \pm 1.7%	89.1 \pm 1.6%	0.862 \pm 0.020
<i>GRU</i>	89.8 \pm 1.6%	89.6 \pm 1.6%	0.869 \pm 0.019

Second, to illustrate more precise comprehension of the behavior of the different classifiers, we report a per-class F-measure comparison in Figure 6. In this figure, the eleven classes are evaluated according to the different methods (*KNN*, *RF*, *SVM*, *LSTM* and *GRU*) used in the classification. In addition, confusion matrices are also reported in Figure 7. In both figures, results show a better performance using RNN-based classification approaches over classical machine learning methods (*KNN*, *RF* and *SVM*). Between the two RNN models, the *GRU*-based method obtains slightly better results than the *LSTM*. This is as expected, due to the fact that the *GRU* unit is considered as an improvement of the *LSTM* unit [23].

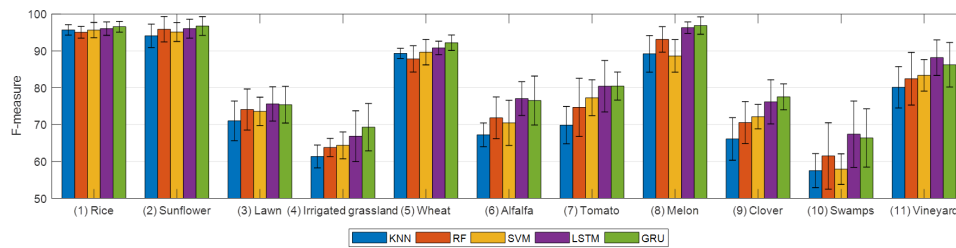


Figure 6. Per Class F-Measure of the different approaches.

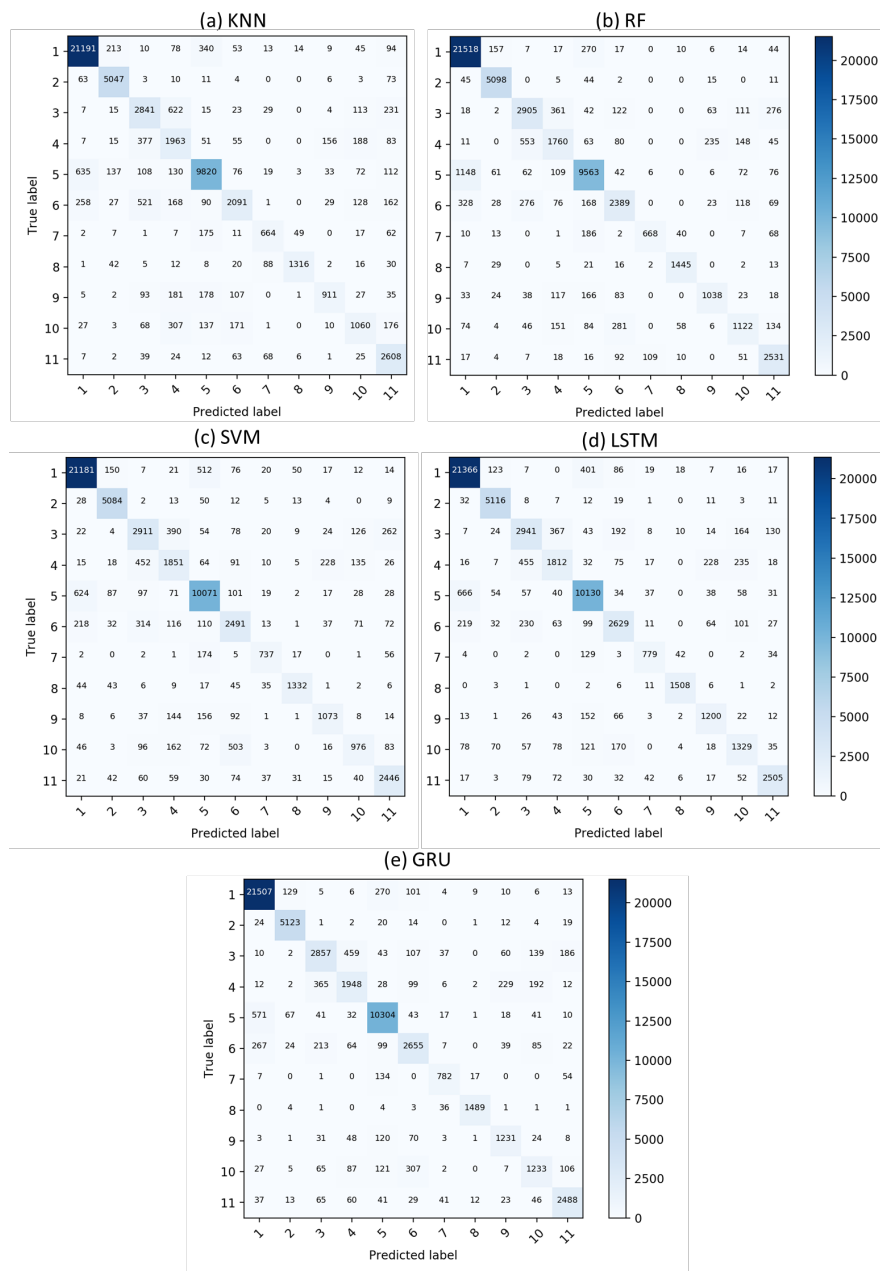


Figure 7. Confusion matrices on the SAR Sentinel-1 time series data of the different approaches: (a) KNN, (b) RF; (c) SVM; (d) LSTM and (e) GRU. The name of the labels: (1) rice; (2) sunflower; (3) lawn; (4) irrigated grassland; (5) durum wheat (winter); (6) alfalfa; (7) tomato; (8) melon; (9) clover; (10) swamps; and (11) vineyard.

Finally, by applying the best RNN-based *GRU* classifier for the whole area study, we established the agricultural land cover map for Camargue in 2017 (see Figure 8). Figure 9 is a zoomed version of the white-border box in the Figure 8, to facilitate visualization of classification results for the RNN-based *GRU* and the *SVM* approach w.r.t the reference plots. The classification results for both approaches were matched with the reference plots, and were slightly smoother in the RNN-based *GRU* result. Among different agricultural classes, rice is the dominant practice (with 29.3% and 10,627 ha, see Table 3) by its extent and presence in almost all areas of the region.

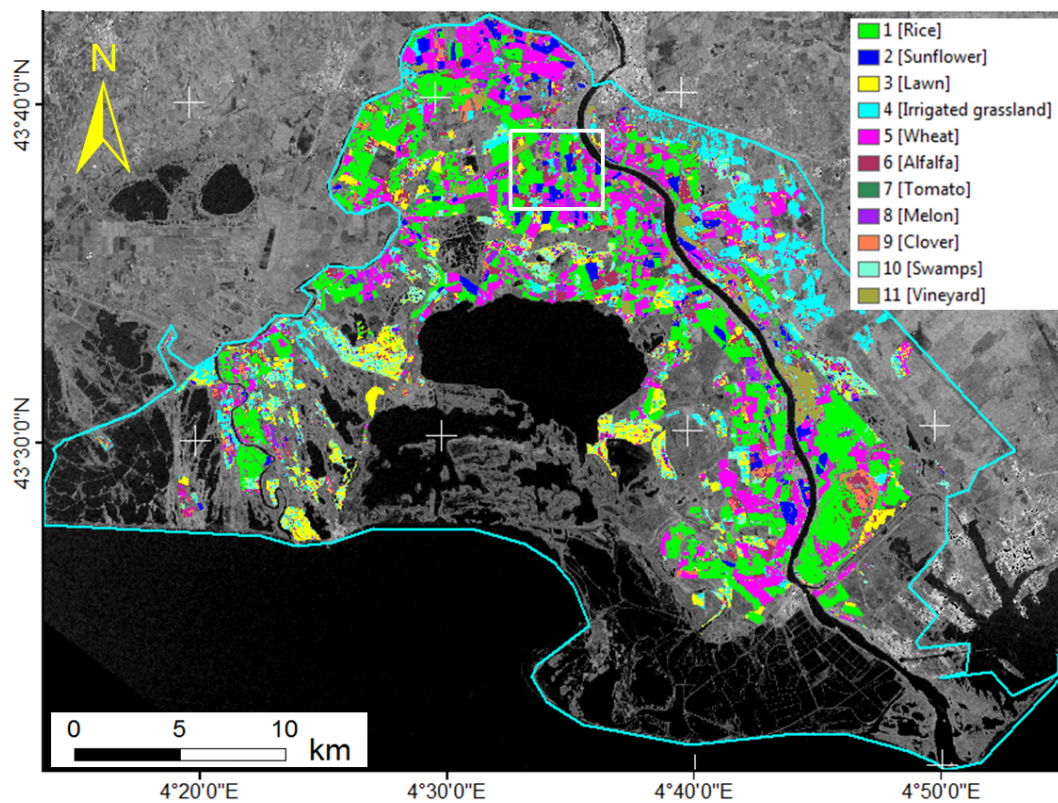


Figure 8. The agricultural land cover map in Camargue using the RNN-based *GRU* multitemporal SAR Sentinel-1.

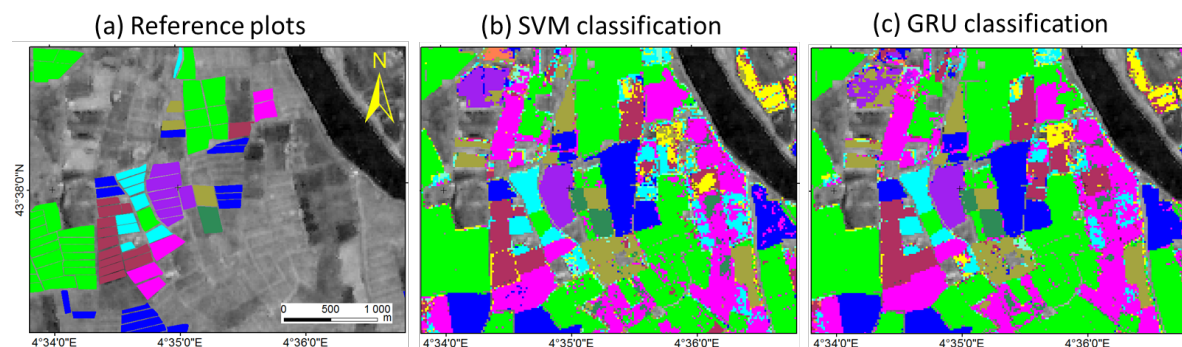


Figure 9. A zoom version of the white-border box in the Figure 8 is provided to facilitate visualization of classification results. (a) reference plots; (b) the classical *SVM* result and (c) the RNN-based *GRU* result.

Table 3. The distribution of the agricultural land cover class in 2017.

ID	Class	Area (ha)	Percent
(1)	Rice	10,627	29.3
(2)	Sunflower	1676	4.6
(3)	Lawn	3357	9.4
(4)	Irrigated grassland	4148	11.5
(5)	Wheat	7439	20.5
(6)	Alfalfa	2593	7.2
(7)	Tomato	592	1.6
(8)	Melon	622	1.7
(9)	Clover	884	2.4
(10)	Swamps	2591	7.2
(11)	Vineyard	1694	4.6
Total		36,223	100

6.3. Discussion

In this work we show that the multitemporal Sentinel-1 data can be used to classify different agriculture classes in Camargue, France. We obtained good results, using both classical approaches and the advance deep RNN techniques. The metric of validation indicates good performance, in which F-measure/Accuracy was greater than 86% and Kappa coefficient was better than 0.82. Together, these results confirm the suitability of Sentinel-1 time series data for agriculture land cover applications.

First, we show that even with the classical approaches, good classification performance could be achieved with radar time series data. This was expected to be challenging, because radar images are characterized by considerable speckle noise, which does not exist in optical images. We note that the same performance can not be straightforwardly transferred to the case of having few radar data. Good performance can be achieved by the fact that Sentinel-1 SAR with 6 days revisit time allows not only a precise temporal follow-up of the agriculture crop growth, but also mostly noise-free data, thanks to the multitemporal speckle filtering. It is worth pointing out that, nowadays, the Sentinel-1 constellation is the only satellite system providing dense time series with global coverage. It is therefore a good candidate for operational agriculture land cover mapping.

We can observe that RNN-based classification approaches have better performance over classical machine learning methods (*KNN*, *RF* and *SVM*). Between the two deep RNN models, the *GRU*-based method has slightly better results than the *LSTM* one. To give a more precise comprehension of the behavior of the different methods, from Figure 6, we can see that the performance gain offered by the RNN-based methods involve all the eleven classes, resulting in equally good result on all the them. Conversely, *KNN*, *RF* and *SVM* show different behaviors for different classes. Both classifiers obtain the best performances on the *Rice* class (1) and the lowest performances on the *Irrigated grassland* class (4). This behavior can be explained by considering the temporal profiles of both VV and VH presented in Figure 2. The *Rice* class (depicted with pink lines in Figure 2) has a clear and distinct profile, with a strong dynamic (with large standard deviation value, see Figure 3), facilitating its detection. The *Irrigated grassland* class (depicted with green diamond lines in Figure 2) has a weak temporal behavior, with a small standard deviation value (see Figure 3), and intersects the temporal profiles of all the other classes multiple times. This is probably the reason why the standard approaches are not able to correctly detect this class, since they ignore the temporal correlation of the data. On the other hand, the RNN-based approaches discriminate well among all the classes, since they can extract and summarize the important signal portions that help the discriminative task among the different agriculture classes.

Based on Figure 7, which shows the confusion matrices for each method, we can see that a high misclassification rate is recorded between the *Irrigated grassland* (4) and *Swamps* (10) classes. This is true for all the different classifiers. However, for the RNN-based approaches, this misclassification error is not as high. Conversely, in the case of *KNN*, *RF* and *SVM*, this misclassification behavior

is significant. In fact, the standard machine learning approaches are under strain, and they are responsible for a considerable misclassification rate. In addition, the standard machine learning approaches are not always good at dealing with imbalanced classification problems [49,50]. Thanks to the joint optimization of nonlinear input transformations along with classification, deep learning approaches provide here a valuable strategy to discriminate among the different agriculture classes. In addition, as expected, the ability of RNNs to deal with the temporal correlations characterizing the SAR Sentinel-1 data result in a gain in performance on all classes, with particular emphasis on those classes that exhibit similar temporal behaviors for longer periods. Together, these results confirm that the RNN models (both *LSTM*-based and *GRU*-based) are well suited to detect and exploit temporal dependencies, as opposed to common classification approaches that do not explicitly leverage temporal correlations. Our finding is consistent with previous reports, in which Deep Learning outperformed the classical machine learning approaches [19–21].

In this paper, we selected *KNN*, *RF* and *SVM* due to their most popular supervised classification algorithms in the remote sensing community. Although they were introduced way back in the early 2000s, they still remain competitive w.r.t. other approaches in many scenarios, and they represent the algorithms to which any new method needs to be compared to. Considering the setting of remote sensing time series analysis (both optical and SAR), to date, no other classifier reaches the same generality and classification performance of these approaches, and this is why we decided to compare our RNNs proposals to them. Unfortunately, to the best of our knowledge, we are not aware of any other (more recent) classification methods that are commonly employed to perform supervised classification on time series SAR data. To summarize our position, this comparison allows us to appreciate more keenly how important it is to have techniques that can be employed to intelligently exploit temporal dependency among data w.r.t. standard machine learning approaches employed in the remote sensing field. Due to the promising results we have obtained with RNNs, we think that, in the near future, these techniques will play an important role in the analysis of remote sensing time series.

For agricultural land cover in Camargue 2017, we can observe that the region areas are occupied mostly by rice (29.3% and 10,627 ha) and wheat (20.5% and 7439 ha) distributions. We note that the performance of both RNN-based *LSTM* and *GRU* classifiers is best on the *Rice* class, with the same F-measure metric of 96%. As a consequence, an RNN-based classifier is a valuable tool to discriminate the rice from other agriculture classes. In Camargue, there is a great variability in the types of rice farms [8], and the rice areas vary according to the year. The rice areas cultivated have significantly decreased from 16,000 ha in 2011 (e.g., in [8]) to 10,627 ha (our estimation) in 2017. The decreased phenomena of the rice extent could lead to a negative effect to the sustainable development of Camargue. Future works on this region could be focused on considering the assimilation of new source remote sensing data, such as Sentinel-1 radar, in crop models to estimate rice production, to follow farming practices, and to be able to propose strategies for sustainable agricultural development.

7. Conclusions

In this paper, we studied the potential of high spatial and temporal resolution Sentinel-1 remote sensing data for different agriculture land cover mapping applications and assessed the new deep learning techniques. We proposed to use two deep RNN approaches to explicitly consider the temporal correlation of Sentinel-1 data, which were applied on the Camargue region.

We demonstrated that even with the classical approaches (*KNN*, *RF* and *SVM*), good classification performance could be achieved with Sentinel-1 SAR image time series. We experimentally demonstrated that the use of recurrent neural networks to deal with SAR Sentinel-1 time series data yields a consistent improvement in agricultural classes as compared with classical machine learning approaches. The experiments highlight the appropriateness of a specific class of deep learning models (RNNs) which explicitly consider the temporal correlation of the data in order to discriminate among agricultural classes of land cover, typically characterized by similar but complex temporal behaviors.

We observed for the *Rice* class the same high performance of both RNN-based *LSTM* and *GRU* classifiers, with a F-measure of 96%. We found that in the Camargue region, rice land cover is still dominant, but decreasing significantly. Future work could be focused on estimating rice production yields in order to propose strategies for sustainable agriculture development.

Finally, although the number of exploitable optical images are limited due to cloud cover, the use of multi-source data including optical and SAR radar data will be an important subject of future research.

Author Contributions: E.N. and D.H.T.M. developed the main idea that led to this paper. E.N. and D.H.T.M. provided SAR processing, classifications and their descriptions. E.N. collected the reference data and was the main author of the paper. INRA has provide the main contacts with farmers on the Camargue area and the main shapefiles including ground observations on crop for various farmers. All authors read and approved the final manuscript.

Funding: This research received no external funding.

Acknowledgments: This work was supported in part by European Space Agency, Centre National d'Etudes Spatiales/Terre, Ocean, Surfaces Continentales, Atmosphere and in part by the National Research Agency within the framework of the program "Investissements d'Avenir" for the GEOSUD under Project ANR-10-EQPX-20. We thank the government of Burundi for funding the PhD research of Emile Ndikumana. We thank Jarlath SLEVIN for English correction. The authors wish to thank Dino Ienco (UMR TETIS—IRSTEA) and Raffaele Gaetano (UMR TETIS—CIRAD) for insight discussion on the deep learning.

Conflicts of Interest: The authors declare no conflict of interest.

References

1. Buckley, C.; Carney, P. The potential to reduce the risk of diffuse pollution from agriculture while improving economic performance at farm level. *Environ. Sci. Policy* **2013**, *25*, 118–126. [[CrossRef](#)]
2. Foley, J.A.; DeFries, R.; Asner, G.P.; Barford, C.; Bonan, G.; Carpenter, S.R.; Chapin, F.S.; Coe, M.T.; Daily, G.C.; Gibbs, H.K.; et al. Global consequences of land use. *Science* **2005**, *309*, 570–574. [[CrossRef](#)] [[PubMed](#)]
3. Polso, A.; Speedy, A.; Kueneman, E. Good Agricultural Practices—A Working Concept. In Proceedings of the FAO Internal Workshop on Good Agricultural Practices, Rome, Italy, 27–29 October 2004; Volume 1, p. 41.
4. Drusch, M.; Bello, U.D.; Carlier, S.; Colin, O.; Fernandez, V.; Gascon, F.; Hoersch, B.; Isola, C.; Laberinti, P.; Martimort, P.; et al. Sentinel-2 ESA Optical High-Resolution Mission for GMES Operational Services. *Remote Sens. Environ.* **2012**, *120*, 25–36. [[CrossRef](#)]
5. Le Toan, T.; Ribbes, F.; Wang, L.F.; Floury, N.; Ding, K.H.; Kong, J.A.; Fujita, M.; Kurosu, T. Rice crop mapping and monitoring using ERS-1 data based on experiment and modeling results. *IEEE Trans. Geosci. Remote Sens.* **1997**, *35*, 41–56. [[CrossRef](#)]
6. Torres, R.; Snoei, P.; Geudtner, D.; Bibby, D.; Davidson, M.; Attema, E.; Potin, P.; Rommen, B.; Floury, N.; Brown, M.; et al. GMES Sentinel-1 mission. *Remote Sens. Environ.* **2012**, *120*, 9–24. [[CrossRef](#)]
7. Mouret, J.C. Etude de l'Agrosystème Rizicole en Camargue dans ses Relations avec le Milieu et le Systeme Cultural: Aspects Particuliers de la Fertilité. Ph.D. Thesis, Université des Sciences et Techniques du Languedoc, Montpellier, France, 1988.
8. Delmotte, S.; Tittone, P.; Mouret, J.C.; Hammond, R.; Lopez-Ridaura, S. On farm assessment of rice yield variability and productivity gaps between organic and conventional cropping systems under Mediterranean climate. *Eur. J. Agron.* **2011**, *35*, 223–236. [[CrossRef](#)]
9. Friedl, M.A.; Brodley, C.E. Decision tree classification of land cover from remotely sensed data. *Remote Sens. Environ.* **1997**, *61*, 399–409. [[CrossRef](#)]
10. Li, C.; Wang, J.; Wang, L.; Hu, L.; Gong, P. Comparison of classification algorithms and training sample sizes in urban land classification with Landsat thematic mapper imagery. *Remote Sens.* **2014**, *6*, 964–983. [[CrossRef](#)]
11. Waske, B.; Braun, M. Classifier ensembles for land cover mapping using multitemporal SAR imagery. *ISPRS J. Photogramm. Remote Sens.* **2009**, *64*, 450–457. [[CrossRef](#)]
12. Lu, D.; Weng, Q. A survey of image classification methods and techniques for improving classification performance. *Int. J. Remote Sens.* **2007**, *28*, 823–870. [[CrossRef](#)]
13. Li, J.; Bioucas-Dias, J.M.; Plaza, A. Semisupervised Hyperspectral Image Segmentation Using Multinomial Logistic Regression With Active Learning. *IEEE Trans. Geosci. Remote Sens.* **2010**, *48*, 4085–4098. [[CrossRef](#)]

14. Gomez-Chova, L.; Camps-Valls, G.; Munoz-Mari, J.; Calpe, J. Semisupervised Image Classification with Laplacian Support Vector Machines. *IEEE Geosci. Remote Sens. Lett.* **2008**, *5*, 336–340. [[CrossRef](#)]
15. Munoz-Mari, J.; Bovolo, F.; Gomez-Chova, L.; Bruzzone, L.; Camp-Valls, G. Semisupervised One-Class Support Vector Machines for Classification of Remote Sensing Data. *IEEE Trans. Geosci. Remote Sens.* **2010**, *48*, 3188–3197. [[CrossRef](#)]
16. Tuia, D.; Volpi, M.; Copa, L.; Kanevski, M.; Munoz-Mari, J. A survey of active learning algorithms for supervised remote sensing image classification. *IEEE J. Sel. Top. Signal Process.* **2011**, *5*, 606–617. [[CrossRef](#)]
17. Inglada, J.; Vincent, A.; Arias, M.; Marais-Sicre, C. Improved Early Crop Type Identification by Joint Use of High Temporal Resolution SAR and Optical Image Time Series. *Remote Sens.* **2016**, *8*, 362. [[CrossRef](#)]
18. Flamary, R.; Fauvel, M.; Mura, M.D.; Valero, S. Analysis of Multitemporal Classification Techniques for Forecasting Image Time Series. *IEEE Geosci. Remote Sens. Lett.* **2015**, *12*, 953–957. [[CrossRef](#)]
19. Ho Tong Minh, D.; Ienco, D.; Gaetano, R.; Lalande, N.; Ndikumana, E.; Osman, F.; Maurel, P. Deep Recurrent Neural Networks for Winter Vegetation Quality Mapping via Multitemporal SAR Sentinel-1. *IEEE Geosci. Remote Sens. Lett.* **2018**, *15*, 464–468. [[CrossRef](#)]
20. Ienco, D.; Gaetano, R.; Dupaquier, C.; Maurel, P. Land Cover Classification via Multitemporal Spatial Data by Deep Recurrent Neural Networks. *IEEE Geosci. Remote Sens. Lett.* **2017**, *14*, 1685–1689. [[CrossRef](#)]
21. Kamilaris, A.; Prenafeta-Boldú, F.X. Deep learning in agriculture: A survey. *Comput. Electron. Agric.* **2018**, *147*, 70–90. [[CrossRef](#)]
22. Hochreiter, S.; Schmidhuber, J. LSTM can Solve Hard Long Time Lag Problems. In Proceedings of the NIPS, Denver, CO, USA, 2–5 December 1996; pp. 473–479.
23. Cho, K.; van Merriënboer, B.; Gülçehre, Ç.; Bahdanau, D.; Bougares, F.; Schwenk, H.; Bengio, Y. Learning Phrase Representations using RNN Encoder-Decoder for Statistical Machine Translation. In Proceedings of the EMNLP, Doha, Qatar, 25–29 October 2014; pp. 1724–1734.
24. Manfron, G.; Delmotte, S.; Busetto, L.; Hossard, L.; Ranghetti, L.; Brivio, P.A.; Boschetti, M. Estimating inter-annual variability in winter wheat sowing dates from satellite time series in Camargue, France. *Int. J. Appl. Earth Observ. Geoinform.* **2017**, *57*, 190–201. [[CrossRef](#)]
25. Prats-Iraola, P.; Scheiber, R.; Marotti, L.; Wollstadt, S.; Reigber, A. TOPS Interferometry With TerraSAR-X. *IEEE Trans. Geosci. Remote Sens.* **2012**, *50*, 3179–3188. [[CrossRef](#)]
26. Quegan, S.; Jiong Jiong, Y. Filtering of multichannel SAR images. *IEEE Trans. Geosci. Remote Sens.* **2001**, *39*, 2373–2379. [[CrossRef](#)]
27. Ho Tong Minh, D.; Ngo, Y.-N.; Baghdadi, N.; Maurel, P. TomoSAR platform: A new Irstea service as demand for SAR, Interferometry, Polarimetry and Tomography. In Proceedings of the 2016 ESA Living Planet Symposium, Prague, Czech Republic, 9–13 May 2016; pp. 1–8.
28. Ho Tong Minh, D.; Ngo, Y.-N. Tomosar platform supports for Sentinel-1 tops persistent scatterers interferometry. In Proceedings of the 2017 IEEE International Geoscience and Remote Sensing Symposium (IGARSS), Fort Worth, TX, USA, 23–28 July 2017; pp. 1680–1683.
29. Khatami, R.; Mountrakis, G.; Stehman, S.V. A meta-analysis of remote sensing research on supervised pixel-based land-cover image classification processes: General guidelines for practitioners and future research. *Remote Sens. Environ.* **2016**, *177*, 89–100. [[CrossRef](#)]
30. Weinberger, K.Q.; Saul, L.K. Distance metric learning for large margin nearest neighbor classification. *J. Mach. Learn. Res.* **2009**, *10*, 207–244.
31. Qian, Y.; Zhou, W.; Yan, J.; Li, W.; Han, L. Comparing machine learning classifiers for object-based land cover classification using very high resolution imagery. *Remote Sens.* **2014**, *7*, 153–168. [[CrossRef](#)]
32. Rodriguez-Galiano, V.F.; Ghimire, B.; Rogan, J.; Chica-Olmo, M.; Rigol-Sanchez, J.P. An assessment of the effectiveness of a random forest classifier for land-cover classification. *ISPRS J. Photogramm. Remote Sens.* **2012**, *67*, 93–104. [[CrossRef](#)]
33. Inglada, J.; Arias, M.; Tardy, B.; Hagolle, O.; Valero, S.; Morin, D.; Dedieu, G.; Sepulcre, G.; Bontemps, S.; Defourny, P.; et al. Assessment of an operational system for crop type map production using high temporal and spatial resolution satellite optical imagery. *Remote Sens.* **2015**, *7*, 12356–12379. [[CrossRef](#)]
34. Belgiu, M.; Drăguț, L. Random forest in remote sensing: A review of applications and future directions. *ISPRS J. Photogramm. Remote Sens.* **2016**, *114*, 24–31. [[CrossRef](#)]
35. Breiman, L. Random forests. *Mach. Learn.* **2001**, *45*, 5–32. [[CrossRef](#)]

36. Abade, N.A.; Júnior, O.A.d.C.; Guimarães, R.F.; de Oliveira, S.N. Comparative analysis of MODIS time-series classification using support vector machines and methods based upon distance and similarity measures in the Brazilian Cerrado-Caatinga boundary. *Remote Sens.* **2015**, *7*, 12160–12191. [\[CrossRef\]](#)
37. Kotsiantis, S.B.; Zaharakis, I.D.; Pintelas, P.E. Machine learning: A review of classification and combining techniques. *Artif. Intell. Rev.* **2006**, *26*, 159–190. [\[CrossRef\]](#)
38. Soma, K.; Mori, R.; Sato, R.; Furumai, N.; Nara, S. Simultaneous Multichannel Signal Transfers via Chaos in a Recurrent Neural Network. *Neural Comput.* **2015**, *27*, 1083–1101. [\[CrossRef\]](#) [\[PubMed\]](#)
39. Linzen, T.; Dupoux, E.; Goldberg, Y. Assessing the Ability of LSTMs to Learn Syntax-Sensitive Dependencies. *TACL* **2016**, *4*, 521–535.
40. Bengio, Y.; Courville, A.C.; Vincent, P. Representation Learning: A Review and New Perspectives. *IEEE TPAMI* **2013**, *35*, 1798–1828. [\[CrossRef\]](#) [\[PubMed\]](#)
41. Graves, A.; Mohamed, A.; Hinton, G.E. Speech recognition with deep recurrent neural networks. In Proceedings of the 2013 IEEE International Conference on Acoustics, Speech and Signal Processing (ICASSP), Vancouver, BC, Canada, 26–31 May 2013; pp. 6645–6649.
42. Pedregosa, F.; Varoquaux, G.; Gramfort, A.; Michel, V.; Thirion, B.; Grisel, O.; Blondel, M.; Prettenhofer, P.; Weiss, R.; Dubourg, V.; et al. Scikit-learn: Machine Learning in Python. *J. Mach. Learn. Res.* **2011**, *12*, 2825–2830.
43. Chang, C.C.; Lin, C.J. LIBSVM: A library for support vector machines. *ACM TIST* **2011**, *2*, 27. [\[CrossRef\]](#)
44. Chollet, F. Keras. Available online: <https://github.com/fchollet/keras> (accessed on 10 May 2015).
45. Dauphin, Y.N.; de Vries, H.; Chung, J.; Bengio, Y. RMSProp and equilibrated adaptive learning rates for non-convex optimization. *arXiv* **2015**, arXiv:1502.04390.
46. Zhang, L.; Du, B. Deep Learning for Remote Sensing Data: A Technical Tutorial on the State of the Art. *IEEE Geosci. Remote Sens. Mag.* **2016**, *4*, 22–40. [\[CrossRef\]](#)
47. Inglada, J.; Vincent, A.; Arias, M.; Tardy, B.; Morin, D.; Rodes, I. Operational High Resolution Land Cover Map Production at the Country Scale Using Satellite Image Time Series. *Remote Sens.* **2017**, *9*, 95. [\[CrossRef\]](#)
48. Kussul, N.; Lavreniuk, M.; Skakun, S.; Shelestov, A. Deep Learning Classification of Land Cover and Crop Types Using Remote Sensing Data. *IEEE Geosci. Remote Sens. Lett.* **2017**, *14*, 778–782. [\[CrossRef\]](#)
49. Tang, Y.; Zhang, Y.Q.; Chawla, N.V.; Krasser, S. SVMs modeling for highly imbalanced classification. *IEEE Trans. Syst. Man Cybern. Part B* **2009**, *39*, 281–288. [\[CrossRef\]](#) [\[PubMed\]](#)
50. Zhao, Z.Q. A novel modular neural network for imbalanced classification problems. *Pattern Recognit. Lett.* **2009**, *30*, 783–788. [\[CrossRef\]](#)





© 2018 by the authors. Licensee MDPI, Basel, Switzerland. This article is an open access article distributed under the terms and conditions of the Creative Commons Attribution (CC BY) license (<http://creativecommons.org/licenses/by/4.0/>).

APPENDIX B

Estimation of Rice Height and Biomass using multi-temporal SAR Sentinel-1 for Camargue,
southern France

Article

Estimation of Rice Height and Biomass Using Multitemporal SAR Sentinel-1 for Camargue, Southern France

Emile Ndikumana ¹, Dinh Ho Tong Minh ^{1,*}, Hai Thu Dang Nguyen ^{1,2}, Nicolas Baghdadi ¹, Dominique Courault ³, Laure Hossard ⁴ and Ibrahim El Moussawi ¹

¹ UMR TETIS, IRSTEA, University of Montpellier, 34093 Montpellier, France; emile.ndikumana@irstea.fr (E.N.); dangnguyenhaithu@gmail.com (H.T.D.N.); nicolas.baghdadi@irstea.fr (N.B.); ibrahim.el-moussawi@irstea.fr (I.E.M.)

² Department of Space and Aeronautics, University of Science and technology of Hanoi, Vietnam Academy of Science and Technology, 122100 Hanoi, Vietnam

³ UMR 1114 EMMAH, INRA, University of Avignon, 84914 Avignon, France; dominique.courault@inra.fr

⁴ UMR 0951 INNOVATION, INRA, University of Montpellier, 34060 Montpellier, France; laure.hossard@inra.fr

* Correspondence: dinh.ho-tong-minh@irstea.fr

Received: 12 July 2018; Accepted: 29 August 2018; Published: 1 September 2018



Abstract: The research and improvement of methods to be used for crop monitoring are currently major challenges, especially for radar images due to their speckle noise nature. The European Space Agency's (ESA) Sentinel-1 constellation provides synthetic aperture radar (SAR) images coverage with a 6-day revisit period at a high spatial resolution of pixel spacing of 20 m. Sentinel-1 data are considerably useful, as they provide valuable information of the vegetation cover. The objective of this work is to study the capabilities of multitemporal radar images for rice height and dry biomass retrievals using Sentinel-1 data. To do this, we train Sentinel-1 data against ground measurements with classical machine learning techniques (Multiple Linear Regression (MLR), Support Vector Regression (SVR) and Random Forest (RF)) to estimate rice height and dry biomass. The study is carried out on a multitemporal Sentinel-1 dataset acquired from May 2017 to September 2017 over the Camargue region, southern France. The ground in-situ measurements were made in the same period to collect rice height and dry biomass over 11 rice fields. The images were processed in order to produce a radar stack in C-band including dual-polarization VV (Vertical receive and Vertical transmit) and VH (Vertical receive and Horizontal transmit) data. We found that non-parametric methods (SVR and RF) had a better performance over the parametric MLR method for rice biophysical parameter retrievals. The accuracy of rice height estimation showed that rice height retrieval was strongly correlated to the in-situ rice height from dual-polarization, in which Random Forest yielded the best performance with correlation coefficient $R^2 = 0.92$ and the root mean square error (RMSE) 16% (7.9 cm). In addition, we demonstrated that the correlation of Sentinel-1 signal to the biomass was also very high in VH polarization with $R^2 = 0.9$ and RMSE = 18% ($162 \text{ g} \cdot \text{m}^{-2}$) (with Random Forest method). Such results indicate that the highly qualified Sentinel-1 radar data could be well exploited for rice biomass and height retrieval and they could be used for operational tasks.

Keywords: rice dry biomass; rice height; Multiple Linear Regression; Support Vector Regression; Random Forest; Sentinel-1, TomoSAR platform; Camargue; southern France

1. Introduction

Rice is one of the most important cereal grains and serves as a staple food resource for more than half of the world's population. For this reason, rice consumption increases dramatically together with population raising, and the demand for rice is predicted to be strong [1,2]. International Food Policy Research Institute analyses show that the demand for rice is increasing by about 1.8% per year. It will be difficult to increase rice production to satisfy this demand because land and water resources become more scarce with increasing competition from fast-growing non-farming sectors [3]. Especially, rice crop is a heat and water-loving crop [4], then, sometimes the rice badly suffers from cold stress during the seedling stage when it is grown in winter environment [5]. Therefore, monitoring the global productivity of rice is one of the adequate solutions to meet the demand for rice.

Rice parameters (height, dry biomass, leaf area index, salinity, etc.) are primarily monitored through two approaches, including field measurements by farmers and model retrievals from remote sensing data. While the field measurement is time-consuming, remote sensing is able to perform rice parameters measurement on a large scale without directly contacting the crop [6]. Spatial remote sensing provides the opportunity to have information on a regional scale with high spatial and temporal resolution. Data acquired from satellites provides a great tool for tracking temporal changes in soil and crop conditions, mapping their characteristics over large areas. There are two kinds of remote sensing techniques: one uses optical sensors and the other uses synthetic aperture radar data (SAR) sensors. In addition, the fusion of optical and SAR data can be exploited as well [7,8]. Optical sensors (e.g., UAV, multispectral, and hyperspectral data) are suited for monitoring agricultural areas [9–11]. For example, the joint analysis of time series of vegetation and water indices derived from these sensors, such as Normalized Difference Vegetation Index (NDVI), Enhanced Vegetation Index (EVI), and Normalized Difference Water Index (NDWI), can be used to estimate rice parameters [9,12]. However, a large cloud coverage can limit the use of optical sensors [13].

Unlike passive optical sensors, SAR systems are capable of producing high-quality images of the earth even in cloud cover conditions. Most rice fields are always found in cloudy cover conditions, and SAR sensors can work in these conditions, so it is more effective for monitoring rice fields than optical sensors [14]. Furthermore, for agriculture, SAR data can provide information on activities such as plowing, field preparation, planting, and the state of growth of the crops from germination to maturity stages. Recent studies have shown the high potentialities of using such data for crop monitoring [15,16]. Thus, the application of SAR data in agriculture is becoming more popular. In previous studies, many investigations have been carried out on monitoring of rice growing. Various of them are based on rice parameters estimation [17–19], the others are focused on the used water within the rice fields [20], and some of them are on soil penology and organic matters [21]. Besides several SAR data which were used to map and monitor rice such as RADARSAT-1/2 [22], ENVISAT ASAR [23], ERS-1/2 [24], Sentinel-1 data is one of them. The Sentinel-1 mission is based on a constellation of two satellites (A and B). Sentinel-1 as a C-band SAR imaging satellite constellation ensures the continuity of ERS and ENVISAT missions [25,26]. Sentinel-1 data are systematically acquired in terrain observation with progressive scan (TOPS) mode with a 6-day revisit period (We note that outside the European zones, it drops to 12 days.). Dense time series of open access Sentinel-1 data at high spatial resolution (20 m) offers new opportunities for monitoring agriculture [27]. In addition, Torres et al., [26] reported that C-band SAR data were particularly well suited for monitoring and mapping rice because of their abilities to acquire information on rice growing areas with frequent cloud cover and a remarkable increase in backscattering coefficients throughout the rice growth cycle. Ferrazzoli et al., [28] also showed that the sensitivity of C-band sensors to plant biomass depends on the type of crop.

In Camargue, the rice crop plays a crucial role for the hydrological balance [29]. This region is one of the main rice producers and suppliers in France [30]. Therefore, understanding and analyzing rice growth of Camargue is significant for agriculture in France. The aim of the paper is to analyze the capability of SAR Sentinel-1 data to assess the rice parameters in Camargue. Rice crop height is an important agronomic feature linked to plant type and yield potential. The rice plant height estimation,

particularly, is considered a simple method for determining rice growth because this parameter greatly influences the yield potential. Rice biomass is regarded as an important indicator of ecological and management processes in the vegetation.

In the literature of remote sensing, various machine learning algorithms are available for regression [31–34]. In practice, the algorithms are selected based on the trade-off between the performances in terms of estimation of a given biophysical parameter, computation time and interpretability of the results [35]. Most of remote sensing works are based on classical algorithms, such as Multiple Linear Regression (MLR), Support Vector Regression (SVR) and Random Forest (RF) [36,37]. Although they have been introduced since the early 2000s, they still compete with other approaches in many applications. In this paper, classical machine learning methods (Multiple Linear Regression, Support Vector Regression and Random Forest) are applied in order to estimate rice height and dry biomass in the Camargue region.

This paper includes six sections. In Section 2, characteristics of the study site, weather, cultivation of Camargue area and the information of ground truth measurement are described. Section 3 presents the principle of three methods used to estimate rice parameters (Multiple Linear Regression, Support Vector Regression and Random Forest). The results are shown in Section 4. The discussions are presented in Section 5 and finally, the Section 6 involves the main conclusions of this paper.

2. Study Area

2.1. Camargue Study Site

Camargue is located in southern France; centered coordination is approximately at 43°32'N latitude and 4°30'E longitude. Among 110,000 ha of total area, 54,000 ha are used for agriculture and the rest is protected for nature conservation [30]. Placed between two branches of the Rhône and the Mediterranean Sea, Camargue region is a low-land containing alluvial deposits of the Rhone and the Mediterranean Sea. That is mainly characterized by the absence of important relief in which we distinguish two areas [38]. Starting from the north to south of Camargue, there are plots behind the Rhône river and from the south along the sea, there are much saltwater regions.

Agriculture is the main economic sector of the Camargue region although the semi-arid Mediterranean climate is disadvantageous for rice cultivation because Mediterranean climate is rainy in winter and dry in summer, then it is not easy for planting paddy rice in summer. Temperature and precipitation are important factors that affect directly crops cultivation, especially rice crops. The annual average temperature of this region is about 7 °C (January) to 26 °C (July). Besides that, precipitation also varies greatly during a year with less than 10 mm in July and 160 mm in September (due to short periods of heavy rain). Based on those features, in Camargue, there is one rice crop activity per year from May to September when the temperature and precipitation are the highest. Flooded rice cultivation allows the water needed for soil desalination and to introduce other crops such as wheat, sunflower, and fodder to be rotated. In the Camargue region, the rice crop has an important impact on the ecological, economic, and social equilibrium [29,39].

2.2. Rice Phenomena

The temporal observation of rice growth is important for understanding the radar responses of rice plots at different stages of growth. Camargue has a single cropping season of rice; the agricultural calendar is shown in Table 1.

Table 1. Agricultural calendar and rice cycle in Camargue [40].

Nature of Work and Vegetative Cycle	Executive Date
Stubble	October to November
Land preparation	March to April
Use of fertilizers and herbicides	Middle April
Watering and seeding	25 April to 16 May
Lifting and sodding	May to June
Post-emergence herbicide	June to July
Earing-flowering	July to August
Maturation, harvest	15–20 September to October

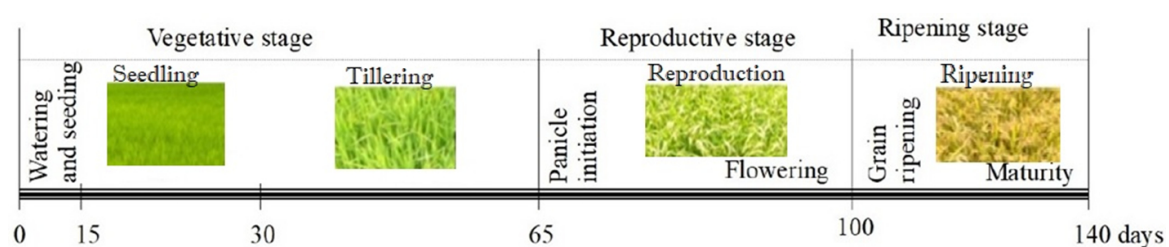
The rice crop in Camargue is an intensive type irrigated with direct seeding. Temperature and light are key factors in crop growth:

- For levee, a minimum temperature of 12 °C;
- For flowering, a minimum temperature of 20 °C.

There are three major periods of rice cultivation: the sowing period (starting according to the weather conditions from the end of April to middle May), the growth period (up to September) and the harvest period (end of September to the beginning of October).

In Camargue, the sowing date is from 24 April to 16 May, followed by a germination stage from May to June. At the germination stage, water is not evacuated. If the surface is bumpy, two risks are present: (1) either the water height is too high and the seedling dies; (2) the land is bare and the seedling germinates badly. Constant monitoring of water levels, which have a significant role as thermal regulators, should be carried out. Continuous water movement compensates the variations of air temperature. A high water depth protects the seedling in case of cooling. However, it is necessary to rapidly lower the level as soon as the ambient conditions become again favorable.

The growing period begins from the successful germination to the flowering/maturation stage. Figure 1 shows clearly the development of rice plants in Camargue.

**Figure 1.** Rice crop growth calendar in Camargue.

Three essential factors play a role in the success of seedling emergence: water temperature, with an average above 15 °C with the nocturnal minimum around 10 °C; the constancy of the insulation; the fight against parasites: larvae or algae. After the emergence, the rice plot is dried up to 10 or 12 times. Drying can last a day or sometimes half a day. Temporary drying inhibits the development of parasites and activates the rice rooting. Between 25 July and 25 August comes the flowering period. The height of crops does not increase much at this stage. Flowering period requires a warm climate, without wind, without rain. After flowering comes the ripening period where the farmers begin to evaluate their future harvest at the end of August. The harvest stage occurs from the end of September to the beginning of October, all ripening rice crops are reaped. At the end of the harvest, two options are possible. For the first option, rice farmers normally have a long period enough to prepare their rice plots. In irrigated rice farming, as is the case in the Camargue, special attention is paid to leveling, using a laser-guided blade. The use of this equipment aims to obtain perfectly

flat plots, in order to manage water precisely. This method is also used after harvest period between seasons for maintenance of irrigation canals (“waterways”). In Spring, once the last surface preparation is carried out to obtain a suitable seedbed, ditches are dug in the plots to facilitate their filling and emptying during cultivation, and then watering is done; we have a continuous cultural cycle. For the second option, farmers work very quickly to sow as early as autumn, usually with wheat which is the second crop in rice farms in Camargue.

2.3. Ground Data Measurement

Ground truth measurements of rice parameters (rice height and rice biomass) were collected in eleven reference plots (Figure 2) which were about 2 to 6 hectares. A plot survey was carried out from May 2017 to September 2017 on the 11 rice reference plots selected to cover the variability encountered in both soils and agricultural practices. The reference plots were chosen in such a way that they could be represented the paddy rice fields in Camargue and they should not be adjacent parcels. The ground surveys were conducted based on the Sentinel-1 data acquisitions to measure rice height and biomass through the full growth rice cycle. In that respect, the following measurements were made every 12 days: 2 locations per plot for biomass assessment (1 m² for each location), 30 points per plot for crop height measurements. Figure 2 shows the position of ground surveys. The rice height has been taken on all the 11 plots. In contrast, rice biomass had been only taken on 1G1, 1G3, 2M1, 2M2, 3M1. The number of plots used to cut the biomass is reduced to five; we could not cut the biomass on all the plots otherwise it would be a waste and it would have had an impact on the production. The biomass was dried to have the dry biomass that is used in our analyses.

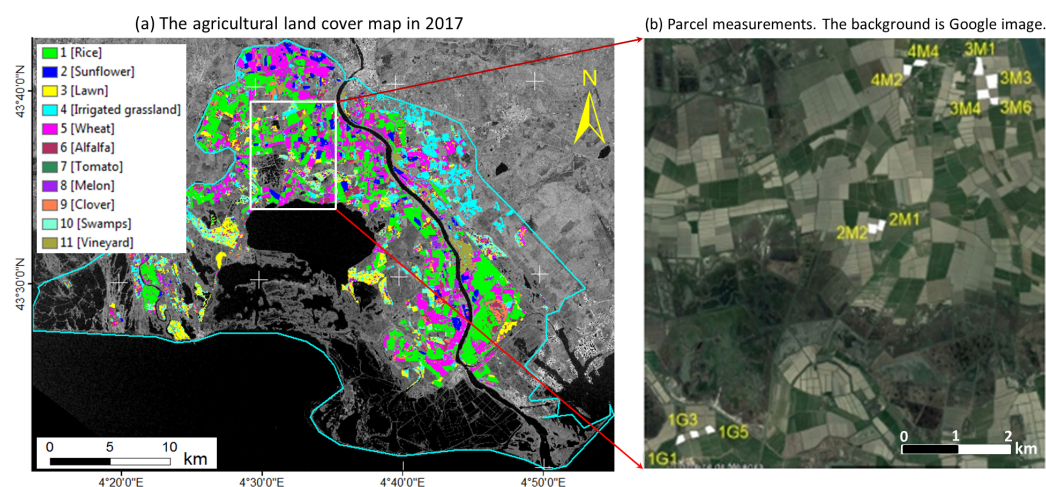


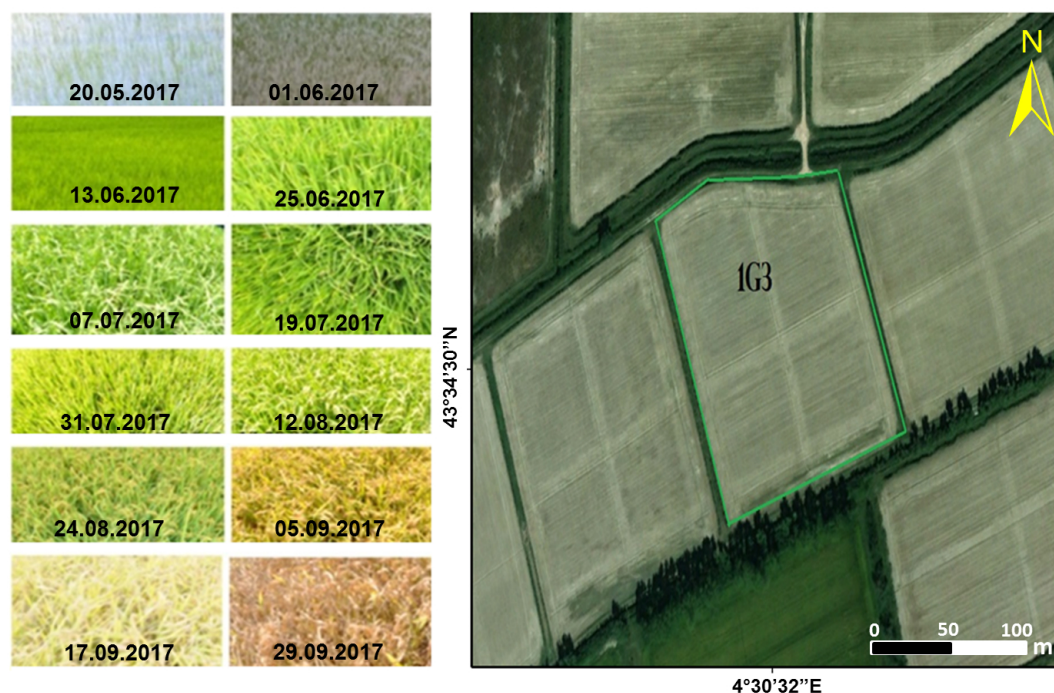
Figure 2. Camargue study area. (a) The agricultural land cover map in 2017 [30]. The green color indicates the rice extent of the Camargue region. (b) The zoom version of the white polygons represents the location of reference plots where measurements were made at every 12 days from May to September 2017.

In addition, information such as the label, surface (in hectare), the sowing date, rice variety and harvest date are known for each plot and represented in Table 2.

Table 2. Description of reference plots in Camargue.

Plot Identity	Area (ha)	Sowing Date	Rice Variety	Harvest Date (DoY)
1G1	2.4	10 May 2017	Ronaldo	09 October 2017 (282)
1G3	2.14	10 May 2017	Ronaldo	09 October 2017 (282)
1G5	2.03	10 May 2017	Ronaldo	09 October 2017 (282)
2M1	3.5	12 May 2017	Eurosis	29 September 2017 (272)
2M2	3	12 May 2017	Eurosis	29 September 2017 (272)
3M1	6	15 May 2017	Ronaldo	11 October 2017 (284)
3M3	5	15 May 2017	Opale	11 October 2017 (284)
3M4	4	15 May 2017	Ronaldo	14 October 2017 (287)
3M6	2.5	15 May 2017	Ronaldo	14 October 2017 (287)
4M2	3.5	15 May 2017	Brio	10 October 2017 (283)
4M4	3.5	15 May 2017	Brio	09 October 2017 (282)

Regarding the parameters displayed in Table 2, the sowing date is not the same for all plots and the harvest date also is not at the same time. The variability observed is due to the local conditions at the time of sowing and also is due to the rice variety. The harvest period takes place between 29 September (DoY 272) and 14 October (DoY 287). After harvesting, the rice in Camargue is dried and preserved in the geographical area at a humidity level allowing its (good) conservation in silos whose temperature conditions are controlled. The ground measurements of rice height and rice biomass were collected at the same time with SAR Sentinel-1 images acquisition over reference plots. The Figure 3 shows one of eleven plots with its pictures that were taken during the ground survey.

**Figure 3.** The reference plot 1G3 is marked in the figure (coordinates of central point 43°34'30''N, 4°30'32''E) together with its photos at different dates.

In summary, for rice height in-situ data, there are 132 measurements, whereas, for rice biomass, we only have 50 measurements.

2.4. SAR Data

The Sentinel-1 SAR data includes 25 TOPS mode acquisitions from May 2017 to September 2017, with 6 revisit days. This is dual-polarization (VV and VH) data, leading to 50 images in total. First of all, a reference image was selected and all images are coregistered to it by taking into account the TOPS acquisition [41]. Five-look (in range) intensity radar data are generated and radiometrically calibrated for antenna gain, range spreading loss, normalized reference area and the calibration constant using information from Sentinel-1 SAR header.

Reliable estimates using backscattering coefficients require that the estimated number of looks (ENL) is large. To increase the ENL, speckle filtering can be used with loss of spatial resolution. In this paper, we improve the time series SAR Sentinel-1 dataset by exploiting a temporal adaptive filtering to reduce speckle while keeping as much as possible the fine structures present in radar images [42].

Finally, all images are orthorectified into map coordinates. This can be done by simulating SAR image from the SRTM DEM 30 m and using it to do coregistration. The image pixel size of the final data is 20 m. The Sentinel-1 SAR data are processed by using the TomoSAR platform (i.e., a platform supports the entire processing from SAR, Interferometry, Polarimetry, to Tomography (so-called TomoSAR)) developed by Dinh Ho Tong Minh and Yen-Nhi Ngo [43]. In details, the full description of this SAR dataset can be found in [30].

3. Method

3.1. Multiple Linear Regressions

Multiple Linear regression (MLR) is one form of Linear Regression which is used to describe the variations of a dependent variable (which varies under the influence of other system parameters) associated with the variations of several independent variables (which varies without being influenced by the other system parameters) [31]. The truth data in use include in-situ measurements of rice height, rice biomass, Day after Sowing (DaS—which is counted from the first day when farmers sow in their plots), backscattering coefficients VV and VH polarizations. The purpose is that using the ground measurements to predict rice height and biomass values based on DaS with single polarization (VV or VH) and dual-polarization (VH and VV). Therefore, the application of MLR equation to estimate rice height and rice biomass in each polarization is different. For example, the equation below was used in case of dual-polarization:

$$biomass = x_0 + x_1\sigma_{VH} + x_2\sigma_{VV} + x_3DaS \quad (1)$$

where σ_{VH} and σ_{VV} are the backscattering coefficients in the decibel unit, in VH and VV polarization, respectively; DaS stands for Day after Sowing. To estimate rice height, we substitute rice biomass by rice height in Equation (1). In VV polarization model, we just exclude the term σ_{VH} in Equation (1). Similarly, in VH polarization model, we just exclude the term σ_{VV} in Equation (1). We use the same input parameters for SVR and RF methods.

3.2. Support Vector Regressions

The Support Vector Machine Regression (SVR) is a non-parametric technique and non-linear regression method. This method is considered a non-parametric technique because it relies on kernel functions. SVR algorithms use kernel functions which take data as input and transform it into the required form [44]. The basic idea is to transform the input data into a higher dimensional feature space, where the problem can be solved in a linearized manner [35]. In the end, training the SVR involves solving a quadratic optimization problem. There are several kernels: linear, polynomial, sinusoidal and radial basis function (RBF) kernels. Although linear kernels can be computationally efficient, nonlinear kernels (e.g., RBF) have a better performance over linear kernels [34]. For RBF kernels, two parameters need to be tuned: (i) the sigma parameter (i.e., the width of the kernel function), and (ii) the complexity C parameter to control the trade-off between the maximization of the margin between the training

error decision limit and the training data vectors. Both parameters are optimized in the estimation process to improve performance.

3.3. Random Forest

As SVR, the Random Forest (RF) method is also a non-parametric method used in vegetation parameters estimation. Random forest is an ensemble learning technique developed by Breiman [33] to improve the classification and regression trees method by combining a large set of decision trees [10]. The classical method of regression is based on the division of the data set according to their homogeneity. A decision tree is from top to bottom on a root node and consists of sharing the data into subsets that contain instances with similar values. In addition, each node of every tree is split based on another random subset of parameters. This randomization provides a certain level of robustness to outliers and overfitting [33]. The result is usually aggregated by taking the average of the predictions from all trees. RF relies on the number of trees and the number of parameters to be used at each node split [37]. To improve performance, both parameters need to be optimized in the estimation process.

3.4. Model Assessment

For the performance analysis of three methods (MLR, SVR, RF), we apply a five-cross-validation method ($KFolds = 5$). In order to verify the effectiveness of three methods applied in Sentinel-1 data (VH, VV, VH and VV polarizations), the retrieved rice height and biomass are compared with ground truth measurements. The model assessments are validated through correlation coefficient (R^2) and Root Mean Square Error (RMSE):

$$RMSE = \sqrt{\frac{1}{n} \sum_{i=1}^n (Y_i - X_i)^2} \quad (2)$$

$$R^2 = \frac{\sum_{i=1}^n [(Y_i - \bar{Y})(X_i - \bar{X})]}{\sqrt{\sum_{i=1}^n (Y_i - \bar{Y})^2} \times \sqrt{\sum_{i=1}^n (X_i - \bar{X})^2}} \quad (3)$$

where Y_i and \bar{Y} are the estimated variables and their mean values, X_i and \bar{X} are the ground truth measurement variables and their mean, n is the number of data. A good retrieval result contains a low RMSE value and a high correlation coefficient.

To select the best model among different machine learning methods, we also use Akaike's Information Criterion (AIC) and Bayesian Information Criterion (BIC) [45].

4. Results

4.1. Experimental Settings

We evaluated rice parameters using Sentinel-1 data with standard machine learning approaches. The aim of these approaches is to use the ground measurements to train models (based on DaS with single polarization (VV or VH) and dual-polarization (VH and VV)) to predict rice height and biomass values. We note that using both VV and VH polarizations we are able to estimate DaS with the RMSE less than 3 days. There is any ways to combine VV and VH polarizations (e.g., VV+VH, VV-VH, VV/VH, etc). However, to avoid many model considerations and also to verify the helpfulness of combination VV and VH, we do a Principal Component Analysis (PCA) [46] to construct a new predictor that combines VH and VV. We keep the first and the second PCA components to run through MLR, SVR, RF methods.

For the MLR model, it does not require to chose the optimal parameters since they can be estimated directly. In contrast, for both RF and SVR models, to improve performance, it is important to tune the parameters which are optimized in the estimation process. In this paper, the parameters are defined by a grid search to get the best performance [37]. For both RF and SVR models, we found

that the parameters were quite similar in both single and dual polarizations. For the SVR model, we use the RBF kernel with the complexity parameter of 50 and the gamma of 0.9 for rice biomass, whereas, for rice height, they equal to 0.7 and 60, respectively. For the RF model, we set the number of parameters to be used at each node split at 7 and the number of trees at 80 for both rice biomass and height estimations. For all three methods, we use the *Matlab* implementation provided by the Regression Learner.

4.2. Ground Measured Results

From all recorded measurements of rice height and biomass, the mean value of each plot was provided. Figure 4a presents the temporal variance of rice height versus the acquisition dates of Sentinel-1 data for all plots.

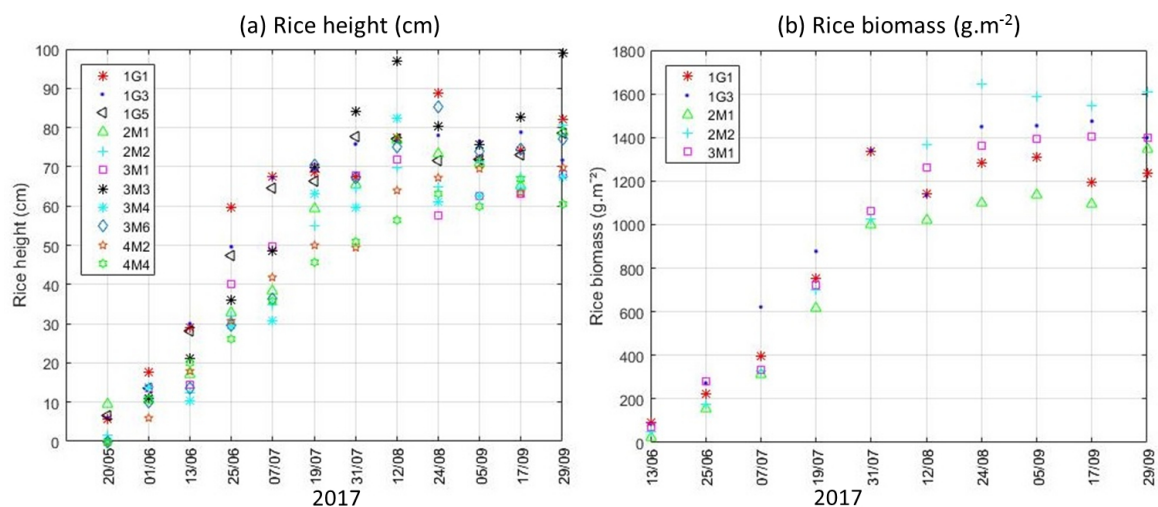


Figure 4. Temporal variation of the rice height and biomass versus to acquisition dates of Sentinel-1 data.

During the vegetative period (from May to July), rice height increases rapidly, and then small variation is observed during the reproductive phase (from July to September), while it stays constant in the ripening period. Rice height measurements show a high variability due to a quick growth of rice during the first three months (Figure 4a). The same observation is found for rice biomass, before the ripening period, it increases rapidly and during this stage, the biomass is stabilized (Figure 4b). The same trend was observed in [14,24,47].

4.3. Backscattering Coefficients According to Rice Parameters

Figure 5a shows the behavior of VV and VH backscattering coefficients during the entire rice growth. As expected, it can be observed that the VV backscatter values are higher than the VV polarization. In the vegetative stage (16 days to 65 days after sowing), the dynamic range of VV and VH backscatters is very high (about 7 dB). In the reproductive stage (65 days to 100 days), the VH backscatter tends to saturate, whereas the VV goes down. In the last ripening stage (after 100 days), both VH and VV backscatters tend to slightly decrease.

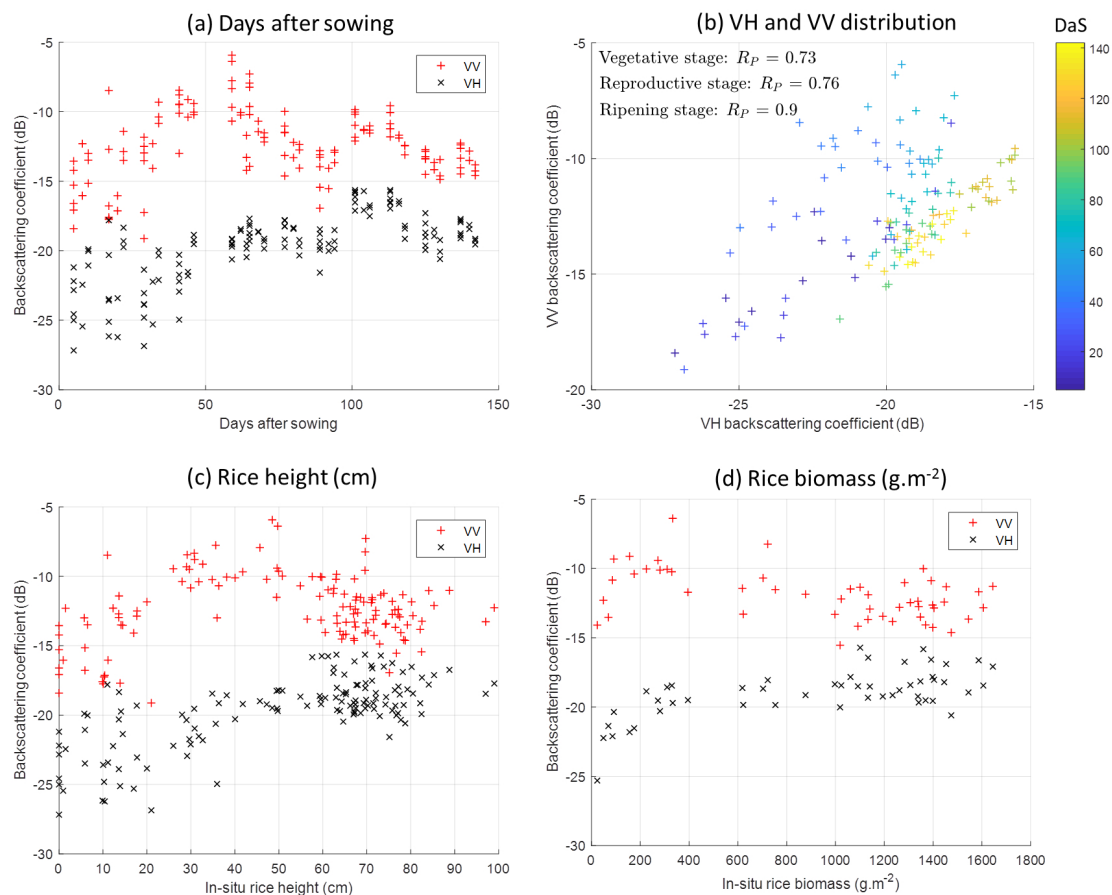


Figure 5. Sentinel-1 backscattering coefficients according to (a) Days after sowing; (b) VV and VH distribution; (c) Rice height; (d) Rice biomass.

Figure 5b shows a scatter plot on VV and VH backscattering coefficients distribution together with their Pearson correlation coefficient R_P according to vegetative, reproductive and ripening stages. Although they are highly correlated at each stage, if we put all together in a full cycle, the Pearson correlation is decreased to 0.52.

In Figure 5c,d, the behavior of VV and VH backscattering coefficients is similar with respect to both rice height and biomass. Both VH and VV backscatters increase strongly in the vegetative stage. On the other hand, in reproductive and ripening stages, while VH backscatter still slightly grows, the VV visibly decreases.

4.4. Rice Height Estimation

The relevance of three methods MLR, SVR and RF applied in Sentinel-1 data with (VH, VV, both VH and VV polarizations) was analyzed using RMSE and R^2 values. Tables 3 and 4 report the regression results of rice height estimation with the three methods MLR, SVR, and RF.

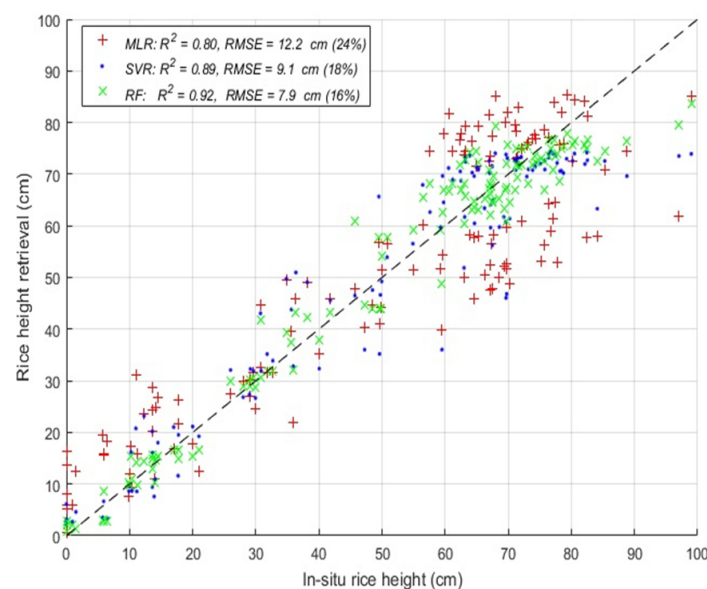
Table 3. Rice height estimation using MLR, SVR and RF methods with 5 folds cross-validation. Best results are in bold.

	VV		VH		VH and VV		PCA (VH and VV)	
Methods	R^2	RMSE (cm)	R^2	RMSE (cm)	R^2	RMSE (cm)	R^2	RMSE (cm)
MLR	0.79	12.5	0.79	12.3	0.80	12.2	0.79	12.4
SVR	0.87	10.3	0.88	10.2	0.89	9.1	0.89	9.2
RF	0.90	8.4	0.88	8.9	0.92	7.9	0.91	8.2

Table 4. AIC and BIC for rice height estimation. The smallest values are in bold.

Methods	AIC				BIC			
	VV	VH	VV and VH	PCA (VH and VV)	VV	VH	VV and VH	PCA (VH and VV)
MLR	295.6	293.7	294.8	296.7	295.9	294.1	295.3	297.1
SVR	273.4	272.3	261.2	262.4	273.8	272.6	261.7	262.9
RF	250.0	256.6	245.0	249.2	250.4	257.0	245.5	249.7

The method used to estimate parameters is supposed to be efficient when its RMSE, AIC and BIC values are as small as possible. The RF method is better than the other methods: $R^2 = 0.92$, RMSE = 16% (7.9 cm) (with the dual-polarization VV and VH model). For PCA (VV and VH) models, as comparison with the dual-polarization VV and VH cases, they are quite similar. In other words, VV and VH give complementary information in the estimations. Figure 6 shows the results of estimating the rice height by plotting the best configuration for each method.

**Figure 6.** Rice height estimation using MLR, SVR and RF methods. In this figure, the configurations that provide the best results are considered (with dual-polarization VV and VH model).

As shown in Figure 6, the correlations (R^2) obtained by using MLR, SVR and RF are 0.8, 0.89, 0.92 respectively. MLR gives the biggest value of RMSE (12.2 cm—24%), followed by SVR with RMSE = 9.1 cm (18%) and RF with the minimum RMSE = 7.9 cm (16%).

Next, in Figure 7, the rice height retrieval respect to in-situ data during the cultured period is shown for example on two plots: 2M2 and 4M2. The continuous line presents the estimated height of rice, while the following small circles show the in-situ rice height measurements. Visibly, the correlation between the retrieved and in-situ rice height of the two parcels is good. The rice height retrieval and the in-situ rice height are increasing and close together as the result of rice growth.

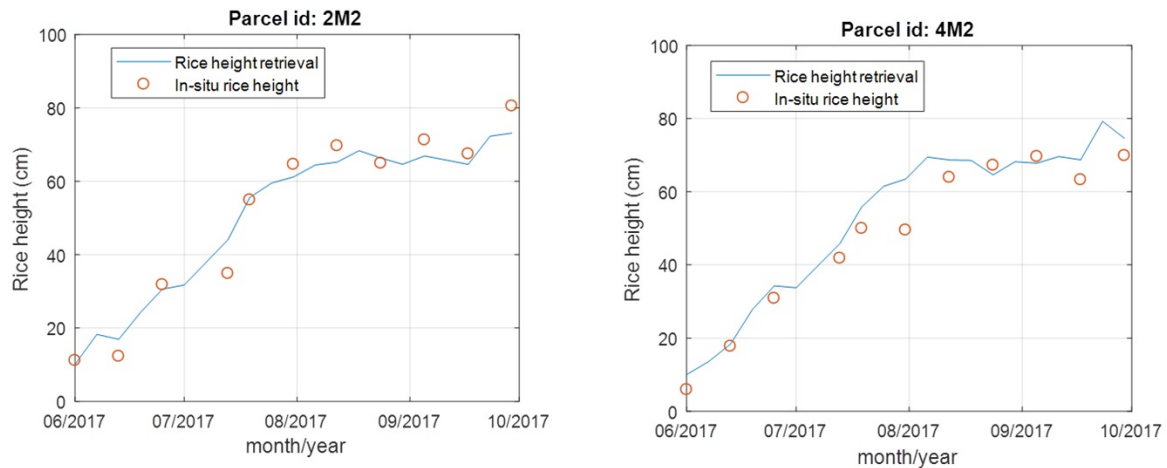


Figure 7. Rice height retrieval and in-situ measurements at two reference plots 2M2 and 4M2.

4.5. Rice Biomass Estimation

Tables 5 and 6 show all the results of rice biomass inversion performance of MLR, SVR, and RF. The best performance is obtained by the MLR method using dual-polarization VV and VH model: $R^2 = 0.85$, $RMSE = 206 \text{ g} \cdot \text{m}^{-2}$ (22%). For SVR and RF methods, the best performance is obtained by using the VH polarization model: $R^2 = 0.87$, $RMSE = 175 \text{ g} \cdot \text{m}^{-2}$ (19%) for the SVR method: $R^2 = 0.9$, $RMSE = 162 \text{ g} \cdot \text{m}^{-2}$ (18%) for the RF method, respectively.

Table 5. Rice biomass estimation from five folds of cross-validation. The best results are in bold.

	VV		VH		VH and VV		PCA (VH and VV)	
Methods	R^2	RMSE ($\text{g} \cdot \text{m}^{-2}$)	R^2	RMSE ($\text{g} \cdot \text{m}^{-2}$)	R^2	RMSE ($\text{g} \cdot \text{m}^{-2}$)	R^2	RMSE ($\text{g} \cdot \text{m}^{-2}$)
MLR	0.81	230	0.81	216	0.85	206	0.83	213
SVR	0.86	178	0.87	175	0.86	207	0.86	193
RF	0.90	167	0.90	162	0.88	177	0.89	174

Table 6. AIC and BIC for rice biomass estimation. The smallest values are in bold.

	AIC				BIC			
Methods	VV	VH	VV and VH	PCA (VH and VV)	VV	VH	VV and VH	PCA (VH and VV)
MLR	242.2	239.4	239.4	240.8	241.3	238.5	238.2	239.6
SVR	231.0	230.3	241.6	236.6	230.1	229.4	240.4	235.4
RF	228.3	227.0	232.8	232.1	227.4	226.0	231.6	230.9

Figure 8 presents the effectiveness of three methods to estimate rice biomass. The correlation coefficients R^2 are 0.85, 0.87, 0.90 for MLR, SVR and RF methods, respectively. In addition, the RMSE values are $206 \text{ g} \cdot \text{m}^{-2}$ (22%), $175 \text{ g} \cdot \text{m}^{-2}$ (19%), and $162 \text{ g} \cdot \text{m}^{-2}$ (18%), respectively.

As seen in Figure 9, for example, at two reference plots 1G3 and 3M1, the scatter plots between retrieved and in-situ rice biomass indicate the same behavior along the growth stage with continuous line for rice biomass retrieval and circles for in-situ rice biomass.

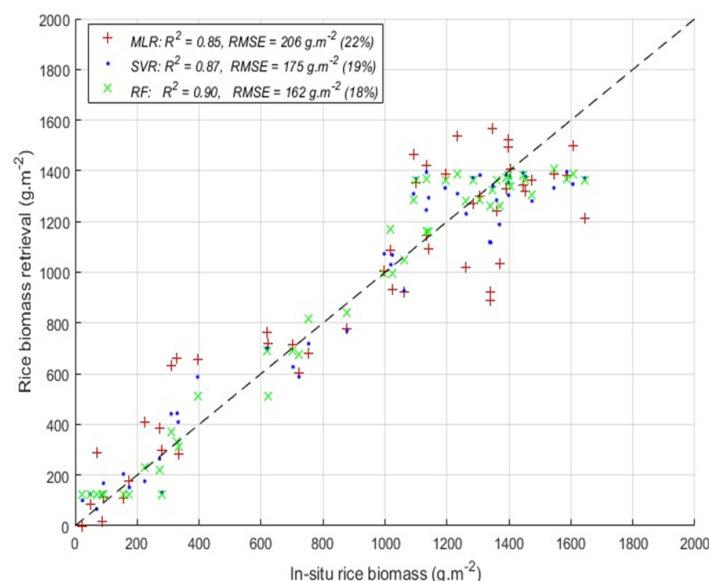


Figure 8. Rice biomass estimation using MLR, SVR and RF methods. In this figure, only the configurations that provide the best results are considered (with dual-polarization VV and VH model for MLR, and with VH model for SVR and RF).

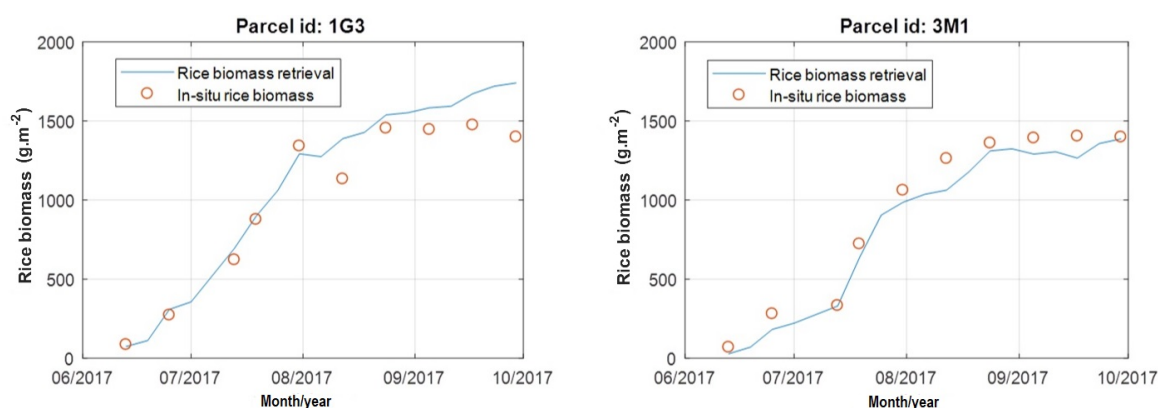


Figure 9. Rice biomass retrieval and in-situ measurements at two reference plots 1G3 and 3M1.

5. Discussion

In this paper, we show that the Sentinel-1 can be used to estimate rice height and biomass in Camargue with a high accuracy. The dynamics in rice height and biomass can be observed by the backscatter behaviors in each of the two polarizations (VV and VH). Good results can be obtained by using classical approaches (MLR, SVR, and RF). The validated metric indicates good performance, in which the correlation coefficient R^2 was greater than 0.8. We show that there is a better performance using non-parametric methods (SVR and RF) over the parametric MLR method. Thus, these demonstrated results confirm the great potential of Sentinel-1 data for rice height and biomass retrievals.

First of all, even with the traditional approaches, we show that good retrieved performance could be yielded with Sentinel-1 SAR data. This is not straightforward due to the speckle noise nature in radar images. Good performance can be explained by the fact that 6 days time series Sentinel-1 SAR data allows not only a good follow-up of the rice growth but also mostly noise-free dataset, thanks to the speckle adaptive filtering. In addition, for rice biophysical parameter estimations, the Day after Sowing information, which can be retrieved directly from Sentinel-1 data within the accuracy of 3 days (our estimation), allows us to mitigate the potential problem on the radar signal

saturation. This situation is different from forest applications, where the forest age is challenged to retrieval. For example, for forest biomass estimations, many works have to use prior knowledge (e.g., Landsat-derived tree cover [48]) or advanced techniques (e.g., SAR tomography [49,50]) to mitigate the radar signal saturated problem. Finally, we note that outside the European zones, there is a limitation for Sentinel-1 data since the revisit period will be 12 days. However, it should be emphasized that, nowadays, the Sentinel-1 constellation is the only system which can provide free and global coverage radar data. Therefore, it is a good candidate for operational rice monitoring tasks.

Using in-situ measurements at Camargue, we show that radar backscattering coefficients are sensitive to rice biophysical parameters and have a strong correlation with rice height and biomass. This observation is consistent with reports from the literature [14,51] due to the sensitivity of radar signals to rice structures. The backscatter of VH and VV polarizations can be separated into two main parts. In the first part, the VV and VH increase with the rice growth until 50 cm height (See Figure 5c). At this stage, the main backscattering mechanism is contributed by the interaction between the stem and the underlying water surface (e.g., double bounce). In the second part (where rice grows from 50 cm to 100 cm (maturity)), although the VV goes down, the VH is still slightly increased. Indeed, at this stage, the backscattering mechanisms are contributed not only by the double bounce interaction but also from the volume stem directly. Beyond 50 cm, the double bounce phenomenon can be reduced, and the stem and leaves of the rice are not remained vertical. While they lead to the power decrease of the VV backscatter, the VH signal is increased due to its sensitivity to random volume backscattering. Similar interactions were also reported by Lopez-Sanchez et al. [52]. The same trend of backscattering coefficients versus rice biomass is observed. When rice biomass reaches around $800 \text{ g}\cdot\text{m}^{-2}$ (See Figure 5d), this is the period when the rice stem is no longer vertical and the leaves have already deviated from the stem. Interestingly, it is worth pointing out that there is a jump in both VV and VH backscatter at 100 DaS days (See figure 5a). This is mainly because there is a rapid transition from always irrigated rice fields at the reproductive stage to no longer irrigated status at the ripening stage.

We can observe that non-parametric methods (SVR and RF) have better performance over the parametric MLR method for estimating rice parameters (See Tables 3 and 5). Between the SVR and RF models, the RF method obtains slightly better results than the SVR. With the RF method, the correlation coefficient R^2 and RMSE were 0.92 and 16% for rice height, 0.90 and 18% for rice dry biomass. For rice height, all methods (MLR, SVR, and RF) yield the best performances with the dual-polarization VV and VH model. For rice biomass, we observe that the combination of VH and VV polarizations does not bring to the good result as a single VH polarization in SVR and RF methods. This can be explained by the fact that the VH backscattering is mainly from the depolarizing part represents a small proportion of biomass, but it is highly correlated with the total biomass [48]. The RMSE was 16% (7.9 cm) for rice height, which is better than the result (13.3 cm) reported in the recent literature [53]. For rice biomass, the RMSE was 18% ($162 \text{ g}\cdot\text{m}^{-2}$), which is better than the recent results (RMSE = $170.49 \text{ g}\cdot\text{m}^{-2}$) reported by Jing et al. [54], who used an Artificial Neural Network (ANN) inversion method on the C-band RADARSAT data. Last but not least, our rice biomass estimation ($162 \text{ g}\cdot\text{m}^{-2}$) is much better than the performance ($200 \text{ g}\cdot\text{m}^{-2}$) from L-band ALOS/PALSAR data [55].

In parallel with machine learning algorithms, there is also another approach to estimate rice parameters. This is physical model-based inversion (such as Karam Model [56], Water Cloud Model [57], etc.). However, physical models are complicated and related to certain rice growth models, which require a wide area for the experiment station to measure model parameters. These limitations of physical model-based inversion methods make sense to work on machine learning methods [36,37]. We demonstrated in this paper that the non-parametric methods (SVR and RF) had a good performance in estimating the rice biophysical parameters.

Finally, among agricultural practices in the Camargue region, the rice crop plays a crucial role in the cropping systems. This is mainly because the rice irrigation allows the leaching of salt and consequently leads to the introduction of other species (e.g., wheat, sunflower, etc) into the rotation

of crops [39]. However, the rice areas tend to decrease from 16,000 ha in 2011 ([29]) to 10,627 ha ([30]) in 2017. The downward trend of the rice extent can lead to a negative impact on the sustainable agricultural development. Future studies should be considered the remote sensing assimilation, such as Sentinel-1 radar for rice height and biomass as our demonstration, in crop models to better follow farming practices, estimate rice production and provide strategies for the sustainable agricultural development.

6. Conclusions

In this work, we studied the potential of Sentinel-1 remote sensing data for rice height and dry biomass estimations. We proposed to use three classical machine learning approaches to predict rice parameters from Sentinel-1 data, which were applied in the Camargue region.

We demonstrated that good regression performance could be yielded with Sentinel-1 data even with the classical approaches (MLR, SVR, and RF). We found that non-parametric methods (SVR and RF) had better performance over the parametric MLR method for estimating rice parameters. Between the SVR and RF models, the RF method obtains slightly better results than the SVR. Correlation coefficient R^2 and RMSE were 0.90 and 18% ($162 \text{ g} \cdot \text{m}^{-2}$) for rice dry biomass, 0.92 and 16% (7.9 cm) for rice height, which indicated a high accuracy of Sentinel-1 SAR retrieval. In other words, we demonstrated that Sentinel-1 remote sensing data could be an alternative and reliable approach to monitor regional rice height and estimate dry biomass, compared with direct field measurements. Future work on the Camargue region could be focused on exploiting Sentinel-1 data to improve crop models to better estimate rice production yields in order to be able to propose strategies for sustainable agricultural development.

In the context of the Copernicus program, there are two missions: radar Sentinel-1 and optical Sentinel-2. In future research, the data combination from the two satellites will be a necessity as it will be possible to carry out large-scale missions. Radar and optical data can be complementary to each other because they offer different perspectives on the Earth's surface providing different information content according to their specificity [7,8,58]. Both types of data can also be merged to provide information from multiple sources and to provide improved results for decision making [59].

Author Contributions: E.N. and D.H.T.M. developed the main idea that led to this paper. E.N., D.N.H.T. and I.E.M. analyzed SAR data for rice parameters estimations and their descriptions. E.N. collected the reference data and was the main author of the paper. INRA has provided the main contacts with farmers on the Camargue area. All authors read and approved the final manuscript.

Funding: This research received no external funding.

Acknowledgments: This work was supported by Centre National d'Etudes Spatiales. We thank the government of Burundi for funding the PhD research of Emile Ndikumana. The authors were grateful to Xavier Guillot and Pierre Megias for the authorisation of accessing their rice parcels.

Conflicts of Interest: The authors declare no conflict of interest.

Reference

1. Van Nguyen, N.; Ferrero, A. Meeting the challenges of global rice production. *Paddy Water Environ.* **2006**, *4*, 1–9. [[CrossRef](#)]
2. Seck, P.A.; Diagne, A.; Mohanty, S.; Wopereis, M.C. Crops that feed the world 7: Rice. *Food Secur.* **2012**, *4*, 7–24. [[CrossRef](#)]
3. Hossain, M. Rice supply and demand in Asia: A socioeconomic and biophysical analysis. In *Applications of Systems Approaches at the Farm and Regional Levels*; Springer: Berlin, Germany, 1997; Volume 1, pp. 263–279.
4. Shao, Y.; Fan, X.; Liu, H.; Xiao, J.; Ross, S.; Brisco, B.; Brown, R.; Staples, G. Rice monitoring and production estimation using multitemporal RADARSAT. *Remote Sens. Environ.* **2001**, *76*, 310–325. [[CrossRef](#)]
5. Singh, B.K.; Singh, A.K.; Meetei, N.; Mukherjee, A.; Mandal, N. QTL Mapping for Cold Tolerance at the Seedling Stage in Rice. *Int. J. Bio-Resour. Stress Manag.* **2016**, *7*. [[CrossRef](#)]

6. Jayawardhana, W.; Chathurange, V. Extraction of agricultural phenological parameters of Sri Lanka using MODIS, NDVI time series data. *Procedia Food Sci.* **2016**, *6*, 235–241. [[CrossRef](#)]
7. Campos-Taberner, M.; Garcia-Haro, F.J.; Camps-Valls, G.; Grau-Muedra, G.; Nutini, F.; Busetto, L.; Katsantonis, D.; Stavrakoudis, D.; Minakou, C.; Gatti, L.; et al. Exploitation of SAR and optical Sentinel data to detect rice crop and estimate seasonal dynamics of leaf area index. *Remote Sens.* **2017**, *9*, 248. [[CrossRef](#)]
8. Ferrant, S.; Selles, A.; Le Page, M.; Herrault, P.A.; Pelletier, C.; Al-Bitar, A.; Mermoz, S.; Gascoin, S.; Bouvet, A.; Saqalli, M.; et al. Detection of irrigated crops from Sentinel-1 and Sentinel-2 data to estimate seasonal groundwater use in South India. *Remote Sens.* **2017**, *9*, 1119. [[CrossRef](#)]
9. Xiao, X.; Boles, S.; Frolking, S.; Li, C.; Babu, J.Y.; Salas, W.; Moore, B. Mapping paddy rice agriculture in South and Southeast Asia using multi-temporal MODIS images. *Remote Sens. Environ.* **2006**, *100*, 95–113. [[CrossRef](#)]
10. Mutanga, O.; Adam, E.; Cho, M.A. High density biomass estimation for wetland vegetation using WorldView-2 imagery and random forest regression algorithm. *Int. J. Appl. Earth Obs. Geoinf.* **2012**, *18*, 399–406. [[CrossRef](#)]
11. Wang, F.M.; Huang, J.F.; Wang, X.Z. Identification of optimal hyperspectral bands for estimation of rice biophysical parameters. *J. Integr. Plant Biol.* **2008**, *50*, 291–299. [[CrossRef](#)]
12. Xiao, X.; Boles, S.; Liu, J.; Zhuang, D.; Frolking, S.; Li, C.; Salas, W.; Moore, B. Mapping paddy rice agriculture in southern China using multi-temporal MODIS images. *Remote Sens. Environ.* **2005**, *95*, 480–492. [[CrossRef](#)]
13. Drusch, M.; Bello, U.D.; Carlier, S.; Colin, O.; Fernandez, V.; Gascon, F.; Hoersch, B.; Isola, C.; Laberinti, P.; Martimort, P.; et al. Sentinel-2 ESA Optical High-Resolution Mission for GMES Operational Services. *Remote Sens. Environ.* **2012**, *120*, 25–36. [[CrossRef](#)]
14. Le Toan, T.; Ribbes, F.; Wang, L.F.; Floury, N.; Ding, K.H.; Kong, J.A.; Fujita, M.; Kurosu, T. Rice crop mapping and monitoring using ERS-1 data based on experiment and modeling results. *IEEE Trans. Geosci. Remote Sens.* **1997**, *35*, 41–56. [[CrossRef](#)]
15. Li, S.; Ni, P.; Cui, G.; He, P.; Liu, H.; Li, L.; Liang, Z. Estimation of rice biophysical parameters using multitemporal RADARSAT-2 images. In *IOP Conference Series: Earth and Environmental Science*; IOP Publishing: Bristol, UK, 2016; Volume 34, p. 012019.
16. Silvestro, P.C.; Pignatti, S.; Yang, H.; Yang, G.; Pascucci, S.; Castaldi, F.; Casa, R. Sensitivity analysis of the Aquacrop and SAFYE crop models for the assessment of water limited winter wheat yield in regional scale applications. *PLoS ONE* **2017**, *12*, e0187485. [[CrossRef](#)] [[PubMed](#)]
17. Rossi, C.; Erten, E. Paddy-rice monitoring using TanDEM-X. *IEEE Trans. Geosci. Remote Sens.* **2015**, *53*, 900–910. [[CrossRef](#)]
18. Yuzugullu, O.; Erten, E.; Hajnsek, I. Estimation of rice crop height from X-and C-band PolSAR by metamodel-based optimization. *IEEE J. Sel. Top. Appl. Earth Obs. Remote Sens.* **2017**, *10*, 194–204. [[CrossRef](#)]
19. Inoue, Y.; Sakaiya, E.; Wang, C. Capability of C-band backscattering coefficients from high-resolution satellite SAR sensors to assess biophysical variables in paddy rice. *Remote Sens. Environ.* **2014**, *140*, 257–266. [[CrossRef](#)]
20. Mazza, G.; Agnelli, A.E.; Orasen, G.; Gennaro, M.; Valè, G.; Lagomarsino, A. Reduction of Global Warming Potential from rice under alternate wetting and drying practice in a sandy soil of northern Italy. *Ital. J. Agrometeorol.-Riv. Ital. Agrometeorol.* **2016**, *21*, 35–44.
21. Ge, T.; Li, B.; Zhu, Z.; Hu, Y.; Yuan, H.; Dorodnikov, M.; Jones, D.L.; Wu, J.; Kuzyakov, Y. Rice rhizodeposition and its utilization by microbial groups depends on N fertilization. *Biol. Fertil. Soils* **2017**, *53*, 37–48. [[CrossRef](#)]
22. Li, K.; Brisco, B.; Yun, S.; Touzi, R. Polarimetric decomposition with RADARSAT-2 for rice mapping and monitoring. *Can. J. Remote Sens.* **2012**, *38*, 169–179. [[CrossRef](#)]
23. Chen, J.; Lin, H.; Pei, Z. Application of ENVISAT ASAR data in mapping rice crop growth in Southern China. *IEEE Geosci. Remote Sens. Lett.* **2007**, *4*, 431–435. [[CrossRef](#)]
24. Kurosu, T.; Fujita, M.; Chiba, K. Monitoring of rice crop growth from space using the ERS-1 C-band SAR. *IEEE Trans. Geosci. Remote Sens.* **1995**, *33*, 1092–1096. [[CrossRef](#)]
25. Snoeij, P.; Attema, E.; Davidson, M.; Duesmann, B.; Floury, N.; Levrini, G.; Rommen, B.; Rosich, B. The Sentinel-1 radar mission: Status and performance. In *Proceedings of the IEEE International Radar Conference-Surveillance for a Safer World (RADAR 2009)*, Bordeaux, France, 12–16 October 2009; pp. 1–6.
26. Torres, R.; Snoeij, P.; Geudtner, D.; Bibby, D.; Davidson, M.; Attema, E.; Potin, P.; Rommen, B.; Floury, N.; Brown, M.; et al. GMES Sentinel-1 mission. *Remote Sens. Environ.* **2012**, *120*, 9–24. [[CrossRef](#)]

27. Torbick, N.; Chowdhury, D.; Salas, W.; Qi, J. Monitoring rice agriculture across myanmar using time series Sentinel-1 assisted by Landsat-8 and PALSAR-2. *Remote Sens.* **2017**, *9*, 119. [\[CrossRef\]](#)
28. Ferrazzoli, P.; Paloscia, S.; Pampaloni, P.; Schiavon, G.; Sigismondi, S.; Solimini, D. The potential of multifrequency polarimetric SAR in assessing agricultural and arboreous biomass. *IEEE Trans. Geosci. Remote Sens.* **1997**, *35*, 5–17. [\[CrossRef\]](#)
29. Delmotte, S.; Tiftonell, P.; Mouret, J.C.; Hammond, R.; Lopez-Ridaura, S. On farm assessment of rice yield variability and productivity gaps between organic and conventional cropping systems under Mediterranean climate. *Eur. J. Agron.* **2011**, *35*, 223–236. [\[CrossRef\]](#)
30. Ndikumana, E.; Ho Tong Minh, D.; Baghdadi, N.; Courault, D.; Hossard, L. Deep Recurrent Neural Network for Agricultural Classification using multitemporal SAR Sentinel-1 for Camargue, France. *Remote Sens.* **2018**, *10*, 1217. [\[CrossRef\]](#)
31. Bernstein, D.S. *Matrix Mathematics: Theory, Facts, and Formulas with Application to Linear Systems Theory*; Princeton University Press: Princeton, NJ, USA, 2005; Volume 41.
32. Rasmussen, C.E.; Williams, C.K.I. *Gaussian Processes for Machine Learning*; MIT Press: Cambridge, MA, USA, 2006.
33. Breiman, L. Random forests. *Mach. Learn.* **2001**, *45*, 5–32. [\[CrossRef\]](#)
34. Huang, T.; Kecman, V.; Kopriva, I. *Kernel Based Algorithms for Mining Huge Data Sets: Supervised, Semi-Supervised, and Unsupervised Learning*; Springer: Berlin, Germany, 2006.
35. Kotsiantis, S.B.; Zaharakis, I.D.; Pintelas, P.E. Machine learning: A review of classification and combining techniques. *Artif. Intell. Rev.* **2006**, *26*, 159–190. [\[CrossRef\]](#)
36. Neumann, M.; Saatchi, S.S.; Ulander, L.M.; Fransson, J.E. Assessing performance of L-and P-band polarimetric interferometric SAR data in estimating boreal forest above-ground biomass. *IEEE Trans. Geosci. Remote Sens.* **2012**, *50*, 714–726. [\[CrossRef\]](#)
37. Vafaei, S.; Soosani, J.; Adeli, K.; Fadaei, H.; Naghavi, H.; Pham, T.D.; Tien Bui, D. Improving accuracy estimation of forest aboveground biomass based on incorporation of ALOS-2 PALSAR-2 and sentinel-2A imagery and machine learning: a case study of the Hyrcanian forest area (Iran). *Remote Sens.* **2018**, *10*, 172. [\[CrossRef\]](#)
38. Bassene, J.B.; Quiedeville, S.; Chabrol, D.; Lançon, F.; Moustier, P. Organisation en réseau et durabilité systémique de deux filières alimentaires (riz biologique et petit épeautre en France). *Actes Des* **2014**, *8*, 24.
39. Mouret, J.C. Etude de l'Agrosystème Rizicole en Camargue dans ses Relations Avec le Milieu et le Système Cultural: Aspects Particuliers de la Fertilité. Ph.D. Thesis, Montpellier 2 University, Montpellier, France, 1988.
40. Beau, J. La culture du riz en Camargue, aspects techniques et commerciaux actuels. *Méditerranée* **1975**, *22*, 53–68. [\[CrossRef\]](#)
41. Prats-Iraola, P.; Scheiber, R.; Marotti, L.; Wollstadt, S.; Reigber, A. TOPS Interferometry With TerraSAR-X. *IEEE Trans. Geosci. Remote Sens.* **2012**, *50*, 3179–3188. [\[CrossRef\]](#)
42. Quegan, S.; Yu, J. J. Filtering of multichannel SAR images. *IEEE Trans. Geosci. Remote Sens.* **2001**, *39*, 2373–2379. [\[CrossRef\]](#)
43. Ho Tong Minh, D.; Ngo, Y.N. Tomosar platform supports for Sentinel-1 tops persistent scatterers interferometry. In Proceedings of the 2017 IEEE International Geoscience and Remote Sensing Symposium (IGARSS), Fort Worth, TX, USA, 23–28 July 2017; pp. 1680–1683.
44. Fan, R.E.; Chen, P.H.; Lin, C.J. Working set selection using second order information for training support vector machines. *J. Mach. Learn. Res.* **2005**, *6*, 1889–1918.
45. Chakrabarti, A.; Ghosh, J.K. AIC, BIC and Recent Advances in Model Selection. In *Philosophy of Statistics: Handbook of the Philosophy of Science*; Bandyopadhyay, P.S., Forster, M.R., Eds.; North-Holland: Amsterdam, The Netherlands, 2011; Volume 7, pp. 583–605. [\[CrossRef\]](#)
46. Jolliffe, I.T. *Principal Component Analysis*, 2nd ed.; Springer: Berlin, Germany, 2002.
47. Wu, F.; Wang, C.; Zhang, H.; Zhang, B.; Tang, Y. Rice crop monitoring in South China with RADARSAT-2 quad-polarization SAR data. *IEEE Geosci. Remote Sens. Lett.* **2011**, *8*, 196–200. [\[CrossRef\]](#)
48. Ho Tong Minh, D.; Ndikumana, E.; Vieilledent, G.; McKey, D.; Baghdadi, N. Potential value of combining ALOS PALSAR and Landsat-derived tree cover data for forest biomass retrieval in Madagascar. *Remote Sens. Environ.* **2018**, *213*, 206–214. [\[CrossRef\]](#)

49. Ho Tong Minh, D.; Le Toan, T.; Rocca, F.; Tebaldini, S.; Mariotti d'Alessandro, M.; Villard, L. Relating P-band Synthetic Aperture Radar Tomography to Tropical Forest Biomass. *IEEE Trans. Geosci. Remote Sens.* **2014**, *52*, 967–979. [[CrossRef](#)]
50. Ho Tong Minh, D.; Le Toan, T.; Rocca, F.; Tebaldini, S.; Villard, L.; Réjou-Méchain, M.; Phillips, O.L.; Feldpausch, T.R.; Dubois-Fernandez, P.; Scipal, K.; et al. SAR tomography for the retrieval of forest biomass and height: Cross-validation at two tropical forest sites in French Guiana. *Remote Sens. Environ.* **2016**, *175*, 138–147. [[CrossRef](#)]
51. Jia, M.; Tong, L.; Zhang, Y.; Chen, Y. Rice biomass estimation using radar backscattering data at S-band. *IEEE J. Sel. Top. Appl. Earth Obs. Remote Sens.* **2014**, *7*, 469–479. [[CrossRef](#)]
52. Lopez-Sanchez, J.M.; Ballester-Berman, J.D.; Hajnsek, I. First results of rice monitoring practices in Spain by means of time series of TerraSAR-X dual-pol images. *IEEE J. Sel. Top. Appl. Earth Obs. Remote Sens.* **2011**, *4*, 412–422. [[CrossRef](#)]
53. Zhang, Y.; Liu, X.; Su, S.; Wang, C. Retrieving canopy height and density of paddy rice from Radarsat-2 images with a canopy scattering model. *Int. J. Appl. Earth Obs. Geoinf.* **2014**, *28*, 170–180. [[CrossRef](#)]
54. Jing, Z.; Zhang, Y.; Wang, K.; Shi, R. Retrieving rice yield and biomass from Radarsat-2 SAR data with artificial neural network (ANN). In *Remote Sensing and Modeling of Ecosystems for Sustainability X*; International Society for Optics and Photonics: San Diego, California, USA, 2013; Volume 8869, p. 88690X.
55. Zhang, Y.; Huang, H.; Chen, X.; Wu, J.; Wang, C. Mapping paddy rice biomass using ALOS/PALSAR imagery. In *Proceedings of the 2008 International Workshop on Education Technology and Training & 2008 International Workshop on Geoscience and Remote Sensing*, Shanghai, China, 21–22 December 2008; Volume 2, pp. 207–210.
56. Karam, M.A.; Fung, A.K.; Antar, Y.M. Electromagnetic wave scattering from some vegetation samples. *IEEE Trans. Geosci. Remote Sens.* **1988**, *26*, 799–808. [[CrossRef](#)]
57. Graham, A.; Harris, R. Extracting biophysical parameters from remotely sensed radar data: A review of the water cloud model. *Prog. Phys. Geogr.* **2003**, *27*, 217–229. [[CrossRef](#)]
58. Irwin, K.; Beaulne, D.; Braun, A.; Fotopoulos, G. Fusion of SAR, Optical Imagery and Airborne LiDAR for Surface Water Detection. *Remote Sens.* **2017**, *9*, 890. [[CrossRef](#)]
59. Hall, D. *Mathematical Techniques in Multisensor Data Fusion*; Artech House Inc.: Norwood, OH, USA, 1992.



© 2018 by the authors. Licensee MDPI, Basel, Switzerland. This article is an open access article distributed under the terms and conditions of the Creative Commons Attribution (CC BY) license (<http://creativecommons.org/licenses/by/4.0/>).

APPENDIX C

Potential value of combining ALOS/PALSAR and Landsat-derived tree cover data for forest biomass retrieval in Madagascar



Contents lists available at ScienceDirect

Remote Sensing of Environment

journal homepage: www.elsevier.com/locate/rse

Potential value of combining ALOS PALSAR and Landsat-derived tree cover data for forest biomass retrieval in Madagascar

Dinh Ho Tong Minh^{a,*}, Emile Ndikumana^a, Ghislain Vieilledent^{b,c}, Doyle McKey^d, Nicolas Baghdadi^a^a Institut national de Recherche en Sciences et Technologies pour l'Environnement et l'Agriculture (IRSTEA), University of Montpellier, UMR TETIS, Montpellier, France^b CIRAD, UPR Forêts et Sociétés, Montpellier F-34398, France^c Joint Research Center of the European Commission, Bio-economy unit, Ispra I-21027, VA, Italy^d CEF, University of Montpellier, CNRS, Institut d'Ecologie et Environnement, route de Mende, Montpellier 5 34293, France

ARTICLE INFO

Keywords:

Aboveground biomass
Biomass
Carbon
Madagascar
ALOS PALSAR
Landsat tree cover
REDD

ABSTRACT

Reducing carbon emissions from deforestation and degradation (REDD) requires detailed insight into how the forest biomass is measured and distributed. Studies so far have estimated forest biomass stocks using rough assumptions and unreliable data. High-resolution data and robust methods are required to capture the spatial variability of forest biomass with sufficient precision. Here we aim to improve on previous approaches by using radar satellite ALOS PALSAR (25-m resolution) and optical Landsat-derived tree cover (30-m resolution) observations to estimate forest biomass stocks in Madagascar, for the years 2007–2010. The radar signal and in situ biomass were highly correlated ($R^2 = 0.71$) and the root mean square error was 30% (for biomass ranging from 0 to 500 t/ha). Using our map at 25-m resolution for the entire island of Madagascar, we estimated the total above-ground forest carbon for the four years 2007, 2008, 2009 and 2010 to be 1.1173 ± 0.0304 , 1.1029 ± 0.0303 , 1.0916 ± 0.0301 and 1.0773 ± 0.0298 PgC, respectively. Carbon stocks were found to have decreased constantly over this period due to anthropogenic deforestation and likely also to climate change. The results are expected to serve as a more accurate benchmark for monitoring progress on REDD and to provide strong supports for current and future spaceborne missions such as ALOS-2, SAOCOM and BIOMASS.

1. Introduction

Forest biomass plays a key role in the global climate (Pan et al., 2011). However, compared to biomass in other ecosystems, forest biomass remains poorly quantified, owing to the practical difficulties in measuring stocks over broad geographic scales. Overcoming this obstacle is important, because quantifying forest biomass is essential for countries planning to participate in the Reducing Emissions from Deforestation and Degradation (REDD) program (Hufty and Haakenstad, 2011). REDD offers incentives (e.g., monetary compensation) for countries to preserve their forestland in the interest of reducing carbon emissions and thereby lessening the risk of climate change. Both above-ground and below-ground biomass are present, but above-ground biomass (AGB) is more commonly measured. In recent years, progress has been made in mapping forest biomass by using a range of remote sensing technologies (Saatchi et al., 2011; Baccini et al., 2012; Vieilledent et al., 2016). Nonetheless, these studies are limited by their dependence on optical sensors (relatively insensitive to biomass), low resolution

(from 250 m (Vieilledent) to 500 m (Baccini) to 1000 m (Saatchi)) and inadequate sampling intensity. For example, the results of Saatchi et al. (2011) and Baccini et al. (2012) show strong discrepancies at the local scale and there are no evident reasons for preferring one map over the other.

Unlike passive optical sensors, radar systems are capable of producing high quality images of the earth even in cloud cover conditions. Synthetic aperture radar (SAR) allows for continuous global spatial coverage and systematic acquisitions, both of which are essential for constructing relevant temporal series. The potential of SAR for forest biomass estimation has been highlighted since the early 1990s (Le Toan et al., 1992). Radar intensity depends on the overall geometrical and dielectric features of these various scatterers, whose geometrical volume and wood density give the whole forest biomass. As a general rule, increasing intensity values goes with increasing biomass whether at L or P-bands, until a saturation value, which occurs earlier at L-band (Dobson et al., 1992).

The L-band ALOS mission is considered pioneering in the systematic

* Corresponding author.

E-mail address: dinh.ho-tong-minh@irstea.fr (D. Ho Tong Minh).<https://doi.org/10.1016/j.rse.2018.04.056>Received 8 August 2016; Received in revised form 16 August 2017; Accepted 28 April 2018
0034-4257/ © 2018 Elsevier Inc. All rights reserved.

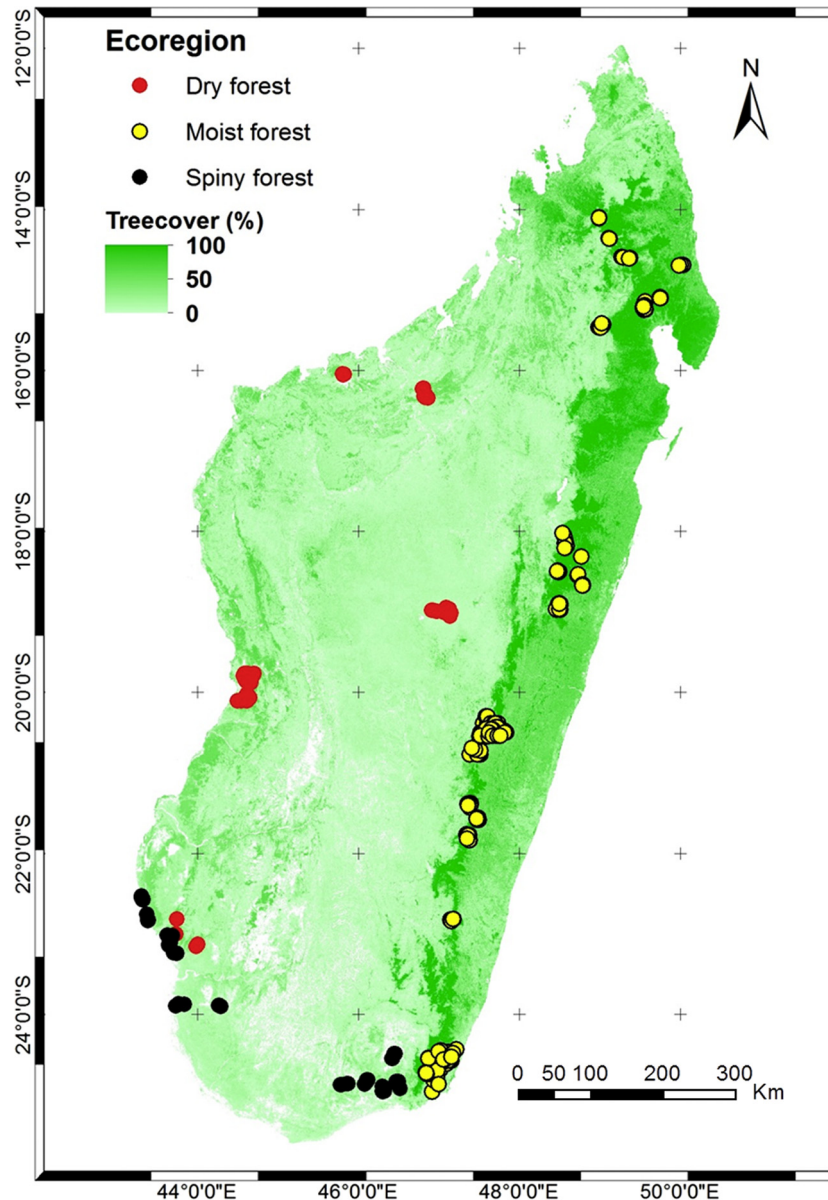


Fig. 1. The study site is the entire island of Madagascar. The background is the Landsat-derived tree cover. Red, yellow and black circles represent field sites in dry forest, moist forest and spiny forest, respectively. (For interpretation of the references to color in this figure legend, the reader is referred to the web version of this article.)

acquisition of data that has allowed the imaging of the planet over time at high resolution. This strategy of systematic acquisition enabled the production by the Japan Aerospace Exploration Agency (JAXA) of mosaic images of up to 25-m resolution (Shimada et al., 2014). These mosaics are radar images preprocessed by the JAXA, made freely available in tiles of 1 degree squared for the years 2007–2010 (Shimada and Ohtaki, 2010). The L-band ALOS PALSAR data have been widely used to estimate the forest biomass. For example, the ALOS PALSAR data were exploited to estimate the biomass of forests threatened by oil palm plantations in Malaysia (Morel et al., 2011), while in Sumatra, texture features from ALOS PALSAR data were used (Thapa et al., 2015). However, estimation of forest biomass using ALOS PALSAR data currently has limitations, because the L-band saturates at about 150 t/ha. Savanna vegetation has lower carbon stocks and is thus more easily estimated with these data. For example, Mermoz et al. (2014) produced a country-level map of Cameroon's savanna biomass at 25-m resolution. In most studies, the cross-polarization (HV) is preferred for estimating biomass because it minimizes the contribution of coupling terms with

the ground. Indeed, the HV intensity mainly from the depolarizing part (oriented branches) represents a small proportion of biomass, but it is highly correlated with the total biomass. These studies are based on the fact that the HV intensities are positively correlated with biomass. However, the signal sensitivity decreases as the biomass increases, up to a point called the saturation point, where sensitivity is lost. At L-band HV, this saturation point is about 150 t/ha (Mermoz et al., 2015). After the saturation point, many studies (Woodhouse, 2006; Lucas et al., 2007; Mermoz et al., 2015) have highlighted a weak negative correlation of intensity with biomass. In other words, with high biomass values, the ALOS PALSAR signals decrease. The non-monotonic relationship between intensity and biomass means that corrective models must be established when the range of biomass includes high values. One attempt to retrieve biomass greater than 150 t/ha is the European Space Agency (ESA) P-band BIOMASS mission, to be launched in 2020. Taking advantage of the 300 t/ha saturation point for P-band, this mission aims for more precise measures of global forest biomass (Le Toan et al., 2011; Ho Tong Minh et al., 2015) and hence better

understanding of the terrestrial carbon cycle by measuring global forest biomass.

However, the potential for using L-band radar to estimate high biomass values has not been completely explored. In this study, we propose a new approach to retrieve the full range of biomass using L-band ALOS PALSAR data based on prior knowledge from the global tree cover map at 30-m resolution produced by Hansen et al. (2013). To do this, we use a very large number of forest plots (572) dispersed across Madagascar from 2007 to 2013. Madagascar has a wide variety of forest types (dry forest, spiny forest, and tropical moist forest) known to differ in AGB. It is thus a particularly interesting region for studying spatial variation in the distribution of biomass (and hence of carbon) stocks using radar data.

The paper is organized as follows: in Section 2, the study site is introduced and the proposed methodology is shown; in Section 3, the relationship between radar measurements and AGB is evaluated and the inversion results are presented; in Section 4, we interpret and discuss for each result; in Section 5, we present our conclusions.

2. Data and methods

2.1. Study area

A continental island almost 1600 km long lying off the south-eastern coast of Africa in Indian Ocean, Madagascar stretches between 12° S and 25° S latitude, from Cape Amber in the north to Cape St. Mary in the south, and averages about 500 km in width. Within its area of 587 040 km², three types of climates occur. The east coast has a humid tropical climate. West of this coast, the climate is moderate in the north and arid in the south. The broad climatic gradients on the island are associated with elevation and position relative to the dominant south-eastern trade winds (Goodman and Benstead, 2003). Over these climatic gradients occur a large range of tropical forest types, from dry spiny forests in the sub-desert southern regions, to cloud forests at the tops of the northern and eastern mountains. The east coast, exposed to the trade winds, receives the highest rainfall with 3500 mm/year. Forests in the northeast, are particularly wet and lush. Vegetation of western, southern and eastern Madagascar is comprised mainly of dry forest, spiny forest and moist forest, respectively. The moist forests are characterized by dense evergreen vegetation with a canopy exceeding 30 m. Trees of the dry forests shed their leaves in the dry season to limit evapotranspiration, whereas plants of the spiny forests are strongly adapted to drought. Fig. 1 shows the study area and biomass measured in situ.

2.2. Field data

Field data are available from nine forest inventories carried out over the period 1996–2013. Collaboration with different institutions (governmental institutions, conservation NGOs, research institutes) allowed us to obtain data from a large number of forest plots (1771) in the three forest ecoregions of Madagascar (moist, dry and spiny forest ecoregions). However, in this work, we used only the forest inventories from 2007 to 2013 to match with the ALOS PALSAR data, in which 572 plots were selected based on flat field slope and homogeneity within plots. The radius of the plots was 30 m in moist forest (plot size of 0.28 ha) and 20 m in dry or spiny forest (plot size of 0.13 ha). Fig. 2 shows the number of plots and its distribution with respect to each ecoregion. We calculated the AGB biomass (in metric tons) of each tree using the pantropical biomass allometric equation developed by Chave et al. (2014):

$$AGB = 0.0673 \times (\rho \times DBH^2 \times H)^{0.976} \quad (1)$$

where ρ is the tree wood density in g/cm³, DBH is the diameter at breast height in cm, H is the tree height in m. Details about the computation of AGB at the plot level are published in Vieilledent et al. (2016).

2.3. Tree cover data

Tree cover data are available globally at 30-m resolution from 2000 to 2012 in Hansen et al. (2013). The primary purpose of that study was to quantify global forest change over the study period. This dataset was obtained by analyzing 654 178 Landsat 7 Enhanced Thematic Mapper Plus scenes, from a total of 1.3 million available. The final results were obtained by training three separate classifiers: one to detect forest loss during the study period, one to detect forest gain during the study period, and one to detect forest cover at the start of the study period. For pixels that were classified as forest loss, the year of loss could essentially be determined by isolating the year of max normalize different vegetation index drop. This resulted in a baseline map of tree cover for the year 2000, forest loss and forest gain during 2001 and 2012. To support our analysis, tree cover maps for Madagascar for 2007, 2008, 2009 and 2010 were generated from the baseline tree cover map of 2000 using the yearly loss/gain information. Detailed discussion of the optical Landsat-derived tree cover dataset can be found in Hansen et al. (2013). In the present study, the dataset for tree cover at 30-m resolution was resampled to 25-m to combine with the SAR data. Fig. 3 shows the distribution of tree cover in 2010 and biomass measured in situ.

2.4. SAR data

520 ALOS PALSAR mosaic tiles with 25-m resolution covering all of Madagascar from 2007 to 2010 were provided freely by the JAXA. Mosaic data are spatially square (1° of latitude and 1° of longitude). The radar signal can be converted into γ^0 values using the following equation:

$$\gamma^0 = 10 \times \log_{10}(DN^2) + CF \quad (2)$$

where γ^0 is the normalized intensity, DN is the digital number and CF is the calibration factor, which equals -83.0 as described in Shimada et al. (2014).

The 520 ALOS images used in this study were processed by JAXA using the large-scale mosaicking algorithm described in Shimada and Ohtaki (2010). This algorithm includes ortho-rectification, slope correction and radiometric calibration between neighboring strips. At this stage, the resulting multilook images were perfectly coregistered, and the equivalent number of looks of ALOS PALSAR data was 16. We further improve this four years SAR dataset by exploiting a multi-image filtering developed by Quegan et al. (2000) to reduce noise while retaining as much as possible the fine structures present in the images.

2.5. Proposed methodology for biomass retrieval

Based on results reported from the literature on sensitivity of the L-band intensity in relation to biomass (see Section 1), it is possible to use the L-band HV to estimate biomass for up to a maximum of 150 t/ha. For higher values of biomass, L-band intensity is weakly sensitive variation in biomass. In this section, we present a method to address this problem.

First of all, we propose to weight the radar intensity by the tree cover factor from Section 2.3 using the following formula:

$$\gamma_{HVtree}^0 = 10 \times \log_{10}(treecover \times DN_{HV}^2) + CF \quad (3)$$

where γ_{HVtree}^0 is the intensity weighted by tree cover and the value for tree cover varies from 0 to 1.

Fig. 4 shows the distribution of γ_{HV}^0 , γ_{HVtree}^0 and biomass measured in situ, for the year 2010. A significant growth was observed in intensity with low biomass levels, followed by a loss of sensitivity and a slight decrease in signal intensity beginning at 150 t/ha. The range of γ_{HVtree}^0 is much higher than that of γ_{HV}^0 . In the high range of biomass values, there is no difference between the sensitivity of γ_{HV}^0 and γ_{HVtree}^0 . In fact, as seen in Fig. 3, we found that of plots where biomass was greater than 150 t/

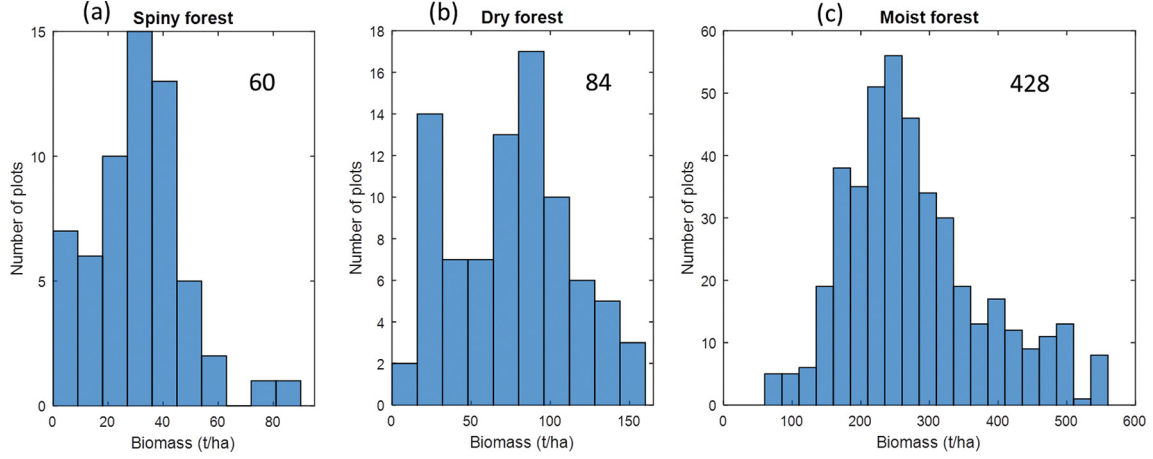


Fig. 2. Biomass measured in situ in spiny (a), dry (b) and moist (c) forest ecoregions. Number of plots sampled were 60, 84 and 428, respectively.

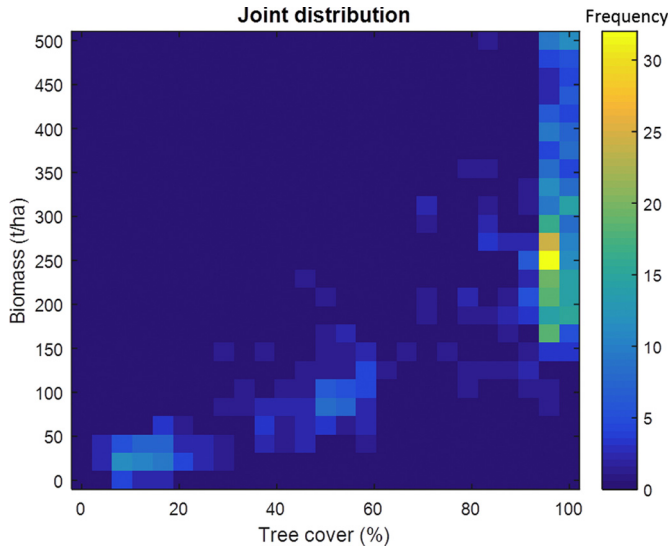


Fig. 3. The joint distribution between Landsat-derived tree cover and biomass measured in situ. More than 98% of plots with AGB > 150 t/ha had tree cover of 95% or greater.

ha, 98% had tree cover of 95% or more. Based on this observation, we proposed to use tree cover of 95% as a threshold to recognize the high range of biomass values.

To highlight the usefulness of γ_{HVtree}^0 in our approach, we compare the sensitivity of γ_{HV}^0 (unweighted radar intensity), γ_{HVtree}^0 (radar intensity weighted by tree cover) and tree cover with in situ biomass values in the low range (e.g., < 150 t/ha) in Fig. 5. The highest correlation is observed with the weighted radar intensity data. The γ_{HV}^0 data exhibit a much lower sensitivity to biomass ($R^2 = 0.34$) than do the γ_{HVtree}^0 data ($R^2 = 0.77$). One possible explanation of this result is that radar intensity integrates noise signals from the ground and this problem can be partly mitigated by incorporating tree cover data from optical images. Finally, by comparing γ_{HVtree}^0 and tree cover in Fig. 5b and c, the γ_{HVtree}^0 data exhibit a higher sensitivity to biomass ($R^2 = 0.77$ versus 0.72) and a smaller root mean square error (RMSE) (26% versus 30%).

For biomass lower than 150 t/ha, we fit an exponential model to link radar signal to biomass (Mitchard et al., 2011), described as

$$\gamma_{HVtree}^0 = a + b \times (1 - e^{-c \times AGB}) \quad (4)$$

where AGB is the biomass measured in situ, a, b and c are coefficients to be estimated from the data.

For higher values of biomass, we fitted a linear model (Mermoz et al., 2015), described as

$$\gamma_{HVtree}^0 = m + n \times AGB \quad (5)$$

where m and n are coefficients to be estimated from the data.

By using Eqs. (4) and (5), an estimation of biomass \widehat{AGB} can be calculated from γ_{HVtree}^0 . However, in our approach, a bias in the inversion can be introduced. In the statistical literature, this phenomenon is

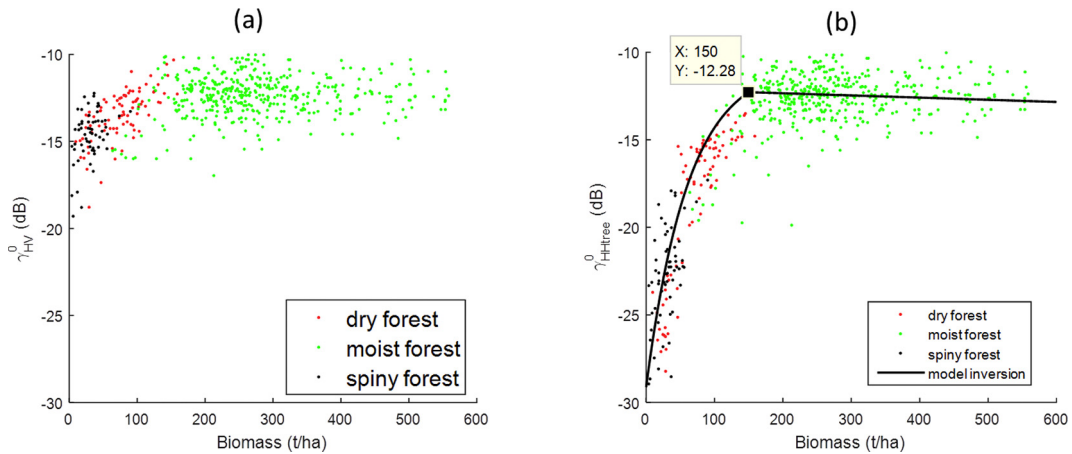


Fig. 4. (a) Biomass measured in situ versus γ_{HV}^0 . (b) Biomass measured in situ versus γ_{HVtree}^0 .

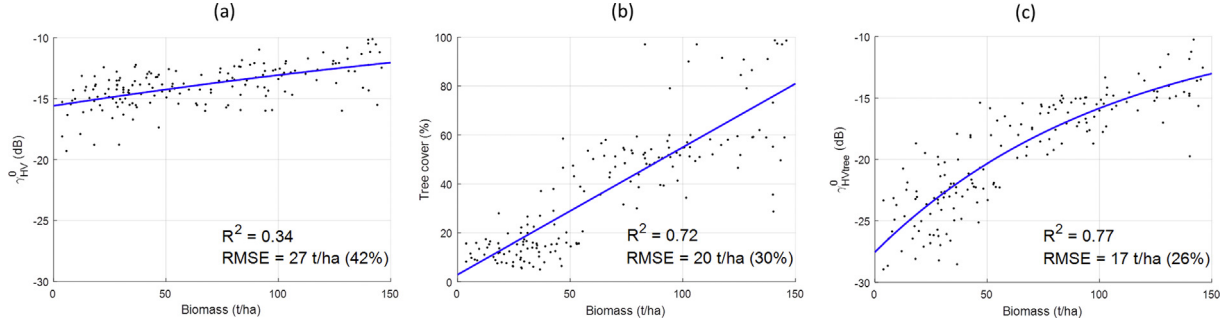


Fig. 5. (a) Biomass measured in situ versus γ_{HV}^0 . (b) Biomass measured in situ versus tree cover. (c) Biomass measured in situ versus γ_{HVtree}^0 . The blue line is the best fit of the data. (For interpretation of the references to color in this figure legend, the reader is referred to the web version of this article.)

referred to as regression dilution, in that random error in the independent variable leads to systematic underestimation of the regression slope (Fuller, 1987; Frost and Thompson, 2000). To correct for such bias, we compensate the biomass by a ratio β , described as

$$Bias[\widehat{AGB}] = \beta \times AGB \quad (6)$$

where $Bias[\widehat{AGB}] = E[\widehat{AGB} - AGB]$ and $E(\cdot)$ denotes expected operator, i.e., averaging over a number of observations.

2.6. Calibration for Madagascar

A common method for biomass retrieval is to exploit an inverse model based on the empirical regression derived from the available set of in situ and radar plot data. In this work, using 572 biomass plots for fitting with each year's SAR data, e.g. for the year 2010, we found that

For biomass lower than 150 t/ha:

$$\widehat{AGB} = -\frac{1}{c} \times \ln\left(1 - \frac{\gamma_{HVtree}^0 - a}{b}\right) \quad (7)$$

With $a = -29.13 \pm 0.09$, $b = 18.47 \pm 0.14$ and $c = 0.01623 \pm 0.00034$. In the low range of biomass values, γ_{HVtree}^0 is very highly correlated with biomass ($R^2 = 0.77$ and $p < 10^{-5}$).

For higher biomass values and tree cover greater than 95%:

$$\widehat{AGB} = \frac{\gamma_{HVtree}^0 - m}{n} \quad (8)$$

With $m = -12.14 \pm 0.28$ and $n = -9.28.10^{-4} \pm 9.35.10^{-5}$. In the high range of biomass values, γ_{HVtree}^0 is less strongly correlated with biomass ($R^2 = 0.18$ and $p = 0.017$).

Fig. 4b plots Eqs. (7) and (8), showing the fit between the weight the radar intensity and the in situ biomass.

Finally, the estimated biomass can be calculated as

$$Biomass = (1 + \beta) \times \widehat{AGB} \quad (9)$$

With $\beta = 0.2392 \pm 0.0515$.

2.7. Carbon estimation and uncertainty

The calibration described in Section 2.6 allows estimation of above-ground biomass in Madagascan forests. To calculate carbon stock, we convert biomass into carbon units using the 0.47 ratio (Vieilledent et al., 2016). We apply a filter to this carbon data based on the tree cover map and only include pixels with $> 25\%$ tree cover. In others words, we follow a conservative approach in defining forest: only land with tree cover not less than 25% was considered as forest (Hansen et al., 2013; Shimada et al., 2014).

The model inversion between biomass and radar is affected by the uncertainties in radar signal, tree cover estimate and in situ biomass data. The radar signal is impacted by a number of factors related to forest structure and environments. The signal can also be affected by

variation in the performance of the signal emitter over time. However, the ALOS PALSAR γ_{HV}^0 was found to be very stable at 0.065 dB over its lifetime 2006–2010 (Shimada et al., 2014). Regarding the tree cover dataset, there is little uncertainty, with classification error less than 1% (Hansen et al., 2013). Regarding in situ biomass measurements, the data collection procedures in the sources we used varied somewhat across organizations, but all the different protocols allowed estimating biomass in t/ha at the center of each forest plot. Application of an uncertainty analysis at each stage is out of the scope of this study. If all sources of uncertainties can be estimated, an explicit equation can be applied to ALOS PALSAR data (Mermoz et al., 2014). Nonetheless, in this work, uncertainties related to the carbon estimates are estimated by Monte Carlo simulations. Such uncertainties affect the definition of the inverse model (imprecision and bias), as the in situ biomass estimates are used to fit parameters of the model. A new inverse model is derived by estimating the coefficients(a, b, c, m, n, β) and biomass is estimated at each generation (with 1000 realisations). For each pixel, the dispersion of biomass values resulting from the 1000 possible models is used to calculate the standard deviation in the uncertainty associated with the estimation of biomass (and hence of carbon).

3. Results

The methods proposed in Section 2.5 were applied to ALOS PALSAR data in Madagascar. The RMSE and the correlation R^2 were used to evaluate performance of the SAR dataset for each year using all in situ plots available. The same performance for biomass retrieval with respect to in situ data was found for all four years. The results, presented in Fig. 6a, showed a RMSE of 30% (for biomass ranging from 0 to 500 t/ha) and $R^2 = 0.71$, for the year 2010. To avoid overfitting, we carried out a 10-fold cross-validation procedure (McLachlan et al., 2005). For biomass values in the range 0–150 t/ha, the average RMSE in 2010 was 26% and $R^2 = 0.77$, whereas for biomass values in the range 0–300 t/ha in the same year, the average RMSE was 28% and $R^2 = 0.72$.

Second, 520 ALOS PALSAR 25-m resolution images were used to retrieve biomass for 2007, 2008, 2009 and 2010. The biomass maps for these four years were found to be similar in their biomass content. An example of the biomass map for 2010 is shown in Fig. 7b. To appreciate the 25-m pixel size of the biomass map, a zoom version in an $0.5^\circ \times 0.5^\circ$ window was shown in the bottom. The distribution of biomass at 25-m resolution shows details of spatial biomass density, indicating a west-east gradient.

Third, using our map at 25-m resolution, we estimated the forest carbon stocks for dry, spiny and moist ecoregions, respectively (see Table 1). The total forest carbon in the four years 2007, 2008, 2009 and 2010 is 1.1173 ± 0.0304 , 1.1029 ± 0.0303 , 1.0916 ± 0.0301 and 1.0773 ± 0.0298 PgC ($1 \text{ PgC} = 10^{15} \text{ g carbon}$), respectively. Over the four years carbon stocks were found to have decreased by approximately 0.01 PgC/year. Finally, using the carbon map in 2007 and in 2010, we established the forest carbon change over the period

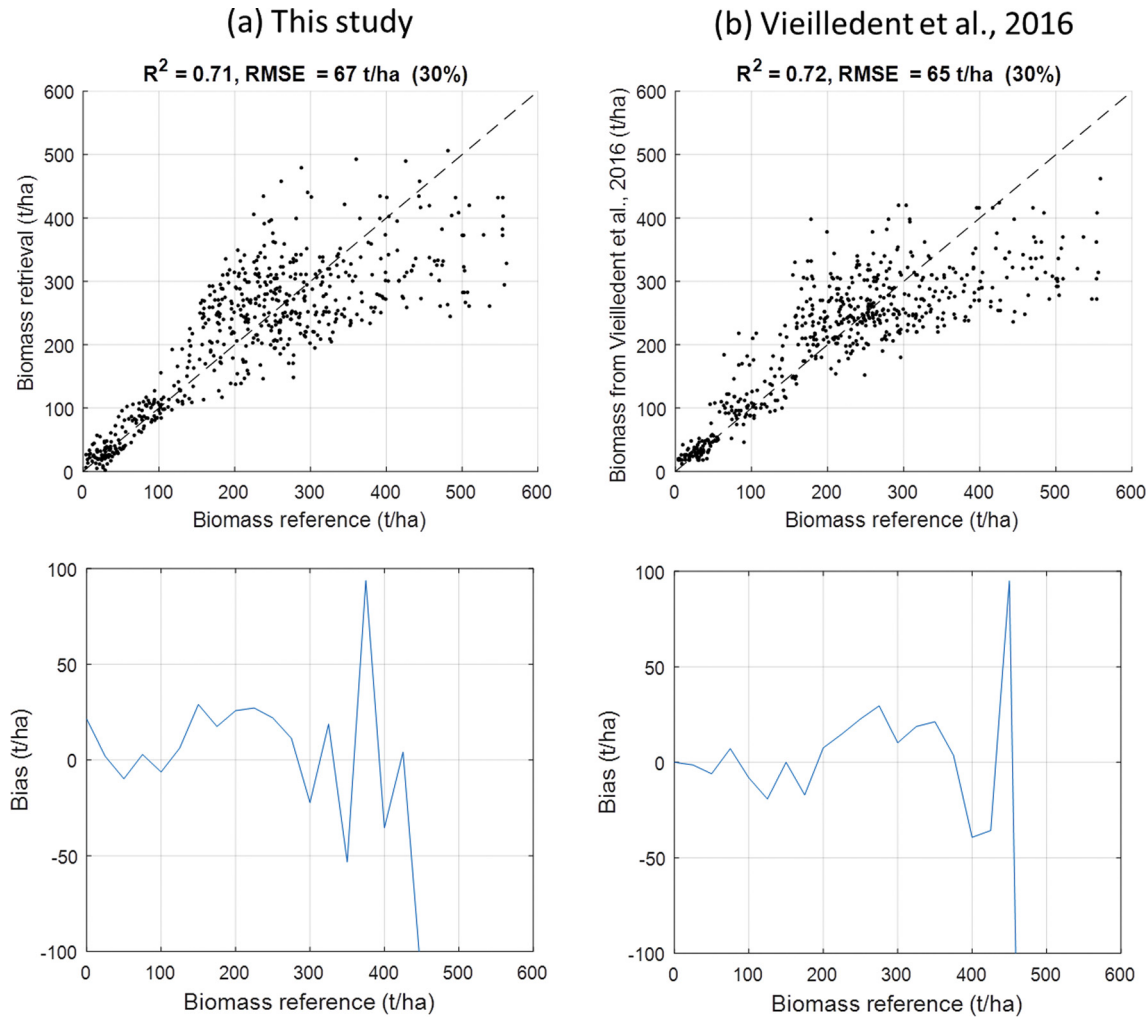


Fig. 6. (a) The biomass inversion performance of this study. (b) Performance in the study of Vieilledent et al. (2016). Top panels are the cross-plot 1:1. Bottom panels are the bias. The biomass retrieval appears to be reliable for biomass ranging from 0 to 300 t/ha.

2007–2010 (see Fig. 8).

4. Discussions

In this work we show that radar signal intensity combined with tree cover data can be used to estimate biomass across the entire range of biomass values in Madagascan forests. As seen in Fig. 5, weighting the radar signal by tree cover data increased the correlation between the radar signal and biomass. The weighted radar intensity follows a logarithmic regression and biomass reaches a certain threshold at which the signal becomes saturated and then quickly decreases. The present analysis confirms the possibility of exploiting such behavior in an inversion scheme to retrieve the full range of biomass up to 500 t/ha. Relative error in performance of biomass retrieval was 30% and the correlation between the weighted radar intensity and biomass was high ($R^2 = 0.71$) at 25-m resolution. Finally, we showed that biomass can be mapped efficiently even in tropical dense forests. Together, these results considerably add to our confidence in the ability of current and future missions such as L-band ALOS-2, L-band SAOCOM and P-band BIOMASS to provide accurate wall-to-wall biomass mapping. In particular, the arrival of the P-band sensor BIOMASS, which will exploit a volume layer through tomographic processing (Ho Tong Minh et al., 2014), will make it possible to estimate forest biomass with relative error of only about 11% at 4-ha resolution (Ho Tong Minh et al., 2015, 2016).

First, we showed that the inversion method described in Section 2.5 can be applied to retrieve the full range of biomass values. Our analysis was successfully conducted for forests of the entire island of Madagascar. It is worth noting that the inversion for high range of biomass values (e.g. greater than 150 t/ha) is mainly based on the fact that L-band radar signal decreases with increasing height of forest vegetation, a phenomenon that is well-known in the L-band literature (Woodhouse, 2006; Lucas et al., 2007; Mermoz et al., 2015). In addition, even at the longer wavelength P-band (wavelength 69 cm), the relationship between the ground layer and biomass exhibits a negative trend (Ho Tong Minh et al., 2014), similar to that observed for the L-band. The decrease can be explained by signal extinction, which likely to be higher in the presence of tall trees (and hence of high biomass).

To place this result in perspective, we compared our analysis with the work of Vieilledent et al. (2016). Their map was generated by using a correlative approach based on a bioclimatic envelope model and data from all 1771 forest plots inventoried during the period 1996–2013 over a large climatic gradient. The reader is referred to Vieilledent et al. (2016) for details. In fact, Vieilledent's map is represented as the most accurate biomass map available at 250-m resolution for the year 2010 in Madagascar. The comparisons are shown in Figs. 6 and 7. For the year 2010, from Fig. 6, the correlation R^2 and relative error are quite similar between the two maps. However, thanks to the 25-m resolution of the ALOS PALSAR data, our map of biomass distribution is more detailed than Vieilledent's map at 250-m resolution (see Fig. 7). For

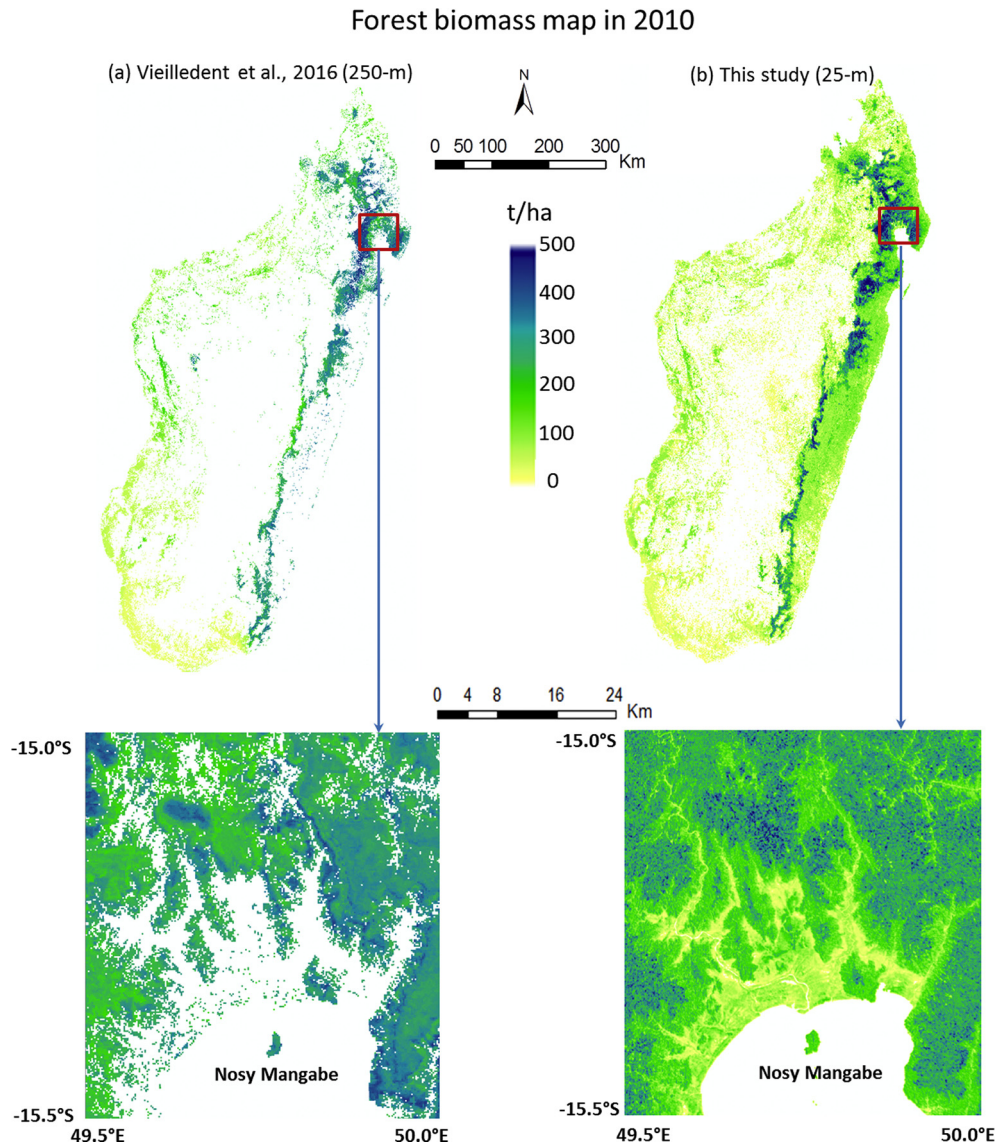


Fig. 7. Biomass maps for Madagascan forests for the year 2010 are shown. The color scale varying from yellow to green to blue illustrates the full biomass range from 0 to 500 t/ha. The spatial distribution of biomass for the entire island of Madagascar shows a west-east gradient. (a) Map from the study of Vieilledent et al. (2016) and (b) map from this work. The bottom panels show a zoom version of red-bordered boxes to facilitate visualization of the biomass results. (For interpretation of the references to color in this figure legend, the reader is referred to the web version of this article.)

example, in the bottom panels of Fig. 7, our map shows details of savanna ecosystems close to the coast such as forest savanna, woody savanna, and gallery forests, whereas in Vieilledent's map, they cannot be shown, owing to the limitation of the data available in the bioclimatic envelope model (Vieilledent et al., 2016). Furthermore, it is worth pointing out that if we only consider the low range of biomass values (i.e., < 150 t/ha), our result is slightly better than that of Vieilledent ($R^2 = 0.77$ versus 0.76 and $RMSE = 26\%$ versus 31%). This is

important because almost 80% of forest cover of Madagascar has biomass values less than 150 t/ha.

Third, we calculated that the values for total forest carbon in 2010 was 1.0773 ± 0.0298 PgC, whereas by using Vieilledent's map at 250-m resolution, it was 0.8738 PgC. It is worth recalling the results of others studies, for example those of Saatchi et al. (2011) and Baccini et al. (2012). These results were predicted for the year 2010 by Vieilledent et al. (2016) as 0.7490 PgC and 0.6392 PgC for Saatchi's and

Table 1

Surface area (ha) and carbon assessment (PgC) in Madagascar with respect to the dry, spiny and moist forest ecoregions.

	2007		2008		2009		2010	
	Area (ha)	Carbon (PgC)	Area (ha)	Carbon (PgC)	Area (ha)	Carbon (PgC)	Area (ha)	Carbon (PgC)
Dry	4,770,533	0.1635 ± 0.0078	4,725,042	0.1623 ± 0.0079	4,695,772	0.1601 ± 0.0079	4,639,216	0.1528 ± 0.0076
Spiny	355,857	0.0112 ± 0.0011	352,230	0.0111 ± 0.0011	346,299	0.0108 ± 0.0011	341,805	0.0104 ± 0.0011
Moist	13,263,951	0.9426 ± 0.0215	13,228,492	0.9295 ± 0.0213	13,193,701	0.9207 ± 0.0211	13,147,997	0.9141 ± 0.0211
Total	18,390,341	1.1173 ± 0.0304	18,305,764	1.1029 ± 0.0303	18,235,772	1.0916 ± 0.0301	18,129,018	1.0773 ± 0.0298

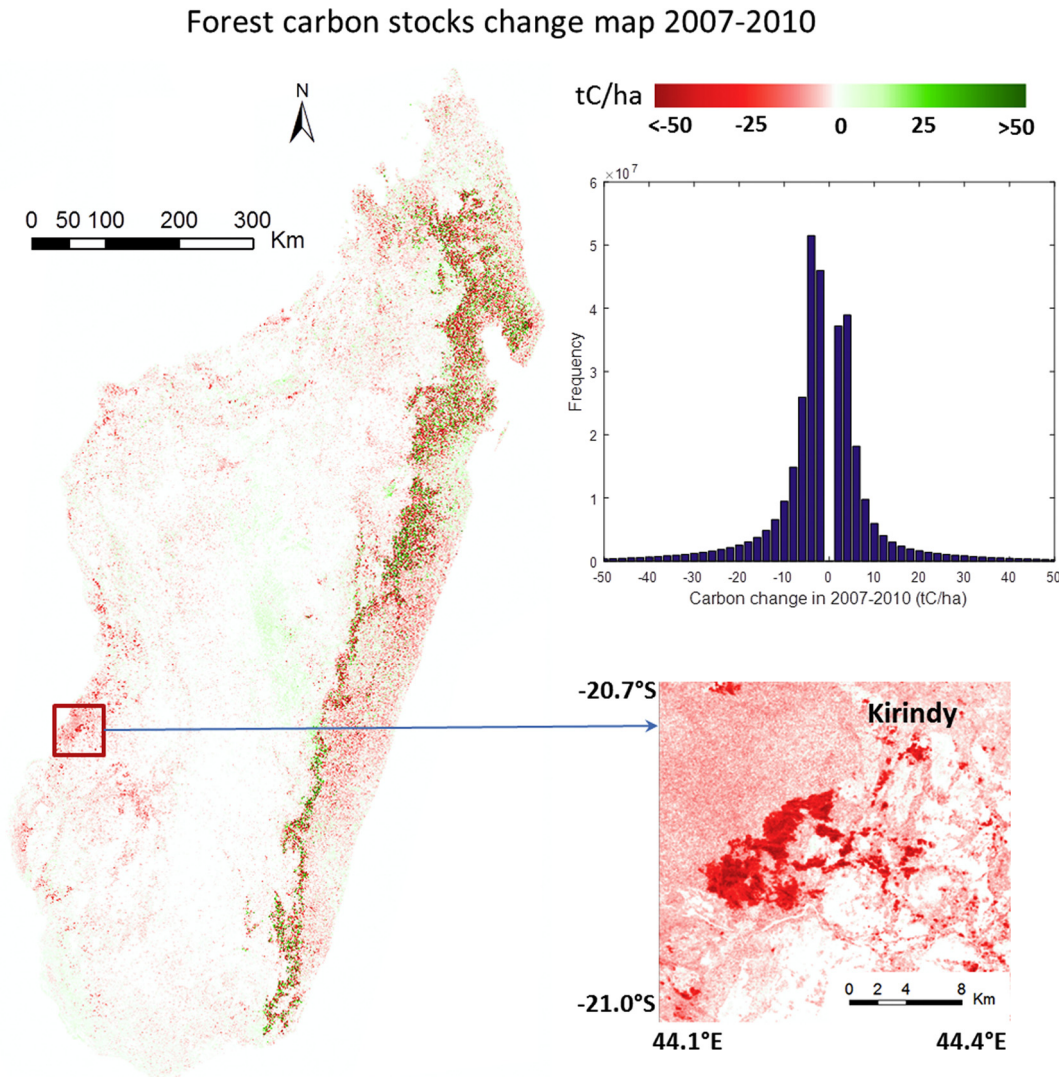


Fig. 8. Map of change in Madagascar forest carbon stocks in the period 2007–2010. A zoom version of the red-bordered box is provided to facilitate visualization of the carbon loss in Kirindy. The top right panel is the histogram showing distribution of values, excluding values of zero. (For interpretation of the references to color in this figure legend, the reader is referred to the web version of this article.)

Baccini's, respectively. In all cases, we found that their results were underestimated for the total forest carbon stocks, owing to the low resolution of the maps used, with pixel size ranging from 250 m (Vieilledent) to 500 m (Baccini) to 1000 m (Saatchi) and to the limitation of the data in the model inversion, where missing data was treated as zeros. In our estimation, carbon stocks tended to decrease over 2007–2010 by approximately 0.01 PgC/year, caused by anthropogenic deforestation and probably climate change, both of which are known or suspected to lead to decrease carbon stocks in tropical forests elsewhere (Vieilledent et al., 2016). As shown by Fig. 8, most of the affected areas nationally are in areas of tropical moist forests, i.e., in the east of the island (see also Table 1). Indeed, in Madagascar, around 57 000 ha were deforested each year in the period 2000–2010 (see Vieilledent et al., 2018). Assuming a mean carbon stock of 100 tC/ha, we obtain an annual carbon loss of 0.006 PgC. The difference (0.004 PgC) could be attributed to degradation (caused by direct human actions, climatic events or both).

Finally, to highlight our results on changes in carbon stocks, Fig. 8 includes a zoom of an area (outlined in red) near Kirindy. This area of strong carbon stock loss is associated with deforestation, caused by the cyclone Fanele in 2009 followed by uncontrolled fires in the following years (Lewis and Bannar-Martin, 2012). In addition, for each year in

Madagascar, the forest carbon gain is usually < 5 tC/year (Fox et al., 2011; Poorter et al., 2016), equivalent to < 15 tC for the three-year period 2007–2010. Interestingly, this was confirmed by the histogram in Fig. 8, showing very few pixels with values of carbon change over 15 tC/ha.

5. Conclusions

In this study, we have developed a methodology for retrieving the full range of forest biomass values in Madagascar. The methods are based on 572 forest plots and 520 ALOS PALSAR mosaic tiles with 25-m resolution acquired from 2007 to 2010 over the entire island. The method improved the biomass inversion by combining radar intensity and data on tree cover, which resulted in increasing the correlation between the radar signal and biomass. The correlation between the radar signal and biomass measured in situ was high ($R^2 = 0.71$), and the RMSE was 30% (for biomass ranging from 0 to 500 t/ha). For the low range of biomass values (e.g., < 150 t/ha), the correlation was higher ($R^2 = 0.77$, $RMSE = 26\%$). The ALOS PALSAR mosaic data from all of Madagascar were inverted into biomass values. The spatial distribution of biomass at 25-m resolution for the entire island shows a west-east gradient. The biomass map also shows details of savanna

ecosystems close to the coast such as forest savanna, woody savanna, and gallery forests. Over 2007–2010 period, carbon stocks were found to have decreased constantly, owing to anthropogenic deforestation and probably to climate change. We expect these results to serve as a more accurate benchmark than the heretofore state-of-the-arts results of Saatchi et al. (2011), Baccini et al. (2012), and Vieilledent et al. (2016). Our results reinforce the science basis for current and future missions such as ALOS-2, SAOCOM and BIOMASS, increasing our confidence that they can provide accurate wall-to-wall biomass mapping, and thereby enabling progress on REDD initiatives. Combining radar signal with optical tree cover data appears to be a promising approach for using by L-band SAR to map forest biomass (and hence carbon) over broad geographical scales.

Acknowledgments

This work was supported in part by the Programme National de Teledetection Spatiale (PNTS, <http://www.insu.cnrs.fr/pnts>), project no. PNTS-2016-06. Ghislain Vieilledent was supported by the FRB-FFEM-BioSceneMada project (project agreement AAP-SCEN-2013I) and the ReCaREDD European Commission project. We thank the government of Burundi for funding the PhD research of Emile Ndikumana. ALOS PALSAR images were provided by the Japan Aerospace Exploration Agency.

References

- Baccini, A., Goetz, S.J., Walker, W.S., Laporte, N.T., Sun, M., Sulla-Menashe, D., Hackler, J., Beck, P.S.A., Dubayah, R., Friedl, M.A., Samanta, S., Houghton, R.A., 2012. Estimated carbon dioxide emissions from tropical deforestation improved by carbon-density maps. *Nat. Clim. Chang.* 2 (3), 182–185.
- Chave, J., Rejou-Mechain, M., Burquez, A., Chidumayo, E., Colgan, M.S., Delitti, W.B., Duque, A., Eid, T., Fearnside, P.M., Goodman, R.C., Henry, M., Martinez-Yrizar, A., Mugasha, W.A., Muller-Landau, H.C., Mencuccini, M., Nelson, B.W., Ngomanda, A., Nogueira, E.M., Ortiz-Malavassi, E., Pelissier, R., Ploton, P., Ryan, C.M., Saldarriaga, J.G., Vieilledent, G., 2014. Improved allometric models to estimate the aboveground biomass of tropical trees. *Glob. Chang. Biol.* 20 (10), 3177–3190. <http://dx.doi.org/10.1111/gcb.12629>.
- Dobson, M., Ulaby, F., LeToan, T., Beaudoin, A., Kasischke, E., Christensen, N., 1992. Dependence of radar backscatter on coniferous forest biomass. *IEEE Trans. Geosci. Remote Sens.* 30 (2), 412–415 (Mar).
- Fox, J.C., Vieilledent, G., Yosi, C.K., Pokana, J.N., Keenan, R.J., 2011. Aboveground forest carbon dynamics in Papua New Guinea: isolating the influence of selective-harvesting and El Niño. *Ecosystems* 14 (8), 1276–1288. <http://dx.doi.org/10.1007/s10021-011-9480-4>.
- Frost, C., Thompson, S.G., 2000. Correcting for regression dilution bias: comparison of methods for a single predictor variable. *J. R. Stat. Soc.* 163 (2), 173–189.
- Fuller, W.A. (Ed.), 1987. *Measurement Error Models*. John Wiley, New York.
- Goodman, S., Benstead, J. (Eds.), 2003. *The Natural History of Madagascar*. University of Chicago Press.
- Hansen, M.C., Potapov, P.V., Moore, R., Hancher, M., Turubanova, S.A., Tyukavina, A., Thau, D., Stehman, S.V., Goetz, S.J., Loveland, T.R., Kommareddy, A., Egorov, A., Chini, L., Justice, C.O., Townshend, J.R.G., 2013. High-resolution global maps of 21st-century forest cover change. *Science* 342 (6160), 850–853.
- Ho Tong Minh, D., Le Toan, T., Rocca, F., Tebaldini, S., Mariotti d'Alessandro, M., Villard, L., 2014. Relating P-band synthetic aperture radar tomography to tropical forest biomass. *IEEE Trans. Geosci. Remote Sens.* 52 (2), 967–979 (Feb).
- Ho Tong Minh, D., Le Toan, T., Rocca, F., Tebaldini, S., Villard, L., Rejou-Mechain, M., Phillips, O.L., Feldpausch, T.R., Dubois-Fernandez, P., Scipal, K., Chave, J., 2016. SAR tomography for the retrieval of forest biomass and height: cross-validation at two tropical forest sites in French Guiana. *Remote Sens. Environ.* 175, 138–147 (Mar).
- Ho Tong Minh, D., Tebaldini, S., Rocca, F., Le Toan, T., Villard, L., Dubois-Fernandez, P., 2015, Feb. Capabilities of BIOMASS tomography for investigating tropical forests. *IEEE Trans. Geosci. Remote Sens.* 53 (2), 965–975.
- Hufty, M., Haakenstad, A., 2011. Reduced emissions for deforestation and degradation - a critical review. *J. Sustain. Dev.* 5 (1), 1–24.
- Le Toan, T., Beaudoin, A., Riou, J., Guyoni, D., 1992. Relating forest biomass to SAR data. *IEEE Trans. Geosci. Remote Sens.* 30 (2), 403–411 (Mar).
- Le Toan, T., Quegan, S., Davidson, M., Balzer, H., Paillou, P., Papathanassiou, K., Plummer, S., Rocca, F., Saatchi, S., Shugart, H., Ulander, L., 2011. The BIOMASS mission: mapping global forest biomass to better understand the terrestrial carbon cycle. *Remote Sens. Environ.* 2850–2860 (Jun).
- Lewis, R.J., Bannar-Martin, K.H., 2012. The impact of cyclone fanele on a tropical dry forest in Madagascar. *Biotropica* 44, 135–140.
- Lucas, R.M., Mitchell, A.L., Rosenqvist, A., Proisy, C., Melius, A., Ticehurst, C., 2007. The potential of L-band SAR for quantifying mangrove characteristics and change - case studies from the tropics. *Aquat. Conserv. Mar. Freshwat. Ecosyst.* 17 (1), 245–264.
- McLachlan, G.J., Do, K.-A., Ambroise, C. (Eds.), 2005. *Analyzing Microarray Gene Expression Data*. John Wiley, New York.
- Mermoz, S., Rejou-Mechain, M., Villard, L., Toan, T.L., Rossi, V., Gourlet-Fleury, S., 2015. Decrease of L-band {SAR} backscatter with biomass of dense forests. *Remote Sens. Environ.* 159 (0), 307–317. <http://www.sciencedirect.com/science/article/pii/S0034425714005112>.
- Mermoz, S., Toan, T.L., Villard, L., Réjou-Méchain, M., Seifert-Granzin, J., 2014. Biomass assessment in the Cameroon savanna using ALOS PALSAR data. *Remote Sens. Environ.* 155, 109–119. <http://www.sciencedirect.com/science/article/pii/S0034425714001540>.
- Mitchard, E., Saatchi, S., Lewis, S., Feldpausch, T., Woodhouse, I., Sonké, B., Rowland, C., Meir, P., 2011. Measuring biomass changes due to woody encroachment and deforestation/degradation in a forest savanna boundary region of central Africa using multi-temporal L-band radar backscatter. *Remote Sens. Environ.* 115 (11), 2861–2873. <http://www.sciencedirect.com/science/article/pii/S0034425711001337> {DESDynI} VEG-3D Special Issue.
- Morel, A.C., Saatchi, S.S., Malhi, Y., Berry, N.J., Banin, L., Burslem, D., Nilus, R., Ong, R.C., 2011. Estimating aboveground biomass in forest and oil palm plantation in Sabah, Malaysian Borneo using {ALOS} {PALSAR} data. *For. Ecol. Manag.* 262 (9), 1786–1798. <http://www.sciencedirect.com/science/article/pii/S0378112711004361>.
- Pan, Y., Birdsey, R.A., Fang, J., Houghton, R., Kauppi, P.E., Kurz, W.A., Phillips, O.L., Shvidenko, A., Lewis, S.L., Canadell, J.G., Ciais, P., Jackson, R.B., Pacala, S.W., McGuire, A.D., Piao, S., Rautiainen, A., Sitch, S., Hayes, D., 2011. A large and persistent carbon sink in the world's forests. *Science* 333, 988–993.
- Poorter, L., Bongers, F., Aide, T., Zambrano, A.A., Balvanera, P., Becknell, J., Boukili, V., Brancalion, P., Broadbent, E., Chazdon, R., Craven, D., de Almeida-Cortez, J., Cabral, G., de Jong, B., Denslow, J., Dent, D., DeWalt, S., Dupuy, J., Duran, S., Espirito-Santo, N., Fandino, M., Czar, R., Hall, J., Hernandez-Stefanoni, J., Jakovac, C., Junqueira, A., Kennard, D., Letcher, S., Licona, J., Lohbeck, M., Marin-Spiotta, E., Martinez-Ramos, M., Massoca, P., Meave, J., Mesquita, R., Mora, F., Munoz, R., Muscarella, R., Nunes, Y., Ochoa-Gaona, S., de Oliveira, A., Orihuela-Belmonte, E., Pena-Claros, M., Perez-Garcia, E., Piotto, D., Powers, J., Rodriguez-Velazquez, J., Romero-Perez, L., Ruiz, J., Saldarriaga, J., Sanchez-Azofeifa, A., Schwartz, N., Steininger, M., Swenson, N., Toledo, M., Uriarte, M., van Breugel, M., van der Wal, H., Veloso, M., Vester, H., Vicentini, A., Vieira, I., Bentos, T.V., Williamson, G., Rozendaal, D., 2016. Biomass resilience of neotropical secondary forests. *Nature* 530, 211–214 (Feb).
- Quegan, S., Le Toan, T., Yu, J.J., Ribbes, F., Floury, N., 2000, Mar. Multitemporal ERS SAR analysis applied to forest mapping. *IEEE Trans. Geosci. Remote Sens.* 38 (2), 741–753.
- Saatchi, S.S., Harris, N.L., Brown, S., Lefsky, M., Mitchard, E.T.A., Salas, W., Zutta, B.R., Buerman, W., Lewis, S.L., Hagen, S., Petrova, S., White, L., Silman, M., Morel, A., 2011. Benchmark map of forest carbon stocks in tropical regions across three continents. *Proc. Natl. Acad. Sci. U. S. A.* 108 (24), 9899–9904 (Jun).
- Shimada, M., Itoh, T., Motooka, T., Watanabe, M., Shiraishi, T., Thapa, R., Lucas, R., 2014. New global forest/non-forest maps from ALOS PALSAR data (2007–2010). *Remote Sens. Environ.* 155, 13–31. <http://www.sciencedirect.com/science/article/pii/S0034425714001527>.
- Shimada, M., Ohtaki, T., 2010, Dec. Generating large-scale high-quality sar mosaic datasets: application to palsar data for global monitoring. *IEEE J. Sel. Top. Appl. Earth Obs. Remote Sens.* 3 (4), 637–656.
- Thapa, R.B., Watanabe, M., Motooka, T., Shimada, M., 2015. Potential of high-resolution ALOS PALSAR mosaic texture for aboveground forest carbon tracking in tropical region. *Remote Sens. Environ.* 160, 122–133. <http://www.sciencedirect.com/science/article/pii/S0034425715000164>.
- Vieilledent, G., Gardi, O., Grinand, C., Burren, C., Andriamananjato, M., Camara, C., Gardner, C., Glass, L., Rasolohery, A., Ratsimba, H., Gond, V., Rakotoarijaona, J., 2016. Bioclimatic envelope models predict a decrease in tropical forest carbon stocks with climate change in Madagascar. *J. Ecol.* 104 (3), 703–715 (May).
- Vieilledent, G., Grinand, C., Rakotomalala, F.A., Ranaivosoa, R., Rakotoarijaona, J.-R., Allnutt, T.F., Achard, F., 2018. Combining global tree cover loss data with historical national forest-cover maps to look at six decades of deforestation and forest fragmentation in Madagascar. *Biol. Conserv.* 222, 189–197. <http://dx.doi.org/10.1016/j.biocon.2018.04.008>.
- Woodhouse, I.H., 2006. Predicting backscatter-biomass and height-biomass trends using a macroecology model. *IEEE Trans. Geosci. Remote Sens.* 44 (4), 871–877 (April).

APPENDIX D

ETUDE DE LA VEGETATION A PARTIR DE NOUVEAUX CAPTEURS SATELLITAIRES RADAR

ETUDE DE LA VEGETATION A PARTIR DE NOUVEAUX CAPTEURS SATELLITAIRES RADAR

1. Introduction

La croissance de la population mondiale, et par conséquent de ses besoins, exerce une pression croissante sur la végétation. Traditionnellement, la végétation est classée en forêts, végétation agricoles et prairies irriguées. La végétation a toujours constitué une ressource naturelle extrêmement importante pour l'homme, par exemple, pour répondre aux besoins en alimentation (agriculture), aux besoins de la vie quotidienne (produits forestiers, chauffage), protéger l'environnement (biomasse forestière) et, enfin, répondre aux besoins économiques des populations. En ce qui concerne la protection de l'environnement, la prise de conscience des problèmes environnementaux a incité la communauté internationale à adopter des solutions pour respecter les contraintes écologiques de manière coordonnée. Divers accords ont été signés, tels que le Protocole de Kyoto (1997) et la Convention-cadre des Nations Unies sur les changements climatiques (1992).

Dans le contexte de la gestion durable des ressources végétales, la mise en œuvre d'outils d'information comprenant la conception de systèmes de mesure et l'acquisition de données par ces systèmes, le traitement et l'analyse des données acquises, est nécessaire. Le suivi des ressources végétales se révèle souvent difficile en raison du manque d'accessibilité des zones agricoles et, en particulier, des zones forestières. En utilisant des données de télédétection disponibles à grande échelle avec différentes résolutions spatiales et temporelles, il est possible de surveiller les forêts, les zones agricoles et les prairies au moment opportun. Actuellement, l'observation de l'espace est présentée comme l'une des solutions efficaces à l'acquisition permanente d'information sur la gestion durable des ressources végétales et des territoires. De ce fait, de nouvelles générations de satellites offrent des opportunités renouvelées d'observation de la terre.

Les données de télédétection offrent une excellente occasion de surveiller et de fournir des informations à grande échelle sur les champs de cultures ou les forêts à un moment donné. Les techniques de télédétection radar sont particulièrement intéressantes car, contrairement aux techniques de télédétection optique, l'acquisition d'images est indépendante des conditions météorologiques et des conditions de luminosité (jour et nuit). Les capteurs optiques sont de plus limités par la couche nuageuse dans les zones tropicales et subtropicales où le riz est cultivé à grande échelle. Les systèmes radar à synthèse d'ouverture (SAR) ont la capacité de pénétrer dans la couche nuageuse jusqu'au sol. Les données SAR sont également bien adaptées pour distinguer le riz des autres types de couvert végétal en raison de la réponse spécifique du radar à la végétation inondée.

Afin d'estimer les paramètres biophysiques de la végétation, la télédétection est préférable aux méthodes de mesure nouvelles car elle permet d'utiliser les propriétés des satellites: la répétitivité et le balayage de grandes surfaces. Parmi les solutions spatiales, les capteurs radar présentent une sensibilité élevée aux éléments constitutifs de la biomasse et semblent donc les plus appropriés pour l'estimer avec une précision suffisante. De plus, les capteurs radar à grande longueur d'onde sont insensibles à la couverture nuageuse, ce qui est bénéfique pour l'observation des forêts tropicales au-dessus desquelles le couvert nuageux est quasi permanent.

Des systèmes de télédétection radar plus avancés sont aujourd'hui déployés, par exemple Sentinel-1 (bande C) et ALOS-1/PALSAR (bande L). Ainsi, le domaine de la télédétection radar continue de fournir des progrès technologiques, une gamme croissante de sources de données et de nouvelles

possibilités de recherche pour le suivi de la végétation. Dans cette thèse, nous avons décidé de nous concentrer sur les apports de ces nouveaux systèmes pour l'étude de la végétation. L'application des données de télédétection à la gestion des forêts a montré qu'elle nécessite l'utilisation de capteurs à grande longueur d'onde (bandes L et P) en raison de la capacité de pénétrer dans la végétation et le sol.

Pour la forêt, premier objet de notre étude, les problèmes de mise en œuvre sont étroitement liés à la connaissance de la quantité de masse forestière: comment évaluer la quantité de biomasse végétale à long terme ? Comment évaluer sa dynamique ? Quelle est sa distribution spatiale? Notre étude nous amène à répondre à tous ces questionnements en choisissant le type de données de télédétection adapté au suivi de la végétation. Cela nous conduit donc au choix des bandes de fréquences dans laquelle opèrent les capteurs sélectionnés.

Le deuxième type de végétation sélectionné pour notre étude est le riz, dont la culture avec celle du blé est capitale pour nourrir la population mondiale. Le riz représente ainsi environ 20 % de la production céréalière mondiale, juste derrière le blé. En sa phase végétative, sa culture ressemble aux prairies irriguées. À maturité, le riz ressemble au blé. Des questions spécifiques se posent néanmoins concernant la culture du riz : notamment, comment estimer ses paramètres biophysiques (la biomasse et la hauteur) ?

Cette recherche est basée sur des travaux expérimentaux avec une corrélation entre les résultats des observations *in situ* et les résultats fournis par les nouveaux satellites radar (Sentinel-1 et ALOS-1/PALSAR). L'objectif général de cette recherche est de fournir une meilleure compréhension des capacités des images radar pour estimer les paramètres (pour le riz et la forêt) et la cartographie des différentes cultures en Camargue. Pour appliquer les données de Sentinel-1 à l'estimation des paramètres du riz ou à la cartographie de la couverture terrestre, nous avons utilisé les méthodes d'apprentissage automatique (Machine Learning). Pour l'estimation de la biomasse forestière à Madagascar, nous combinons ALOS-1/PALSAR avec des données optiques Landsat (paramètre *tree cover*).

Notre étude comporte trois axes principaux :

- Premièrement, nous avons développé une nouvelle méthode qui démontre l'utilité des données SAR Sentinel-1 pour la classification de l'occupation du sol. Nos travaux ont mis en évidence la pertinence des deux approches de classification (LSTM¹ et GRU²) de réseaux neuronaux récurrents (RNN) qui considèrent explicitement la corrélation temporelle entre les données Sentinel-1 et les paramètres *in situ* afin de distinguer les classes agricoles de l'occupation du sol, généralement caractérisées par des comportements temporels similaires mais complexes.
- Deuxièmement, nous avons évalué la capacité des données SAR Sentinel-1 pour estimer les paramètres biophysiques du riz dans la région de Camargue, où trois approches classiques d'apprentissage automatique ont été appliquées aux données Sentinel-1: en l'occurrence, la méthode Régression Linéaire Multiple (MLR), la méthode de Régression à Support de Vecteur (SVR) et la méthode de Random Forest (RF).

¹ LSTM (Long Short-Term Memory) sont des unités d'un réseau neuronal récurrent. Une unité LSTM est composée d'une cellule, d'une porte d'entrée, d'une porte de sortie et d'une porte d'oubli.

² GRU (Gated Recurrent Unit) est une variante des LSTM introduite en 2014. Les réseaux GRU ont des performances comparables aux LSTM pour la prédiction de séries temporelles.

- Troisièmement, nous combinons les données ALOS/PALSAR avec des données de *tree cover* estimées à partir des données optiques Landsat pour étudier l'utilité de cette combinaison dans l'estimation de la biomasse forestière. Nous avons adapté une méthode qui améliore la récupération de la biomasse en combinant les données d'intensité radar et les données *tree cover*, ce qui a augmenté la corrélation entre le signal radar et la biomasse.

Cette thèse est composée de plusieurs chapitres. Le chapitre 2 donne un aperçu de la littérature sur les applications SAR sur la végétation. Le but de ce chapitre est de fournir les informations de base sur les données SAR utilisées dans cette thèse. Les chapitres suivants sont écrits en tant qu'ouvrages indépendants soumis à des revues scientifiques et publiés. Par conséquent, chaque chapitre peut être lu sans qu'il soit nécessaire de lire le chapitre précédent. Dans le chapitre 3, le problème de classification de l'occupation du sol à l'aide des données multitemporelles Sentinel-1 par application de la méthode de *Deep Learning* est discuté. Ce chapitre présente les résultats liés à la classification de l'occupation du sol en Camargue, au sud de la France, lors de la campagne 2017. Le chapitre 4 présente l'estimation de la hauteur et de la biomasse du riz en utilisant des données multitemporelles Sentinel-1 sur Camargue. Ce chapitre propose une meilleure compréhension de l'estimation des paramètres du riz *via* des données multitemporelles Sentinel-1 en appliquant des méthodes de *Machine Learning*. Le chapitre 5 évalue le potentiel de la combinaison des données ALOS/PALSAR aux données *tree cover* de Landsat pour la récupération de la biomasse forestière à Madagascar. La combinaison d'un signal radar aux données optiques et *tree cover* semble être une approche prometteuse à l'utilisation des données SAR en bande L pour cartographier la biomasse forestière à larges échelles géographiques.

2. Chapitre 2

Ce chapitre est consacré à la présentation de l'application des données SAR sur la végétation. Nous discutons des différentes caractéristiques de l'imagerie SAR, puis nous analysons la sensibilité des données SAR à la végétation et, finalement, nous parlons des différentes méthodes que nous avons utilisées dans nos applications pour le suivi la végétation avec des données SAR.

3. Chapitre 3

L'objectif de ce chapitre est d'évaluer le potentiel des données de télédétection Sentinel-1 à hautes résolutions spatiales et temporelles pour (i) cartographier l'occupation du sol (différentes cultures); et (ii) évaluer la nouvelle technique d'apprentissage en profondeur en la comparant aux approches standard d'apprentissage automatique (*K Nearest Neighbors*, *Random Forest*, and *Support Vector Machines*). Pour cela, nous proposons d'utiliser deux approches RNN³ (LSTM, GRU) pour estimer explicitement la corrélation temporelle des données de Sentinel-1 pour la région de Camargue.

Une enquête de terrain a été menée sur 921 parcelles de référence en juillet 2017 pour collecter les informations sur l'occupation du sol en Camargue. Nous avons choisi 11 classes de cultures observées : (1) riz ; (2) tournesol ; (3) pelouse ; (4) prairies irriguées ; (5) blé dur ; (6) luzerne; (7) tomate; (8) melon; (9) trèfle; (10) marécages; et (11) vignobles.

³ RNN (réseau de neurones récurrents) est un réseau de neurones artificiels présentant des connexions récurrentes. Ce réseau est constitué d'unités (neurones) interconnectés interagissant non-linéairement et pour lequel il existe au moins un cycle dans la structure.

Les résultats des différentes approches de classification sont satisfaisants. Avec la validation croisée (5 fois) de toutes les méthodes sur les données multitemporelles Sentinel-1, tous les indicateurs de performance des classificateurs sont très élevés, montrant ainsi la qualité de l'ensemble de données Sentinel-1 pour la classification des terres agricoles. Pour une meilleure compréhension du comportement des différents classificateurs, nous avons comparé F-Mesures par classe. Les onze classes sont évaluées selon les différentes méthodes (KNN⁴, RF, SVM, LSTM et GRU) utilisées dans la classification. De plus, les matrices de confusion sont également présentées suivant les différentes méthodes. Dans les deux cas, les résultats montrent une meilleure performance en utilisant des approches de classification basées sur le RNN par rapport aux méthodes classiques d'apprentissage automatique (KNN, RF et SVM). Entre les deux modèles RNN (LSTM et GRU), la méthode basée sur GRU obtient des résultats légèrement meilleurs que ceux de LSTM. En appliquant le meilleur classificateur GRU de la méthode RNN pour la zone d'étude, nous avons établi la carte de couverture des terres agricoles pour la Camargue en 2017. Parmi les différentes classes agricoles, le riz est la culture dominante (avec 29.3 % et 10 627 ha) par son étendue et sa présence partout dans la région.

Nous avons démontré que, même avec les approches classiques (KNN, RF et SVM), une bonne performance de classification pouvait être obtenue avec les séries temporelles d'images Sentinel-1. Nous avons aussi montré que l'utilisation de réseaux neuronaux récurrents pour gérer des données multitemporelles Sentinel-1 permet une visualisation des classes agricoles supérieure aux méthodes classiques d'apprentissage automatique. Les expériences menées mettent en évidence la pertinence d'une classe spécifique de modèles d'apprentissage profond (RNN) qui considère explicitement la corrélation temporelle des données afin de discriminer entre les classes agricoles de l'occupation du sol, généralement caractérisées par des comportements temporels similaires mais complexes.

4. Chapitre 4

Ce chapitre a pour but d'analyser la capacité des données SAR Sentinel-1 à estimer les paramètres du riz en Camargue (hauteur et biomasse). La hauteur du riz est une caractéristique agronomique importante. L'estimation de la hauteur des plants est considérée comme une méthode simple pour suivre la croissance du riz, car ce paramètre influence grandement le rendement. La biomasse du riz est également considérée comme un indicateur important des processus écologiques et de gestion de la végétation.

En Camargue, il existe une seule saison rizicole, de mai à septembre, quand la température et les précipitations sont les plus élevées. La riziculture inondée permet la rotation de l'eau nécessaire à la désalinisation du sol et l'introduction d'autres cultures telles que le blé, le tournesol et la vigne. En Camargue, la récolte de riz a un impact important sur l'équilibre écologique, économique et social.

L'observation temporelle de la croissance du riz est importante pour comprendre les réponses radar des parcelles de riz à différents stades de croissance. Il existe trois grandes périodes de culture du riz : la période de semis (suivant les conditions météorologiques, de fin avril à mi-mai), la période de croissance (jusqu'en septembre) et la période de récolte (fin septembre à début octobre).

⁴ La méthode des K plus proches voisins (*K Nearest Neighbor*) est une méthode d'apprentissage supervisé, qui nécessite de connaître K , le nombre de voisins à considérer.

Une campagne de suivi des parcelles de riz a été réalisée de mai 2017 à septembre 2017 sur 11 parcelles de référence de riz sélectionnées. Parallèlement, les données radar Sentinel-1 ont été acquises (25 acquisitions en mode TOPS) de mai 2017 à septembre 2017, à un intervalle de 12 jours. Il s'agit de données à double polarisation (VV et VH), conduisant à 50 images au total. Tout d'abord, une image de référence a été sélectionnée, et toutes les images y sont enregistrées en tenant compte de l'acquisition de TOPS.

Dans ce chapitre, nous avons amélioré le jeu de données de série temporelle SAR Sentinel-1 en exploitant un filtrage adaptatif temporel pour réduire le chatoiement, tout en conservant autant que possible les structures fines présentes dans les images radar. Enfin, toutes les images sont orthorectifiées en coordonnées cartographiques. Cela peut être fait en simulant une image SAR à partir du SRTM DEM 30 m. Pour estimer les paramètres biophysiques du riz, différentes méthodes ont été appliquées à ces données multitemporelles Sentinel-1 : en l'occurrence, les méthodes de Régression linéaire multiple (MLR), la régression à Support de Vecteur (SVR) et la méthode Random Forest (RF).

La régression linéaire multiple (MLR) est utilisée pour décrire les variations d'une variable dépendante (qui varie sous l'influence d'autres paramètres du système) sous l'influence de plusieurs variables indépendantes (qui varient sans être influencées par d'autres paramètres du système). La régression de vecteur de support (SVR) est une technique non paramétrique et une méthode de régression non linéaire. La SVR est considérée comme une technique non paramétrique car elle repose sur les fonctions kernel. Les algorithmes SVR utilisent les fonctions kernel qui prennent les données en entrée et les transforment dans la forme requise.

Comme SVR, la méthode Random Forest (RF) est aussi une méthode non paramétrique utilisée dans l'estimation des caractéristiques de la végétation. Random Forest est une technique d'apprentissage développée par Breiman pour améliorer la méthode de classification et de régression en combinant un grand ensemble d'arbres de décision. Pour l'analyse de performance de trois méthodes (MLR, SVR, RF), nous appliquons une méthode de validation croisée (K-Folds = 5). Afin de vérifier l'efficacité de trois méthodes appliquées sur les données Sentinel-1 (polarisations VH, VV, VH et VV), la hauteur et la biomasse de riz estimées sont comparées aux mesures de vérité terrain.

Nous avons évalué les paramètres du riz en utilisant les données Sentinel-1 avec des approches standard d'apprentissage automatique. Le but de ces approches est d'utiliser les mesures terrain pour former des modèles basés sur les jours après semis (DaS) avec polarisation simple (VV ou VH) et double polarisation (VH and VV) pour prédire les valeurs de hauteur et de biomasse du riz.

Pour le modèle MLR, il n'est pas nécessaire de choisir les paramètres optimaux, car ils peuvent être estimés directement. En revanche, pour améliorer les performances des modèles RF et SVR, il est important d'ajuster les paramètres optimisés dans le processus d'estimation. Dans ce chapitre, les paramètres sont définis par une recherche de grille pour obtenir les meilleures performances. Pour les modèles RF et SVR, nous avons constaté que les paramètres étaient assez similaires dans les polarisations simple et double. Pour le modèle SVR, nous utilisons la fonction de base radiale (RBF⁵) kernel avec le paramètre de complexité de 50 et le gamma de 0.9 pour la biomasse de riz, tandis que pour la hauteur, ils sont respectivement de 0.7 et 60. Les paramètres de complexité et gamma sont des

⁵ En apprentissage automatique, la fonction de base radiale (RBF : Radial Basis Function) est une fonction populaire du noyau utilisée dans divers algorithmes d'apprentissage noyau. En particulier, il est couramment utilisé dans la classification des machines à vecteurs de support.

indicateurs utilisés dans le modèle SVR. Pour le modèle RF, nous avons défini le nombre de paramètres à utiliser à chaque nœud à 7 et le nombre d'arbres à 80 pour l'estimation de la biomasse et de la hauteur du riz.

Quant au signal radar, il croît au fur et à mesure que la hauteur du riz et la biomasse augmentent. Les rétrodiffusions en VH et VV s'élèvent fortement au stade végétatif. Par contre, au stade de la reproduction et de la maturation, alors que la rétrodiffusion VH continue de croître légèrement, le VV diminue. La rétrodiffusion des polarisations VH et VV peut être séparée en deux parties principales. Dans la première partie, VV et VH augmentent avec la croissance du riz jusqu'à 50 cm de hauteur. A ce stade, le principal mécanisme de rétrodiffusion est dû à l'interaction entre la tige et la surface de l'eau sous-jacente. Dans la deuxième partie (alors que le riz pousse de 50 cm à 100 cm jusqu'à sa maturité), bien que le VV décroisse, le VH continue à augmenter légèrement. En effet, à ce stade, les mécanismes de rétrodiffusion sont apportés non seulement par l'interaction à double rebond, mais aussi directement à partir de la tige du volume. Au-delà de 50 cm, le phénomène de double rebond peut être réduit : la tige et les feuilles de riz ne sont plus verticales. Même si nous constatons une diminution de la puissance de la rétrodiffusion VV, le signal VH continue à augmenter en raison de sa sensibilité à la rétrodiffusion au volume de la canopée du riz.

La pertinence des trois méthodes MLR, SVR et RF appliquées en utilisant des données Sentinel-1 avec plusieurs configurations de polarisations (VH seul, VV seul, VH et VV ensemble) a été analysée en utilisant les valeurs RMSE (*Root Mean Square Error*) et R^2 . La méthode utilisée pour estimer les paramètres est supposée être efficace lorsque le RMSE est aussi faible que possible. Nous constatons que les méthodes non paramétriques (SVR et RF) ont de meilleures performances que la méthode paramétrique MLR pour estimer les paramètres du riz. Entre les modèles SVR et RF, la méthode RF fournit des résultats légèrement meilleurs que le SVR. Avec la méthode RF, le coefficient de corrélation R^2 et RMSE sont respectivement de 0.92 et 16 % (7.9 cm) pour l'estimation de hauteur de riz, de 0.90 et de 18 % (162 g.m⁻²) pour l'estimation de la biomasse sèche de riz. Pour la hauteur du riz, toutes les méthodes (MLR, SVR et RF) donnent les meilleures performances en utilisant ensemble VV et VH. Pour la biomasse de riz, nous observons qu'avec les méthodes SVR et RF la combinaison des polarisations VH et VV fournit des moins bons résultats que l'utilisation simple de la polarisation VH.

Dans cette étude, nous avons démontré que les données de télédétection Sentinel-1 pourraient constituer une approche alternative et fiable pour suivre la croissance de riz et estimer la biomasse sèche. Les futurs travaux dans la région de la Camargue pourraient être axés sur l'exploitation des données de Sentinel-1 afin d'améliorer les modèles de culture, de mieux estimer la production du riz et de pouvoir proposer des stratégies de développement agricole durable.

5. Chapitre 5

Dans ce chapitre, nous proposons une approche qui améliore l'estimation de la biomasse forestière à Madagascar par la combinaison des données d'intensité radar et des données *tree cover*. Les données de terrain sont disponibles à partir de neuf inventaires forestiers réalisés sur la période 1996-2013. La collaboration avec différentes institutions (institutions gouvernementales, ONGs, instituts de recherche en particulier le CIRAD) nous a permis d'obtenir des données sur un grand nombre de parcelles forestières (1 771) dans les trois régions forestières de Madagascar (forêts humides, sèches et épineuses). Cependant, dans ce travail, nous n'avons utilisé que les inventaires forestiers de 2007-2013 pour les comparer aux données ALOS/PALSAR, dans lesquelles 572 parcelles ont été sélectionnées

sur la base de la pente du terrain et de l'homogénéité dans les parcelles. La largeur des parcelles était de 30 m dans la forêt humide (taille de la parcelle de 0.28 ha) et de 20 m dans la forêt sèche ou épineuse (taille de la parcelle de 0.13 ha).

Les données ALOS/PALSAR, d'une résolution de 25 m couvrant l'ensemble de Madagascar de 2007 à 2010, ont été fournies gratuitement par la JAXA (Japan Aerospace Exploration Agency). Les données *tree cover* à une résolution de 30 m ont été ré-échantillonnées à 25 m pour être combinées avec les données SAR. Les images ALOS/PALSAR utilisées dans cette étude ont été traitées par la JAXA en utilisant l'algorithme de mosaïquage à grande échelle. Cet algorithme comprend l'ortho-rectification, la correction de la pente et l'étalonnage radiométrique entre les bandes voisines.

Sur la base des résultats de la littérature sur la sensibilité de l'intensité de la bande L par rapport à la biomasse, il est possible d'utiliser la bande L (polarisation HV) pour estimer la biomasse forestière jusqu'à un maximum de 150 t/ha. Pour des valeurs plus élevées de biomasse, l'intensité de la bande L est faiblement sensible à la biomasse forestière. Nous présentons une méthode pour résoudre ce problème. Tout d'abord, nous proposons de pondérer l'intensité du radar par le facteur *tree cover* en utilisant la formule suivante:

$$\gamma_{HVtree}^0 = 10 \times \log_{10}(treecover \times DN_{HV}^2) + CF \quad (1)$$

Où γ_{HVtree}^0 correspond à l'intensité du signal radar pondérée par *tree cover* (valeur entre 0 et 1), DN_{HV} est le compte numérique (valeur du pixel) du pixel en polarisation HV et CF, un coefficient de calibration de -83dB.

Pour mettre en évidence l'utilité de γ_{HVtree}^0 dans notre approche, nous comparons la sensibilité de γ_{HV}^0 (intensité radar non pondérée), de γ_{HVtree}^0 et des données *tree cover* avec les valeurs de biomasse *in situ* pour une petite gamme de biomasse (par exemple, < 150 t/ha). La corrélation la plus élevée est observée avec les données d'intensité radar pondérées. Les données en γ_{HV}^0 montrent une sensibilité à la biomasse beaucoup plus faible ($R^2 = 0.34$) que les données en γ_{HVtree}^0 ($R^2 = 0.77$). Une explication possible de ce résultat est que l'intensité du radar intègre les signaux de bruit provenant du sol. Ce problème peut être partiellement atténué en incorporant des données de *tree cover* à partir d'images optiques. Enfin, en comparant γ_{HVtree}^0 et *tree cover*, les données de γ_{HVtree}^0 sont d'une grande sensibilité à la biomasse ($R^2 = 0.77$ versus 0.72) avec une erreur quadratique moyenne plus faible (RMSE) (26 % contre 30 %).

Pour les biomasses inférieures à 150 t/ha, nous adaptons un modèle exponentiel pour relier le signal radar à la biomasse suivant la relation :

$$\gamma_{HVtree}^0 = a + b \times (1 - e^{-c \times AGB}) \quad (2)$$

Où AGB est la biomasse *in situ*, et a, b et c sont des coefficients qui sont estimés par moindres carrés à partir des données du signal radar.

Pour des valeurs de biomasse supérieures à 150 t/ha, nous avons adapté un modèle linéaire, décrit comme suit :

$$\gamma_{HVtree}^0 = m + n \times AGB \quad (3)$$

Où m et n sont aussi des coefficients qui sont estimés par moindres carrés à partir des données du signal radar.

En utilisant les équations (2) et (3), l'estimation de la biomasse AGB peut être calculée à partir de γ_{HVtree}^0 . Dans notre approche, un biais dans l'inversion de ces deux équations peut être introduit. Dans la littérature, ce phénomène est appelé « dilution par régression » car une erreur aléatoire dans la variable indépendante conduit à une sous-estimation systématique de la pente de régression. Pour corriger ce biais, nous compensons la biomasse par un ratio β , décrit comme suit:

$$Biais[\widehat{AGB}] = \beta \times AGB \quad (4)$$

Une méthode courante d'estimation de biomasse consiste à exploiter un modèle inverse, basé sur la régression empirique obtenue à partir de l'ensemble de données disponibles *in situ* et radar. Dans ce travail, nous avons choisi 572 parcelles de biomasse pour les suivre avec des données SAR, séparément, année par année (2007, 2008, 2009 et 2010). Par exemple, pour l'année 2010, nous avons constaté que :

1. pour des biomasses inférieures à 150 t/ha:

$$AGB = -\frac{1}{c} \times \ln\left(1 - \frac{\gamma_{HVtree}^0 - a}{b}\right) \quad (5)$$

Avec $a = -29.13 \pm 0.09$; $b = 18.47 \pm 0.14$ and $c = 0.01623 \pm 0.00034$.

Pour cette gamme de biomasse, γ_{HVtree}^0 est très fortement corrélé à la biomasse

($R^2 = 0.77$ et $p < 10^{-5}$).

2. pour des biomasses supérieures à 150 t/ha et *tree cover* supérieure à 95 %:

$$\widehat{AGB} = \frac{\gamma_{HVtree}^0 - m}{n} \quad (6)$$

Avec $m = -12.14 \pm 0.28$ et $n = -9.28 \times 10^{-4} \pm 9.35 \times 10^{-5}$

Pour de grandes valeurs de biomasse, γ_{HVtree}^0 est faiblement corrélé à la biomasse ($R^2 = 0,18$ et $p = 0,017$).

Enfin, la biomasse estimée peut être calculée comme suit :

$$Biomasse = (1 + \beta) \times AGB \quad (7)$$

Avec $\beta = 0.2392 \pm 0.0515$

Pour calculer le stock de carbone, nous convertissons la biomasse en unité de carbone en utilisant le rapport de 0.47. Nous appliquons un filtre à ces données de carbone en fonction de la carte de *tree cover* et n'incluons que des pixels avec des valeurs de *tree cover* supérieures à 25 %. En d'autres termes, nous suivons une approche conservatrice dans la définition de la forêt : seules les zones avec un *tree cover* d'au moins 25 % sont considérées comme de la forêt.

Les méthodes proposées ont été appliquées aux données ALOS/PALSAR à Madagascar. Le RMSE et la corrélation R^2 ont été utilisés pour évaluer la performance de l'ensemble de données SAR pour chaque année, en utilisant toutes les parcelles *in situ* disponibles. Les mêmes performances pour la récupération de la biomasse par rapport aux données *in situ* ont été observées pour les quatre années (2007, 2008, 2009 et 2010).

Les résultats ont montré un RMSE de 30 % (pour la biomasse allant de 0 à 500 t/ha) et $R^2 = 0.71$ pour l'année 2010. Nous avons effectué une procédure de validation croisée 10 fois. Pour les valeurs de biomasse comprises entre 0 et 150 t/ha, le RMSE moyen en 2010 était de 26 % et $R^2 = 0.77$, alors que pour les valeurs de biomasse comprises entre 0 et 300 t/ha la même année, le RMSE moyen était de 28 % et $R^2 = 0.72$.

Les images ALOS/PALSAR à 25 m de résolution ont été utilisées pour estimer la biomasse pour les années 2007, 2008, 2009 et 2010. Les cartes de biomasse pour ces quatre années se sont avérées similaires dans leur contenu en biomasse. Nous avons montré que la biomasse peut être cartographiée efficacement même dans les forêts tropicales denses. Ces résultats renforcent considérablement notre confiance dans la capacité des missions actuelles et futures, telles que ALOS-2 (la bande L), le SAOCOM en bande L et la BIOMASS en bande P, de fournir une cartographie précise de la biomasse. En particulier, l'arrivée du capteur BIOMASS en bande P, qui exploitera une couche de volume par le traitement tomographique qui permettra d'estimer la biomasse forestière avec une erreur relative d'environ 11 % à une résolution de 4 ha.

6. Conclusion générale

L'objectif général de ce travail de thèse était d'évaluer la contribution des données radar satellitaires acquises par Sentinel-1 et ALOS-1/PALSAR combinées aux données optiques (Landsat) à la surveillance des forêts et au suivi des cultures, en particulier du riz. Cette recherche a nécessité l'acquisition de données satellitaires et de terrain pour déterminer la répartition spatiale de la couverture terrestre, analyser la sensibilité des données radar pendant la période végétative et évaluer différents paramètres biophysiques de la végétation. Ce travail de thèse a été réalisé en trois parties.

Le but de la première partie était de mieux comprendre l'utilité des images radar Sentinel-1 pour la cartographie de la couverture des terres agricoles grâce à l'utilisation de techniques *Deep Learning*. L'analyse a été effectuée à partir des données multi-temporelles Sentinel-1 sur une zone de la Camargue, en France. L'ensemble de données radar a été traité sur une période allant de mai 2017 à septembre 2017. Nous avons amélioré cet ensemble de données multi-temporelles en exploitant le filtrage temporel pour réduire le bruit, tout en conservant autant que possible les fines structures présentes dans les images. Nous avons constaté que, même avec les approches classiques d'apprentissage automatique (KNN, RF, SVM), une bonne classification des performances pourrait être obtenue avec précision supérieure à 86 % et un meilleur coefficient Kappa de 0.82. Nous avons trouvé que les résultats des deux classificateurs basés sur le réseau neuronal récurrent profond (RNN) ont clairement surpassé les approches classiques. Enfin, nos analyses des résultats de la zone Camargue montrent que la même performance a été obtenue avec deux méthodes de classifications de RNN (LSTM et GRU) appliquées sur la classe riz, qui est la culture dominante de cette région, donne une F-Mesure de 96 %. Ces résultats mettent ainsi en évidence que, dans un avenir proche, ces techniques basées sur le RNN joueront un rôle important dans l'analyse des séries temporelles de télédétection. Enfin, comme le pouvoir des images optiques est parfois limité en raison de la

couverture nuageuse, l'utilisation de données multi-sources, y compris optiques, et des données radar constitueront un sujet de recherche important.

Dans la seconde partie, l'objectif était d'étudier les capacités des images radar multi-temporelles pour l'estimation de la hauteur du riz et de la biomasse sèche à l'aide des données Sentinel-1. Pour ce faire, nous avons utilisé les données Sentinel-1 et les mesures *in situ* avec des techniques classiques de *Machine Learning* : Régression Linéaire Multiple (MLR), Régression du vecteur Support (SVR) et Random Forest (RF)). L'étude a été réalisée sur le même ensemble de données Sentinel-1 que dans la première partie. Les mesures *in situ* ont été effectuées au cours de la même période d'acquisition des images radar pour collecter la hauteur de riz et la biomasse sèche sur 11 parcelles. Les données Sentinel-1 ont été traitées afin de produire un *stack* d'images comprenant des données en polarisations VV et VH. Nous avons trouvé que les méthodes non paramétriques (SVR et RF) ont une meilleure performance par rapport à la méthode paramétrique MLR pour l'estimation des paramètres biophysiques du riz.

La précision sur l'estimation de la hauteur du riz a montré que celle-ci était fortement corrélée à la hauteur de riz *in situ*. La méthode RF présente la meilleure performance, avec un coefficient de corrélation $R^2 = 0.92$ et une erreur quadratique moyenne de 16 % (7.9 cm). De plus, nous avons démontré que la corrélation du signal Sentinel-1 à la biomasse était également très élevée en polarisation VH, avec $R^2 = 0.9$ et RMSE = 18% (162 g.m⁻²) (avec la méthode Random Forest). Ces résultats indiquent que les données radar de Sentinel-1 pourraient être exploitées pour la récupération de la biomasse et de la hauteur du riz et qu'elles pourraient être utilisées pour des tâches opérationnelles.

Dans les recherches futures, la combinaison de données des deux satellites Sentinel-1 et Sentinel-2 sera une nécessité car il sera possible de mener des missions à grande échelle de l'un ou l'autre. Les données radar et optiques peuvent apporter un autre complément car elles offrent des perspectives différentes sur la surface de la Terre, fournissant des informations différentes selon leur spécificité. Les deux types de données peuvent également être fusionnés pour fournir des informations provenant de sources multiples et fournir des résultats améliorés pour la prise de décision.

Enfin, la réduction des émissions de carbone dues à la déforestation nécessite un aperçu détaillé de la manière dont la biomasse forestière est mesurée et distribuée. Les études réalisées à ce jour ont estimé les stocks de biomasse forestière à l'aide d'hypothèses approximatives et de données peu fiables. Des données à haute résolution et des méthodes robustes sont nécessaires pour saisir la variabilité spatiale de la biomasse forestière avec une précision suffisante. Nous visons à améliorer les approches précédentes en utilisant des observations de satellites radar ALOS/PALSAR (résolution de 25 m) et optiques dérivant de Landsat (résolution de 30 m) pour estimer les stocks de biomasse forestière à Madagascar, pour les années 2007-2010. Le signal radar et la biomasse *in situ* étaient fortement corrélés ($R^2 = 0.71$) et l'erreur quadratique moyenne était de 30 % (pour la biomasse allant de 0 à 500 t/ha). Les stocks de carbone ont diminué de façon constante au cours de cette période en raison de la déforestation anthropique et probablement aussi du changement climatique. Nous pensons que ces résultats serviront avant tout de référence dans les études ultérieures. Nos résultats renforcent la base scientifique des missions actuelles et futures telles ALOS-2 et BIOMASS. Nous sommes ainsi convaincu qu'elles sauront fournir une cartographie mondiale de biomasse, permettant ainsi de faire progresser les initiatives REDD. La combinaison d'un signal radar avec des données optiques *at tree cover* semble être une approche prometteuse pour l'utilisation de SAR en bande L afin de cartographier la biomasse forestière (et donc le carbone) à de larges échelles géographiques.

